NOVA SCHOOL OF SCIENCE & TECHNOLOGY

DEPARTMENT OF CHEMISTRY

Ana Rita Reis

BSc in Chemistry

SENSING OF BIORELEVANT MOLECULES WITH METAL-ORGANIC FRAMEWORK FILMS

MASTER IN BIOORGANIC CHEMISTRY

NOVA University Lisbon

October, 2022

NOVA SCHOOL OF SCIENCE & TECHNOLOGY

DEPARTMENT OF CHEMISTRY

SENSING OF BIORELEVANT MOLECULES WITH METAL-ORGANIC FRAMEWORK FILMS

Adviser: Paulo Nuno Martinho
Auxiliary Researcher, Faculdade de Ciências, Universidade de Lisboa

Co-adviser: Clara S. B. Gomes
Auxiliary Researcher, NOVA University Lisbon

MASTER IN BIOORGANIC CHEMISTRY

NOVA University Lisbon
October, 2022

Sensing of biorelevant molecules with metal-organic framework films

Copyright © Ana Rita Reis, NOVA School of Science and Technology, NOVA University Lisbon.

The NOVA School of Science and Technology and the NOVA University Lisbon have the right, perpetual and without geographical boundaries, to file and publish this dissertation through printed copies reproduced on paper or on digital form, or by any other means known or that may be invented, and to disseminate through scientific repositories and admit its copying and distribution for non-commercial, educational or research purposes, as long as credit is given to the author and editor.

To my eternal Clotilde.

Acknowledgements

My first acknowledgement goes to Dr. Sara Realista, my true pillar over this last year. Thank you for being such a dedicated and hard-working researcher and for being the perfect role model. For being there whenever needed and to help me overcome all my thesis limitations. You helped me to grow, not only as a researcher, but as a person.

I also want to acknowledge Dr. Paulo Nuno Martinho for supervising me and for being as great a researcher as a person. Thank you for always having an answer to my questions and for once again accepting the challenge of supervising me. I am truly blessed to have such motivating researchers along the way.

Next, I want to thank Dr. Clara Gomes for co-supervising me along this year, for always being available and for the fruitful discussions.

I would also like to thank the helpful collaborations for the film characterisations, namely, Prof. Dr. Ana Rego and Dr. Ana Ferraria for XPS, Dr. Telmo Nunes for SEM, Prof. Dr. Estrela Jorge for XRD, Drs. Victoria Corregidor and Luis Alves for PIXE and RBS, Prof. Dr. João Pires da Silva for BET surface area, Prof. Dr. Ana Viana for AFM and Profs. Drs. Liliana Ferreira and Margarida Cruz for the help with the deposition with an external magnetic field.

I would also like to thank Prof. Dr. Paula Branco for warming my way into FCT NOVA and for enhancing my interest for organic chemistry. From all the teachers, Prof. Dr. Maria Manuel Marques stood out as an extremely kind teacher that motivated me to never settle in terms of learning.

Following, I thank the rest of my laboratory colleagues for the mutual help and for the crazy ride. To my friends, who made me laugh and still heard me out in the most stressful moments - this crazy friend loves you.

Finally, I would like to thank Marcos, for the unconditional love and support.

ABSTRACT

Uric acid plays a major role in medical applications since its abnormal concentration translates into a diagnostic tool for clinical disorders such as gout, hyperuricemia or the Lesch–Nyhan syndrome. Therefore, the development of purine sensors became significant and relies on the fabrication of thin films and/or membranes based on nanomaterials. Metal-organic frameworks are constituted by organic linkers and metal ions. These have shown some promising results as sensors that can be attributed to their crystallinity, high and permanent porosity, and the presence of several active sites. This work will focus on Fe-MOF-74, with a crystal structure consisting of hexagonal channels and highly reactive metal sites. Metal-organic frameworks are conventionally prepared by solvothermal/hydrothermal methods, obtained as microcrystalline powders. These indirect techniques become limited by the complexity in casting the material to the desired shape. Direct techniques have been used to overcome these limitations, namely, the electrochemical method. This work reports the cathodic deposition of Fe-MOF-74 for the electrochemical detection of uric acid. Herein, pro-ligands were synthesised and characterised by nuclear magnetic resonance, Fourier transform infrared spectroscopy and elemental analysis. The electro-synthesised films were characterised by Fourier transform infrared spectroscopy, elemental analysis, atomic force microscopy, X-ray diffraction, Brunauer, Emmett and Teller surface area from N_2 adsorption, scanning electron microscopy, particle-induced X-ray emission and Rutherford backscatter spectrometry. Finally, these films were applied to the electrochemical detection of uric acid and evaluated based on their limit of detection, sensitivity, and linear range.

Keywords: Cyclic voltammetry, cathodic deposition, films, uric acid

RESUMO

O ácido úrico desempenha um papel importante em aplicações medicinais, dado que a sua concentração anormal se traduz num diagnóstico de alterações clínicas, como a gota, hiperuricemia, ou a síndrome the Lesch-Nyhan. Posto isto, o desenvolvimento de sensores de purinas tornou-se significante, estando dependente do fabrico de filmes finos e/ou membranas baseados/as em nanomateriais. As redes metal-orgânicas são constituídas por ligandos orgânicos e iões metálicos. Estas têm vindo a apresentar resultados promissores enquanto sensores, atribuídos à sua elevada cristalinidade e porosidade, assim como à presença de vários sítios ativos. Este trabalho será focado na Fe-MOF-74, que apresenta uma estrutura cristalina constituída por canais hexagonais e centros metálicos altamente reativos. As redes metal-orgânicas são convencionalmente preparadas através de métodos solvotérmicos/hidrotérmicos, obtendo-as na forma de pó microcristalino. Estas técnicas indiretas tornam-se limitadas pela complexidade na moldagem dos materiais na forma desejada. As técnicas diretas têm vindo a colmatar estas limitações, nomeadamente, o método eletroquímico. Este trabalho reporta a deposição catódica da Fe-MOF-74 e derivados para a deteção eletroquímica de ácido úrico. Para tal, pró-ligandos foram sintetizados e caracterizados através de ressonância magnética nuclear, espetroscopia de infravermelho com transformada de Fourier e análise elementar. Os filmes eletrosintetisados foram caracterizados através de espetroscopia de infravermelho com transformada de Fourier, análise elementar, espetroscopia de força atómica, difração de raios-X, área superficial de Brunauer, Emmett and Teller obtida através da adsorção de N_2, microscopia eletrónica de varrimento, emissão de raios-X induzida por partículas e espectrometria de retroespalhamento de Rutherford. Por fim, estes filmes foram aplicados na deteção eletroquímica de ácido úrico avaliados com base no limite de deteção , sensibilidade e gama linear.

Palavras chave: Voltametria cíclica, deposição catódica, filmes, ácido urico

CONTENTS

LIST OF FIGURES

LIST OF TABLES

LIST OF SCHEMES

LIST OF EQUATIONS

SYMBOLS AND ABBREVIATIONS

1D	Unidimensional
2D	Bidimensional
4-ASA	4-aminosalicylic acid
A	Ampere
Å	Angstroms
AFM	Atomic force microscopy
Aq.	Aqueous
ATP	Adenosine triphosphate
B	Base (**Chapter 2.2.3**) or external magnetic field (**Chapter 2.2.5**)
BCNT	Boron-doped carbon nanotube
BDC	Benzene-1,4-dicarboxylate
BET	Brunauer-Emmett-Teller
BnBr	Benzyl bromide
$B(pin)_2$	Bis(pinacolato)diboron
BTC	Benzene-1,3,5-tricarboxylate
BTEC	1,2,4,5-benzene-tetra-carboxylate
CE	Counter electrode
cm^{-1}	Wavenumber units
CME	Chemically modified electrode
COSY	Homonuclear correlation spectroscopy

CP	Coordination polymer
CT	Charge transfer
C_{UA}	Uric acid concentration
CV	Cyclic voltammetry
DMF	*N*,*N*-dimethylformamide
DMSO	Dimethyl sulfoxide
DOBDC	2,5-dioxido-1,4-benzenedicarboxylate
Dppf	1,1′-ferrocenediyl-bis(diphenylphosphine)
DPV	Differential pulse voltammetry
DRIFT	Diffuse reflectance infrared Fourier transform spectroscopy
DWCNT	Double-walled carbon nanotube
EA	Elemental analysis
E_{app}	Working potential
e.g.	For example (from Latin, *exempli gratia*)
E_p^c	Cathodic peak potential
Eqv.	Molar equivalents
Et_2O	Diethyl ether
EtOAc	Ethyl acetate
EtOH	Ethanol
Fc	Ferrocene
Fc^+	Ferrocenium
FTIR	Fourier-transform infrared spectroscopy
FTO	Fluorine tin oxide
GC	Glassy carbon
g-C_3N_4	Graphitic carbon nitride
GC-MS	Gas chromatography coupled to mass spectrometry
h	Hour
H_2BDC	Benzene-1,4-dicarboxylic acid

H_3BTC	Benzene-1,3,5-tricarboxylic acid
H_4BPTC	Biphenyl-3,3′,5,5′-tetracarboxylic acid
HBPTC	4-(3-carboxy-4-carboxylatobenzoyl)phthalate
H_4DOBDC	2,5-dihydroxyterephthalic acid
HKUST	Hong Kong University of Science and Technology
H_4L	2,5-dihydroxyterephthalic acid
H_4L1	3,3'-dihydroxy-[1,1'-biphenyl]-4,4'-dicarboxylic acid
H_4L2	4,4'-(1*H*-benzo[*d*]imidazole-4,7-diyl)bis(2-hydroxybenzoic acid)
H_4L3	4,4'-((3,4-dioxocyclobut-1-ene-1,2-diyl)bis(azanediyl))bis(2-hydroxybenzoic acid)
HMBC	Heteronuclear multiple quantum coherence
HMQC	Heteronuclear multiple bond correlation
HPLC	High performance liquid chromatography
i	Current density
I_A	Methyl 2-(benzyloxy)-4-iodobenzoate
I_B	Methyl 2-(benzyloxy)-4-(pinacolboronic ester) benzoate
I_C	Dimethyl 3,3'-bis(benzyloxy)-[1,1'-biphenyl]-4,4'-dicarboxylate
I_D	3,6-dibromobenzene-1,2-diamine
I_E	4,7-dibromo-1*H*-benzo[*d*]imidazole
I_F	Dimethyl 4,4'-(1*H*-benzo[*d*]imidazole-4,7-diyl)bis(2-(benzyloxy)benzoate)
i_f	Final current density
I_G	4-aminosalicylic acid
I_H	3,4-dimethoxy-3-cyclobutene-1,2-dione
i_p	Peak current density
IR	Isoreticular
ITO	Indium tin oxide
L	2,5-dioxido-1,4-benzenedicarboxylate

L1	3,3'-dioxido-[1,1'-biphenyl]-4,4'-dicarboxylate
L2	4,4'-(1*H*-benzo[*d*]imidazole-4,7-diyl)bis(2-oxidobenzoate)
L3	4,4'-((3,4-dioxocyclobut-1-ene-1,2-diyl)bis(azanediyl))bis(2-oxidobenzoate)
LC-MS/MS	Liquid chromatography coupled to tandem mass spectrometry
LOD	Limit of detection
M	Metal ion
MeOH	Methanol
MIL	*Matériaux de l'Institut Lavoisier*
MOF	Metal-organic framework
NMP	*N*-methyl-2-pyrrolidone
NMR	Nuclear magnetic resonance spectroscopy
NU	Northwestern University
OTf	Trifluoromethanesulfonate
P	Precipitate
PB	Pro-base
PBS	Phosphate buffer solution
PIXE	Particle-induced X-ray emission
ppm	Parts per million
pyr	Pyridine
Q	Charge
q	Charge density
RBS	Rutherford backscatter spectrometry
RE	Reference electrode
Redox	Reduction-oxidation reactions
Refs.	References
RT	Room temperature
SA	Salicylic acid

SA@FTO	Salicylic acid functionalised in fluorine tin oxide
SBU	Secondary building unit
SEM	Scanning electron microscopy
SPC	Screen-printed carbon
SWCN	Single-walled carbon nanohorns
T	Tesla
TA	Tannic acid
$TBAPF_6$	Tetrabutylammonium hexafluorophosphate
TGA	Thermogravimetric analysis
THF	Tetrahydrofuran
Tris	Tris(hydroxymethyl)aminomethane
UA	Uric acid
UiO	University of Oslo
UV-vis	Ultraviolet-visible spectroscopy
V	Volt
VNU	Vietnam National University
V/V	Volume/volume
w/	With
w%	Weight percentage
WE	working electrode
w/V	Weight/volume
XPS	X-ray photoelectron spectroscopy
XRD	X-ray diffraction
ZIF	Zeolitic imidazolate framework
ºC	Celsius degrees
Δ	Temperature
δ	Chemical shift (when referring to NMR) or vibrational bending (when referring to FTIR/DRIFT)

ΔE_p	Peak potentials difference
ε	Molar extinction coefficient
Γ_e	Electroactive surface concentration
η	Yield
λ	Wavelength
ν	Stretching vibration
σ	Conductivity (**Chapter 1.2.1**) or standard deviation (**Chapter 2.4**)
υ	Wavenumber

1

INTRODUCTION

1.1 Biorelevant molecule sensing

Over the past decade, the scientific community has been working on developing rapid, sensitive, and selective analytical methods for the quantitative determination of target molecules. The determination of small biomolecules, such as glucose,[1] dopamine,[2] L-tyrosine,[3] L-cysteine,[4] adenosine triphosphate (ATP),[5] hydrogen peroxide (H_2O_2),[6] ascorbic acid,[7], or urea,[8] has been of particular interest. This is due to their important physiological functions in life processes and various biochemical reactions, such as life signal transmission, genetic expression, and metabolism.[9] Consequently, their abnormal values are associated with harmful effects in human health, showing toxic or even carcinogenic properties.[10] As a result, researchers have been detecting biorelevant small molecules for the early diagnosis and treatment of the related diseases.[11–14]

To quantify such species, chemical sensors are a suitable option. Regarding the type of the obtained signal, diverse methodologies can be used to obtain different sensors, such as electrical, electrochemical, optical, thermometric, magnetic or mechanical devices.[15] These are constituted by two main components: the chemical receptor, which will interact with the targeted analyte and emit sensing information to the transducer; the transducer, which will transform the previous into an electrical signal.[15] For example, in electrochemical sensing (**Figure 1.1**) a given analyte will interact with a receptor. Such interaction will result in an electron flow that will be transformed by the transducer which is, in this case, the working electrode.[16] Such transformation will result into an electrical signal (e.g., amperometric) that will be processed, amplified, and finally displayed in a readable manner. Regarding its fabrication, important sensing characteristics include sensitivity, selectivity, response time, reusability, long-term stability, simplicity and low cost.[16]

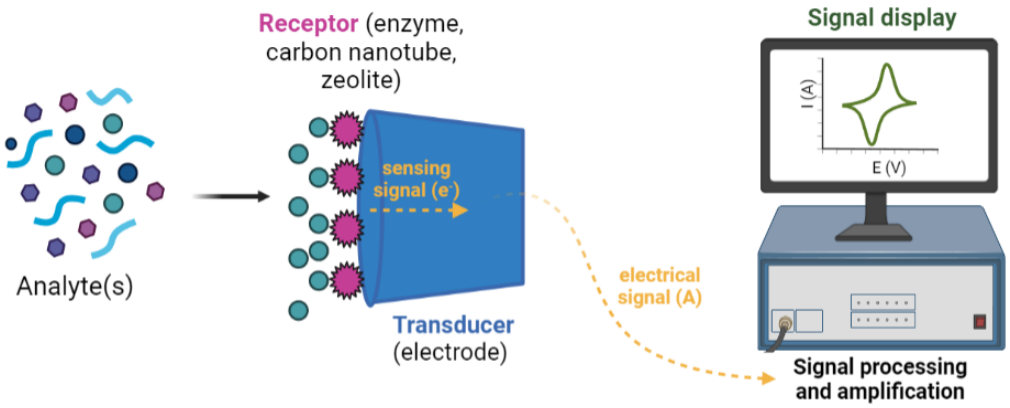

Figure 1.1 - Schematic diagram of an electrochemical sensor.

1.1.1 Purine sensing

Purines (**Figure 1.2**) are small biorelevant molecules included in a class of heterocyclic aromatic and natural organic compounds. Their ring system can be viewed as a pyrimidine ring fused to an imidazole unit. Not only do they constitute the genetic code, but they also have a huge role in metabolism, protein synthesis and signalling processes.[17] Consequently, if the metabolism of these compounds is somehow affected, it can lead to neurologic disorders.[18]

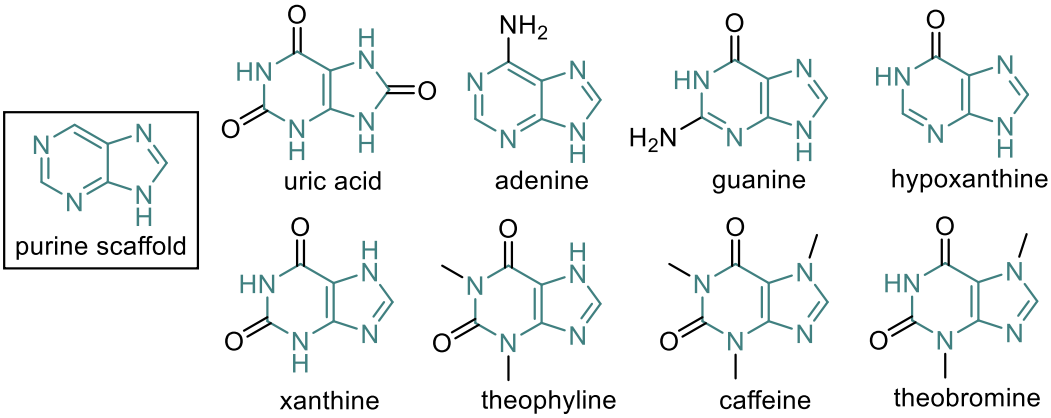

Figure 1.2 - Purine scaffold (represented in turquoise) and some of its principal derivatives.

Uric acid (UA) is the final metabolic product, produced from the breakdown of purines present in the cells. Its normal concentration levels range from 0.13 to 0.46 mM in the blood and from 1.49 to 4.5 mM in the urine.[19,20] Abnormal values may be associated with different clinical disorders, including gout, cardiovascular diseases, the Lesch–Nyhan syndrome, type 2 diabetes, multiple sclerosis, Parkinson's and Alzheimer's diseases, renal failure, hyperuricemia, and others.[21–23] Consequently, the concentration level of UA translates into a useful diagnostic marker for related diseases.

The conventional method for UA detection and quantification remains the enzyme-based assay. Yet, it is limited in terms of interference from other biological analytes, long incubation time, strict pH conditions, expensive enzymes, and low determination accuracy.[24] Other

analytical techniques have been implemented, such as high-performance liquid chromatography (HPLC),[25] liquid chromatography coupled to tandem mass spectrometry (LC-MS/MS),[26] gas chromatography coupled to mass spectrometry (GC-MS),[27] fluorescence,[28] and spectrophotometry[29]. However, these also display several drawbacks such as the requirement of expensive apparatus, complex sample treatment, skilled operators, and are time-consuming.[24] Electrochemical detection is an attractive alternative due to its simplicity, offering a sensitive and rapid analysis response towards these small molecules, adding that it is inexpensive, portable, and easy to operate.[30] There has been a steady increase in the development of stable electrochemical sensor films, also known as chemically modified electrodes (CMEs, see **Table 1.1**) for uric acid sensing.

Table 1.1 - Examples of CMEs used for the electrochemical detection of uric acid.

Film material	Specification	Detected analytes	[Ref] (year)
Organic polymers	Poly(bromocresol purple)	Uric acid, xanthine, and hypoxanthine	[31] (2010)
	Poly(L-methionine)	Uric acid, xanthine, and hypoxanthine	[32] (2013)
Carbon nanotubes (CN)	DWCNT[a]/Choline	Uric acid, ascorbic acid, and dopamine	[33](2013)
	BCNT[b]	Uric acid and dopamine	[34](2019)
	SWCN[c]	Uric acid, ascorbic acid, and dopamine	[35](2009)
Nanoparticles (NP)	Au NP/Ch[d]	Uric acid and dopamine	[36](2007)
	Ni/C NP[d]	Uric acid, ascorbic acid, and dopamine	[37](2016)
	SnO_2@Mn NP	Uric acid, ascorbic acid, and folic acid	[38](2016)
Zeolitic imidazolate frameworks (ZIFs)	CD@ZIF-CuNC	Uric acid	[39](2021)
	ZIF-67/GO	Uric acid and dopamine	[40](2018)
	ZIF-11	Uric acid	[41](2021)
	ZIF-8@Co-TA[e]	Uric acid, dopamine, acetaminophen, and tryptophan	[42](2020)
	ZIF-67/g-C_3N_4[f]	Uric Acid and acetaminophen	[43](2020)
Metal-organic frameworks (MOFs)	Eu-MOF	Uric acid	[44](2021)
	MOF-71	Uric acid	[45](2021)
	Ce@Zn-MOF	Uric acid	[46](2021)

[a] DWCNT: doubled-walled carbon nanotube [c] SWCN: single-walled carbon nanohorn [e] TA: tannic acid
[b] BCNTs: boron-doped carbon nanotube [d] NP: nanoparticles; Ch:choline [f] g-C_3N_4: graphitic carbon nitride
@:doped /: mixed

Nanomaterials and organic polymers have been developed as uric acid electrochemical sensors.[47] Based on the electrochemical activity of the metal ions and the well-ordered porous structure, MOFs are excellent candidates for the electrochemical detection of biorelevant molecules and have been recently developed towards uric acid detection.

1.2 Metal-organic frameworks

Metal-organic frameworks (MOFs) or coordination polymers (CPs) constitute a class of 1 to 3-dimensional crystalline porous materials. This prominent type of reticular structures have been reported since the 1990s with pyridyl ligands, obtaining MOFs with permanent porosity, through the pioneering work of Yaghi and Hoskins.[48–50] MOFs are composed of a coordination interaction between a metal node and a ligand/linker **(Figure 1.3)** achieving a geometrically well-defined structure.[51]

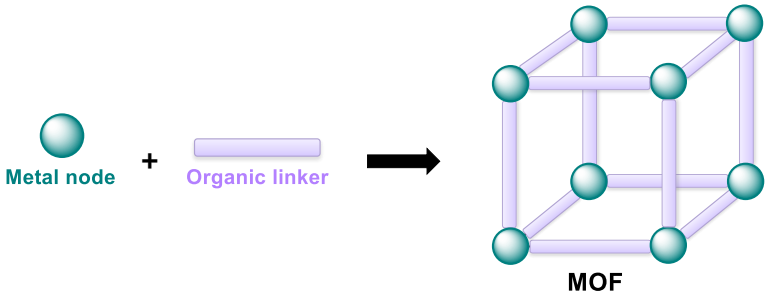

Figure 1.3 - Simple representation of MOF formation, by coordination between a metal node and an organic linker, where the metal ions are the vertices, and the organic linkers are the edges.

Common organic linkers are benzene-1,3,5-tricarboxylate (BTC), benzene-1,4-dicarboxylate (BDC) and 2,5-dioxido-1,4-benzenedicarboxylate (DOBDC). Depending on the coordination sites of the linker, as well as the metal size and *d*-electron coordination, different topologies may be obtained and, consequently, different MOFs (**Figure 1.4**).

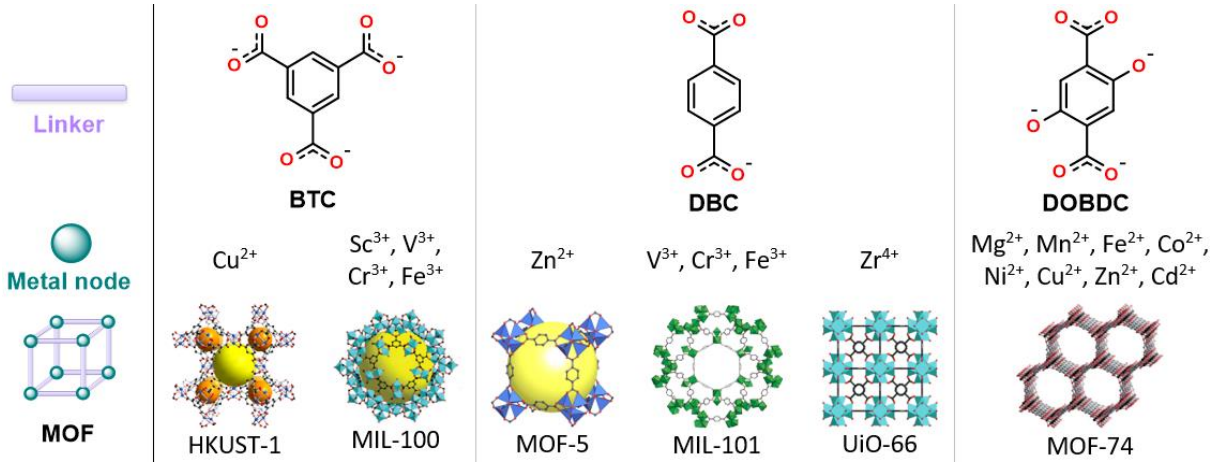

Figure 1.4 -Representation of BTC, DOBDC and DBC ligand structures with the related MOFs and ion metals, adapted from refs.[52–58]

Typically, these frameworks are synthesised by hydro- or solvothermal techniques. The former involves the MOF preparation from high-temperature aqueous solutions (ranging from 80 to 220 ºC) under high pressures, while the latter uses organic solvents instead.[59] Such coordination polymers can be characterised by Fourier-transform infrared spectroscopy (FTIR), Brunauer-Emmett-Teller (BET) surface area from N_2 adsorption, scanning electron

microscopy (SEM) atomic force microscopy (AFM), X-ray diffraction (XRD), solid-state nuclear magnetic resonance (NMR), or thermogravimetric analysis (TGA).[59]

Metal-organic frameworks exhibit extraordinary structure properties, such as high crystallinity, permanent porosity, high surface area, and availability of active sites, which makes them promising and versatile compounds towards a variety of applications. Examples are host-guest chemistry,[60] luminescence,[61] gas storage,[62] sensing,[63] proton conductivity,[64] hydrocarbon separation,[65] catalysis,[66] drug delivery,[67] polymerisation and oligomerisation reactions,[68] magnetism,[69] membrane fabrication,[70] and removal of toxic and warfare chemicals.[71] For this reason, a wide range of MOFs has already been extensively studied and is expected to exist around 20000 structures already reported in the literature.[72]

MOFs' functionalisation or modulation can be applied to enhance the host-guest interactions and to enhance or expand the scope of their chemical applications.[73] Linker design has shown to be a useful approach by both pre- and post-synthetic MOF functionalisation.[74] Therefore, organic structures can be tailored in terms of their geometry, length, ratio and functional groups, resulting in different framework sizes, shapes and internal surfaces.[58] One great example of MOF pre-synthetic functionalisation is the introduction of functional groups on the ligand main chain that behave as guest-interactive sites. These groups can be crucial to improve the host-guest interactions, by enhancing the hydrogen bonding, donor-acceptor, polarisation, and/or dipole-quadrupole interactions.[73] For instance, the pro-ligand biphenyl-3,3′,5,5′- tetracarboxylic acid (H_4BPTC), a benzene-1,3,5-tricarboxylic acid (H_3BTC) derivative, has been functionalised with amide, oxalamide, isoquinoline, squaramide, diazine and oxalamide moieties (**Figure 1.5**).[75–80] These were successfully assigned for gas adsorption (C_2H_2, CO_2 and CH_4) as well as Friedel Crafts catalysis.

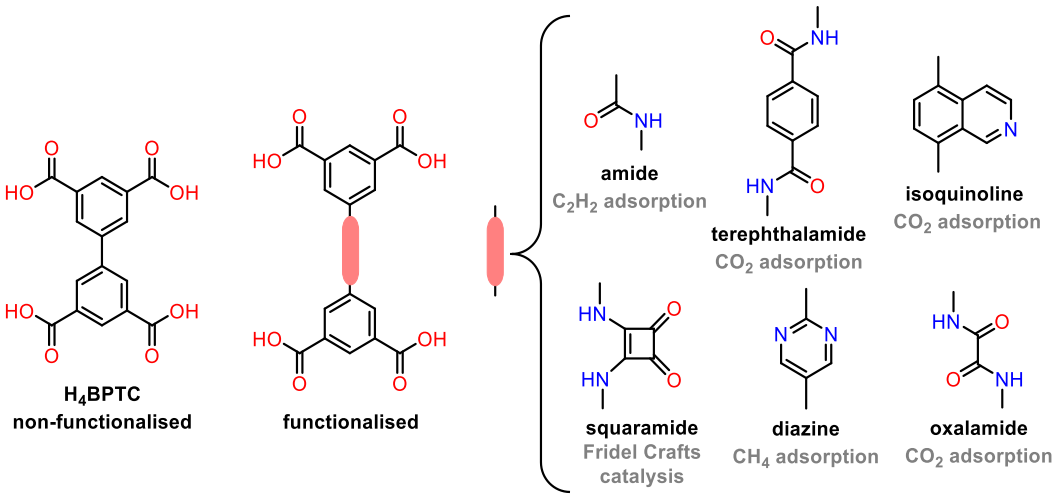

Figure 1.5 - Representation of H_4BPTC non-functionalised pro-ligand and possible moiety functionalisation for the construction of pre-synthetic functionalised MOFs.

1.2.1 MOF-74 series

This work will be focused on MOF-74, constituted by the 2,5-dioxido-1,4-benzenedicarboxylate ligand (DOBDC, see **Figure 1.6a**) with an approximate 7 Å length.[81] Its structural range has been expanded by altering the metal node (M), forming the M-MOF-74 series, where M=Mg^{2+}, Mn^{2+}, Fe^{2+}, Co^{2+}, Ni^{2+}, Cu^{2+}, Zn^{2+} and Cd^{2+}.[82] Zn-MOF-74 was the first reported M-MOF-74 structure by Rosi *et al.*[83]. In these frameworks, the coordination between the ligands with the metal nodes results into edge-connected {MO_6} octahedra and forms a rod-shaped secondary building unit (SBU, see **Figure 1.6b** with Zn-MOF-74 as an example).[52] The solvent molecules, normally DMF and/or water molecules will complete the pre-activated octahedral coordination environment of the metal centre. These series presents characteristic hexagonal channels along the *c*-axis (**Figure 1.6c** with Zn-MOF-74 as an example) with a diameter of approximately 11 Å.[84] Such porosity translates into Langmuir surface areas ranging from 1957-1277 m^2g^{-1}, with the highest value attributed to Mg-MOF-74 and the lowest to Zn-MOF-74.[84]

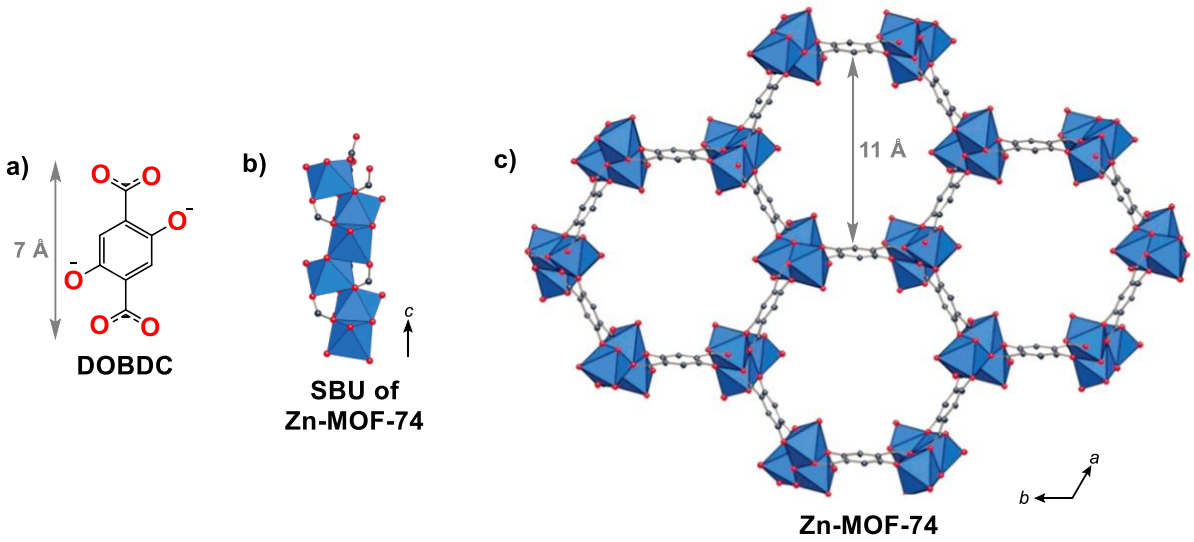

Figure 1.6 - a) DOBDC ligand structure; b) Zn-MOF-74 SBU; c) Crystalline framework structure of Zn-MOF-74. Adapted from refs.[83,85]

When the material is exposed to high temperatures under vacuum, it is expected to release the solvent molecules coordinated with the metal ions. This results in a square pyramidal geometry, where each metal ion possesses an open coordination site (**Figure 1.7** with Mg-MOF-74 as an example). The structure is then considered in its active state, with highly reactive and electron-deficient metal sites, enabling enhanced host-guest interactions.[86]

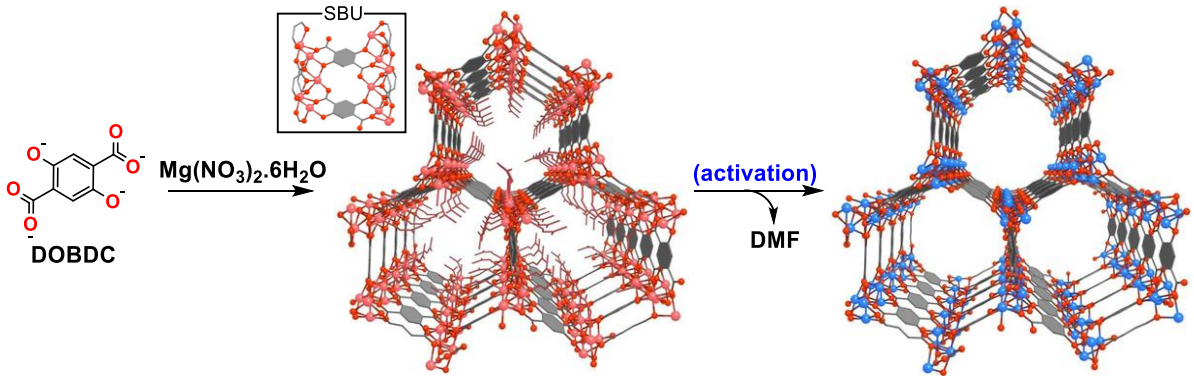

Figure 1.7 - Example of Mg-MOF-74 formation and activation. Adapted from ref.[86]

These frameworks have been extensively investigated for gas sensing and separation applications. They perform an excellent CO_2 adsorption capacity,[84,87–89] being Mg-MOF-74 the most promising framework for low-pressure physisorption of CO_2, as described by Caskey *et al.*[90]. Adsorption of H_2 was also demonstrated by Stavila *et al.*[91] with a titanium-functionalised Mg-MOF-74.

MOF-74 inspired frameworks had also been produced with the MOF pre-synthetic functionalisation technique. Nguyen *et al.*[92] reported the methanol uptake capacity of two new MOF-74 derivatives, denoted as VNU-74-I and -II (VNU: Vietnam National University. For the

ligand structures, see **Figure 1.8a**). Tran *et al.*[93] also developed MOF-74 analogues, reporting MOF-184 (for ligand structure, see **Figure 1.8b**), for the catalytic cycloaddition of CO_2.

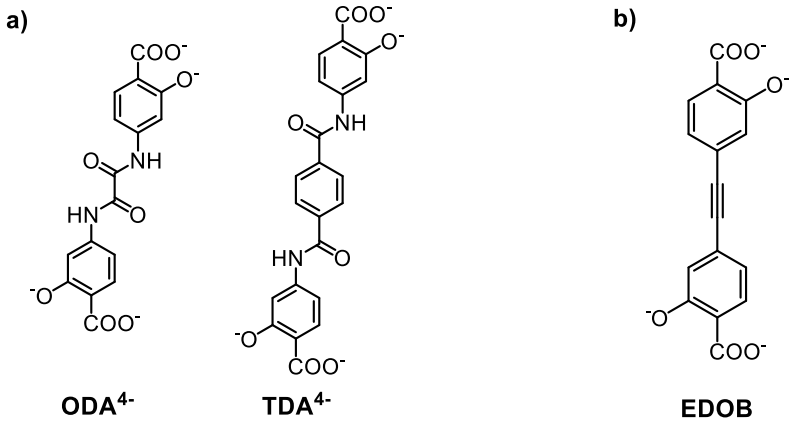

Figure 1.8 – a) VNU-74-I and -II ligands, developed by Nguyen *et al.*[92] and b) MOF-184 ligand, developed by Tran *et al.*[93].

Although MOF-74 series reveals to be successful for gas sensing, it also showed promising results for molecule sensing applications. Deng *et al.*[81] reported isoreticular (IR) MOF-74 derivatives with one to eleven phenylene rings (denoted as IRMOF-74-I to -XI, see **Figure 1.9**) between the salicylic acid fragments at the ends of the chains, which expanded the MOF pores from 11 to 98 Å, reporting IRMOF-74-XI as the material with the largest pore aperture in crystalline materials to date. Larger pore MOFs, such as IRMOF-74-XI and IRMOF-74-VII were tested for the accommodation and adsorption of proteins, respectively.

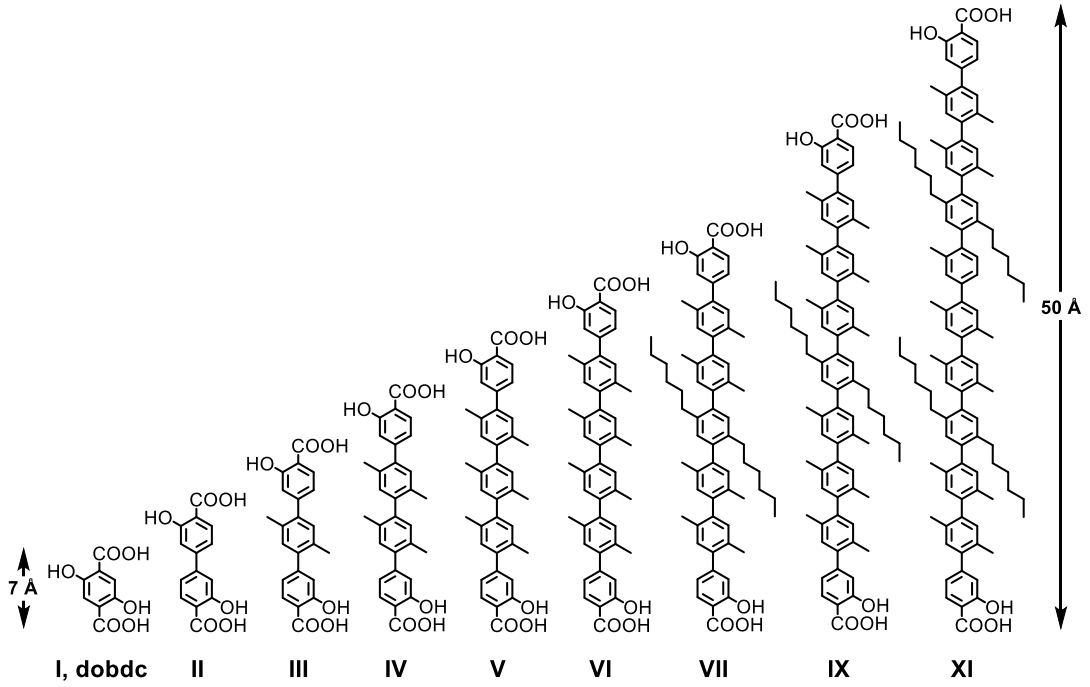

Figure 1.9 - Ligand structures of IRMOF-74-I to -XI, developed by Deng *et al.*[81].

Although the MOF-74 series has already displayed some remarkable results for CO_2 sensing and cycloaddition catalysis, as well as protein adsorption, a wide range of guest molecules remains unstudied. As previously discussed, MOF-74 series is particularly attractive by the highly reactive and electron-deficient metal sites, enlargeable hexagonal channels, high porosity and high surface areas. Hence, efforts are being made to produce MOF-74 as a chemical sensor.[94,95]

For uric acid sensing, amongst all the possible ion metals in M-MOF-74, Fe^{2+} is, by far, the most advantageous, since it is non-toxic, low-cost and earth-abundant.[96] Moreover, Fe-MOF-74 has been proven to be more conductive ($\sigma = 4.8\times10^{-8}$ S.cm^{-1}) than the other M-MOF-74 by about 5 orders of magnitude, which could lead to electronic applications.[97] Nevertheless, Fe^{2+}-MOF-74 is known for its instability in the presence of oxygen, as the metal nodes easily oxidise to Fe^{3+}.[98,99] Since most applications require the exposure of Fe-MOF-74 to air, alternatives must be developed. To overcome this limitation, Wang *et al.*[100] reported the production of Fe^{3+}-MOF-74 and found that both Fe^{2+}- and Fe^{3+}-MOFs yielded similar XRD patterns, meaning a similar structural topology.

1.3 Metal-organic frameworks as sensor devices

Researchers have been developing nanotechnological and electric devices, namely, smart membranes, catalytic coatings, and sensors.[101] Although zeolites and metal oxides remain conventional for these types of applications, associated with a well-defined structure and stability, they are also limited by their non-versatile structural range, high-temperature operation requirement, cross-selectivity, and baseline drifts caused by ageing effects.[102]

Until recent years, metal-organic frameworks were viewed as insulators and therefore excluded from such devices. This was due to their common electrochemical instability and low conductivity.[103] Nevertheless, synthetic advances have been producing MOFs electrically conductive and with charge mobility,[104] including the MOF-74 series.[97] MOFs may be a useful alternative to overcome the limitations of zeolites and metal oxides due to their reversible adsorption, high catalytic activity, high porosity or wide structural diversity. Moreover, to the possibility to operate at room temperature and their stability, self-assembled nanostructure, switchable response to external stimulus, structural diversity and host-guest interaction possibilities.[105–107] Moreover, functional moieties can also be easily introduced into the framework, by either pre- or post-synthetic modifications, giving an infinite scope of structural diversity.[108] Combining the conductivity missing puzzle with the highly attractive characteristics enables a new generation of MOF-based sensor devices. Such frameworks have been recently studied for molecule sensing applications regarding gas,[109,110] nitrobenzene

derivatives,[111] persistent organic pollutants,[112] heavy metal ion sensing,[113] antibiotics,[114] and explosives.[115]

Regarding the implementation of MOFs as components or interfaces for such technological devices, they are needed in the form of deposited films or coatings into solid substrates. Such films must also exhibit defined porosity combined with tunable chemical functionality, thickness, and high homogeneities, as well as the presented morphology.[116,117] Although solvothermal and hydrothermal are the conventional MOF fabrication techniques, described in **Chapter 1.2**, these yield the product as a fine powder with intrinsic brittleness, insolubility, and non-thermoplastic properties. Hence, can hardly be shaped onto the intended configuration and the MOF layers do not lead to a firm bond with the substrate.[118] They are also limited by time and energy consumption, need a great amount of solvents, and are often exposed to thermally induced film cracking.[119] Thus, the development of effective and direct fabrication approaches are necessary to readily deposit the MOF film on the solid substrates, ideally in a dense, homogeneous and oriented fashion. To date, several direct fabrication alternatives have been developed to produce crystalline nanomaterial films, such as mechanochemical, electrochemical, layer-by-layer, sonochemical or self-assembly growths.[119,120]

1.4 Metal-organic framework films by cathodic deposition

Although the previous techniques can overdue the conventional limitations, the majority are still complex and time-consuming. Amongst all, electrochemical fabrication has already shown several advantages over the conventional methods, such as shorter synthesis times and milder conditions.[121] Moreover, its straightforwardness to scale up and optimise the film morphology and thickness makes it an ideal technique for the new MOF-film generation.[122] Electrochemical MOF thin films are generally prepared in solutions containing metal ions, organic ligands and electrolyte sources, commonly in a three-electrode cell.[122] Moreover, the working electrodes that are normally used, e.g., Si, metals, fluorine or indium tin oxides (FTO or ITO, respectively), polymers, meshes or carbon-based substrates are compatible with the electronic devices.[123] Through the years, metal-organic frameworks have been deposited by all four electrochemical procedures: galvanic displacement and anodic, cathodic and electrophoretic depositions (**Figure 1.10**).[105,121,124]

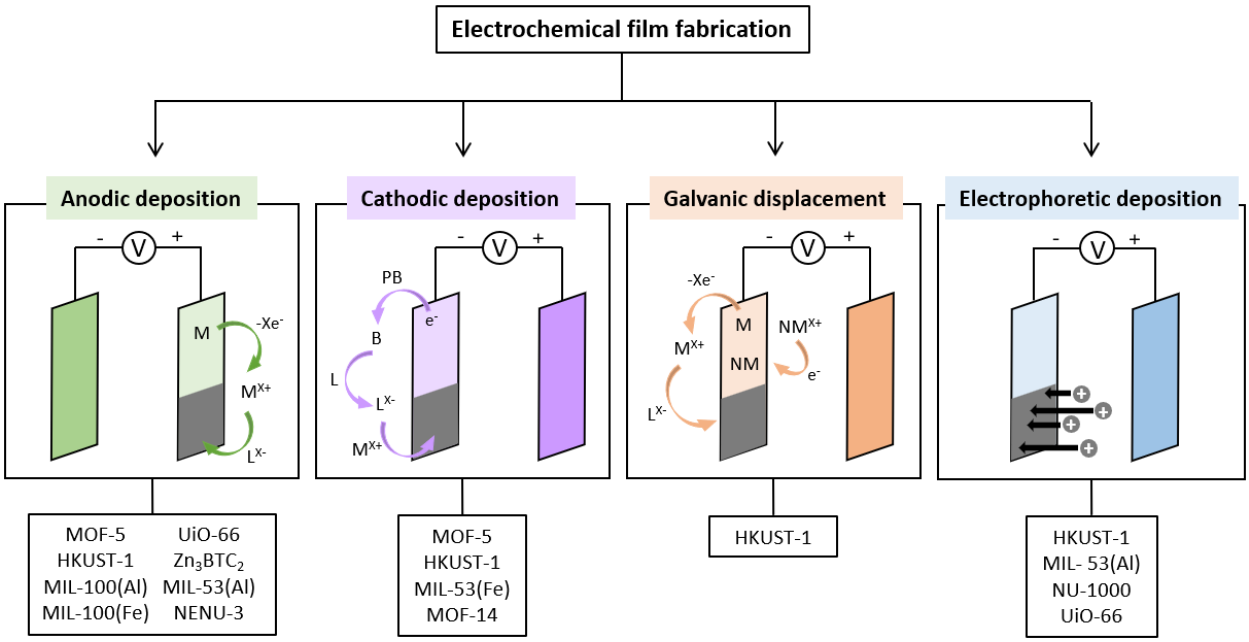

Figure 1.10 - Different categories of electrochemical MOF film fabrication.

Although anodic is the conventional electrochemical deposition technique, it has some drawbacks caused by the interference of reactions occurring at the anode. Furthermore, the choice of anodic materials is limited and the durability of those electrodes is low due to corrosion.[125] Alternatively, reductive/cathodic deposition can be viewed as an alternative to solve those limitations, since any conductive surface can be used as a cathode and is less affected by secondary reactions. It was firstly implemented by Dincă *et al.*[126,127] for the deposition of MOF-5, constituted by Zn^{2+} as the metal ion and BDC as the ligand. It has a very attractive mechanism since the metal ion and organic ligand precursors are simply added in an electrolytic solution along with the pro-base (PB) source in appropriate concentrations. Then, the deposition is initiated with the application of a reductive/cathodic potential. During the experiment, a series of successive reactions are triggered by this potential (**Figure 1.11**), starting with the reduction of a pro-base (Et_3NHCl) to the respective base (Et_3N). This base will deprotonate the pro-ligand (H_2BDC) and release the ligand (BDC). This leads to the interaction of BDC with the metal ion (Zn^{2+}) and the deposition of the MOF-5 film on the cathode surface.

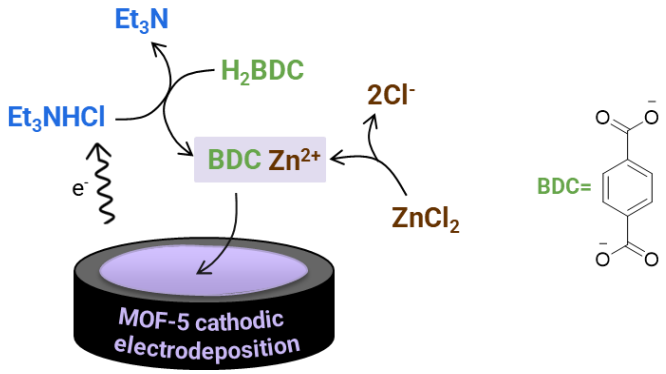

Figure 1.11 - Cascade electrochemical reactions occurring during the cathodic deposition of MOF-5, described by Dincă *et al.*[127].

Throughout the last decade, a new generation of MOF films are being produced by the cathodic method into different types of working electrodes (WE, represented in **Table 1.2**), that could be applied to further technological applications, such as sensor devices. Regarding the choice of pro-bases, amine sources remain the most relevant due to their behaviour as mild bases and low-cost. Greener alternatives have been reported with H_2O_2 or even atmospheric O_2.[124,128]

Table 1.2 - Electro-synthesised MOFs by cathodic deposition, represented accordingly to its pro-base source.

PB source	PB reduction	E_p^c	MOFs	WE	[Ref]
Et_3NH^+	$2Et_3NH^+ + 2e^- \rightleftharpoons H_2 + 2Et_3N$	-1.05 V (vs. $Ag/Ag(cryptand)^+$)	$(Et_3NH)_2Zn_3(BDC)_4$ | MOF-5	Pt gauze	[127]
		np	Cu-BTEC Cu-BDC	GC	[129]
		np	Cu-BTC	SPC	[130]
		np	HKUST-1@Ag		[131]
		-0.9 (vs. SCE)	HKUST-1	GC	[96]
			HKUST-1(Fe)/Fe		
O_2	$O_2 + e^- \rightleftharpoons O_2^-$	-0.79 V (vs. 3 M $Ag/AgCl$)	HKUST-1 MOF-14	GC	[128]
NO_3^-	$NO_3^- + 2e^- \rightleftharpoons NO_2^- + H_2O$ $2H_2O + 2e^- \rightleftharpoons H_2 + 2OH^-$	-1.75 V (vs. $Ag/Ag(cryptand)^+$)	MOF-5	FTO	[126]
		np	Eu-HBPTC		[132]
		np	$Cu_2(BTEC)(DMF)_2$	Graph-ite	[133]
H_2O_2	$H_2O_2 + e^- \rightleftharpoons 2H_2O + O_2^-$	-0.70 V (vs. $Ag/Ag(cryptand)^+$)	HKUST-1 MIL-53(Fe) MOF-5	ITO	[124]

E_p^c: cathodic peak potential | GC: glassy carbon | SPC: screen-printed carbon
np: not presented | \|: bilayer | @: doped | /: mixed

According to the available information, MOF-74 has not yet been synthesised by any electrochemical method. Combining MOF-74 properties (e.g., open metal sites, large pores, catalytic and sensing activity) with a film morphology could lead to endless possibilities in terms of industrial and technological applications. Hence, it is necessary to find optimisation strategies to develop new MOF-74 films and to test their sensing applications.

1.5 Aim of this thesis

This work relies on the production of novel metal-organic films for the electrochemical sensing of uric acid. From all the metal-organic structures available, the MOF-74 series was selected for this thesis and focused on Fe-MOF-74 as the sensing probe due to its higher conductivity and unharmful properties. With the purpose of enhancing the supramolecular interactions between the host (Fe-MOF-74) and guest (uric acid) components, MOF pre-synthetic functionalisation was suggested by synthesising **H_4L** analogues, identified as **H_4L1, H_4L2** and **H_4L3** (**Figure 1.12**). All three analogues would have a higher ligand length than **H_4L**. **H_4L2 and H_4L3** were suggested as novel pro-ligands, by incorporation of benzimidazole and squaramide moieties, respectively.

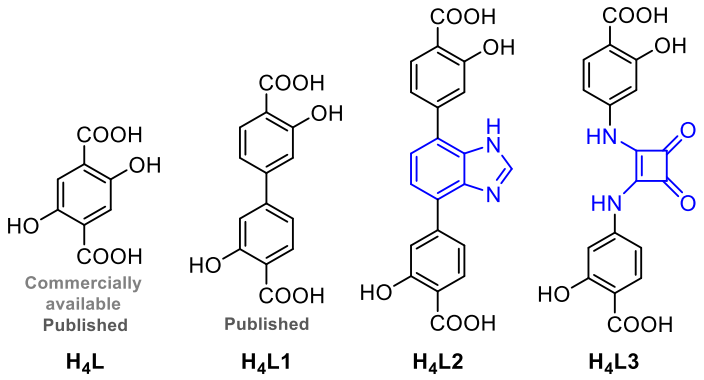

Figure 1.12 - Synthesised pro-ligands in this work.

To obtain the MOF films, cathodic deposition was selected as an electrochemical method to immobilise Fe-MOF-74 and derivatives on the working electrodes.

Once the films were characterised, the final step would be to test their ability to electrochemically detect uric acid. For this, the films would have to respond to different uric acid concentrations and their performance would be evaluated regarding their limit of detection, sensitivity, linear range, and standard deviation.

2

RESULTS AND DISCUSSION

2.1 Pro-ligand synthesis and characterisation

This chapter contains a brief description of the synthesis of organic pro-ligands **H_4L1**, **H_4L2** and **H_4L3**. Moreover, their FTIR and NMR characterisations will be shown and discussed.

2.1.1 H_4L1 synthesis and characterisation

The synthesis of **H_4L1** pro-ligand (**Scheme 2.1**) was adapted from Grunder *et al.*[134] using a total of 4 reaction steps and the preparation of 3 intermediates, **I_A**, **I_B** and **I_C** which will be described below.

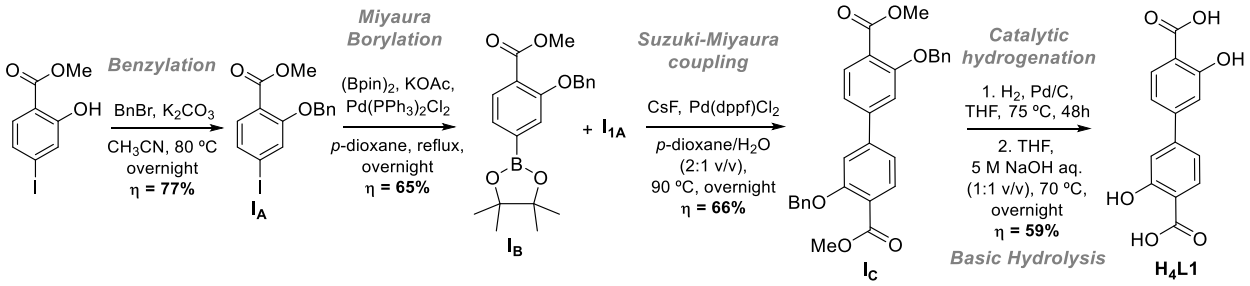

Scheme 2.1 - Synthetic steps employed to obtain pro-ligand **H_4L1**.

The first synthetic step consisted of the protection of the hydroxyl group of the phenol function, from the commercial reagent methyl 2-hydroxy-4-iodobenzoate. This reagent was reacted with benzyl bromide in a basic medium and yielded **I_A** (see **Scheme A.1** in Annexes for the suggested mechanism). To obtain a complete reaction, the benzyl bromide reagent was added in excess (1.5 eqv.). However, benzyl bromide was still detected in the final crude by ^{1}H NMR in $CDCl_3$ (residual peak at 7.26 ppm) by its characteristic aliphatic proton at 4.5 ppm (**Figure A.1** in Annexes). Recrystallisation in hot hexanes successfully removed the undesired reagent, yielding **I_A** as white needles. Even though the reaction seemed complete when monitored by TLC, a lower yield than expected was obtained (η=77%), which can be related with the

recrystallisation process. Intermediate **I_A** was characterised by ^{1}H and ^{13}C NMR spectroscopy (**Figure A.2** and **Figure A.3**, respectively, in Annexes), in $CDCl_3$ (residual peak at 77.16 ppm for ^{13}C NMR) and agrees with the published data.[134]

For the next step, the **I_B** boronic ester was prepared (see **Scheme A.2** in Annexes for the suggested mechanism). This intermediate was synthesised through a Miyaura borylation coupling between **I_A** and bis(pinacolato)diboron, identified as $(Bpin)_2$. It was catalysed by $Pd(PPh_3)_2Cl_2$ and resorted to KOAc as the transmetalation reagent. Moreover, the reaction was performed in a Schlenk flask under inert atmosphere, with dry *p*-dioxane as solvent. The reaction mixture was filtered and treated with activated charcoal. The remaining crude was purified by flash-chromatography in a silica gel column (1:9 acetone/petroleum ether), yielding **I_B** as white needles. This intermediate was also characterised by ^{1}H and ^{13}C NMR spectroscopy (**Figure A.4** and **Figure A.5**, respectively, in Annexes) and, once again, agrees with the reported spectra.[134]

The final intermediate **I_C** was obtained by coupling **I_A** and **I_B** through a Suzuki-Miyaura reaction (see **Scheme A.3** in Annexes for the suggested mechanism). Herein, $Pd(dppf)Cl_2$ (10 mol%) was the catalyst and CsF the transmetalation reagent, also performed in a Schlenk flask under inert atmosphere, in a previously N_2 degassed mixture of *p*-dioxane/H_2O (2:1 V/V, respectively).

The crude was further purified by flash-chromatography in a silica gel column (1:9 acetone/petroleum ether) and characterised by ^{1}H and ^{13}C NMR (**Figure A.6** and **Figure A.7**, respectively, in Annexes) in $CDCl_3$, also consistent with the published data.[134]

H_4L_1 was obtained by the hydroxyl deprotection reactions, respectively, catalytic hydrogenation and basic hydrolysis (see **Scheme A.4** in Annexes for the suggested mechanism). For the hydrogenation reaction, Pd/C (20 mol%) was added to a previously degassed Schlenk flask with dry tetrahydrofuran (THF), followed by the addition of **I_C**, with a H_2 balloon adapted on top of a condenser. The reaction was monitored by TLC until no reagent was left and was filtered through a celite pad to remove the Pd/C catalyst. The crude was then directly used in the next reaction step, by the addition of a solution of 0.5 M NaOH aq. (1:1 V/V). Once the reaction was complete, the volume of the mixture was reduced in vacuum and was followed to an acidic work-up. It resulted in a precipitate that was filtered and washed with H_2O, yielding **H_4L_1** as a white powder. It was characterised by ^{1}H and ^{13}C NMR spectroscopy (**Figure A.8** and **Figure A.9**, respectively, in Annexes) in $(CD_3)_2SO$ (residual peak at 2.50 ppm), which are also in agreement with the ones reported.[134]

H_4L_1 was also characterised by FTIR spectroscopy (**Figure A.10** in Annexes). The bands attribution can be found in **Table A.1** in Annexes. The spectrum showed bands at 3417 cm^{-1} and 3011 cm^{-1} that were assigned to the stretching of hydroxyl bond (ν_{O-H}) from both phenol and carboxylic acid functions, respectively. Although the stretching of aromatic C-H bonds (ν_{C-H})

is usually detected at wavenumbers higher than 3000 cm^{-1}, it was only possible to detect a peak at 2959 cm^{-1}. As there are no aliphatic C-H bonds in this molecule and this band was frequently detected throughout this thesis, it was assigned to the aromatic C-H bonds. The bands between 1667 and 1619 cm^{-1} were assigned to carbonyl group stretching ($\nu_{C=O}$). The ones observed in the range of 1453 and 1462 cm^{-1} were assigned to the bending of the C-O-H bond from the carboxylic acid function ($\delta_{C\text{-}O\text{-}H}$). The C-O bond stretching ($\nu_{C\text{-}O}$) from either carboxylic acid and/or phenol functions was also observed in from 1291 to 1222 cm^{-1}. The bending of the C-H bonds ($\delta_{C\text{-}H}$) from the aromatic ring was attributed to the bands between 1095 and 770 cm^{-1}.

2.1.2 H_4L2 synthesis and characterisation

To the best knowledge, **H_4L2** is a new pro-ligand, and its synthesis was based on the reactions used to prepare **H_4L1**. During this procedure, 3 intermediates, **I_D**, **I_E** and **I_F** were also synthesised (**Scheme 2.2**) and will be described below.

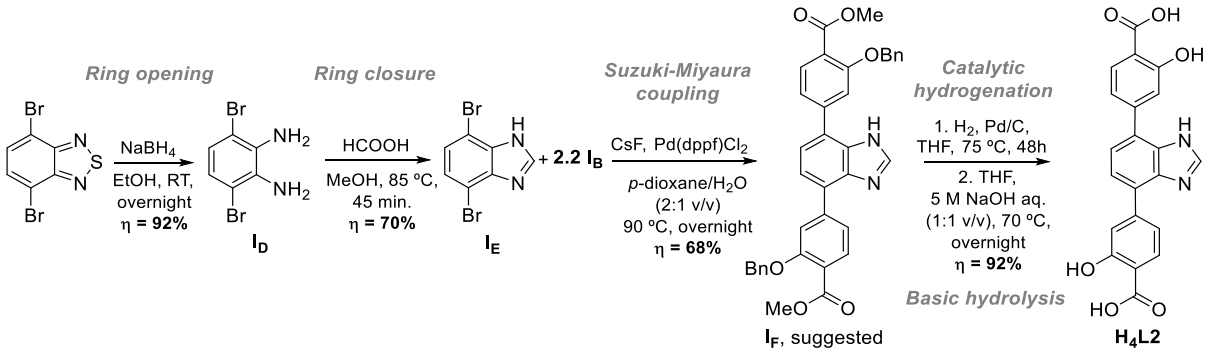

Scheme 2.2 - Synthetic steps employed to obtain pro-ligand **H_4L2**.

To obtain the halogenated benzimidazole intermediate, **I_E**, a first step was employed by the reduction of the commercially available 4,7-dibromobenzo[*c*][1,2,5]thiadiazole reagent with $NaBH_4$ (see **Scheme A.5** in Annexes for the suggested mechanism), adapting a reported procedure.[135] The reaction was monitored by TLC and, once it was complete, the organic phase from the reaction mixture was extracted and concentrated, yielding **I_D** as a beige solid. It was characterised by ^1H NMR spectroscopy (**Figure A.11** in Annexes) in $(CD_3)_2SO$, and the spectrum agrees with the literature.[135]

The preparation of **I_E** (see **Scheme A.6** in Annexes for the suggested mechanism) was also adapted from the literature with modifications.[136] **I_D** and formic acid (HCOOH) were added to a round-bottom flask and sealed with a septum. It was heated at 85 ºC for 45 minutes. This was followed by a basic work-up and yielded **I_E** as a beige solid. The product was also characterised by ^1H NMR spectroscopy (**Figure A.12** in Annexes) in $(CD_3)_2SO$. The spectra of **I_E** and **I_D** were overlayed and do not coincide, proving that there was no reagent left (**Figure A.13** in Annexes). Moreover, **I_E** spectrum is in agreement with the literature.[137]

To yield **IF**, **IE** and **IB** were coupled by a Suzuki-Miyaura reaction (see **Scheme A.7** in Annexes for the suggested mechanism) and were purified by a flash-chromatography in a silica gel column (1:9 acetone/petroleum ether). The product was characterised by ^{1}H NMR spectroscopy (**Figure A.14** in Annexes) in $(CD_3)_2SO$. The ^{1}H spectrum showed a peak at 12.85 ppm, in the same range as the peak found in the ^{1}H spectrum of **IE** at 13.24 ppm, and so, it was attributed to the NH group from the imidazole moiety. Moreover, the peak at 8.40 ppm was attributed to the proton of the imine group of the same moiety. In the aromatic range, it was expected, at least, 7 peaks, leading to a total of 18 protons. In this case, only 4 signals were attributed to the 18 aromatic protons of the molecule. The ^{1}H spectrum of **IF** was compared with both **IE** (**Figure A.15** in Annexes) and **IB** (**Figure A.16** in Annexes) reagents. Since the spectra did not match, it was possible to state that a new product was formed, suggesting **IF** as the most plausible structure.

H_4L_2 was obtained by catalytic hydrogenation and hydrolysis reactions of **IF** (see **Scheme A.8** in Annexes for the suggested mechanism). It was characterised by 1D ^{1}H and ^{13}C NMR (**Figure 2.1** and **Figure 2.2**), 2D homonuclear COSY and TOCSY (**Figure A.17** and **Figure A.18**, respectively, in Annexes) and heteronuclear HSQC and HMBC (**Figure A.19** and **Figure A.20**, respectively, in Annexes). The NMR spectra were performed in $(CD_3)_2SO$ (residual peak at 2.50 ppm for ^{1}H and 39.52 ppm for ^{13}C NMR). Residual acetone was observed in both ^{1}H and ^{13}C NMR spectra at 2.08 and 30.77 ppm, respectively. The ^{1}H NMR spectrum showed a broad and weak peak at 11.42 ppm, with an integration of 2 protons, that could be attributed to the proton of the carboxylic acids (COOH). Moreover, the characteristic peak at 8.46 ppm could also be attributed to the proton of the imine function, H_{11}. HSQC showed the direct correlation between the ^{1}H peak at 7.48 ppm with two ^{13}C peaks at 116.90 and 122.32 ppm. This ^{1}H peak had an integration of 4 protons and so, it was constituted by a mixture of two ^{1}H peaks with two equivalent protons each.

From the ^{13}C NMR spectrum, it was possible to identify an isolated peak at 171.87 ppm in the typical chemical shift range of the carbonyl group, therefore attributed to C_1. At a lower chemical shift, it was found another unshielded and isolated peak at 161.25 ppm that could be attributed to C_3, which is directly bounded to an electronegative oxygen atom. Moreover, two peaks were detected at 144.67 and 143.50 ppm, respectively. HSQC showed the correlation between H_{11} (8.46 ppm) and C_{11} (143.50 ppm). The closer peak at 144.67 ppm was assigned to C_2, which is bonded to the electronegative carboxylic acid function.

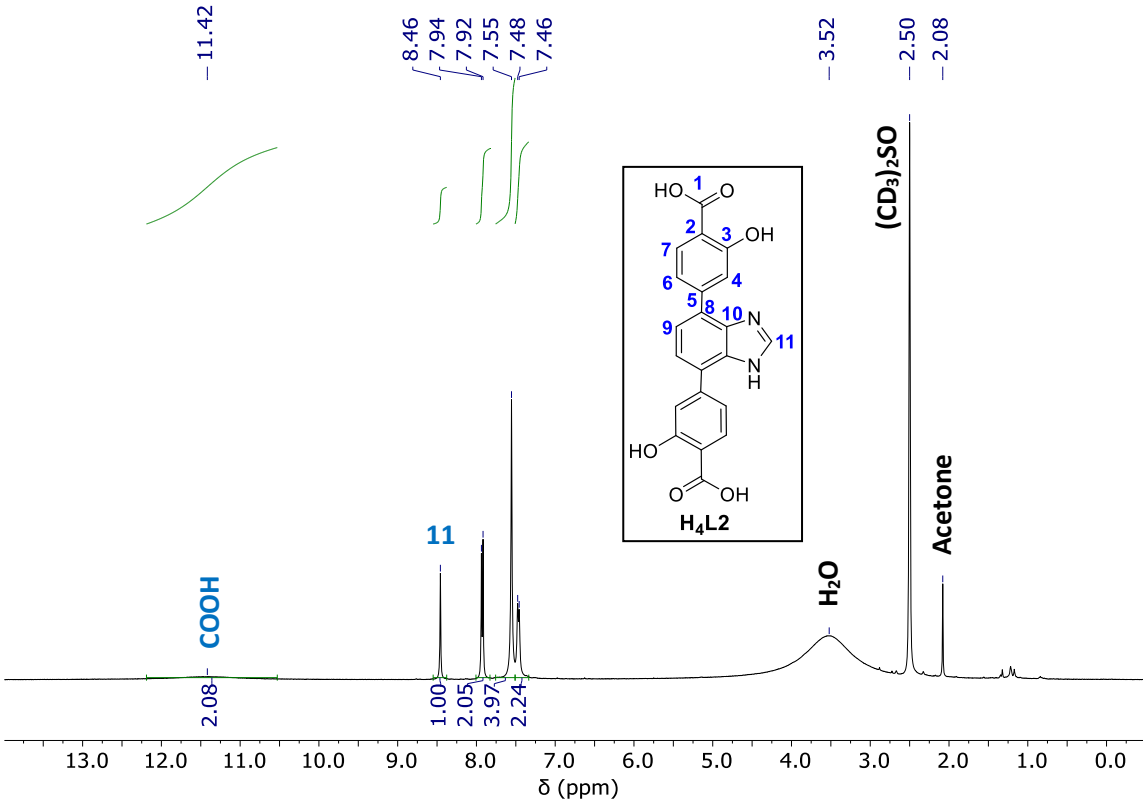

Figure 2.1 - ^{1}H NMR spectrum of **H_4L2** in $(CD_3)_2SO$.

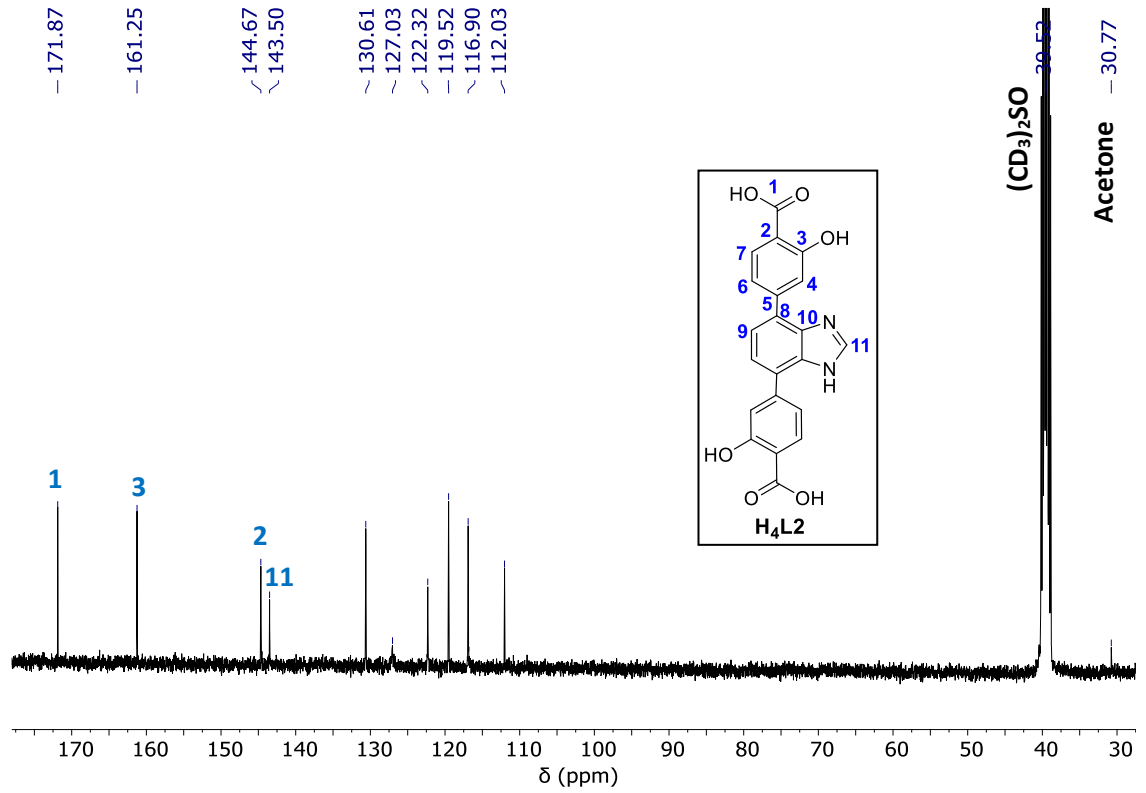

Figure 2.2 - ^{13}C NMR spectrum of **H_4L2** in $(CD_3)_2SO$.

The HMBC spectrum showed the correlation between C_1 (171.86 ppm) and H_7 (7.93 ppm) as the closest proton to the carbonyl group (^3J). Moreover, C_2 (144.67 ppm) correlated with both H_7 (7.93 ppm) and a multiplet at 7.48 ppm, which could be either attributed to H_6 or H_4. COSY confirmed the correlation between H_6 (7.47 ppm) and H_7 (7.93 ppm). TOCSY showed the correlation between all the protons of this aromatic ring, confirming the presence of H_4 in the mixture at 7.48 ppm. With no peaks left, by default, the multiplet was also assigned to H_9. The ^{13}C peaks directly correlated with H_7, H_{4+9} and H_6 were attributed using the HSQC spectrum. The missing quaternary carbon peaks at 112.03 and 127.00 ppm were attributed to C_{10}, C_5 and C_8, concerning the expected chemical shift range. C_{10} is directly correlated to a nitrogen atom, and so, it was expected to be more unshielded than the other carbons. Therefore, C_{10} was assigned to the 122.31 ppm peak. Since C_5 and C_8 have very similar nuclear environments, both were assigned to the peak at 112.03 ppm. Although H_{4+9} is a proton mixture, their ^{13}C peaks are well resolved, detected at 122.31 and 116.90 ppm. Due to the electron-donating effect of the hydroxyl group in the aromatic ring, the nucleus on *ortho*- and *para*-positions are expected to be more shielded than the *meta*-position. Based on that information C_4, *ortho*-positioned to the hydroxyl group was assigned to the peak at 116.90 ppm and C_9 to the peak at 122.31 ppm. The attribution data is presented in **Table A.2** In Annexes.

The **H_4L2** pro-ligand was also characterised by FTIR (**Figure A.21** in Annexes) with a very similar spectrum to **H_4L1**. The attributions are presented in **Table A.3** in Annexes. It showed the ν_{O-H} bands at 3407 and 3126 cm^{-1}, from the phenol and carboxylic acid functions, respectively, and ν_{C-H} between 2959 and 2842 cm^{-1}. In this case, the $\nu_{C=O}$ band is more complex which can be due to overlapping of the C=N stretching ($\nu_{C=N}$) between 1670 and 1576 cm^{-1}. Additional bands were attributed to δ_{C-O-H} at 1438 cm^{-1}, as well as ν_{C-O} from either phenol or acid functions, between 1337 and 1153 cm^{-1}. Finally, it was also possible to detect bands assigned to δ_{C-H} from 879 to 695 cm^{-1}.

H_4L2 composition was obtained by elemental analysis (EA), with an experimental percentage of % 51.84 (C), 4.92 (H) and 4.66 (N). These were different from the expected, respectively, % 64.62 (C), 3.62 (H) and 7.18 (N). Since the product was not in the form of a loose powder, before sending the sample for analysis, the product was dissolved in CH_2Cl_2, dried, and washed with Et_2O. Hence, **H_4L2** could be solvated by the previous molecules, and it was attributed a molecular formula of **$3H_4$L2**.$4CH_2Cl_2$.$3Et_2O$.$9H_2O$, with a calculated composition of % 52.55 (C), 4.94 (H) and 4.90 (N), with the highest shift of 0.71 for the C atoms. These values were closer to the obtained experimentally and **$3H_4$L2**.$4CH_2Cl_2$.$3Et_2O$.$9H_2O$ was the suggested composition of the sample.

Motivated by the successful preparation of **H_4L2**, efforts were made to synthesise two additional pro-ligands with benzobistriazole- and benzobisthiadiazole-based moieties (**Scheme A.9**, in Annexes) by the same coupling procedure as **H_4L1** and **H_4L2**. For the first case,

although it was possible to synthesise the bromated intermediate by a reported procedure,[138] the coupling reaction was not successful, suggesting that the product degraded in the purification step (flash-chromatography in silica-gel column). In the case of the benzothiadiazole, it was not possible to obtain the bromated intermediate by the selected procedure.[139] Instead, an insoluble powder was obtained and was not further characterised.

2.1.3 H_4L3 synthesis and characterisation

Similar to the previous pro-ligand, **H_4L3** is also a new structure. Its synthesis was adapted from analogues already reported in the literature.[75,140] This procedure involved a zinc catalysed coupling (**Scheme 2.3**) of 4-amino salicylic acid (**IG**) with 3,4-dimethoxy-3-cyclobutene-1,2-dione (squaric ether). These will be described below.

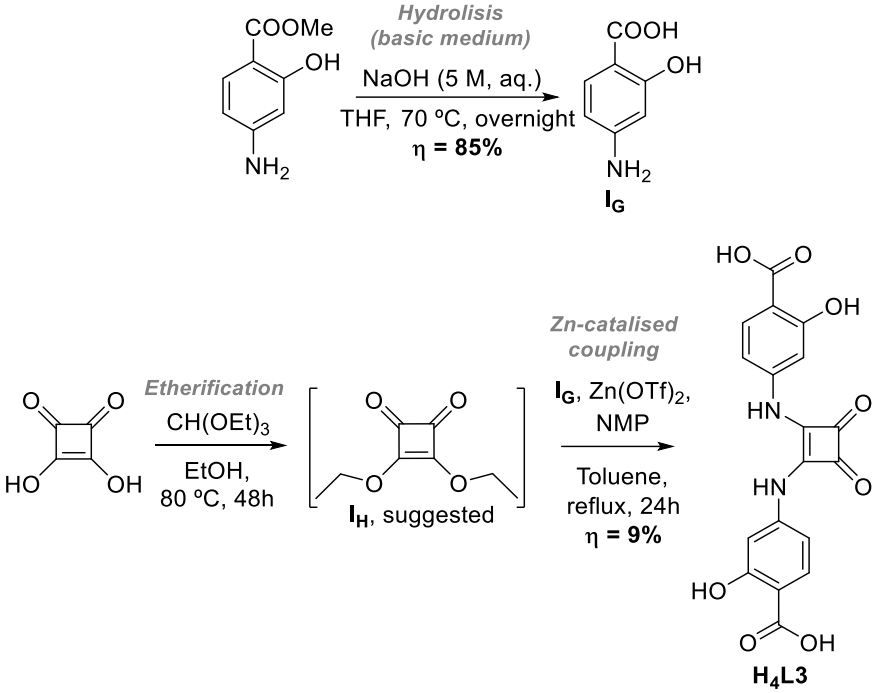

Scheme 2.3 - Synthetic steps employed to obtain pro-ligand **H_4L3**.

The preparation of **IG** began with the deprotection of the commercially available methyl 4-amino-2-hydroxybenzoate using the same hydrolysis conditions as those used to obtain **H_4L1**, yielding the intermediate as a white powder (see **Scheme A.10** in Annexes for the suggested mechanism). It was characterised by ^{1}H NMR (**Figure A.22** in Annexes) in the deuterated solvent $(CD_3)_2SO$, in agreement with the literature.[141]

An initial attempt to synthesise squaric ether (**IH**) was followed by reacting 3,4-dihydroxy-3-cyclobutene-1,2-dione (squaric acid) with triethylortoformate ($CH(OEt)_3$) in dry ethanol (EtOH, see **Scheme A.11** in Annexes for the suggested mechanism), also adapted by a literature procedure.[142] The crude was characterised by ^{1}H NMR and COSY spectroscopy (**Figure A.23** and **Figure A.24** in Annexes) in $(CD_3)_2SO$. The ^{1}H NMR spectrum showed ethanol residual

peaks (at 4.64 and 3.37 ppm), as well as a highly shifted water residual peak (at 6.30 ppm), which could be due to the possible intermolecular H-bonds between water and squaric derivatives. Two peak groups were also observed, both constituted by a triplet and a quartet. According to the literature,[143] it was possible to assign the 4.57/1.33 ppm peak group to the squaric ether and the remaining to the triethyl orthoformate reagent. Additionally, two singlets were also detected at 4.21 and 3.16 ppm, suggesting the presence of the squaric acid reagent, or even mono-etherified products. It was possible to conclude that the crude contained a mixture of both reagents and the product. Unfortunately, this mixture was highly unstable, as it quickly decomposed to an insoluble compound that was not characterised. Given the difficulty to isolate **I_H**, the **H_4L3** pro-ligand synthesis was performed by a one-pot reaction with no isolation of the intermediates (see **Scheme A.12** in Annexes for the suggested mechanism), yielding **H_4L3** as a yellow powder, in a very low yield (η=9%). This value could be caused by competing reactions involving the impurities from the first step and, due to the lack of opportunity, no further synthesis optimisations were performed. **H_4L3** was characterised by 1D ^{1}H and ^{13}C NMR (**Figure 2.3** and **Figure 2.4**), 2D homonuclear COSY (**Figure A.25** in Annexes) and heteronuclear HSQC and HMBC (**Figure A.26** and **Figure A.27**, respectively, in Annexes). NMR spectra were performed in $(CD_3)_2SO$. In the ^{1}H NMR spectrum, acetone and water were observed with residual peaks at 2.08 and 3.39 ppm, respectively. Moreover, the spectrum showed two highly unshielded peaks at 11.51 and 10.15 ppm, in a typical shift of acidic protons of aromatic ring substituents. These could be attributed to either the carboxylic acid or the amine functions.

The ^{13}C NMR spectrum also showed additional peaks at typical chemical shifts, such as the ketone group, C_9, as well as the carboxylic acid function, C_1 (at 182.18 and 171.70 ppm, respectively). COSY showed the interaction between two peaks at 7.78 and 6.92 ppm, which could either be H_6 or H_7, and the uncorrelated peak at 7.22 ppm was attributed to H_4. HSQC showed the direct correlation between H_4 and C_4 (105.50 ppm). HMBC showed the correlation between C_9 (182.19 ppm) and the acidic proton at 10.15 ppm, which could only be attributed to the NH function. The other unshielded ^{1}H peak at 11.51 ppm was attributed to the proton from the carboxylic acids (COOH).

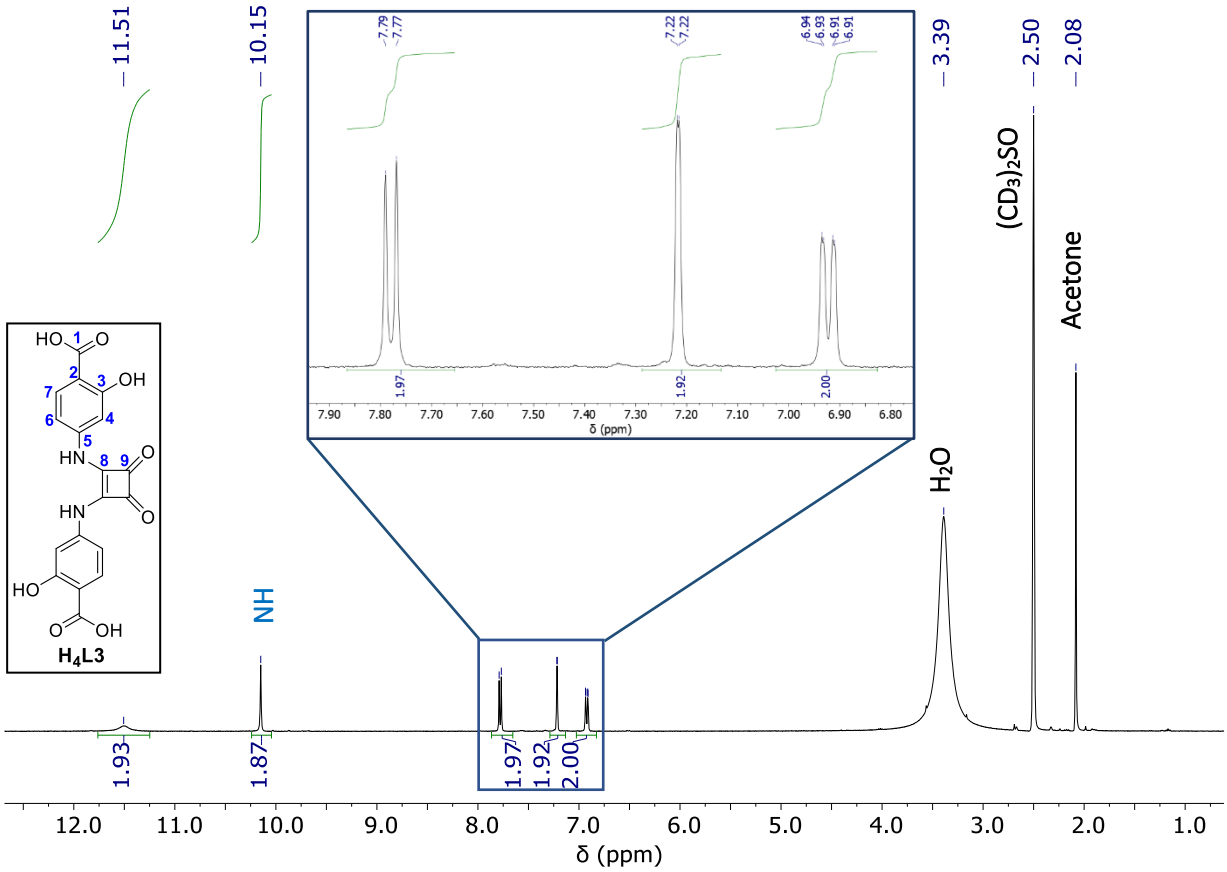

Figure 2.3 - ^{1}H NMR spectrum of **H_4L3** in $(CD_3)_2SO$.

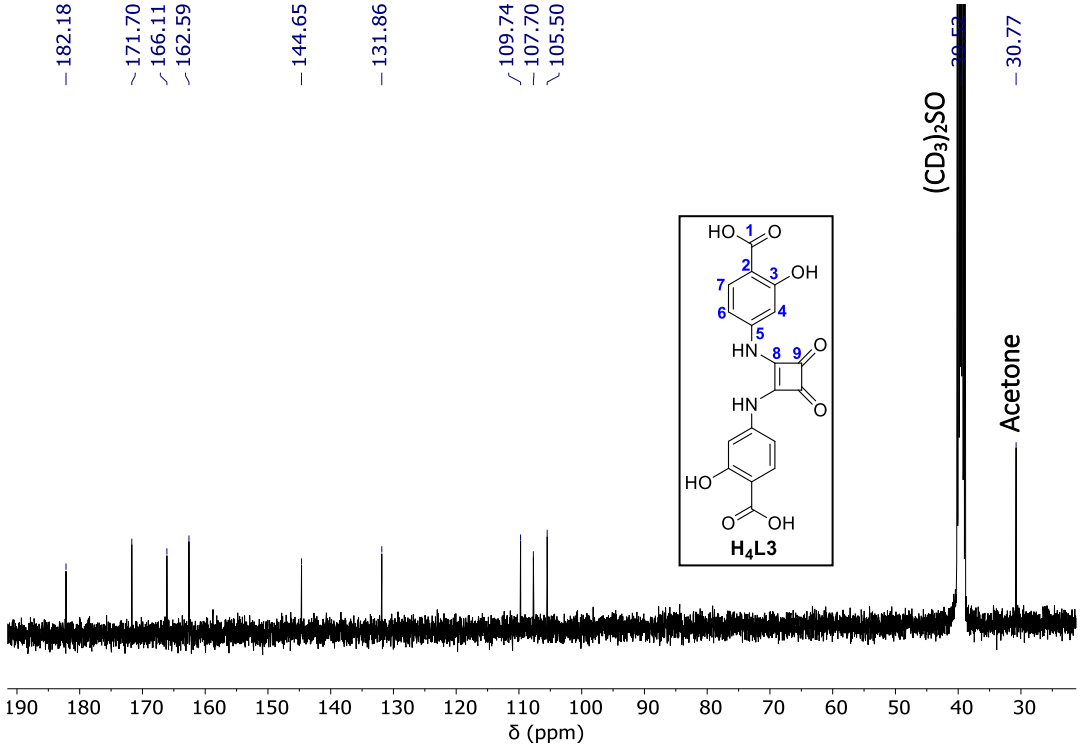

Figure 2.4 - ^{13}C NMR spectrum of **H_4L3** in $(CD_3)_2SO$.

NH correlated with another unshielded ^{13}C peak at 166.11 ppm, which was assigned to C_8. Additionally, it correlated with two ^{13}C peaks in the typical sift range of aromatic C-H functions, C_4, at 105.50 ppm and another at 109.74 ppm, which could be attributed to C_6. By HSQC, C_6 correlated with the ^{1}H peak at 6.93 ppm. Also, C_1 (171.70 ppm) correlated only with one ^{1}H peak at 7.78 ppm, which could only be assigned to H_7, being the closest proton to the carbonyl function (^{3}J). H_7 (7.78 ppm) also correlated with two more quaternary carbons at 162.59 and 144.65 ppm, which were assigned to C_3 and C_2, respectively. Finally, H_6 (6.93 ppm) correlated with an extra quaternary carbon at 107.70 ppm, and, since it appeared in the typical aromatic carbon range, it was attributed to C_5. The remaining ^{13}C or ^{1}H peaks from C-H groups were further obtained by HSQC and the overall attribution data is presented in **Table A.4** In Annexes.

H_4L3 pro-ligand was also characterised by FTIR spectroscopy (**Figure A.28** in Annexes). It is structurally more complex than **H_4L1** or **H_4L2**, therefore it was possible to identify extra bands, with the attribution data in **Table A.5** in Annexes. A band ranging from 3473 to 3417 cm^{-1} was identified, constituted by two humps. These were attributed to the stretching of N-H (ν_{N-H}) and ν_{O-H}. Moreover, in the typical range of $\nu_{C=O}$ it was detected an additional sharp band, that could be attributed to the ketone functional group, at 1789 cm^{-1}. The overlapped bands between 1684 and 1606 cm^{-1} could be attributed to the $\nu_{C=O}$ from the carboxylic acid, the stretching of C=C from the α,β-unsaturated ketone ($\nu_{C=C}$). The remaining bands in the spectrum were attributed to δ_{C-O-H} at 1404 cm^{-1}, ν_{C-O} from phenol or carboxylic acid between 1295 and 1173 cm^{-1}, and δ_{C-H} from 957 to 620 cm^{-1}.

The elemental composition of **H_4L3** was also obtained by EA, with experimental values of % 55.47 (C), 3.54 (H) and 7.10 (N). These were very close to the ones predicted, respectively, % 56.26 (C), 3.15 (H) and 7.29 (N) and so, it was assumed that the sample was constituted by pure **H_4L3**.

2.2 Fe/L film: optimisations and characterisations

To the best knowledge, MOF-74 films have not yet been reported. Therefore, it was necessary to optimise experimental conditions to obtain films using the cathodic deposition method. In this thesis, the parameters chosen to be optimised were the precursors' concentrations, time of deposition, working electrode areas and temperature. The film precursors were $FeCl_3 \cdot 6H_2O$ (**M**) as the metal ion, H_4DOBDC (**H_4L**) as the pro-ligand and Et_3NHCl (**PB**) as the pro-base. The selected PB has been reported in the literature and forms Et_3N, a mild base.[96,127,129]

2.2.1 Cathodic deposition of Fe/L with a ratio of 7:2:2 (M:H_4L:PB, respectively)

According to the literature, ratios between 5:2 and 7:2 (**M:H_4L**, respectively) are commonly used to produce MOF-74 by solvothermal conditions.[98,102] Herein, the ratio of 7:2 (**M:H_4L**, respectively) was selected as a first approach. It is also reported that the **PB** is regenerated during the deposition process.[127] Hence, the ratio of 1:1 (**H_4L:PB**, respectively) was also selected, which led to a first approach with a precursor ratio of 7:2:2 (**M:H_4L:PB**, respectively).
The redox behaviour of the precursor species (**M**, **H_4L** and **PB**) was studied by cyclic voltammetry (CV). These studies were performed in a previously degassed DMF solution containing 0.1 M of tetrabutylammonium hexafluorophosphate ($TBAPF_6$) as the supporting electrolyte. The one-compartment electrochemical cell was assembled with fluorine tin oxide (FTO, A=1 or 0.7 cm^2) as working, platinum wire as counter and 3M Ag/AgCl as reference electrodes. All potentials are referenced to the 3 M Ag/AgCl reference. The CV of **M** (**Figure 2.5a**) showed a redox pair peak at -0.19 and 0.36 V, attributed to $Fe^{3+/2+}$ (**Equation 1**), similar to the reported values.[96]

$$Fe^{3+} + e^- \rightleftharpoons Fe^{2+} \qquad \text{(Equation 1)}$$

It also displayed a reduction shoulder at approximately -0.65 V, followed by a current crossing starting at -1.3 V. This suggested the reduction of Fe^{2+} to Fe^0 and its deposition on the FTO electrode, also in agreement with the literature.[96] Fe^0 is then re-oxidised to Fe^{2+} and the process can be observed at -0.44 V (**Equation 2**).

$$Fe^{2+} + 2e^- \rightleftharpoons Fe^0 \qquad \text{(Equation 2)}$$

To confirm the relationship between the current crossing and the oxidation peak at -0.44 V, a second CV was performed (**Figure 2.5b**) to a higher cathodic limit (-1.5 V). Although the peak for $Fe^{3+/2+}$ remains identical, a more intense current crossing and oxidation peak was observed (at -1.3 V and -0.41 V, respectively). This proved that both processes are related and that, by increasing the potential to more negative values, more Fe^{2+} species are reduced to Fe^0 and re-oxidized to Fe^{2+}. For subsequent depositions, the growth potential must be more negative than -0.19 V, so that Fe^{2+} species are present. Moreover, if a potential close to -1.3 V is applied, the reduction of Fe^{2+} to Fe^0 is also possible.

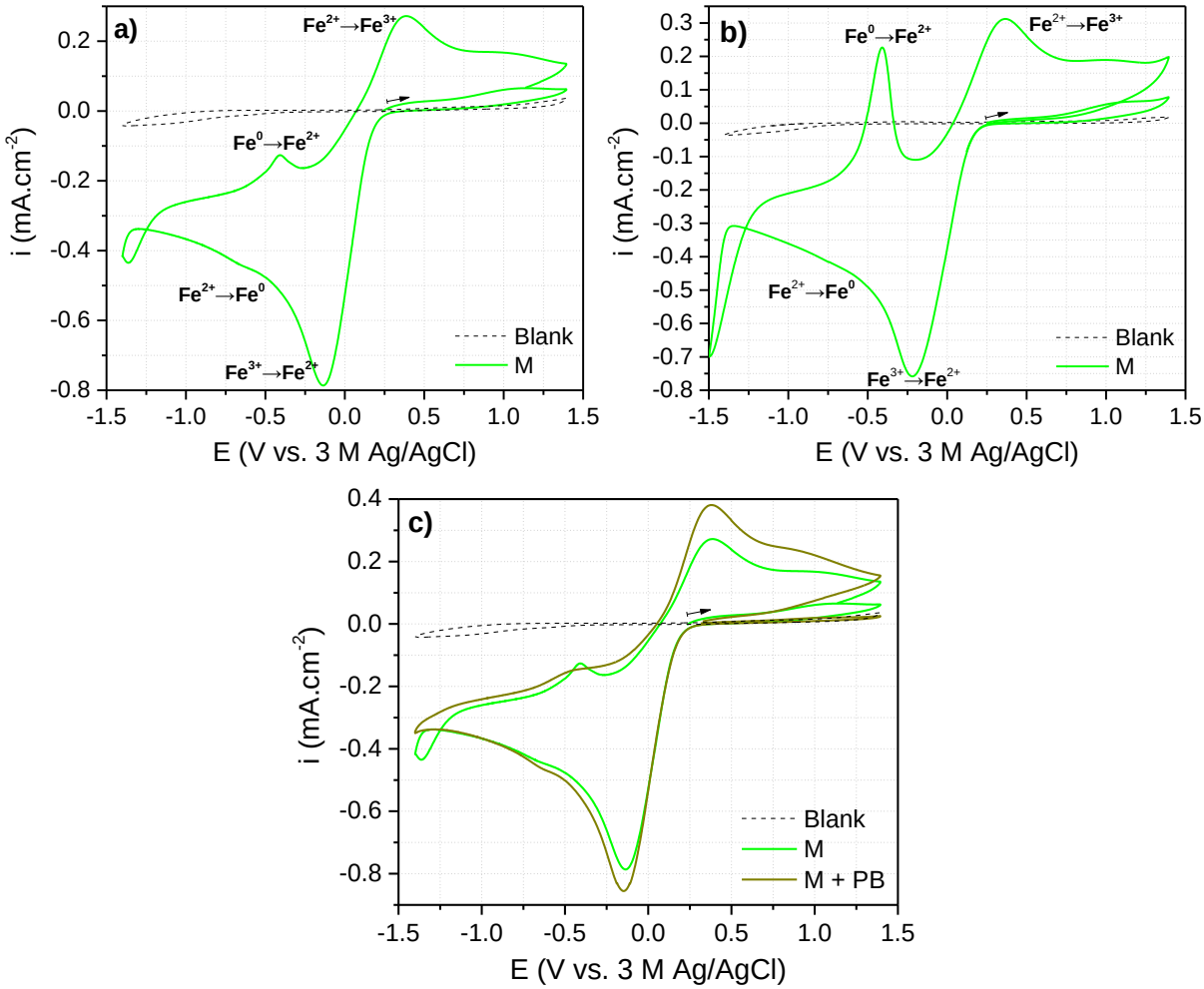

Figure 2.5 - Cyclic voltammograms of a) **M**; b) **M** with a cathodic limit of -1.5 V and c) overlay of **M** and **M**+**PB**. Species were added in 10 mL of N_2 saturated DMF with $TBAPF_6$ as the supporting electrolyte and recorded at 100 $mV.s^{-1}$. The one-compartment electrochemical cell was also constituted by FTO as working, platinum wire as counter and 3 M Ag/AgCl as reference electrodes. Species quantities: 7 mM of **M** and 2 mM of **PB**.

The CV of the **M**+**PB** mixture (**Figure 2.5c**), showed the disappearance of the current crossing and the minimisation of the Fe^0 oxidation peak, originally observed at -1.3 and -0.44 V, respectively. This indicated the presence of a competitive reaction that was preventing the Fe^{2+} reduction to Fe^0 and consequent deposition. The minimisation of these peaks can be attributed to the Fe^0 oxidation by **PB** (**Equation 3**), as mentioned in the literature.[127]

$$2Et_3NH^+ + Fe^0 \rightarrow Fe^{2+} + 2Et_3N + H_2 \qquad \textbf{(Equation 3)}$$

The CV of **H4L** was also performed (**Figure 2.6a)** and it showed less defined redox processes that can be associated with a less electroactive species. Yet, it was possible to observe oxidation peaks in the -0.7 to 0.4 V range and another oxidation peak at -0.9 V. Moreover, it was also possible to observe reduction peaks at -0.03 and -0.72 V.

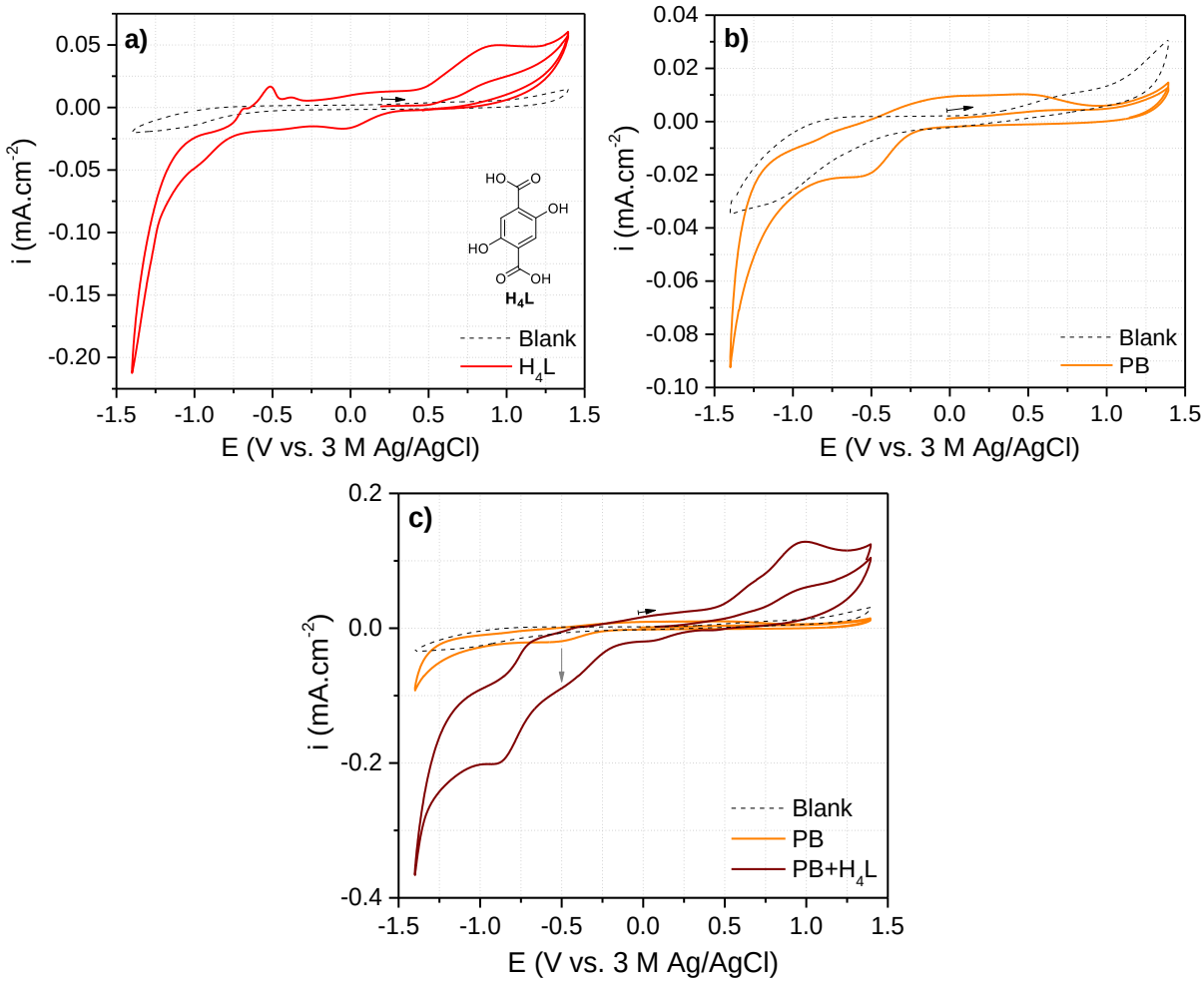

Figure 2.6 - Cyclic voltammograms of a) **H4L**, b) **PB** and c) overlay of **PB** and **PB+H4L** mixture. Species were added in 10 mL of N_2 saturated DMF with $TBAPF_6$ as the supporting electrolyte and recorded at 100 $mV.s^{-1}$. The one-compartment electrochemical cell was also constituted by FTO as working, platinum wire as counter and 3 M Ag/AgCl as reference electrodes. Species quantities: 2 mM of **H4L** and 2 mM of **PB**.

The CV of the **PB** (**Figure 2.6b**) showed a reduction peak at -0.58 V, attributed to the triethylammonium proton reduction (**Equation 4**).[96,127]

$$2Et_3NH^+ + 2e^- \rightarrow H_2 + 2Et_3N \qquad \textbf{(Equation 4)}$$

Comparing the CVs of **PB** and the **PB+H4L** mixture (**Figure 2.6c**), it was found an increase of the reduction peak response at -0.58 V. Since the peak potential did not shift when compared to the CV of **PB**, it could be attributed to a higher H^+ reduction induced by the ligand deprotonation.[96,127] The CV showed an additional reduction peak at -0.87 V. As reported,[144,145] this structure undergoes a two-step deprotonation process. Hence, the peaks at -0.58 and -0.87 V can be attributed to the deprotonation of the carboxylic acid and phenol functions, respectively.

The CVs of **H4L+M** and **H4L+M+PB** mixtures (**blue** and **pink**, respectively, in **Figure 2.7**), showed a very similar behaviour, except for the higher peak response in the case of the **H4L+M+PB**. The oxidation peaks between -0.76 and -0.65 V could be attributed to **H4L**

oxidations. The presence of the $Fe^{3+/2+}$ redox pair peaks was also observed, as described above (see **Figure 2.5** for comparison). Moreover, two new peaks were observed: an oxidation peak at -1.3 V and a reduction peak at 0.65 V. These were attributed to redox peaks of the metal-ligand interaction.

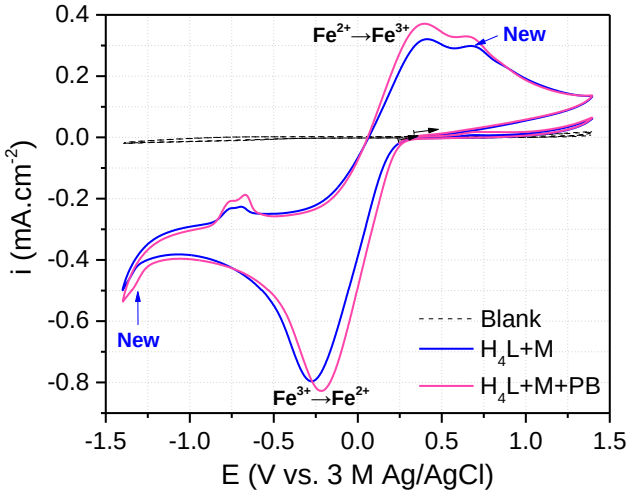

Figure 2.7 - Cyclic voltammograms overlay of **H_4L+M** (**blue**) and **H_4L+M+PB** (**pink**) mixtures. Species were added in 10 mL of N_2 saturated DMF with $TBAPF_6$ as the supporting electrolyte and recorded at 100 $mV.s^{-1}$. The one-compartment electrochemical cell was also constituted by FTO as working, platinum wire as counter and 3 M Ag/AgCl as reference electrodes. Precursor quantities: 7 mM of **M**, 2 mM of **H_4L** and 2 mM of **PB**.

After studying the electrochemical behaviour of the precursors, cathodic depositions were made, using chronoamperometry. The three precursors were added to the one-compartment electrochemical cell and degassed with N_2 for at least 30 minutes (**Figure 2.8**). Then, a cathodic potential was applied for one hour, measuring the current vs. time. After the deposition, the films were washed with DMF and H_2O, dried at room temperature and further characterised. In this thesis, the films deposited with all three precursors (**M+ H_4L+PB**) are identified as **Fe/L** films.

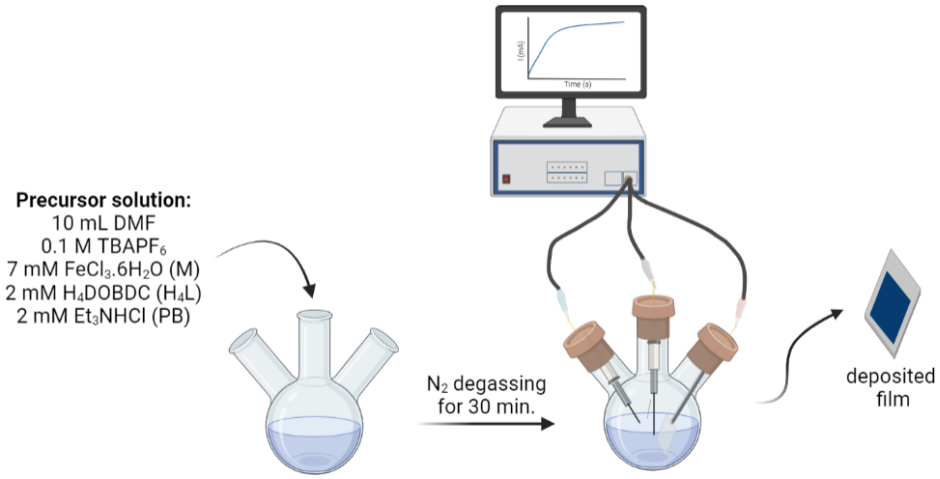

Figure 2.8 - Schematic representation of the cathodic deposition experiment.

From the CVs, electrodepositions should occur at potentials where the Fe^{3+} is reduced to Fe^{2+} (-0.19 V), **PB** is reduced to triethylamine (-0.58 V) and **H_4L** is deprotonated (-0.87 V). Electrodepositions were performed at different working potentials (E_{app}), ranging from -1.4 V to -1.1 V (**Figure 2.9**), which will be further referred to as growth potentials. All depositions yielded a thick dark-blue film, except when the growth potential was -1.1 V. The cathodic current was measured along the deposition and the chronoamperograms behaviour were analysed. The chronoamperogram with a growth potential of -1.1 V (**Figure 2.9a**) displayed an abrupt current decay after 50 seconds, until it reached a current limit and remained constant through the rest of the deposition time. Hence, an abrupt behaviour can be associated with impossibility to obtain the film.

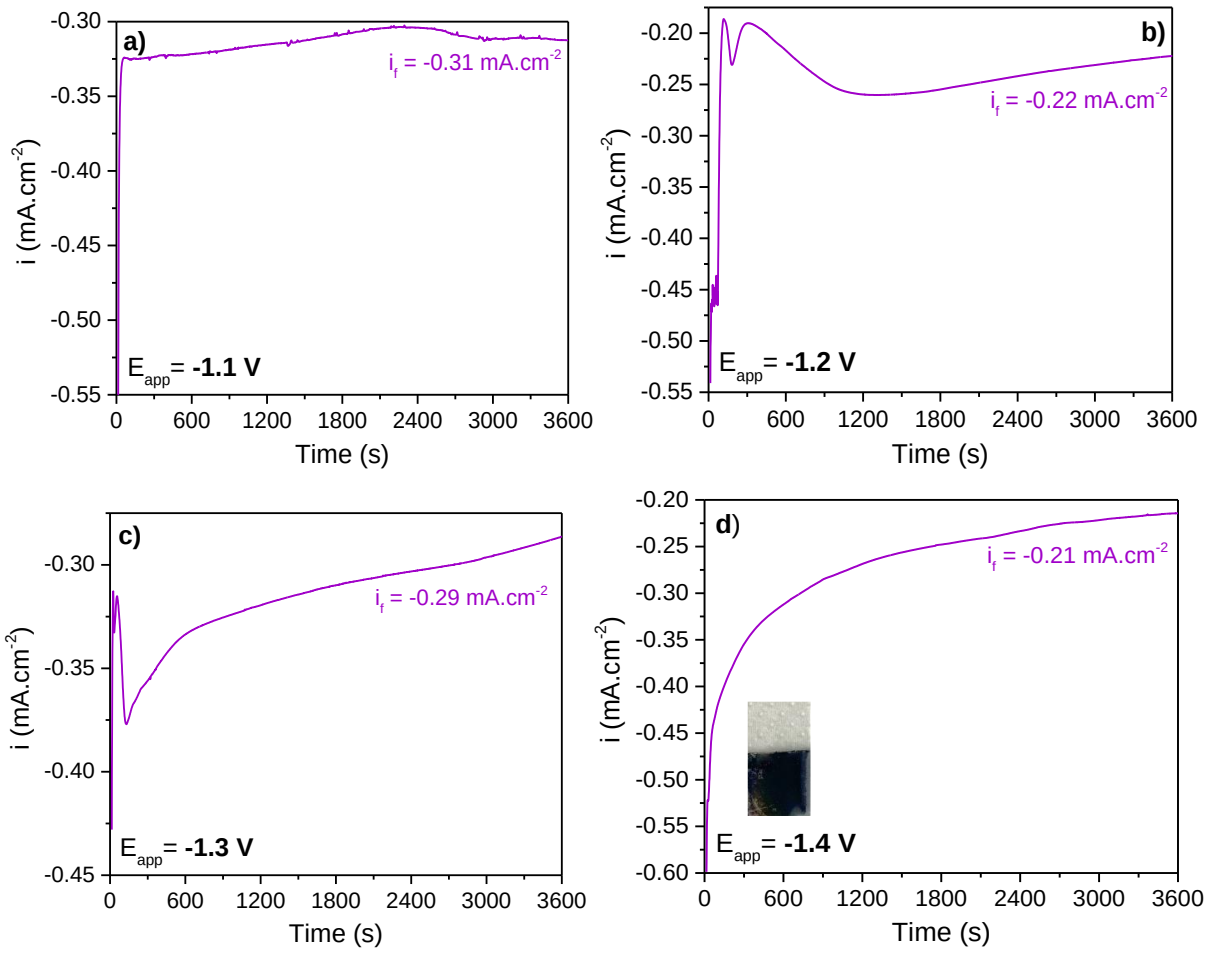

Figure 2.9 - Chronoamperograms following the deposition of the **Fe/L** films with growth potentials of a) -1.1 V, b) -1.2 V, c) -1.3 V and d) -1.4 V. Electrodepositions were performed in 10 mL of N_2 saturated DMF with $TBAPF_6$ as the supporting electrolyte and recorded at 100 mV.s^{-1}. The one-compartment electrochemical cell was also constituted by FTO as working, platinum wire as counter and 3 M Ag/AgCl as reference electrodes. Precursors quantities: 7 mM of **M**, 2 mM of **H_4L** and 2 mM of **PB**.

The growth potentials of -1.2 V or -1.3 V show a different behaviour (**Figure 2.9b,c**). Current fluctuations were observed in the initial part of the process that could be attributed to the precursor transformations into the required species (e.g., **PB** reduction to base, **H_4L**

deprotonation to the **L** ligand, iron complexation with the ligand, and so on). When -1.2 V and -1.3 V were used as growth potentials, the current gradually increased up to approximately 1200 and 140 seconds, respectively. Afterwards, both have an exponential decay towards the approximate current value of the double layer. The chronoamperogram with a growth potential of -1.4 V (**Figure 2.9d**) does not show current fluctuations. Since -1.4 V is a growth potential more negative than -1.3 and -1.2 V, competitive reactions may occur at a faster rate and are not observed.

Although it was possible to deposit dark-blue films, part of these detached during the washing and drying process. It was possible to observe an orange pre-layer by naked eye. Fe_2L is reported as a red-orange material,[98] which did not match to the colour of the film's surfaces and could be due to partial Fe^{2+} oxidation. On the other hand, it was also reported the presence of an iron composite with the deposition of another Fe-MOF.[96] This phenomenon could also be possible in this work, since the **M** CV showed a current crossing at around -1.3 V. To conclude about the possibility of an iron composite, the **M+PB** mixture was deposited with a growth potential of -1.4 V, yielding an orange/brown thin film. Contrarily to the **Fe/L** film, this chronoamperogram (**Figure 2.10a**), did not show a gradual behaviour with a single current decay. Hence, it was concluded that the deposition of iron was possible. By colour similarities, it can be suggested that the pre-layer was constituted by an iron composite.

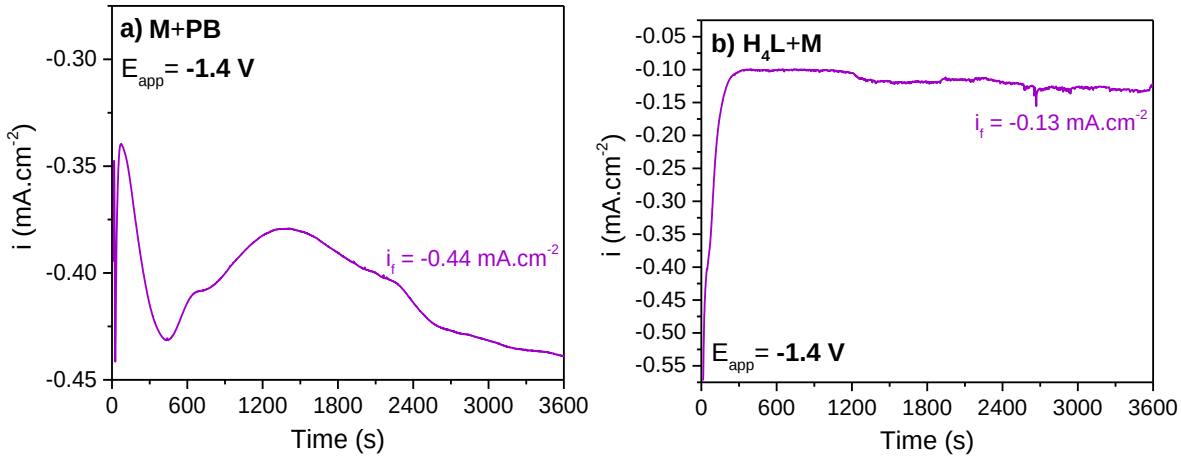

Figure 2.10 - Chronoamperograms following the deposition of a) the **M+PB** and b) **M+H4L** mixtures. Electrodepositions were performed in 10 mL of N_2 saturated DMF with $TBAPF_6$ as the supporting electrolyte and recorded at 100 $mV.s^{-1}$. The one-compartment electrochemical cell was also constituted by FTO as working, platinum wire as counter and 3 M Ag/AgCl as reference electrodes. Precursors quantities: 7 mM of **M**, 2 mM of **H4L** and 2 mM of **PB**.

To study the importance of the **PB**, the **H4L+M** mixture was deposited with a potential growth of -1.4 V and yielded a light-blue film. The chronoamperogram (**Figure 2.10b)** showed an abrupt current decay, although not as fast as the deposition of **Fe/L** with a growth potential of -1.1 V (**Figure 2.9a**). The presence of a thin film could be attributed to the presence of water in solution from **M** ($FeCl_3.6H_2O$). Once water is reduced it releases OH^- ions that could also

deprotonate the ligand and behave as an additional pro-base. The presence of water from **M** will always be present because the depositions were not obtained in anhydrous conditions. Since the presence of **PB** resulted in a thicker film, it can be assumed that **PB** is an essential precursor.

2.2.1.1 Characterisation of the Fe/L film (7:2:2 ratio of M:H_4L:PB, respectively)

FTIR and DRIFT characterisation

The **H_4L** precursor was firstly analysed by FTIR (**Figure A.29** and **Table A.6** in Annexes) and the spectrum is in agreement with the literature.[146] The bands found at 3520 and 3082 cm^{-1} were attributed to the typical wavenumbers of ν_{O-H} from the carboxylic acid and phenol functions, respectively. It was also observed the presence of aromatic ν_{C-H} at 2880 cm^{-1}, and $\nu_{C=O}$ at 1646 cm^{-1}. The band at 1427 cm^{-1} and the group found at 1357 and 1288 cm^{-1} were assigned to δ_{C-O-H} and ν_{C-O}, respectively. Finally, the bands on 905-696 cm^{-1} could be attributed to δ_{C-H}.

Films were analysed by diffuse reflectance infrared Fourier transform spectroscopy (DRIFT), which is a non-destructive surface FTIR spectroscopy. This technique is useful to analyse the surface of the films, without sample preparation. DRIFT takes use of the diffuse reflectance of the incident infrared radiation, obtaining a spectrum identical to FTIR.[147]

The FTIR of **H_4L** and DRIFT of **Fe/L** were compared (**Figure 2.11**). The **Fe/L** spectrum (see attributions in **Table A.7**, in Annexes), showed a band at 3226 cm^{-1} attributed to ν_{O-H} from water. The presence of ν_{C-H} bands was also observed between 2963 and 2861 cm^{-1}, which could be either attributed to aromatic bonds from the **H_4L** or aliphatic groups from the DMF, $TBAPF_6$, or Et_3N impurities. The spectrum of the **Fe/L** film showed two sharp bands at 1537 and 1422 cm^{-1} that do not match the **H_4L** spectrum. **H_4L** is composed by carboxyl functions, by the presence of the $\nu_{C=O}$ band at 1646 cm^{-1}. Since the **PB** deprotects **H_4L**, it was expected that the film presented carboxylate functions. Hence, the new bands can be attributed to the symmetric and asymmetric stretching of the O-C-O function (ν_{O-C-O}). Additional bands were attributed to ν_{C-O} of the phenoxide function ranging from 1236 to 1204 cm^{-1}. The DRIFT showed a band ranging from 890 to 802 cm^{-1}, assigned to δ_{C-H}. Finally, the presence of iron coordinated to oxygen atoms was also observed by the presence of a band at 560 cm^{-1}, attributed to the stretching of the Fe-O bond (ν_{Fe-O}).[96] The presence of the ν_{O-C-O} and ν_{Fe-O} was indicative of the **H_4L** deprotonation and coordination to **M**.

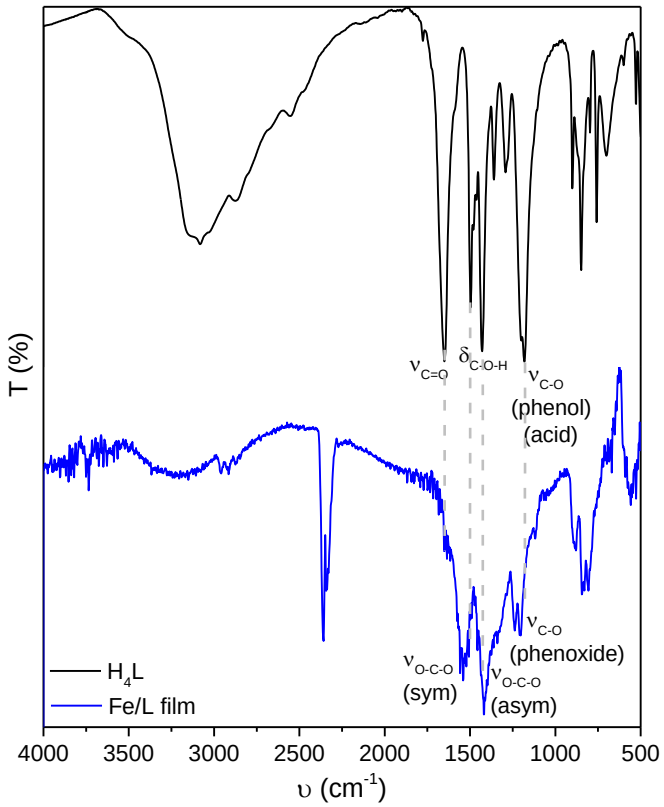

Figure 2.11 - FTIR spectrum of **H_4L** (**black**) and DRIFT spectrum of the **Fe/L** film (**blue**, with a 7:2:2 ratio of **M**:**H_4L**:**PB**, respectively) deposited at -1.4 V. Spectra were recorded in a range of 4000-500 cm^{-1}.

The **M+PB** film was also characterised by DRIFT (**Figure A.30**, in Annexes). It showed a different spectrum to the **Fe/L** film, suggesting the presence of a different material. DRIFT showed the ν_{O-H} band at 3393 cm^{-1}, attributed to the presence of water or hydroxyl groups from iron hydroxide species. It also displayed the ν_{C-H} bands around 2921 cm^{-1} that could be attributed to the aliphatic bonds from the Et_3N or $TBAPF_6$ impurities. The observed band at 544 cm^{-1} was attributed to the ν_{Fe-O} from possible iron oxide or hydroxide species. Other than that, it was possible to find a band along with instrument noise, characteristic of O-H bending (δ_{O-H}) from water. This DRIFT study suggested that the **M+PB** film was constituted by iron oxide/hydroxide species. Moreover, the **M+PB** film spectrum was different from the **Fe/L** one, meaning that **Fe/L** is not mainly constituted by an iron composite and contains the **H_4L** component.

SEM characterisation

SEM characterisation was employed to analyse the morphology of the films. Images of the surfaces of the films deposited at -1.2 V, -1.3 V and -1.4 V were obtained with different magnifications (**Figure A.31** to **Figure A.33** in Annexes). **Figure 2.12** presents the SEM images of the **Fe/L** film with same magnifications (x5000) deposited at different growth potentials. The last image shows the **H_4L+M** film deposited at -1.4 V, also magnified at x5000. The **Fe/L** films

showed a similar morphology, constituted by a set of disc-shaped aggregates that grows by staking discs on top of each other. The aggregates have similar sizes, except for the growth potential of -1.2 V, that shows a higher size disparity.

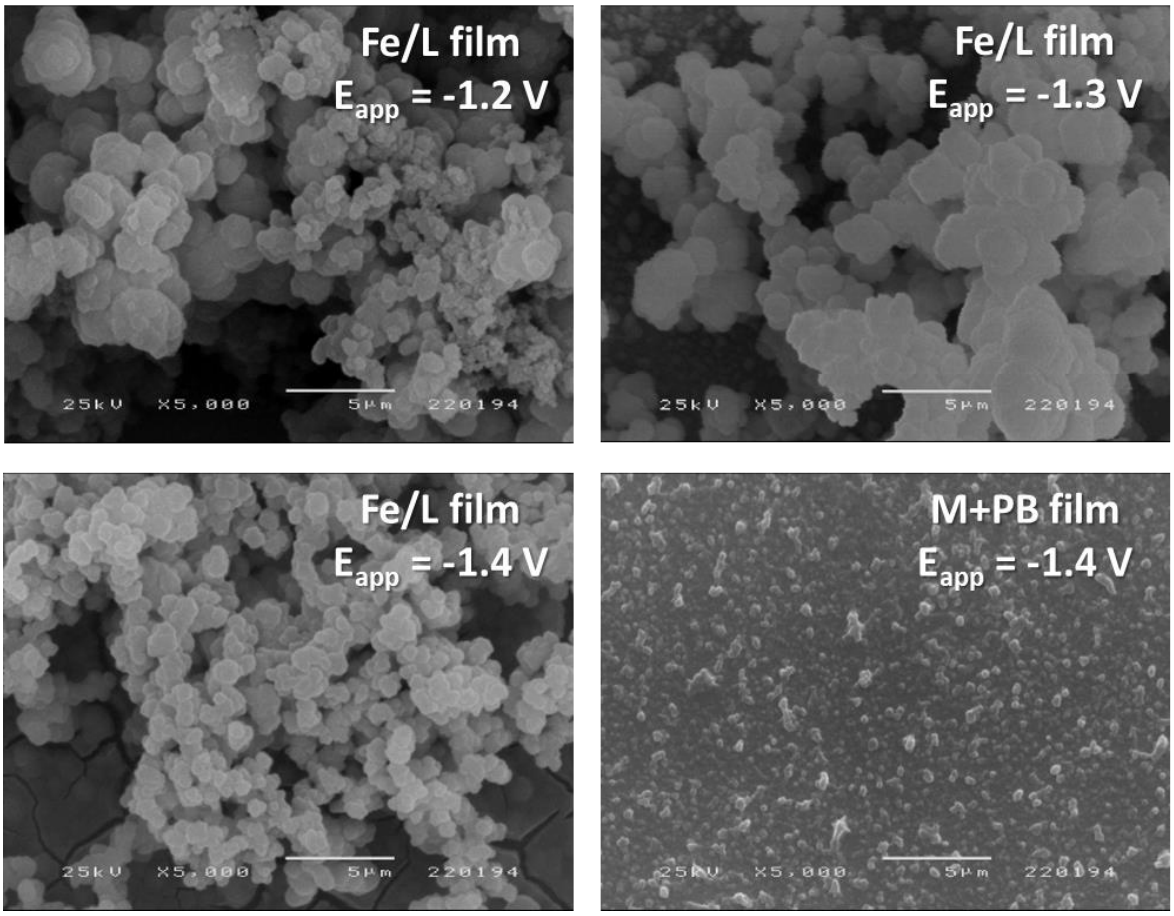

Figure 2.12 - SEM images (x5000) of the **Fe/L** films (7:2:2 ratio of **M**:**H4L**:**PB**, respectively) deposited at -1.2 V, -1.3 V and -1.4 V, and the **M**+**PB** film deposited at -1.4 V.

This work only shows one image of the surface of the **H4L**+**M** film, which was representative of all the film area. Although it showed the presence of small aggregates, the film was not nearly as thick as the **Fe/L** ones, meaning that the presence of the **PB** was crucial for the overall growth of the film.

The image of the **Fe/L** film with a growth potential of -1.4 V with lower magnification (x50, **Figure 2.13a**) showed an overview of the heterogeneity of the film. The images of the **Fe/L** film with a growth potential of -1.4 V and a higher magnification (x5000, **Figure 2.13b**), show accentuated slits. The slits were not observed in the SEM images of the remaining films. The FTO electrode was still stable at -1.4 V (**Figure A.34**, in Annexes) and so, it was not expected to suffer any morphological modification caused by the growth potential. Hence, a different material might have been previously deposited to what was assumed to be the **Fe/L** film, in a more uniform and homogenous way.

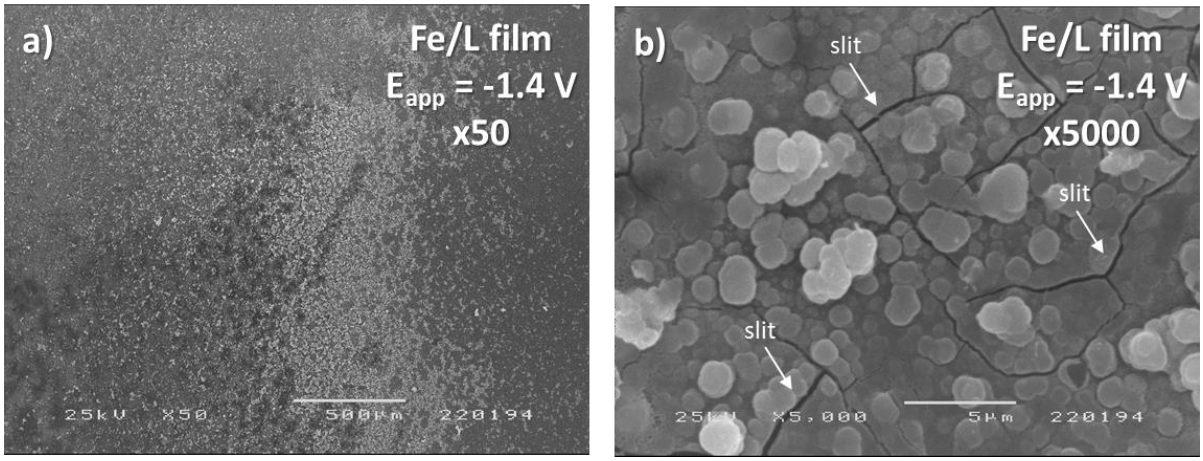

Figure 2.13 - SEM image of the **Fe/L film** (7:2:2 ratio of **M**:**H_4L**:**PB**, respectively) deposited at -1.4 V and magnified at a) x50 and b) x5000.

As stated above, the **M** CV showed the deposition of Fe^0 at a potential around -1.3 V. Although it would be expected that Fe^{2+} reacted with the ligand to yield the MOF film, this approach follows a precursor ratio of 7:2:2 (**M**:**H_4L**:**PB**, respectively). The high excess of Fe^{2+} can be reduced to Fe^0 and further deposited to form the pre-layer. Although it was not possible to confirm the presence of the pre-layer in the remaining films, a growth potential of -1.4 V results on a cracked pre-layer.

XPS characterisation

The surface of the **Fe/L** and **M+PB** films were analysed by X-ray photoelectron spectroscopy (XPS). The survey spectra were focused on the C 1s, O 1s and Fe 2p peak deconvolution (**Table A.8** in Annexes). If not stated otherwise, the peaks were attributed based on refs.[96,148–150]

The C 1s peak of both films (**Figure 2.14**) was deconvoluted into a peak at 285.0 eV attributed to C in the sample holder and C-C and C-H bonds from surface C atoms, respectively, which are impurities. The **Fe/L** film could be further deconvoluted into two peaks centred at 286.7 and 288.9 eV. These were attributed to the C-O bonds from the phenoxide function, and C-O bonds from the carboxylate function. The **M+PB** film was not constituted by the **L** component. Yet, it could still be constituted by triethylamine, composed by C atoms. Its C 1s spectrum could be deconvoluted into similar binding energy peaks centred at 286.8 and 288.6 eV. These were attributed to the C-N function by either triethylamine or DMF, and the amide O=C-N function.

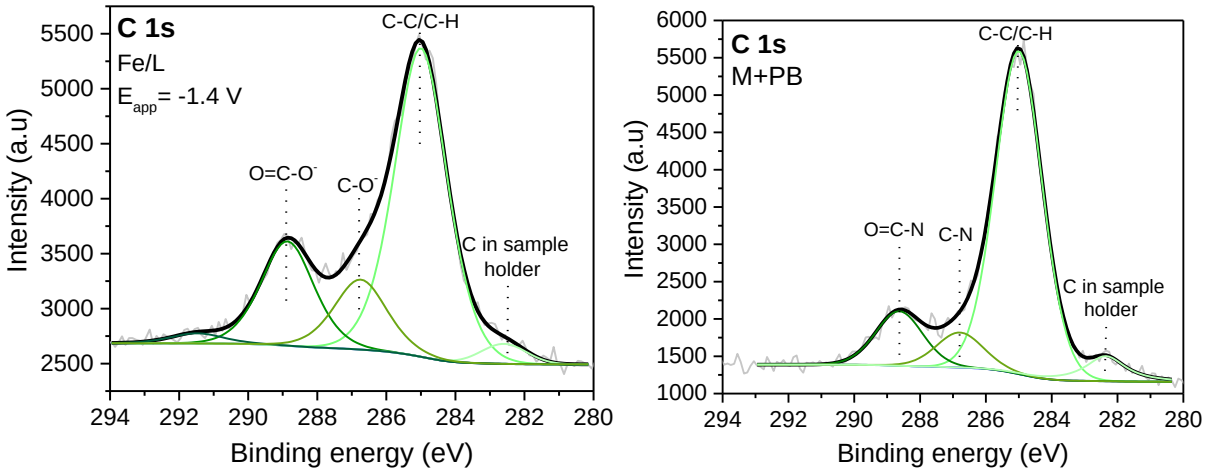

Figure 2.14 - XPS spectra of the **Fe/L** (7:2:2 ratio of **M**:**H$_4$L**:**PB**, respectively) and **M+PB** (7:2 ratio of **M**:**PB**, respectively) films deposited at -1.4 V, amplified in the C 1s peak.

The Fe 2p zone of both **M+PB** and **Fe/L** films (**Figure 2.15**) showed the Fe 2p$_{1/2}$ and 2p$_{3/2}$ peaks. The Fe2p$_{3/2}$ peak was deconvoluted and showed a high number of peaks. This can be associated with a variety of $Fe^{3+/2+}$ species from both films. Although they were expected to have different compositions, it has been suggested the presence of an iron oxide/hydroxide pre-layer on **Fe/L** film. XPS indicates that this pre-layer has a similar constitution of the **M+PB** film. Moreover, the possibility to obtain the content of the pre-layer of **Fe/L** proves the heterogeneity and roughness of the film.

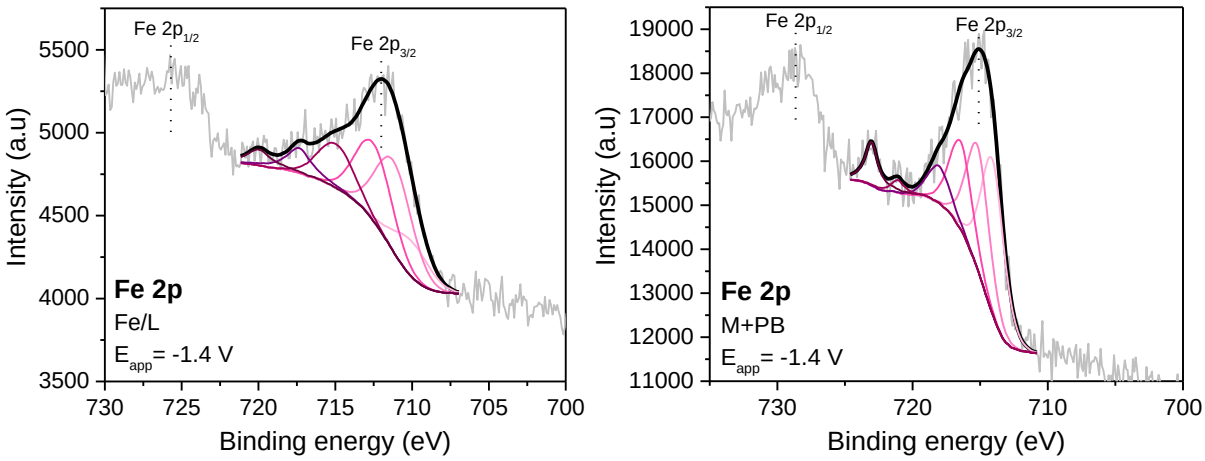

Figure 2.15 - XPS spectra of the **Fe/L** (7:2:2 ratio of **M**:**H$_4$L**:**PB**, respectively) and **M+PB** (7:2 ratio of **M**:**PB**, respectively) films deposited at -1.4 V, amplified in the Fe 2p peak.

It was not possible to deconvolute the O 1s peak of the **Fe/L** film. The O 1s peak of the **M+PB** film (**Figure 2.16**) was deconvoluted into three peaks centred at 530.0, 531.3 and 532.1 eV, attributed to the oxygen from metal oxides/hydroxides, as expected.

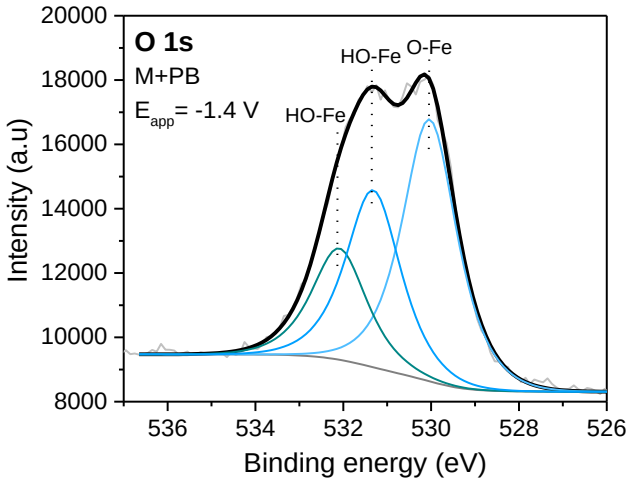

Figure 2.16 - XPS spectra of the the **M+PB** film (7:2 ratio of **M**:**PB**, respectively) deposited at -1.4 V, amplified in the O 1s peak.

The atomic concentration (%) of the Fe, C, O, and N atoms was quantified (**Table A.9** in Annexes). The experimental values were compared with the expected values of Fe_2L. The **Fe/L** film agrees with the C and O content with minimal differences, except for the Fe content. This could be due to the interference of the surface C atoms, blocking the Fe response. The minimal C and O atomic differences could be assigned to the presence of H_2O or DMF completing the octahedral metal geometry. XPS concluded that **Fe/L** is composed by both iron metal ion and **L**. The **M+PB** film showed a similar iron content, contrarily to the C and O. The percentage of C was lower than the predicted for Fe_2L, and the O content was higher, which agrees with the absence of the organic ligand component and the presence of iron oxide/hydroxide mixtures.

XRD characterisation

As already discussed in **Chapter 1.2.**, metal-organic frameworks are characteristic for their high crystallinity. The FTO substrate was firstly characterised by XRD, **Figure A.35** in Annexes) and found to have two peaks. The diffractogram of the **Fe/L** film deposited with a growth potential of -1.4 V was also characterised (**Figure A.36** in Annexes). The **Fe/L** film and FTO diffractograms were identical, proving that the film was overall amorphous. This was not a surprise, since the reported Fe-MOF films do not show a high crystallinity.[96,124] The diffractogram of the **M+PB** film (**Figure A.37**, in Annexes) did not display additional peaks as it was also amorphous.

The lack of crystallinity could be explained by the presence of the iron oxide/hydroxide pre-layer, that could be affecting the film growth organisation. Since one of the main goals of this work was to obtain a crystalline framework, different strategies were necessary to minimise the pre-layer and to induce film crystallinity.

2.2.2 Grafting

To facilitate an homogeneous nucleation and growth, electrode surface modification, also known as grafting, could be a useful technique to anchor the metal nodes to the substrate (working electrode).[151] This method takes use of the *in-situ* covalent bonding of the functionalising molecule to the surface of the electrode. Herein, 4-aminosalicylic acid (4-ASA) was selected to functionalise the FTO working electrode. It has a similar structure to the **H_4L** proligand, constituted by the same coordination sites. The grafting procedure (**Scheme 2.4**) was adapted from Wu *et al.*[152]. It involved the N_2 degassing of 4-ASA dissolved in an acidic solution in an one-compartment electrochemical cell. It was followed by the addition of $NaNO_2$ and was expected to yield a diazonium salt. Running a CV showed an irreversible peak at -0.34 V, caused by the reduction of the diazonium salt and covalent binding of the salicylic acid (SA) to the FTO working electrode. The functionalised FTO will be further referred to as SA@FTO.

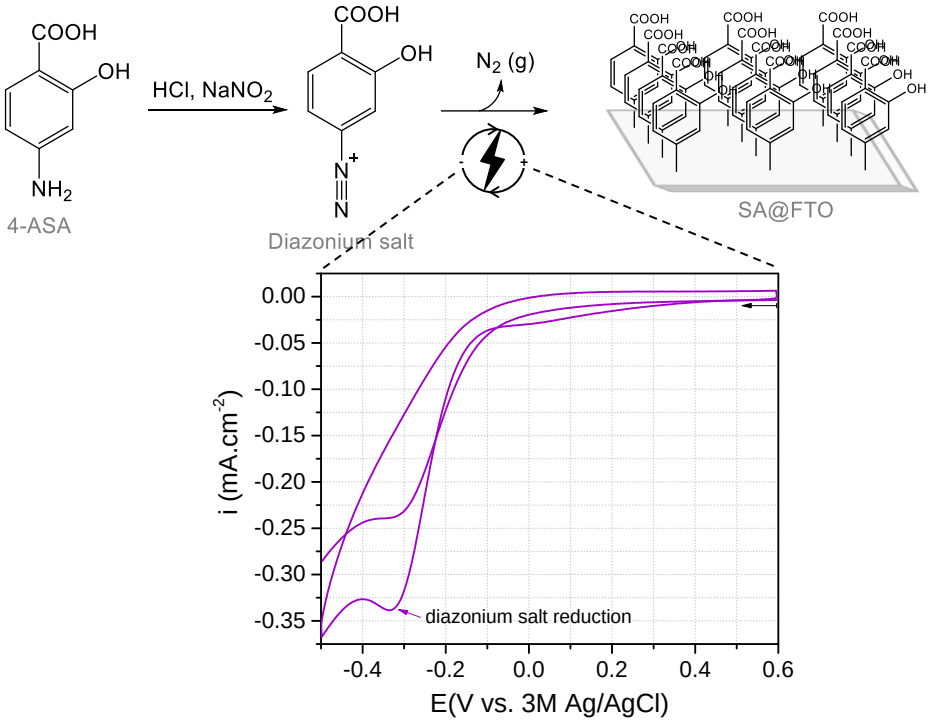

Scheme 2.4 - Schematic representation of FTO electrode functionalisation. Species were added in 10 mL of N_2 saturated DMF with $TBAPF_6$ as the supporting electrolyte and recorded at 100 $mV.s^{-1}$. The one-compartment electrochemical cell was also constituted by FTO as working, platinum wire as counter and 3 M Ag/AgCl as reference electrodes.

The CVs of FTO and SA@FTO were performed in a solution containing 1 mM of ferrocene (**Figure 2.17**) Ferrocene/ferrocenium (Fc/Fc^+) is considered a well-defined redox couple and often recurred as an internal standard for potential values. Since SA@FTO and FTO display different redox behaviours, it can be assumed that at least some content of SA has been

successfully attached to the FTO. The SA@FTO redox peaks have a smaller potential difference (ΔE_p= 0.6 V) and the FTOs' (ΔE_p= 0.87 V), meaning that SA@FTO enhances the electron transfer.

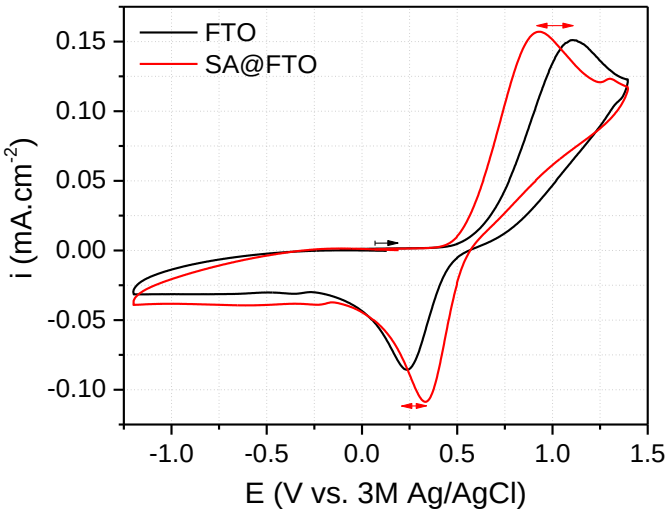

Figure 2.17 - Cyclic voltammograms of 1 mM of ferrocene with FTO (**black**) and SA@FTO (**red**) as working electrodes. Studies were performed in 10 mL of N_2 saturated DMF with $TBAPF_6$ as the supporting electrolyte and recorded at 100 $mV.s^{-1}$. The one-compartment electrochemical cell was also constituted by platinum wire as counter and 3 M Ag/AgCl as reference electrodes.

The electrochemical behaviour of the **H_4L**, **PB** and **M** precursors on SA@FTO was studied. The precursor CVs in FTO and SA@FTO were compared (**Figure A.38**, in Annexes) and showed some differences regarding the peak response. The CV of the **PB** on SA@FTO revealed an additional reduction peak. SA is a molecule with both carboxylic and phenolic functions. Similar to the CV of **H_4L+PB** in FTO (for comparison, see **Figure 2.6**), the **PB** could also deprotonate the functionalised layer, which also contains carboxylic acids and phenolic functions. Therefore, the reduction peaks at -0.60 and -0.97 V could be attributed to the deprotonation of the carboxylic and phenol functions of SA.

The **Fe/L** films were also deposited on SA@FTO working electrode. Similar to the FTO deposition approach, films were deposited with growth potentials between from -1.1 V and -1.4 V. Depositions yielded dark-blue films at -1.4 and -1.3 V and no visible films at -1.2 and -1.1 V. The chronoamperograms with growth potentials of -1.4 V and -1.3 V (**Figure 2.18**) show some charge fluctuations in the first seconds followed by a gradual current decay.

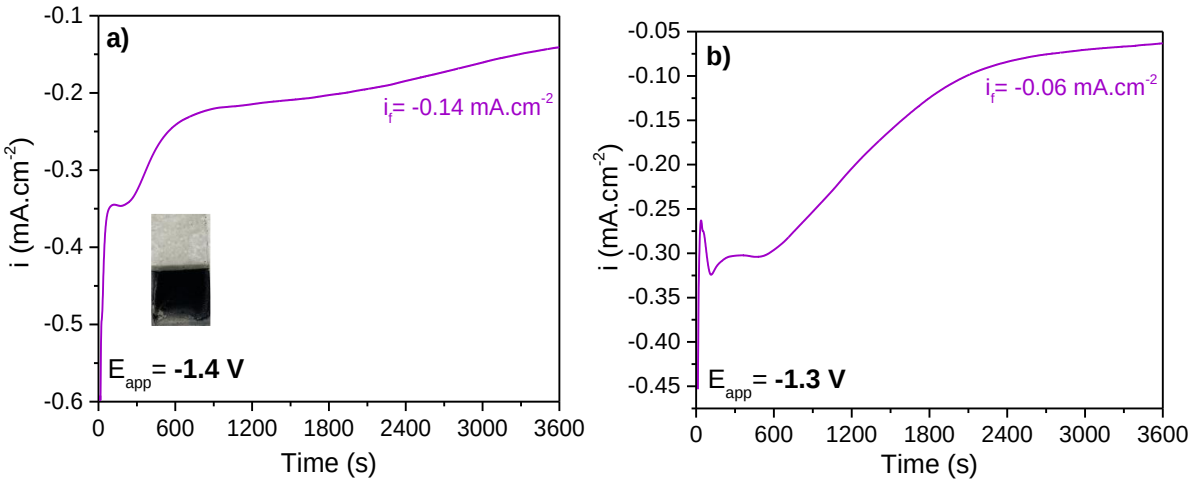

Figure 2.18 - Chronoamperograms following the deposition of the **Fe/L** films on SA@FTO, with growth potentials of a) -1.4 V and b) -1.3 V. Electrodepositions were performed in 10 mL of N_2 saturated DMF with $TBAPF_6$ as the supporting electrolyte and recorded at 100 mV.s^{-1}. The one-compartment electrochemical cell was also constituted by FTO as working, platinum wire as counter and 3 M Ag/AgCl as reference electrodes. Precursors quantities: 7 mM of **M**, 2 mM of **H_4L** and 2 mM of **PB**.

On the other hand, the chronoamperograms obtained with growth potentials of -1.2 and -1.1 V (**Figure A.39** in Annexes) displayed a fast current decay. After the decay to less negative currents, the chronoamperogram at -1.2 V starts to invert the deposition behaviour and gradually decays to more negative currents.

The same behaviour was observed in the deposition of the **M+PB** film at -1.4 V (**Figure A.40** in Annexes). This decay could be attributed to the interference of oxidation reactions (e.g., Fe^{2+} oxidation to Fe^{3+}) competing with the film deposition.Since the **M+PB** film was obtained with identical colour/texture from either FTO or SA@FTO working electrodes (orange/brown film) it suggests that the functionalisation may not minimise the iron deposition.

2.2.2.1 Characterisation of the Fe/L films on SA@FTO (7:2:2 of M:H_4L:PB, respectively)

DRIFT characterisation

The **Fe/L** film with a growth potential of -1.4 V on SA@FTO was characterised by DRIFT. **Fe/L** showed identical spectra, either by deposition of FTO or SA@FTO (**Figure 2.19**). The spectra are constituted by the same vibrational modes and without bands shifts. The bands assigned to $\nu_{O\text{-}H}$ at 3226 cm^{-1}, $\nu_{C\text{-}H}$ ranging from 2963 to 2861 cm^{-1} and symmetric and asymmetric $\nu_{O\text{-}C\text{-}O}$ at 1537 and 1422 cm^{-1}, respectively, were also observed. Also, $\nu_{C\text{-}O}$ from phenoxide at 1217 cm^{-1}, $\delta_{C\text{-}H}$ at 843 cm^{-1} and $\nu_{Fe\text{-}O}$ at 562 cm^{-1}.

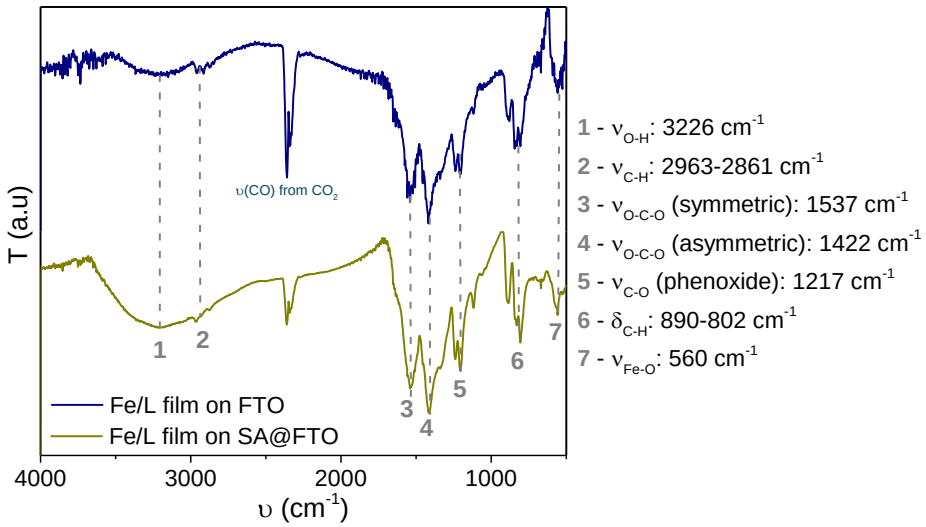

Figure 2.19 - DRIFT spectra of the **Fe/L** films (7:2:2 ratio of **M**:**H4L**:**PB**, respectively) deposited at -1.4 V on a) FTO (**dark blue**) and b) SA@FTO (**olive**). Spectra were obtained in a range of 4000-750 cm^{-1} and blank was measured with a gold coated plate.

XRD characterisation

The SA@FTO electrode was firstly analysed by XRD (**Figure A.41** in Annexes) and the diffractogram only showed the characteristic FTO peaks. The **Fe/L** film (**Figure A.42** in Annexes) deposited with a growth potential of -1.4 V on SA@FTO was also characterised and still no additional peaks were found. XRD helped to conclude that the FTO functionalisation was not useful to induce film crystallinity. This could be explained by the continued presence of the iron pre-layer.

2.2.3 Additional precursor interaction studies

The ratio of 7:2:2 (**M**:**H4L**:**PB**, respectively) was not successful to obtain a crystalline film nor to minimise the iron deposit pre-layer. To optimise the deposition conditions, NMR, FTIR and ultraviolet–visible (UV-vis) spectroscopies were used, and the precursor interactions were studied.

NMR studies (pro-ligand/base)

The MOF film formation is dependent on the pro-ligand deprotonation by the basic species (triethylamine), formed by the **PB** *in-situ* reduction. To prove that this chemical transformation happened, **H4L** was characterised by ^{1}H NMR in $(CD_3)_2SO$, with triethylamine (identified as **B**) mixtures. These differed in ratios ranging from 1:0 to 1:2 (**H4L**:**B**, respectively). The ^{1}H spectrum of **H4L** (**Figure A.43** in Annexes) showed residual water at 3.43 ppm, and a singlet peak at 7.27 attributed to the aromatic protons, in agreement with the literature.[153] It also showed a very broad band at 10.61 ppm, which can be attributed to the carboxylic acid protons. The peak of the phenol group was not observed, and the NMR studies proceeded without focusing

on that signal. When **B** was gradually added (**Figure A.44** in Annexes) the ^{1}H spectra showed the disappearance of the carboxylic acid proton at 10.61 ppm (**Figure A.45** in Annexes) and revealed the appearance of a peak at 8.94 ppm that shifts to 9.17 ppm (**Figure A.46** in Annexes). This indicated a chemical transformation, which could likely be the **H_4L** deprotonation. The ^{1}H spectra also showed the shift of H_1 (**Figure A.47** in Annexes) suggesting a different chemical environment. The addition of **B** also originated two peaks at 3.10 and 1.17 ppm (**Figure A.48** in Annexes), attributed to the aliphatic H_6 and H_7 from triethylamine/triethylammonium species. These correlated in COSY spectrum of the 1:2 mixture (L:B respectively, **Figure A.49** in Annexes).

The TOCSY spectrum of the 1:2 mixture (**H_4L**:**B**, respectively, **Figure A.50** in Annexes) showed the correlation between H_6/H_7 and the peak at 9.17 ppm, which was assigned to the NH of triethylammonium. This study demonstrated that the triethylamine base was able to deprotonate the ligand in a mixture of 1:2 (**H_4L**:**B**, respectively). Since the **PB** is regenerated through the deposition process, the 1:1 ratio was also selected for the next approach.

FTIR and DRIFT studies (ligand/metal ion)

When performing electrochemical studies, it was noticed that the colour of the solution changed whenever **H_4L** was mixed with **M** or vice-versa (**Figure A.51** in Annexes). The colours of the precursor solutions were light yellow in the case of **L** and canary yellow in the case of **M**. When mixing, a dark-green solution was formed, to what was assumed to be the coordination of **L** and **M**. One cause to the impossibility to obtain a crystalline film could be due to the deposition of the coordinated species formed in solution with no structural rearrangement. To conclude if this was occurring, the **M**+**H_4L** mixture was dissolved in DMF and left to evaporate for a couple weeks. The resulting precipitate (further identified as **P**) was washed with dichloromethane and dried in vacuum. It was analysed by FTIR and compared with the FTIR of **H_4L** and DRIFT of the **Fe/L** film (7:2:2 ratio of **M**:**H_4L**:**PB**, respectively) deposited at -1.4 V for 1 hour. Some spectral differences were addressed, starting from the **P** FTIR showing a band at 3437 cm^{-1}, assigned to $\nu_{O\text{-}H}$, that did not coincide with **H_4L** nor **Fe/L**. The **P** spectrum also displayed a band at 2994 cm^{-1} coincident with the film and attributed to $\nu_{C\text{-}H}$. This band was more intense than the other spectra and could be due to a higher C-H content from DMF solvent molecules. To confirm the presence of DMF, additional bands at 2835 and 2785 cm^{-1} are at the typical wavenumbers of the Fermi resonance from the aldehyde function.

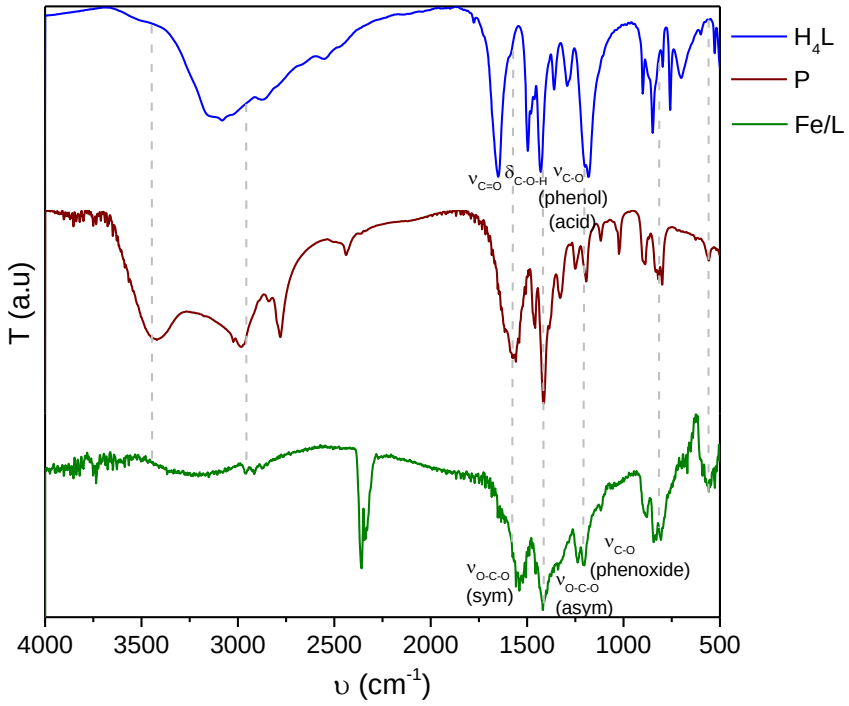

Figure 2.20 - FTIR spectra of **H_4L** (**blue**) and **P** (**brown**) and DRIFT spectrum of the **Fe/L** film (7:2:2 ratio of **M**:**H_4L**:**PB**, respectively) deposited at -1.4 V (**green**).

The FTIR spectrum of **P** also showed a band at 1561 cm^{-1} that did not match with any of the other spectra. It showed an intermediate wavenumber value between the $\nu_{C=O}$ band of **H_4L** at 1654 cm^{-1} and one of the $\nu_{O\text{-}C\text{-}O}$ bands of **Fe/L** at 1537 cm^{-1}. This suggested that **P** may be constituted by a mixture of carboxylic acid and carboxylate species. The bands at around 1220 cm^{-1} were identical to the ones found in the **Fe/L** film, attributed to the $\nu_{C\text{-}O}$ of phenoxide groups. There were two bands remaining that only coincide with the **Fe/L** spectrum, assigned to the $\delta_{C\text{-}H}$ at approximately 822 cm^{-1} and the $\nu_{Fe\text{-}O}$ at 562 cm^{-1}.

The **P** spectrum proved the presence of pre-film complexes, by the shifting of the $\nu_{C=O}$ band from **H_4L** and the presence of the $\nu_{Fe\text{-}O}$ band. Moreover, it does not show any band coincident with the carboxylate band of **Fe/L** film at 1537 cm^{-1}. This means that the coordination environment was different, and so, **Fe/L** and **P** had a different composition.

UV-vis studies (ligand/metal ion)

With the formation of pre-film complexes, the UV-vis spectroscopy could give additional information about the optimum ratio of **M** and **H4L**. The UV-vis spectrum of **M** (**Figure 2.21** and **Table A.10**, in Annexes) showed four peaks at 276, 322, 363 and 521 nm. It was expected that, in solution, $FeCl_3 \cdot 6H_2O$ forms the respective hexaaquairon(III) complex, $[Fe(H_2O)_6]^{3+}$. This complex is a d^5 high-spin compound and no spin transitions to excited states are allowed.[154] Hence, these bands could be attributed to charge transfer (CT) transitions between the Fe^{3+} ion metal and the H_2O ligands. **H4L** was also characterised by UV-vis, showing a band at 370 nm, in agreement with the literature.[155] This could be attributed to n→π* or π→π* transitions. The UV-vis spectrum of the **M**+**H4L** mixture with a ratio of 1:1 showed new bands at 298, 316 nm and 364 that coincide with the **M** and **H4L** bands. A more isolated band was spotted at 580 nm, assigned to the coordination between **M** and **H4L**, and was selected for the concentration studies.

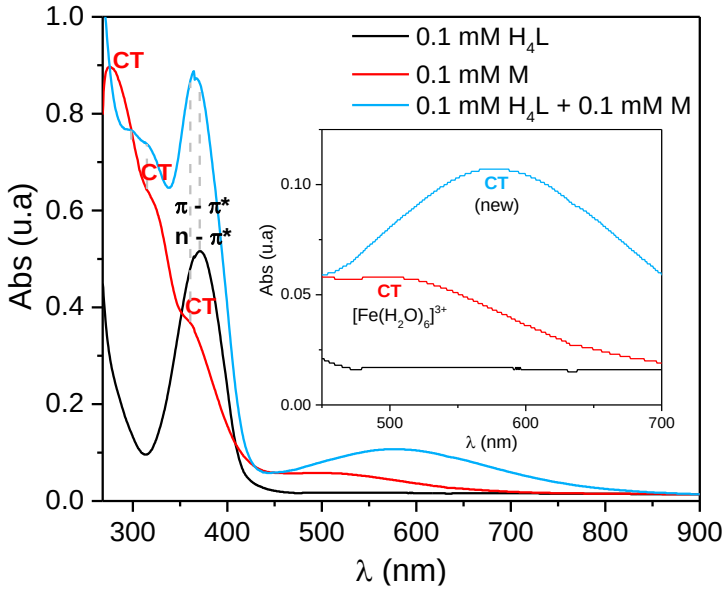

Figure 2.21 - UV-vis spectra of **H4L** (**black**), **M** (**red**) and **H4L**+**M** (**blue**) in DMF. Species quantities: 0.1 mM of **M** and 0.1 mM of **H4L.**

UV-vis spectra were acquired with different **H4L**+**M** concentration ratios (**Figure 2.22**). The **H4L** concentration was kept constant at 0.1 mM and **M** concentrations ranged from 0 mM to 0.275 mM. The extinction coefficients (ε_{max}, $dm^3.mol^{-1}.cm^{-1}$) values at around 580 nm were calculated from the Beer Lambert Law (**Equation 5**), ranging from 438 to 628 $dm^3.mol^{-1}.cm^{-1}$ (**Table A.11** in Annexes).

$$A = \varepsilon_{max} l c \qquad \textbf{(Equation 5)}$$

Where A: Absorbance, l: path length (l cm) and c: concentration of the specie(s) ($dm^3.mol^{-1}$).

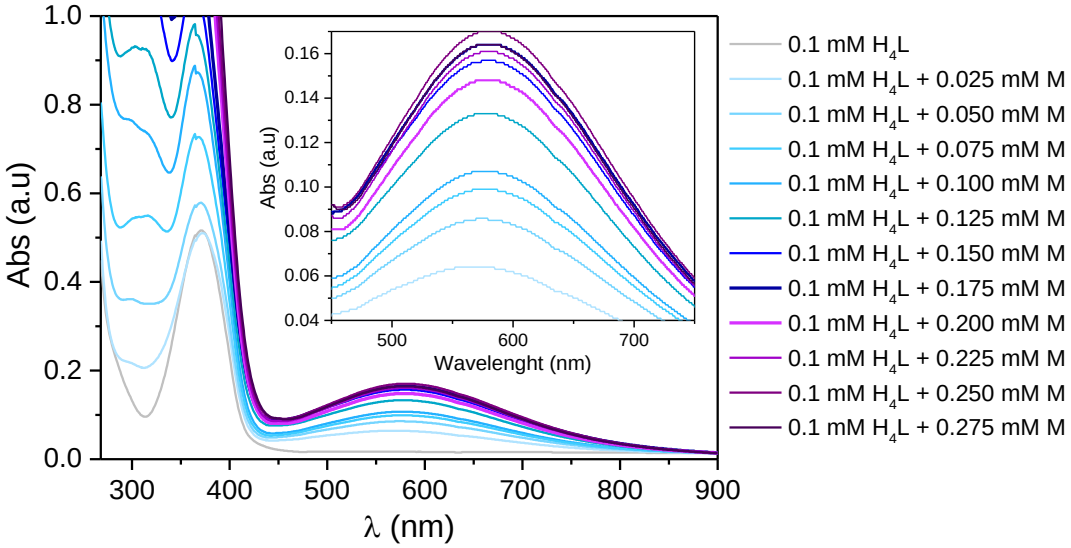

Figure 2.22 - UV-vis spectra of **H_4L:M** mixtures with different ratios in DMF.

The UV-vis spectra showed a higher peak absorbance as the **M** concentration also increased, until it reached a limit at the 1.5:1 ratio (of **M**:**H_4L**, respectively) and stabilised at an absorbance of around 0.16. Since Fe_2L is constituted by a stoichiometric ratio of 2:1 (**M**:**H_4L**, respectively), this precursor quantity could be a better alternative than the 7:2 ratio. UV-vis confirmed this by showing that the 2:1 ratio band at around 580 nm, previously attributed to the charge transfer between **M** and **H_4L**, belongs to the maximum response limit.

2.2.4 Cathodic deposition of Fe/L with a ratio of 2:1:1 (M:H_4L:PB, respectively)

Aiming to promote better film organisation, the iron excess was minimised to the Fe_2L stoichiometric ratio (2:1 of **M**:**H_4L**, respectively) and the ratio of **H_4L** and **PB** was maintained as previously (1:1). This approach uses concentrations of 4 mM of **M**, 2 mM of **H_4L** and 2 mM of **PB**. The CV of 4 mM and 7 mM of **M** were compared (**Figure 2.23a**) and showed unshifted $Fe^{3+/2+}$ redox pair peaks. The redox peaks of 4 mM of **M** display an inferior peak response, which was expected due to the less concentration. The CV of 4 mM of **M** also showed unshifted $Fe^{2+/0}$ redox pair peaks with the same peak response as the 7 mM CV.

The CV of the **M**+**PB** mixture was also run. Comparing it with the **M** CV, (**Figure 2.23b**), it also showed the reduction of the Fe^0 oxidation peak and the current crossing. Similar to the previous approach, it proves that **PB** has the ability to oxidise Fe to Fe^{2+}, thus minimising the Fe deposition. The CV with the **H_4L**+**M**+**PB** mixture (**Figure A.52** in Annexes) displays an identical behaviour to the one performed at a 7:2:2 ratio (**M**:**H_4L**:**PB**, respectively, see **Figure 2.7**).

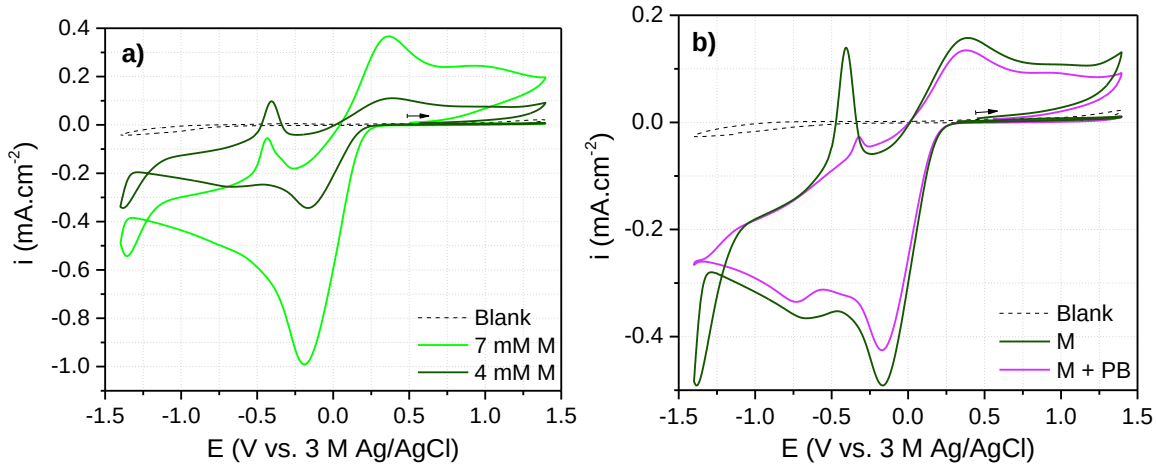

Figure 2.23 - a) Cyclic voltammograms overlay of 7 mM of **M** (light green) and 4 mM of **M** (dark green); b) Cyclic voltammograms overlay of 4 mM of **M** (dark green) and the mixture of 4 mM **M** and 2 mM **PB** (violet). Species were added in 10 mL of N_2 saturated DMF with $TBAPF_6$ as the supporting electrolyte and recorded at 100 $mV.s^{-1}$. The one-compartment electrochemical cell was also constituted by FTO as working, platinum wire as counter and 3 M Ag/AgCl as reference electrodes.

The films were deposited following growth potentials of -1.4 V, -1.3 V and -1.2 V. The potentials of -1.4 and -1.3 V yielded a dark-blue film, and -1.2 V did not yield a visible film. The chronoamperogram obtained at -1.2 V (**Figure A.53** in Annexes) showed an irregular behaviour and a low current produced, which agrees with the impossibility to obtain a visible film. Both -1.3 V and -1.4 V (**Figure 2.24**) showed a current decay with a gradual behaviour, similar to an exponential function. The -1.3 V plot also showed current fluctuations, attributed to the coupled reactions expected to happen in the first moments of the deposition process, already mentioned above.

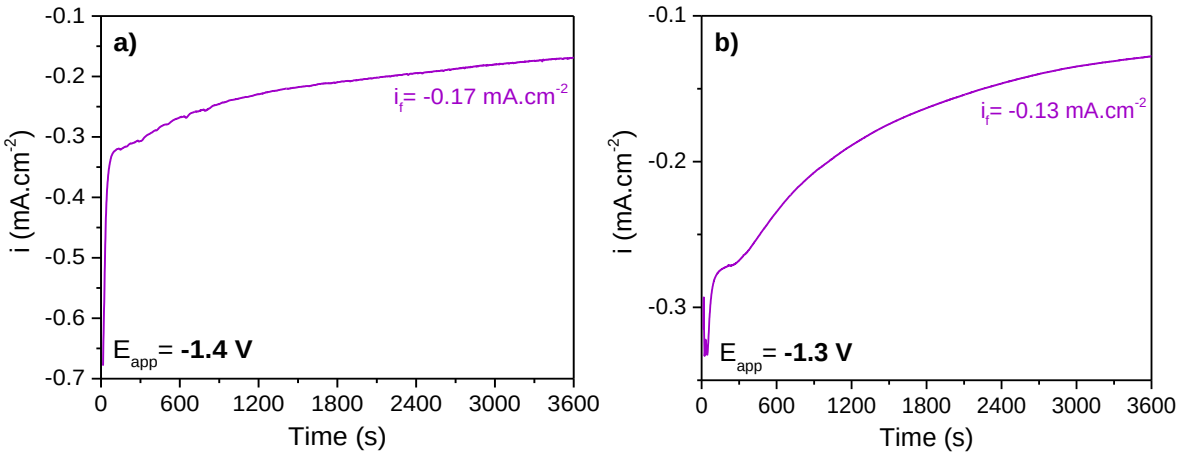

Figure 2.24 - Chronoamperograms following the deposition of the **Fe/L** films with growth potentials of a) -1.4 V and b) -1.3 V. Electrodepositions were performed in 10 mL of N_2 saturated DMF with $TBAPF_6$ as the supporting electrolyte and recorded at 100 $mV.s^{-1}$. The one-compartment electrochemical cell was also constituted by FTO as working, platinum wire as counter and 3 M Ag/AgCl as reference electrodes. Precursors quantities: 4 mM of **M**, 2 mM of **H_4L** and 2 mM of **PB**.

2.2.4.1 Characterisation of the Fe/L films (2:1:1 of M:H_4L:PB, respectively)

DRIFT characterisation

The **Fe/L** films obtained at -1.3 V and -1.4 V were characterised by DRIFT (**Figure A.54** in Annexes). Both spectra are identical to the **Fe/L** film deposited at -1.4 V with a 7:2:2 ratio (**M:H_4L:PB**, respectively). The bands do not present any wavenumber shifts, and so, it can be suggested that the films deposited with a 2:1:1 ratio (**M:H_4L:PB**, respectively) have a similar composition to the ones obtained by a 7:2:2 ratio (**M:H_4L:PB**, respectively).

SEM characterisation

The same films were characterised by SEM (**Figure A.55** and **Figure A.56** in Annexes), obtained with different magnifications. The films morphology was identical to the 7:2:2 (**M:H_4L:PB**, respectively) approach, observing stacked aggregates with similar sizes. In this case, both film images show the presence of slits underneath what was assumed to be the **Fe/L** film (**Figure 2.25**). This has already been suggested to be an iron pre-layer. Hence, it was possible to admit that the 2:1:1 (of **M:H_4L:PB**, respectively) approach may not be useful to minimise this pre-layer.

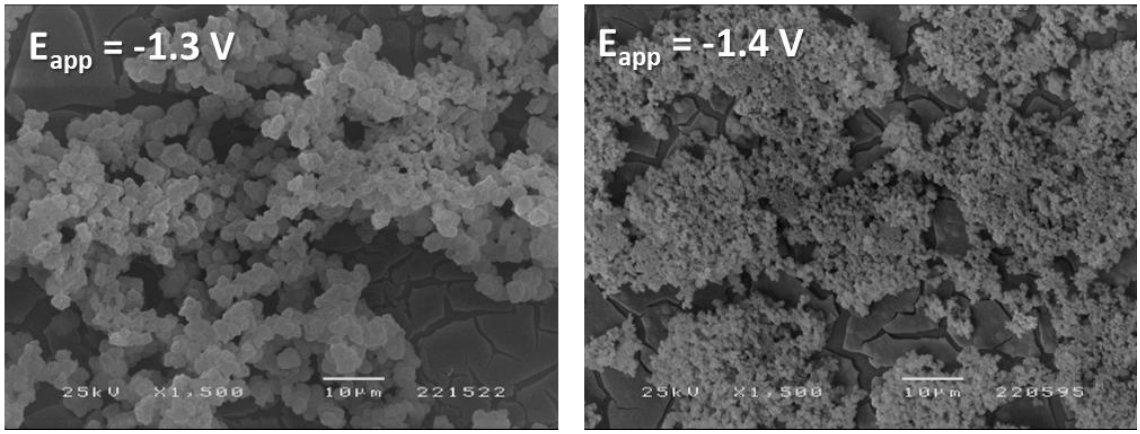

Figure 2.25 - SEM images (x1500) of the **Fe/L** films (2:1:1 ratio of **M:H_4L:PB**, respectively) deposited at -1.3 V (left) and -1.4 V (right) for 1 hour.

PIXE characterisation

Particle-induced X-ray emission (PIXE) and Rutherford backscatter spectrometry (RBS) were used to characterise the composition of the **Fe/L** film deposited with a growth potential of -1.3 V. The content of the Fe, Cl and Sn atoms was obtained by the 2D compositional maps from PIXE spectrum (**Figure 2.26**). The presence of Cl was observed and follows the presence of Fe. Cl species are likely present as counter ions of Fe^{3+}. This suggests that the films are constituted by a mixed valence of $Fe^{3+/2+}$. For further analysis, the Fe and Cl content was associated with the presence of the **Fe/L** film and Sn is a constituent FTO electrode. These maps show that the Fe and Cl atoms partially covered the FTO surface, with the presence of both warm- and cold-

toned zones. For clarity, different film zones were selected, identified as 1 and 2. Zone 1 was constituted by a high content of film on the top in contrast with Sn that was almost undetectable. On the other hand, 2 was constituted by a film hole, followed by minimal Fe and Cl and with a high presence of Sn. This means that the films are heterogeneous and have high concentration zones.

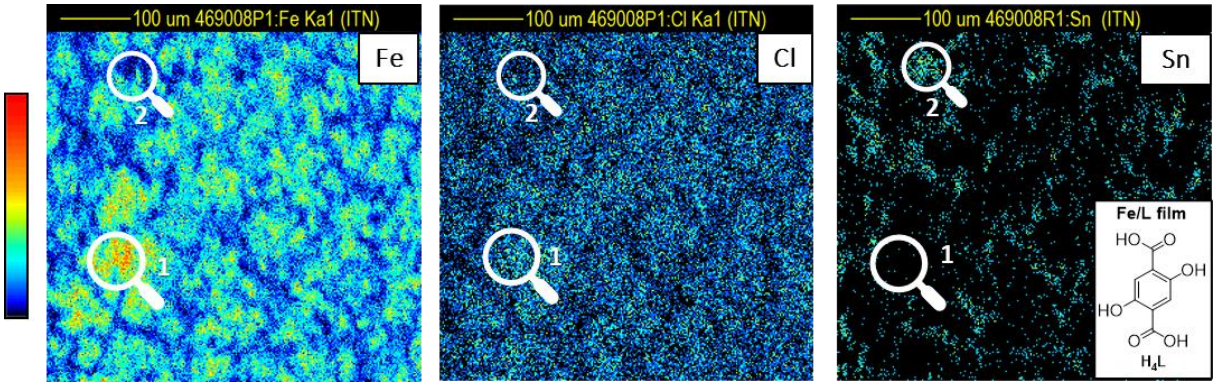

Figure 2.26 - Fe, Cl and Sn atom mapping of the **Fe/L** film (2:1:1 ratio of **M:H4L:PB**, respectively) deposited at -1.3 V, obtained by PIXE (beam size of 530×530 μm^2).

Four film zones were selected, identified as 003 to 006 (**Figure 2.27**) and the RBS spectra were obtained. The spectra are not equivalent, revealing different peak intensities. This was expected since the film was not homogeneous. Since elements emit characteristic X-rays, it was possible to attribute each peak to the matching atom. The presence of C, O and Fe atoms was detected in the film, with minimal Sn. This agrees with the presence of the expected **Fe/L** film.

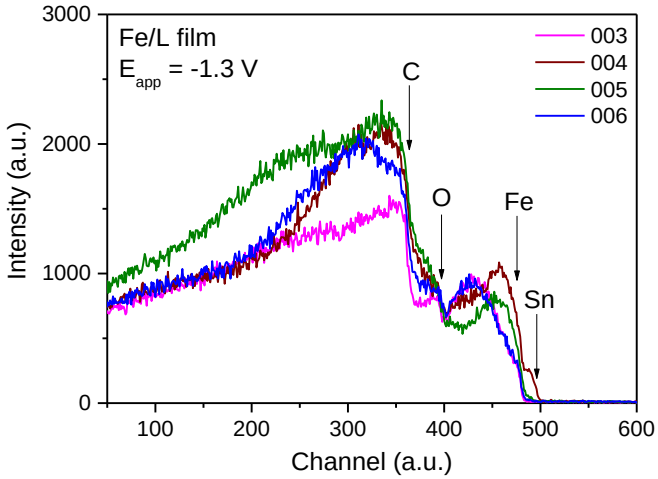

Figure 2.27 - RBS spectra (beam dimension: 3x4 μm^2) obtained by different zones of the **Fe/L** film (2:1:1 ratio of **M:H4L:PB**, respectively) deposited at -1.3 V, identified as 003 to 006.

The Fe/O and Fe/C atomic ratios were calculated from the RBS spectra in the zones 003, 005 and 006 (**Table 2.1**). The experimental vales were compared with the expected for Fe2L. The approximate thickness of the film zones was also obtained, based on the atom number per cm^2. Zone 005 was almost 3 times thicker than zone 003, proving the roughness and heterogeneity of the film. Focusing on the Fe/O and Fe/C ratios, all film zones displayed a higher Fe

content than expected. Moreover, Fe/C ratio was much higher than Fe/O, meaning that both Fe and O atoms are found with higher quantities than the C atoms. This agrees with the possibility of a pre-layer constituted by iron oxide/hydroxide. Zone 005 has the higher ratio disparity to the expected values. Although it was a thicker film zone, the Fe/O and Fe/C ratios were expected to have remained constant, if the composition was only based on the **Fe/L** film. It did not happen, which suggests that zone 005 has a higher content of iron oxide/hydroxide.

Table 2.1 - Fe/O and Fe/C film atomic ratios obtained from the RBS spectra.

Atomic ratio	Expected for Fe_2L	003	005	006
Fe/O	0.33	0.75	0.83	0.66
Fe/C	0.25	0.45	1.92	1.33
Thickness (nm)	-	>4182	>11208	>11146

XPS characterisation

The surfaces of the **Fe/L** films deposited with a growth potential of -1.4 and -1.3 V were analysed by XPS. The survey spectra were focused on the C 1s, O 1s and Fe 2p peak deconvolution (**Table A.12** in Annexes). The attributions were based on the same references as the XPS characterisations from the previous film approach.

The C 1s peak (**Figure 2.28**) of the **Fe/L** film deposited at -1.4 V showed a peak at around 282.5 eV that was attributed to the C from the sample holder. Moreover, both XPS spectra showed a peak at 285 eV assigned to C-C and C-H bonds from surface C atoms. Both films display two additional peaks deconvoluted at 286.5/286.9 and 288.7/288.8 eV, attributed C-O bonds from the phenoxide function, and C-O bonds from the carboxylate function, respectively.[148]

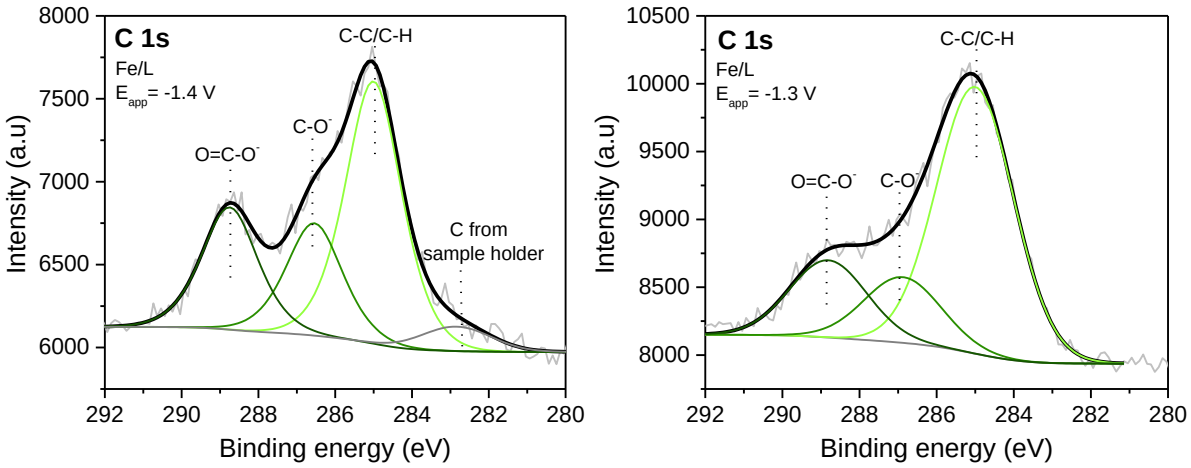

Figure 2.28 - XPS spectra of the **Fe/L** films (2:1:1 ratio of **M:H_4L:PB**, respectively) deposited at -1.4 and -1.3 V, amplified in the C 1s peak.

The Fe $2p_{1/2}$ and $2p_{3/2}$ peaks were also identified in the Fe 2p zone (**Figure 2.29**). The $Fe2p_{3/2}$ peak was deconvoluted and, similarly to the 7:2:2 (**M:H_4L:PB**, respectively) approach, these

films are also constituted by different $Fe^{3+/2+}$ species. Although it seemed that the -1.3 V film presented a higher diversity of the Fe species, the lowest energy peaks are attributed to satellites, which were not possible to recognise at the -1.4 V film spectrum.

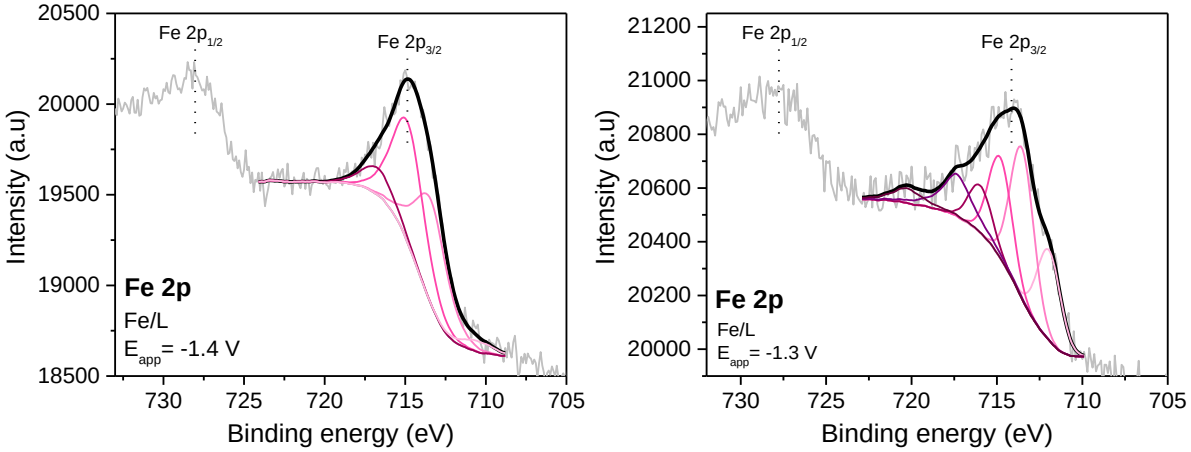

Figure 2.29 - XPS spectra of the **Fe/L** films (2:1:1 ratio of **M:H4L:PB**, respectively) deposited at -1.4 and -1.3 V, amplified in the Fe 2p peak.

The O 1s peak (**Figure 2.30**) was deconvoluted into two identical peaks at 532.4/532.2 and 531.8/531.6 eV, attributed to the phenoxide and carboxylate functions. The XPS spectrum of **Fe/L** deposited with a growth potential of -1.4 V showed an additional peak at 530.3 eV, assigned to the O found from iron oxides.

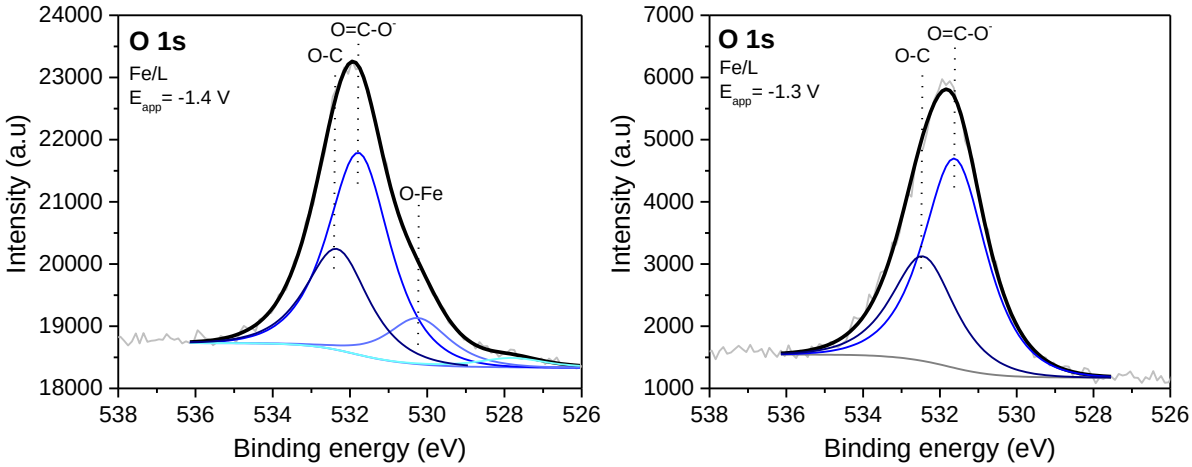

Figure 2.30 - XPS spectra of the **Fe/L** films (2:1:1 ratio of **M:H4L:PB**, respectively) deposited at -1.4 and -1.3 V, amplified in the O 1s peak.

The atomic concentration (%) of the Fe, C and O atoms was obtained (**Table A.13** in Annexes). Once again, the experimental values were compared with Fe_2L. Both films presented close values of C and O, except for Fe, attributed to the interference from the surface C atoms. The **Fe/L** film deposited at -1.4 V showed a higher content of Fe and O, but fewer C than the -1.3 V film. This could be associated with a higher heterogeneity of the -1.4 V film that could

uncover more zones of the pre-layer and be detected by XPS. This agrees with the O 1s peak at around 530.2 eV from the same film.

Elemental analysis characterisation

The **Fe/L** film deposited with a growth potential of -1.3 V for 1 hour was characterised by elemental analysis (EA). For this, several films were deposited at -1.3 V and scrapped, until a **Fe/L** powder of approximately 2 mg was reached. It was obtained an experimental composition of % 14.98 (C), 0.84 (N), 1.79 (H) that did not match to the theorical values of Fe_2DODBC, respectively % 31.42 (C), 0.66 (H) and 0 (N). Hence it was necessary to adjust film compositions to find the closest values to the experimental.

First, theorical compositions of the sample were obtained considering the **Fe/L** film constituted by DMF, Et_3N or H_2O coordinated to the metal ion to complete an octahedral geometry (**Table A.14** in Annexes). Yet, the theorical compositions were still very far from the experimental.

The film has a minimal constitution of N atoms (0.84%). So, nitrogen-containing molecules (DMF or Et_3N) would still be present in the film, but not coordinated to all metal sites. OH^- and Cl^- species could also be present as counter-ions, considering a $Fe^{3+/2+}$ mixed valence film. It should also be considered the presence of water and an iron oxide/hydroxide mixture. Taking all this factors into account, compositions including a mixture of H_2O, DMF Et_3N, OH^-, Cl^- and iron oxide/hydroxide leaded to values closer to the experimental (**Table A.15** in Annexes). This characterisation suggested that the film was not constituted by an isolated coordination polymer, but a mixture of different species completing the octahedral geometry, counter ions, and an additional layer composed by iron oxide/hydroxide.

BET characterisation

A BET surface area of approximately 1161 $m^2.g^{-1}$ was obtained from the **Fe/L** film deposited with a growth potential of -1.3 V for 1 hour. The experimental value was lower than the reported BET surface area of Fe_2L (1360 $m^2.g^{-1}$).[98] This means that the material was less porous than expected and could be explained by a possible unorganised structural arrangement caused by the presence of a $Fe^{3+/2+}$ mixed valence film or an iron oxide/hydroxide pre-layer. Moreover, the presence of Fe^{3+} implies the presence of counter ions balancing the charge, that would reduce the free pore volume and area.

XRD characterisation

The diffractogram of the **Fe/L** film deposited with a growth potential of -1.3 V for 1 hour did not show additional peaks than the ones already attributed to the FTO working electrode (**Figure A.57** in Annexes). This concluded that this new approach was not useful to induce an organised film growth.

For further reference, the depositions of the **Fe/L** films with a ratio of 2:1:1 (**M:H$_4$L:PB**, respectively) deposited with a growth potential of -1.3 V for 1 hour are identified as the optimised/original conditions.

2.2.5 Other approaches to induce crystallinity

Post-synthetic heating under ambient atmosphere

To try to induce crystallinity, the films were deposited following the optimised conditions on both FTO and SA@FTO, for comparison. The films were then exposed to a post-synthetic heating procedure adapted from the literature[74,156] The instrumentation consisted of a furnace at atmospheric pressure (**Figure 2.31**). The films were heated with a ramp rate of 4 ºC/min until reaching 100 ºC. The temperature was kept for 12 hours after which was further increased to 200 ºC at the same rate and maintained at this temperature for 2 hours. The films were naturally cooled to room temperature.

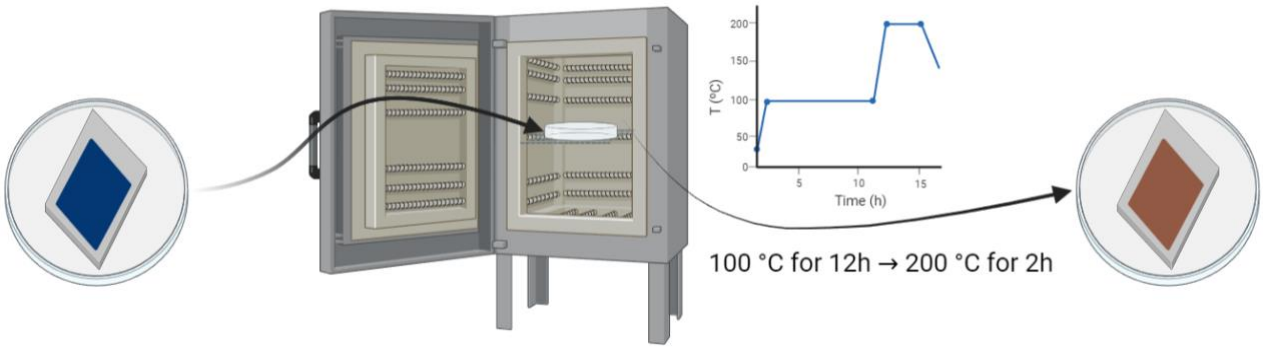

Figure 2.31 - Schematic representation of the post-synthetic heating approach.

The temperature-treated films showed a colour change from dark blue to brownish orange and were visibly more heterogeneous. They were characterised by DRIFT obtaining a distinct spectrum from the original films (**Figure 2.32**). It did not show $\nu_{C\text{-}H}$ bands, that were expected to appear in the range of 2900-3000 cm^{-1}. The bands presented a very broad shape, and it was not possible to make any attributions. This characterisation suggested that the structure has been degraded.

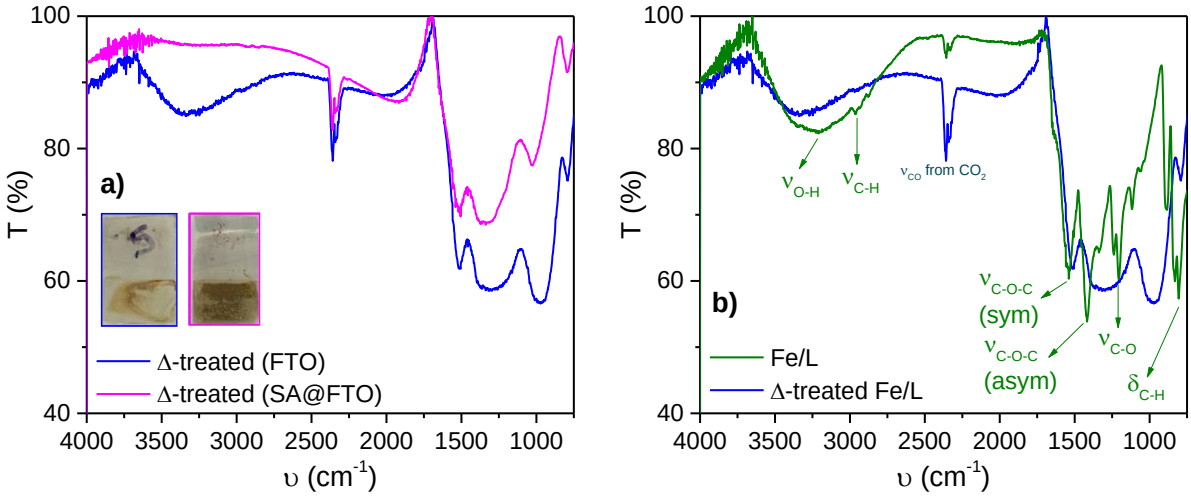

Figure 2.32 - DRIFT spectra of a) temperature-treated films on FTO (**blue**) and SA@FTO (**pink**); b) original **Fe/L** film (**green**) and heated temperature-treated film (**blue**) on FTO. Spectra were recorded in a range of 4000-750 cm^{-1} and the blank was measured with a gold coated plate.

The temperature-treated films were also characterised by SEM (**Figure A.58** and **Figure A.59** in Annexes). It was noted that the temperature induced an increased pre-layer cracking and shrinking into more localised zones (**Figure 2.33**). Yet, the morphology of the temperature treated **Fe/L** films remained like the non-thermal treated films.

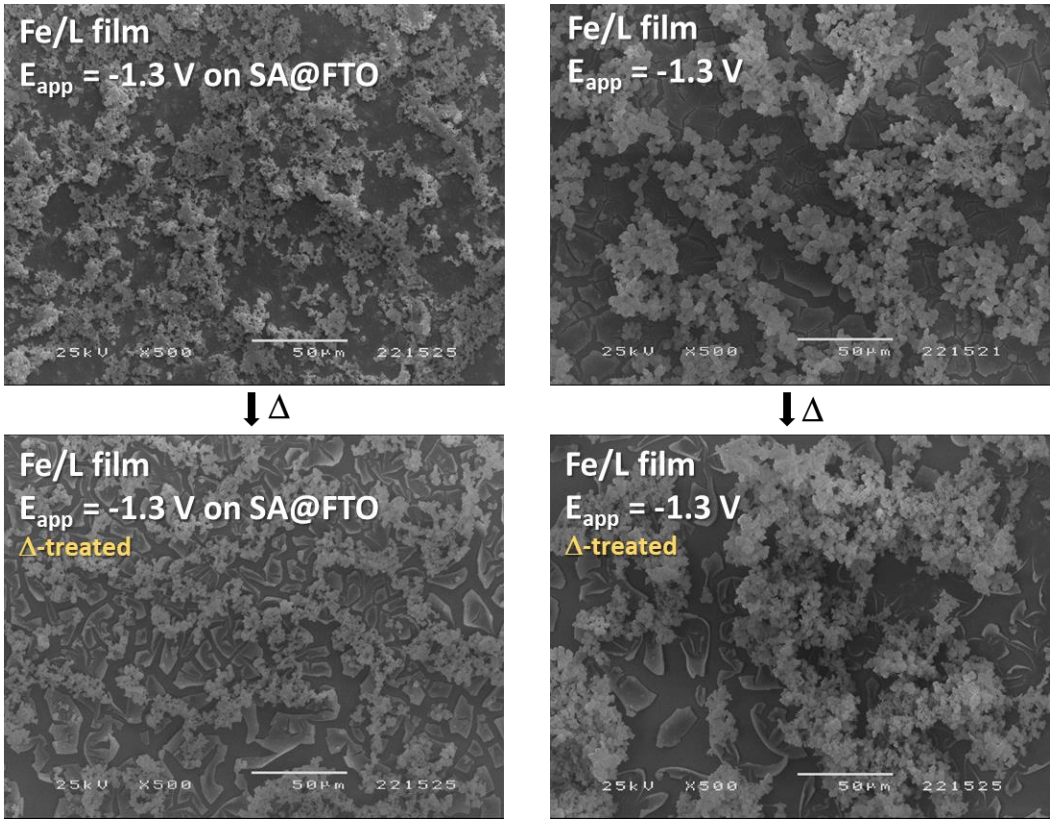

Figure 2.33 - SEM images of the **Fe/L** films (2:1:1 ratio of **M:H4L:PB**, respectively) deposited at -1.3 V before and after the temperature treatment. The temperature-treated films are identified as "w/T".

Since this information was not in agreement with DRIFT, the temperature treated **Fe/L** film previously deposited on SA@FTO was selected to be characterised by PIXE and RBS. The 2D PIXE maps of the Fe, Cl and Sn atoms (**Figure 2.34**) show the presence of a more heterogeneous film, with a more localized concentration of iron and chlorine.

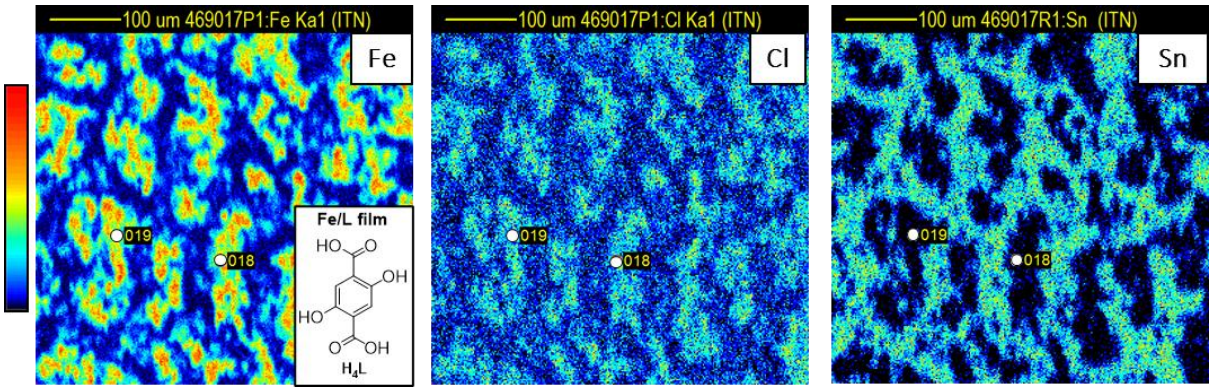

Figure 2.34 - Fe, Cl and Sn atom mapping of temperature-treated **Fe/L** film (2:1:1 ratio of **M:H_4L:PB**, respectively) deposited at -1.3 V on SA@FTO, obtained by PIXE (beam size of 530×530 μm^2).

Two highly concentrated Fe zones were selected to obtain the RBS spectra, identified as 018 and 019 (**Figure A.60** in Annexes). From the peaks, it was also possible to obtain the Fe/O and Fe/C atomic ratios (**Table 2.2**). Although there are no significant changes in Fe/O or the overall thickness, the Fe/C ratio has abruptly increased to abnormal values with differences of 8.55 and 2.78 for zones 019 and 018, respectively. This could only mean that the temperature treatment degraded most of the organic component, and it was mainly left with an iron deposit. This carbonisation process has already been described in the literature for Co-, Zn- and Ni-MOF-74 with higher temperatures (more than 300 ºC).[157,158]

Table 2.2 - Fe/O and Fe/C film atomic ratios obtained from the RBS spectra.

Atomic ratio	Theoretical	Zone 019	Zone 018
Fe/O	0.33	0.78	0.55
Fe/C	0.25	8.80	3.03
Thickness (nm)	-	>10900	>11884

The temperature-treated **Fe/L** film in FTO was characterised by XRD (**Figure A.61** in Annexes). The diffractogram still did not show any additional peaks rather than the ones attributed to the FTO electrode. Hence, this technique was unsuccessful to obtain a crystalline film.

<u>Film activation</u>

The **Fe/L** film previously deposited by optimised conditions was activated adapting a procedure from the literature[159] It was exposed to DMF solvent changes followed by CH_2Cl_2. Then, it was placed in a furnace under vacuum and heated at 150 ºC overnight. The goal was to

remove DMF and other impurities and obtain open $Fe^{3+/2+}$ sites, that could result in a better film organisation. The post-activated film was characterised by DRIFT (**Figure A.62** in Annexes). The spectrum was identical to the original film, except for a shift of the ν_{OH} band at 3040 cm^{-1} that covered the expected ν_{CH} band. This shift could be attributed to a higher content of water.

The post-activated film was also characterised by XRD (**Figure A.63** in Annexes), still not showing any additional peaks. So, this approach was not viable to obtain a crystalline film.

Less deposition time (growth study)

The morphology of the **Fe/L** films was studied over different deposition times to conclude about the film organisation along the different deposition stages. These were deposited with a growth potential of -1.3 V with durations ranging from 8 seconds to 45 minutes (**Figure A.64** in Annexes). The films obtained between 8 and 190 seconds were not visible. From 15 minutes ahead, a dark-blue film was obtained.

The 15-minute film was characterised by DRIFT (**Figure A.65** in Annexes). Comparing it with the original 1-hour film, it was possible to conclude that the spectra coincide, and the bands have not shifted.

The FTO electrode, as well as the films deposited for 8 and 20 seconds and 15, 20 and 30 minutes were characterised by AFM, obtaining both 2D and 3D images (**Figure A.66** to **Figure A.71** in Annexes). Although AFM did not characterise the films crystallinity, it revealed morphological information, as well as approximate values of film depth. The AFM images of FTO showed a rough material, with a morphology characteristic of metal oxides. The images of the 8- and 20-second films show a very ordered morphology, with a dune-like consistency at 8 seconds, that formed terraces at 20 seconds (**Figure 2.35**). The morphologies of the 15-, 20- and 30-minute films agree with the SEM images of the 1-hour films. Herein, it was also noted that the films were constituted by disc-shaped aggregates stacked on top of each other. Moreover, the AFM image of the 30-minute film presents a different layer depositing on top of the stacked aggregates, which could be due to an unorganised growth. This new layer could be further analysed by the 45-minute or 1-hour films, however, they were too thick to be characterised by AFM.

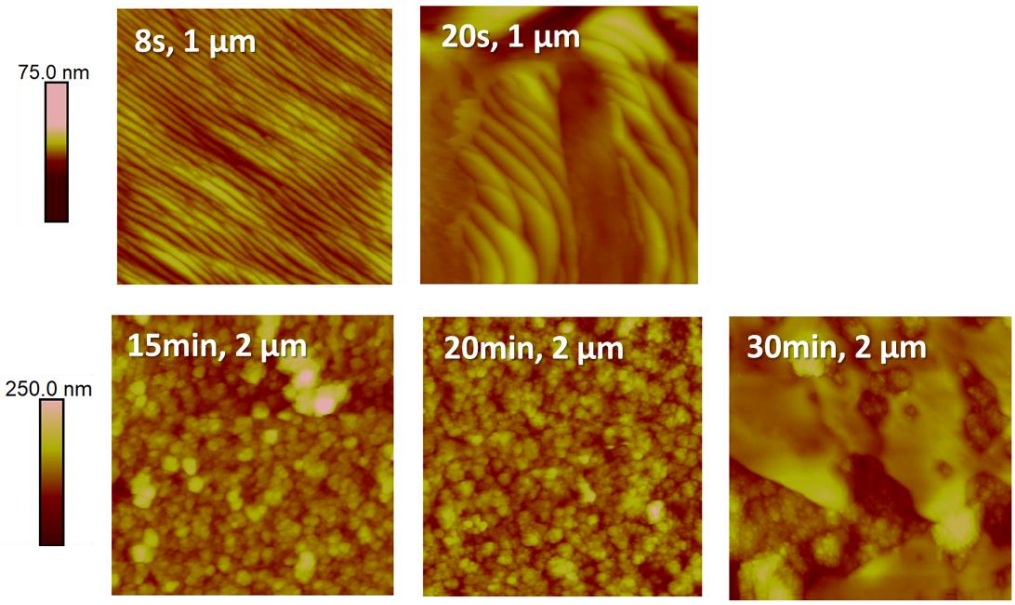

Figure 2.35 - 2D AFM images of deposited **Fe/L** films (2:1:1 ratio of **M:H4L:PB**, respectively) deposited for 8 and 20 seconds (1 x 1 µm) and 15, 20 and 30 minutes (2 x 2 µm).

The approximate thickness of the 8- and 20-second films was obtained by the 2D maps, reaching values of at least 15 nm and 185 nm, respectively (**Figure 2.36**). These shorter deposition approaches could be advantageous if the films were proven to be crystalline by XRD. On the other hand, this fast rate could be associated with a random growth and be one of the causes of obtaining an amorphous **Fe/L** film.

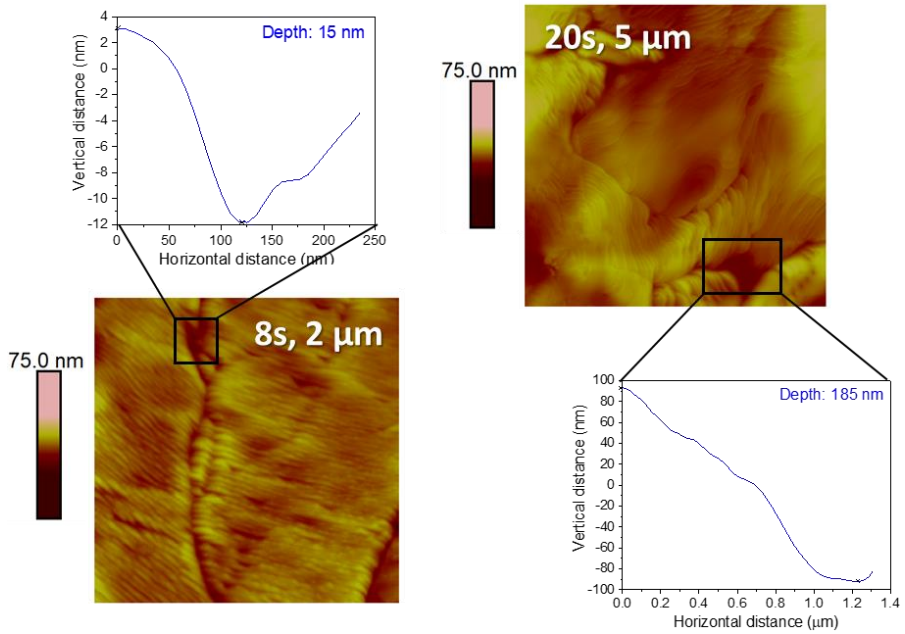

Figure 2.36 - 2D AFM image of the **Fe/L** film (2:1:1 ratio of **M:H4L:PB**, respectively) deposited for 8 (2 µm x 2 µm) and 20 seconds (5 µm x 5 µm) with identified zones showing films depths of 15 nm and 185 nm, respectively.

For comparison, the **M+PB** film was also analysed by AFM (**Figure A.72** in Annexes). The images showed a typical metal oxide morphology, similar to FTO, as already expected. This agrees with the presence of an iron oxide/hydroxide film.

Longer deposition time (1h vs. 24h)

Other cause to the lack of crystallinity could be a fast nucleation rate. Hence, by applying a less negative potential, the film could deposit by a slower rate and obtain a more organised growth. Moreover, Fe-MOF-74 is conventionally prepared by reactions that take between 18 to 24 hours.[98,100] Hence, a longer deposition time with a less negative potential growth could result in a higher crystallinity. Thus, a **Fe/L** film was deposited with a growth potential of -1.0 V for 24 hours. This approach yielded a dark-blue film, visibly thinner than the original **Fe/L** film. The chronoamperogram (**Figure A.73** in Annexes) showed an irregular behaviour through the hole deposit time, which could be caused by a slower deposition rate. It was also displayed abrupt current fluctuations from 4 hours of deposition, which could be attributed to film detaching, and was further proven by the presence of precipitate in the bulk solution. Focusing in the first hour of deposition, it was possible to note an exponential decay, in agreement with the chronoamperogram behaviour of the original **Fe/L** film.
The 24-hour film was characterised by DRIFT (**Figure A.74** in Annexes). Comparing it with the original **Fe/L** film, it showed identical spectra, with coincident and unshifted bands.
The film was also characterised by XRD (**Figure A.75** in Annexes), and the diffractogram still did not show extra peaks, concluding that this approach was still not useful to obtain a crystalline film.

Synthesis with temperature (90 ºC)

Solvothermal/hydrothermal conventional techniques rely on high temperatures (80 to 220 ºC)[59]. Hence, producing the films under a higher temperature could induce crystallinity. Moreover, since the high temperatures would conduct in a faster deposition rate, it was selected a less negative growth potential. The one-compartment electrochemical cell was placed in an oil bath at 90 ºC and **Fe/L** films were deposited with a growth potential of -1.2 V for two depositions times: 1 hour and 15 minutes. A light-blue film was obtained after 15 minutes, and a dark-blue film after 1 hour. The 1-hour film was visibly thicker than the 15-minute. Similar to the 24-hour approach, the chronoamperograms (**Figure A.76** in Annexes) do not show gradual decay along the deposition time. This behaviour could also be due to the influence of a slower diffusion or/and film detaching.
Only the 1-hour film was characterised by DRIFT (**Figure A.77** in Annexes). It coincides with the original **Fe/L** film spectrum, with unshifted bands, except for the impossibility to find the

$\nu_{C\text{-}H}$ bands. The spectrum of the 1-hour film showed a more intense $\nu_{O\text{-}H}$ band that could be masking the $\nu_{C\text{-}H}$.
The 1-hour film was also characterised by XRD (**Figure A.78** in Annexes), showing a diffractogram only containing the characteristic FTO peaks. Hence, it was still not possible to obtain a crystalline film.

Higher quantity of pro-base (4 mM vs. 2 mM)

To optimise the conditions, it was attempted a higher quantity of **PB**, from 2 mM to 4 mM. **Fe/L** films were deposited with growth potentials of -1.3 V for two selected deposition times: 1 hour and 15 minutes. This depositions contained a precursor ratio of 2:1:2 instead of the original 2:1:1 (**M:H$_4$L:PB**, respectively). The 15-minute film was almost not visible, and the 1-hour film yielded a dark-blue film with a worse aspect than the original **Fe/L** film. It presented undeposited zones that could be associated with a higher film detaching. The chronoamperograms of the 1-hour and 15-minute films (**Figure A.79** in Annexes) diverged from the expected exponential behaviours, which could be associated with a higher content of parallel reactions between the base and the other present species.
The 1-hour film was characterised by DRIFT and overlayed with the original **Fe/L** film (**Figure A.80** in Annexes). Once again, the spectra coincide, apart from a slight shift of the ν_{OH} band which could indicate a higher content of water.
The 1-hour film was characterised by XRD (**Figure A.81** in Annexes), and still no additional peaks to the ones attributed to the FTO electrode were observed.

Deposition with an applied magnetic field

The **Fe/L** film was deposited with an external magnetic field (B) parallel to the FTO working electrode. This approach was motivated by the possibility of B inducing an organised film growth, as already reported by other works.[160,161] A Teflon-electrochemical cell was assembled and displayed in the centre of a magnet (**Figure A.82** in Annexes) and the three electrodes were connected to a portable potentiostat. The film was deposited with a growth potential of -1.3 V and a magnetization of 1 T for 1 hour.
This film was analysed by DRIFT (**Figure A.83** in Annexes) and, by comparing it with the original **Fe/L** film, it also displayed the same spectrum, with the exact same bands, differing from a slight shift of the $\nu_{O\text{-}H}$ band.
It was also characterised by XRD (**Figure A.84** in Annexes) and the diffractogram showed a different behaviour from the diffractograms presented throughout this thesis. This difference was attributed to the modification of the FTO structure organisation induced by magnetization.

2.3 Fe/L1, Fe/L2 and Fe/L3 films: production and characterisation

Aiming to improve the supramolecular interactions between the host (film) and the guest (uric acid), **Fe/L** analogues were produced, identified ad **Fe/L1**, **Fe/L2** and **Fe/L3**.

Similar to the **Fe/L** approaches, the redox behaviour of the precursors was also studied. The CVs of the **H_4L1**, **H_4L2** and **H_4L3** pro-ligands (**Figure A.85** in Annexes) show similar electrochemical responses to **H_4L**. Overall, they all are weak electroactive species. The CVs of the **PB** mixtures with **H_4L1**, **H_4L2** and **H_4L3** were expected to show an enhanced reduction peak coincident to the isolated **PB** reduction peak at around -0.58 V, that was previously attributed to the pro-ligand deprotonation. Moreover, the presence of two reduction peaks was also expected if the deprotonation was also controlled by a two-step process. Yet, CVs only display a reduction peak at around -0.87 V (**Figure A.86** in Annexes). This does not discard the pro-ligands deprotonation but indicates a different protonation process than **H_4L**.

The mixtures of **M** with **H_4L1**, **H_4L2** and **H_4L3** (**Figure A.87** in Annexes) show a current crossing at around -1.25 V, and the $Fe^{2+/0}$ redox peaks, at around -0.88 V and -0.39 V, in agreement with the **M+H_4L** CV.

The addition of **PB** to the previous mixture (**Figure A.88** in Annexes) minimises the current crossing at around -1.25 V assigned to the Fe deposition and the Fe^{2+} oxidation peak at around -0.39 V.

The optimised deposition of the **Fe/L** film was set with a precursor ratio of 2:1:1 (**M:H_4L:PB**) and a growth potential of -1.3 V for 1 hour. The solutions containing **H_4L1**, **H_4L2** or **H_4L3** as pro-ligand precursors were deposited following those same conditions. All depositions yielded marron films, differing from the dark blue **Fe/L** films. The chronoamperograms (**Figure 2.37**) display gradual current decays, resembling exponential functions. All depositions show minimal current fluctuations in the first seconds of electrodeposition. **Fe/L3** showed the highest current variation of around 0.1 mA.

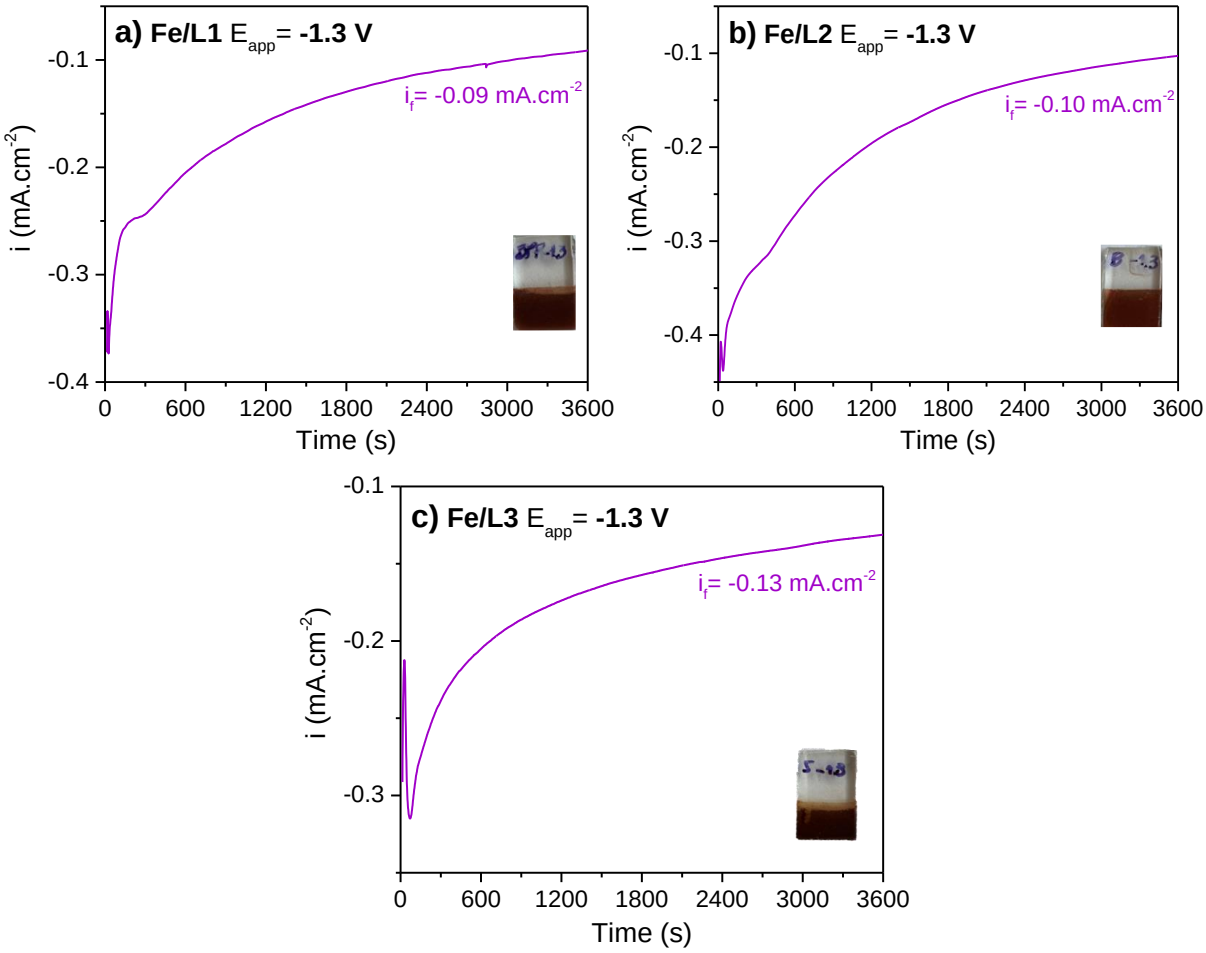

Figure 2.37 - Chronoamperograms following the deposition of a) **Fe/L1**, b) **Fe/L2** and c) **Fe/L3** films at -1.3 V. Electrodepositions were performed in 10 mL of N_2 saturated DMF and $TBAPF_6$ as the supporting electrolyte. The one-compartment electrochemical cell was also constituted by FTO as working, platinum wire as counter and 3 M Ag/AgCl as reference electrodes. Precursor quantities: 4 mM of **M**, 2 mM of **H_4L1**, **H_4l2** or **H_4L3** and 2 mM of **PB**.

To test if less potential could be used for the deposition, films were also produced with a growth potential of -1.2 V. The depositions also yielded marron films. This time, the chrono-amperograms (**Figure 2.38**) showed a less gradual current decay, with more fluctuations. This can be associated with a slower rate of deposition.

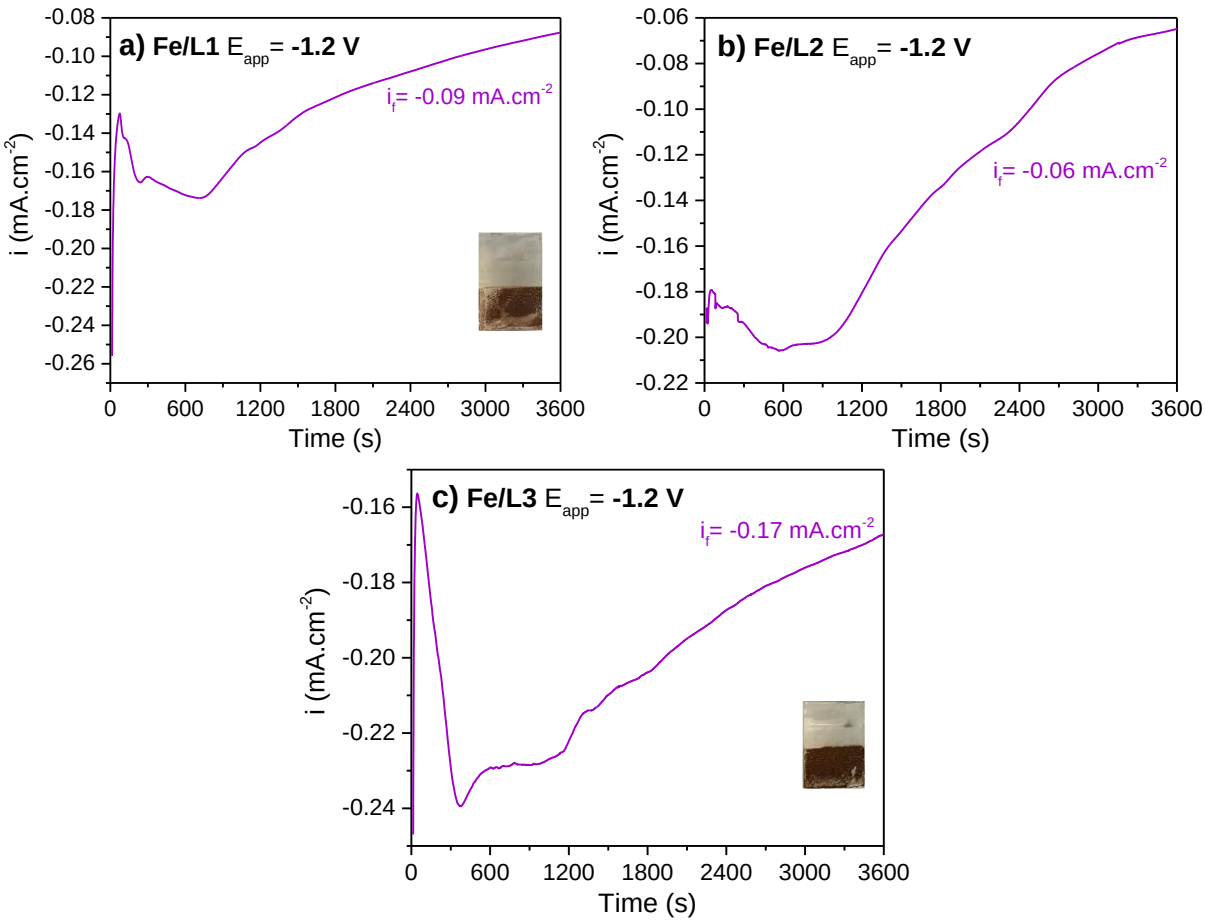

Figure 2.38 - Chronoamperograms following the deposition of a) **Fe/L1**, b) **Fe/L2** and c) **Fe/L3** films at -1.2 V. Electrodepositions were performed in 10 mL of N_2 saturated DMF and $TBAPF_6$ as the supporting electrolyte. The one-compartment electrochemical cell was also constituted by FTO as working, platinum wire as counter and 3 M Ag/AgCl as reference electrodes. Precursor quantities: 4 mM of **M**, 2 mM of **H_4L1**, **H_4L2** or **H_4L3** and 2 mM of **PB**.

DRIFT characterisation

The **Fe/L1**, **Fe/L2** and **Fe/L3** films deposited at -1.3 V were characterised by DRIFT (**Figure 2.39** in main text and **Figure A.89** and **Figure A.90** in Annexes, respectively). All films were compared with the matching pro-ligands and showed band shifts, which agrees with the pro-ligand deprotonation and respective coordination to the metal ion. For example, **Fe/L1** still showed the $\nu_{C\text{-}H}$ and $\delta_{C\text{-}H}$ bands from **H_4L1**. Yet, the $\nu_{O\text{-}H}$ bands of **H_4L1** are altered to a single band at around 3400 cm^{-1}, which could be attributed mainly to the presence of water.

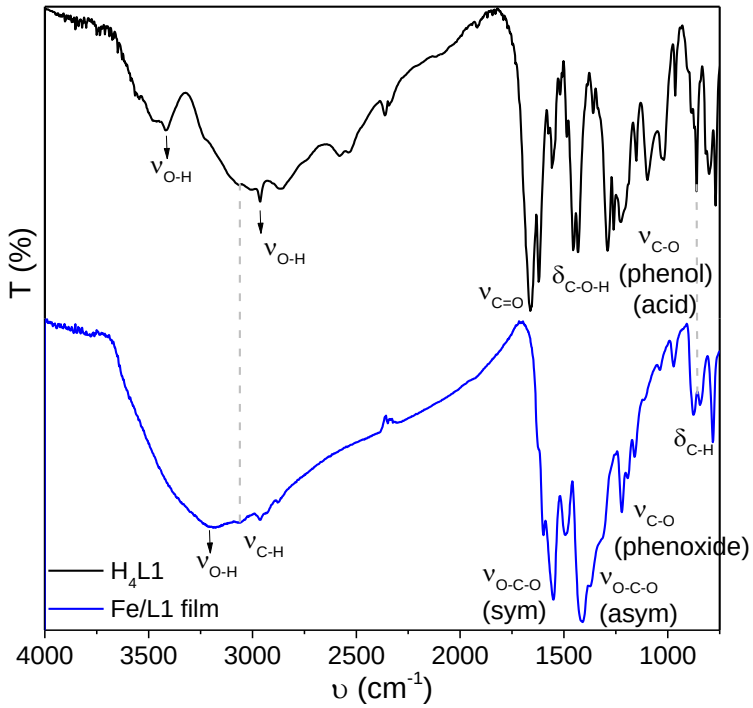

Figure 2.39 - FTIR spectrum of **H_4L1** (**black**) and DRIFT spectrum of the **Fe/L1** film (**blue**) deposited at -1.3 V. Spectra were recorded in a range of 4000-500 cm^{-1}.

Similar to **Fe/L**, the $\nu_{C=O}$ band from the pro-ligands was not observed in the **Fe/L1**, **Fe/L2** or **Fe/L3** films. Moreover, the presence of two new bands (**Table 2.3**) at around 1500 cm^{-1} and 1400 cm^{-1} confirmed the presence of carboxylate functions by deprotonation of the pro-ligands.

Table 2.3 - Symmetric and asymmetric ν_{O-C-O} bands from **Fe/L1**, **Fe/L2** and **Fe/L3**.

Band (cm^{-1})	**Fe/L1**	**Fe/L2**	**Fe/L3**
Symmetric ν_{O-C-O}	1546	1564	1497
Asymmetric ν_{O-C-O}	1413	1413	1355

SEM characterisation

The **Fe/L1**, **Fe/L2** and **Fe/L3** films deposited with a growth potential of -1.3 V were characterised by SEM (**Figure A.91** to **Figure A.93** in Annexes). Comparing the previous with the **Fe/L** image in the same magnification (**Figure 2.40**), they were also constituted by disc-shaped aggregates stacked on top of each other. **Fe/L2** showed a cracked pre-layer and, likewise **Fe/L,** could be assigned to the iron pre-layer. All SEM images show slight differences in the aggregates' sizes. From all, **Fe/L** and **Fe/L2** have the most regular size distribution, with medium-sized aggregates. Contrarily, **Fe/L3** displays the most irregular distribution, with distinctly big aggregates on the surface that were not found in the remaining films.

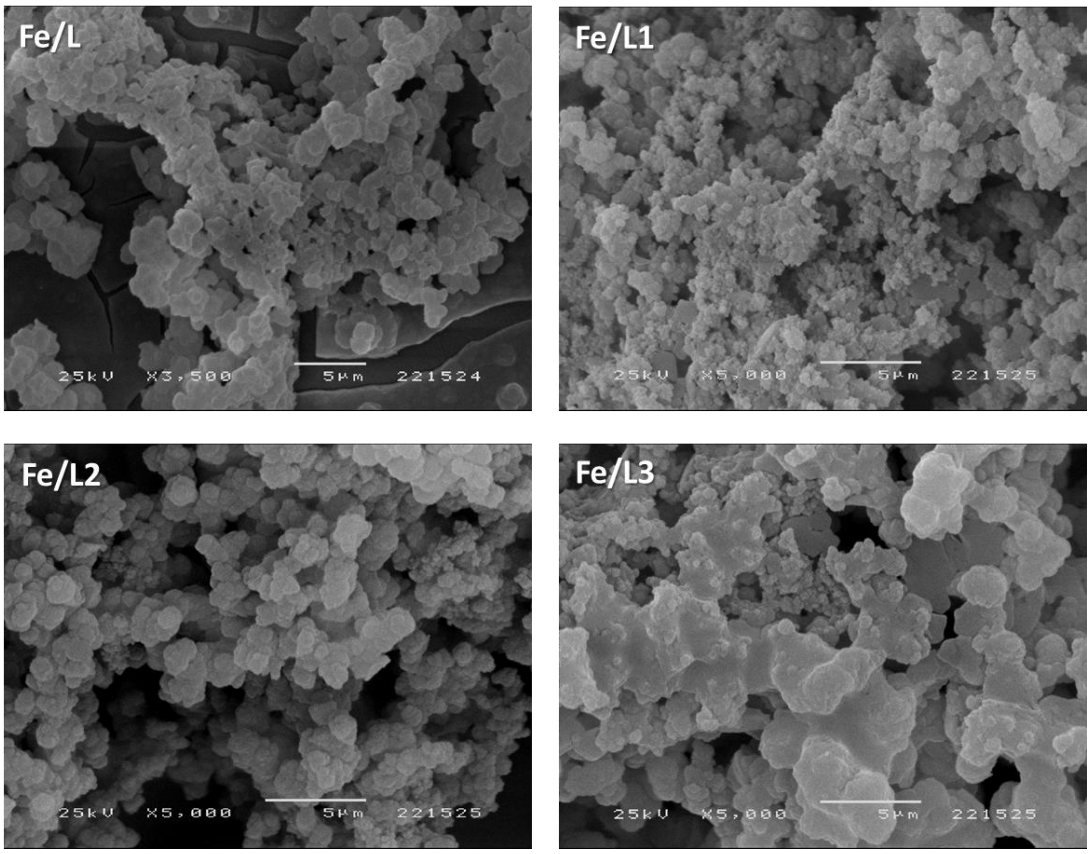

Figure 2.40 - SEM images of the **Fe/L1**, **Fe/L2** and **Fe/L3** films deposited at -1.3 V and amplified at x5000.

PIXE/RBS characterisation

The **Fe/L1**, **Fe/L2** and **Fe/L3** films deposited at -1.3 V were characterised by PIXE and RBS. The PIXE 2D maps of **Fe/L1** (**Figure 2.41**) showed a similar pattern to the 2D maps of the **Fe/L** film. On the other hand, it showed a higher distribution of Sn, which suggests that **Fe/L1** may be thinner than **Fe/L**.

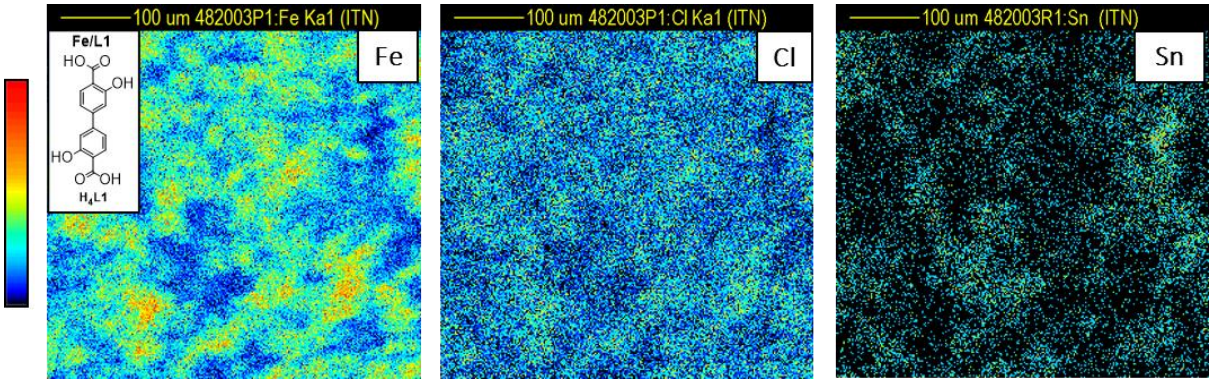

Figure 2.41 - Fe, Cl and Sn atom mapping of the **Fe/L1** film deposited at -1.3 V, obtained by PIXE (beam size of 530×530 μm^2).

An RBS spectrum was obtained by selecting a zone identified as 007 (**Figure A.94** in Annexes). The spectrum showed an intense Si peak, and a Sn peak that was more intense than the one

attributed to Fe. The approximate thickness was obtained with a value of 2000 nm and agrees with the previous conclusions, since the **Fe/L** film had a thickness of around 11000 nm. The approximate Fe/C and Fe/O ratios of **Fe/L1** were obtained (**Table A.16** in Annexes) from the film zones identified as 006, 007 and 008. All show close values to the expected for Fe_2L1, except for 006 that showed a higher Fe content than expected. This could be influenced by the presence of an iron pre-layer.

The PIXE 2D atomic maps of **Fe/L2** and **Fe/L3** (**Figure 2.42** and **Figure 2.43**) showed an identical morphology to **Fe/L1** in terms of film heterogeneity and atomic distribution of the films.

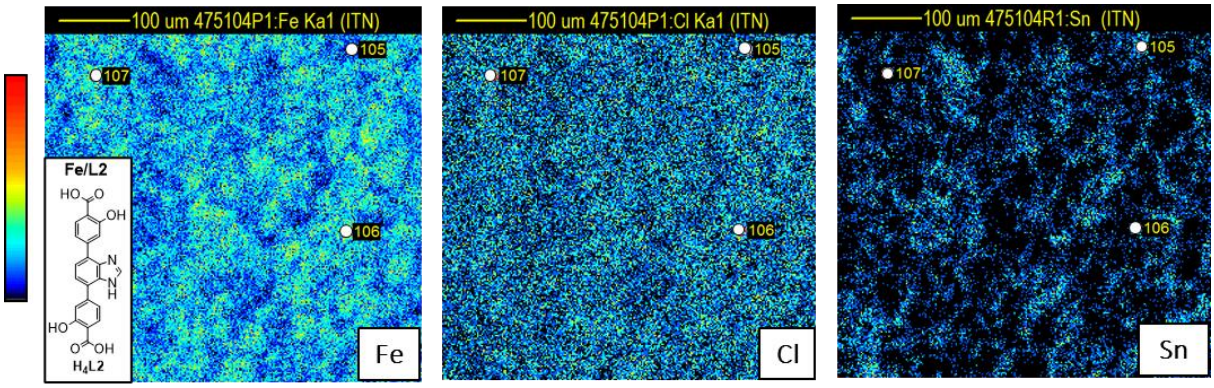

Figure 2.42 - Fe, Cl and Sn atom mapping of the **Fe/L2** film deposited at -1.3 V, obtained by PIXE (beam size of 1060×1060 μm).

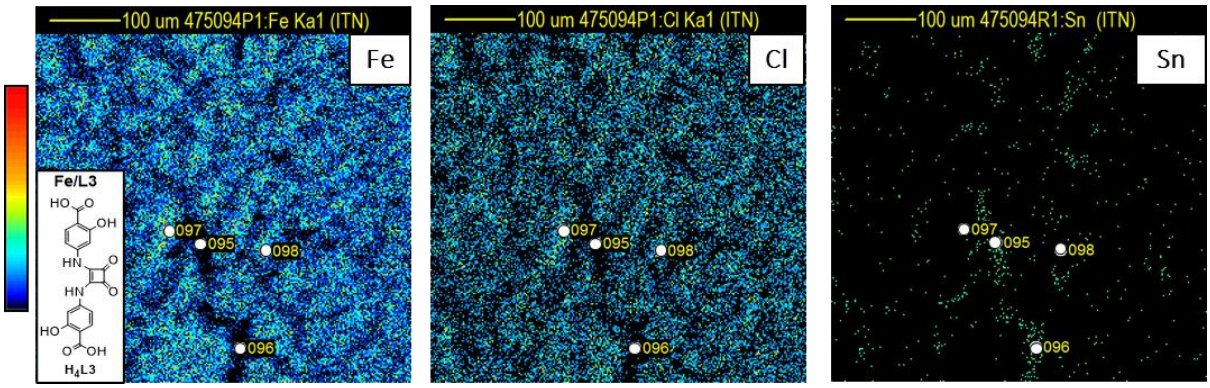

Figure 2.43 - Fe, Cl and Sn atom mapping of the **Fe/L3** film deposited at -1.3 V, obtained by PIXE (beam size of 1060×1060 μm).

It was not possible to obtain adjusted RBS spectra of neither **Fe/L2** or **Fe/L3** so far. Hence, the atom ratios were be based on unadjusted RBS spectra of different zones of the films. The Fe/C and Fe/O ratios for **Fe/L2** (**Table A.17** in Annexes) were based on a zone identified as 106. Moreover, it showed an approximate thickness of 1900 nm, which was even lower than the **Fe/L1** film. It displayed similar Fe/O and Fe/C ratios to Fe_2L2, except for the N/O content, which was higher. This could be due to the interference of DMF or Et_3N molecules. The experimental ratios of **Fe/L3** were also obtained by (**Table A.18** in Annexes) the film zones identified as 97 and 98. Although they show close values to the Fe/O ratio of Fe_2L3, N/O ratios are lower and Fe/C are higher, which agrees with the presence of an iron oxide/hydroxide

pre-layer. Surprisingly, this film reached a thickness of approximately 18000??, thicker than the original **Fe/L** film. The **Fe/L3** was selected to perform a Fe, C, O and N distribution in depth (**Figure 2.44**) by the 097 zone. The plot showed that, closer to the FTO electrode, the **Fe/L3** film was constituted by a pre-layer only constituted by Fe and O, in agreement with the existence of an iron oxide/hydroxide pre-layer.

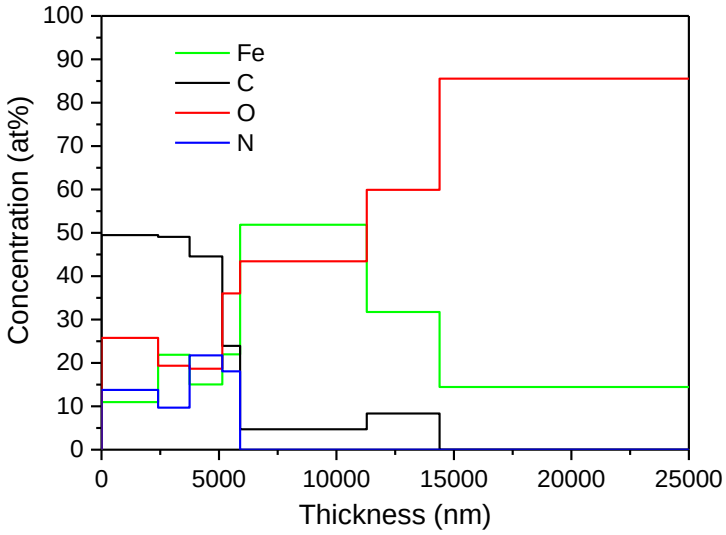

Figure 2.44 - Atomic in-depth distribution of Fe, C, O and N.

XPS characterisation

The **Fe/L1**, **Fe/L2** and **Fe/L3** films deposited with a growth potential of -1.3 V were analysed by XPS by focusing on the C 1s, O 1s and Fe 2p peaks. The attributions can be found in **Table A.19**, in Annexes. The peaks agreed with the ones found in **Fe/L** film and the attributions were also based on the same references.

The C 1s peaks were deconvoluted (**Figure 2.45**) and the **Fe/L2** film showed a peak at around 283 eV, attributed to the C from the sample holder. Moreover, all spectra show a peak at 285 eV, assigned to C-C and C-H bonds from surface C atoms. The peaks found at around 286.4 and 288.8 eV were assigned to C-O bonds from the phenoxide function, and C-O bonds from the carboxylate function, respectively. This once again proves the deprotonation of the pro-ligands.

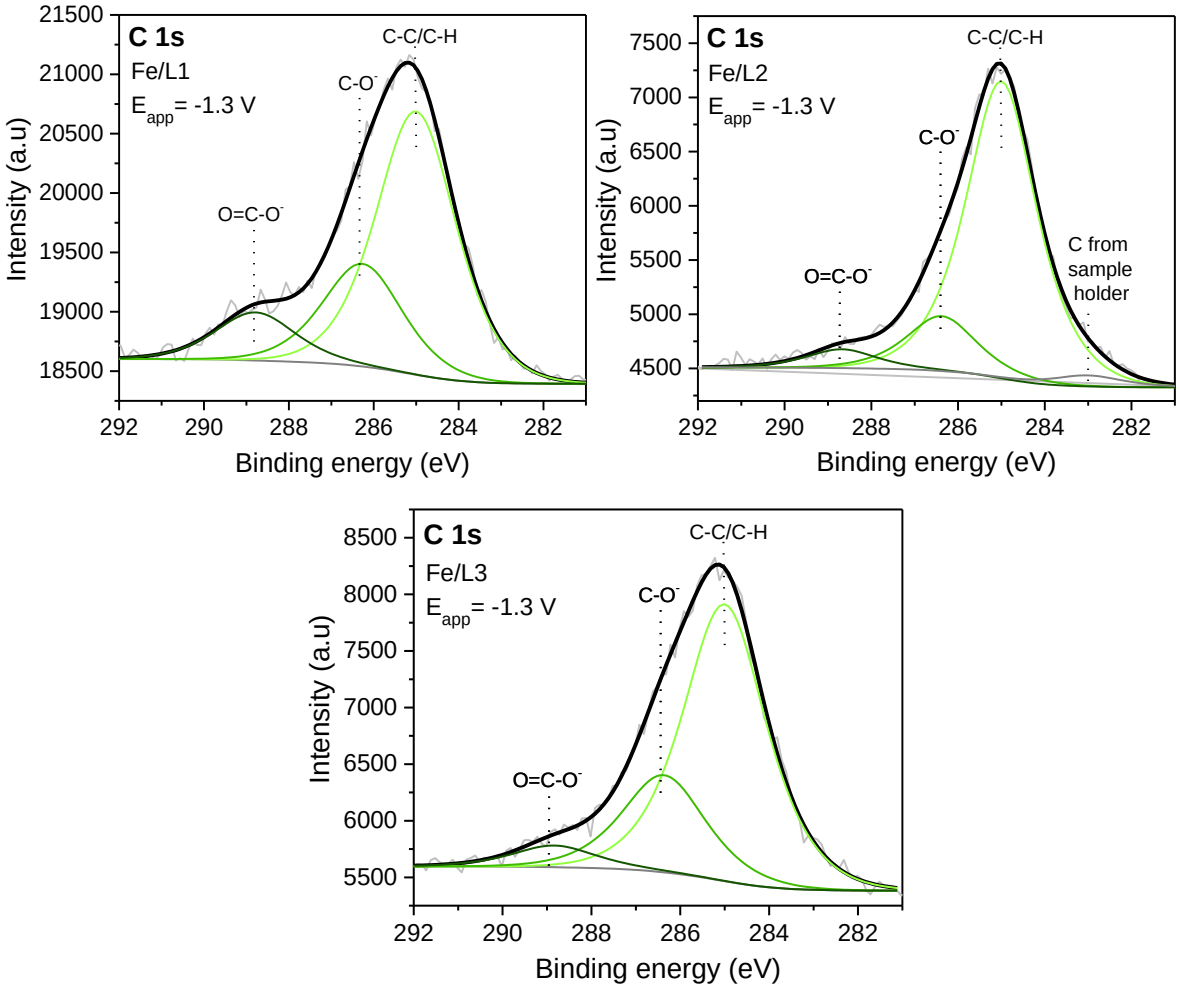

Figure 2.45 - XPS spectra of the **Fe/L1**, **Fe/L2** and **Fe/L3** films deposited at -1.3 V, amplified in the C 1s peak.

The Fe 2p1/2 and 2p3/2 peaks could also be identified in the Fe 2p zone (**Figure 2.46**). Herein, the 2p3/2 deconvolutions also show a complex Fe constitution. This also means that the beam can reach the iron oxide/hydroxide and detect the different constituted Fe^{2+} and Fe^{3+} species.

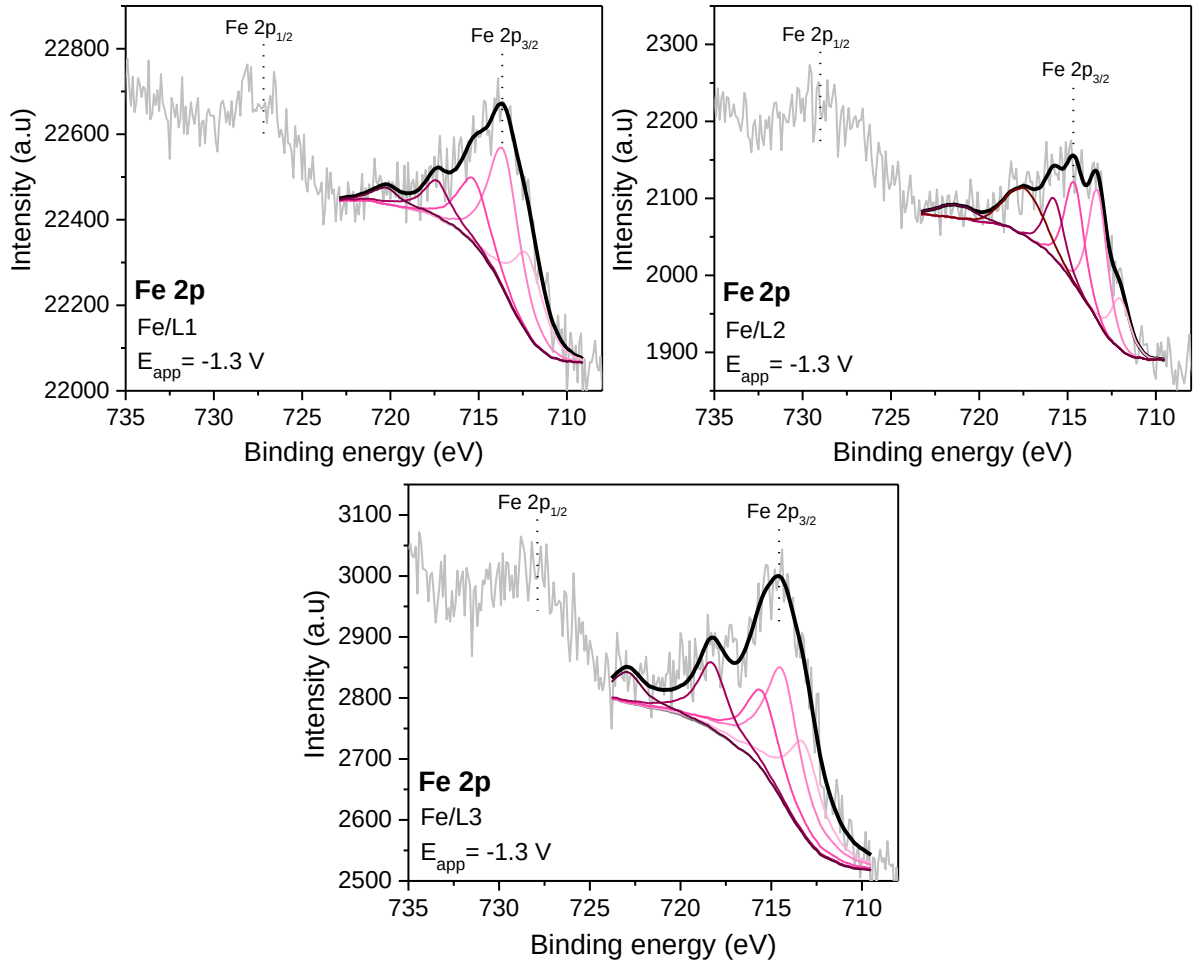

Figure 2.46 - XPS spectra of the **Fe/L1**, **Fe/L2** and **Fe/L3** films deposited at -1.3 V, amplified in the Fe 2s peak.

The O 1s peak of the **Fe/L1** (**Figure 2.47**) was the only one that was possibly deconvoluted so far. Nevertheless, it was expected that all films presented the observed peaks at around 531.7 and 532.7 eV, attributed to the phenoxide and carboxylate functions. These peaks are in agreement with the C 1s peaks, regarding the pro-ligands deprotonation.

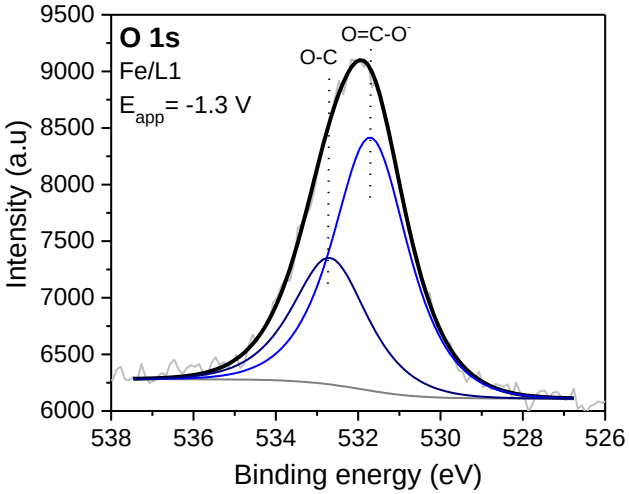

Figure 2.47 - XPS spectra of the **Fe/L1** film deposited at -1.3 V, amplified in the O 1s peak.

The atomic concentration (%) of the Fe, C and O atoms was quantified for all three films and compared with the expected values. The **Fe/L1** (**Table A.20** in Annexes) showed a smaller content of Fe, which can be associated with interferences from the surface C contamination. Since it was obtained a N percentage of 3.3%, the experimental values were also compared with the predicted composition of $Fe_2L1(DMF)(H_2O)$. Although the N content was closer to this structure (predicting 2.2%), as well as the Fe content, C and O quantities remain closer to the Fe_2L1 composition. Hence, it was possible to assume the Fe distorted value by C surface and the presence of N that could also be due to contamination, or a minimal content of DMF molecules. In the case of **Fe/L2** and **Fe/L3** (**Table A.21** and **Table A.22**, respectively, in Annexes), the Fe content was also far from the expected, but all the other components agree with the expected Fe_2L structures. Once again, slight shifts can be associated with C surface contamination which are more pronounced on the Fe content.

XRD characterisation

From the three films, **Fe/L3** was selected for XRD characterisation (**Figure A.95** in Annexes) and, once again, only the FTO characteristic peaks are observed. Although several approaches were attempted to induce film crystallinity, none of them were successful so far. Although amorphous, these films were still tested the uric acid sensing.

2.4 Electrochemical behaviour of the films

The electrochemical behaviour of the **Fe/L**, **Fe/L1**, **Fe/L2** and **Fe/L3** films was studied by cyclic voltammetry (**Figure 2.48**). The **Fe/L** film deposited for 15 minutes was also included for this application. Overlaying all CVs, **Fe/L** deposited for 1 hour had, by far, the highest electrochemical response and **Fe/L2** the lower. The **Fe/L** film deposited for 15 minutes was less electroactive than the 1-hour film, as expected, since it was a thinner film. Nevertheless, the 15-minute film was still more electroactive than the films constituted by the the **H_4L1**, **H_4L2** or **H_4L3** pro-ligands.

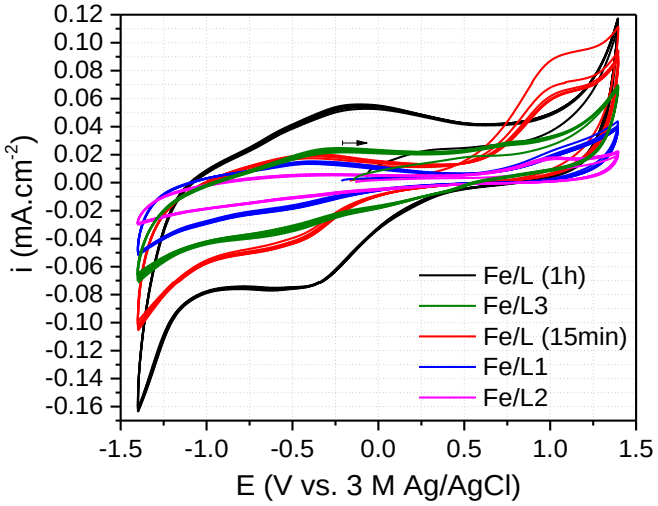

Figure 2.48 - Cyclic voltammograms of the **Fe/L** films deposited for 1 hour (**black**) and 15 minutes (**red**), as well as the **Fe/L1** (**blue**), **Fe/L2** (**pink**) and **Fe/L3** (**green**) films, all deposited at -1.3 V. CVs were performed in 10 mL of N_2 saturated DMF and recorded at 100 mV.s^{-1}. The one-compartment electrochemical cell was also constituted by platinum wire as counter and 3 M Ag/AgCl as reference electrodes.

The electroactive surface coverage (Γ_e, mol.cm^{-2}) of all films was calculated by **Equation 6** and shown in **Table 2.4**. The charge was obtained by integration of the redox peaks of $Fe^{3+/2+}$.

$$\Gamma_e = \frac{Q}{nFA} = \frac{q}{nF} \qquad \text{(Equation 6)}$$

where Q (C): charge obtained by the integration of the $Fe^{3+/2+}$ peaks; A (0.7 cm^2): geometric area of the electrode; q (C.cm^{-2}): charge density; n (1): number of electrons of the process; F (96485 C.mol^{-1}): Faraday constant.

Γ_e depends on the density of iron active sites and so, it will also vary with the thickness of the films. The coverage values agree with the approximate thicknesses obtained by PIXE, since **Fe/L** presented the highest density of active sites. Although the 15-minute **Fe/L** film was not characterised by PIXE, it was still thicker than the **Fe/L1**, **Fe/L2** and **Fe/L3** films. Finally, as predicted by PIXE, **Fe/L3** was thicker than **Fe/L1** and **Fe/L2**.

Table 2.4 - Electroactive surface coverage of the **Fe/L** (1h and 15min), **Fe/L1**, **Fe/L2** and **Fe/L3** films deposited at -1.3 V.

	Fe/L (1h)	Fe/L (15min)	Fe/L1	Fe/L2	Fe/L3
Γ_e (mol.cm^{-2})	7.8×10^{-9}	4.6×10^{-9}	2.18×10^{-9}	1.3×10^{-9}	3.8×10^{-9}

2.5 Uric acid sensing

In terms of application, the films were tested for the electrochemical detection of uric acid. As an initial attempt, the redox behaviour of the **Fe/L** films deposited for 1 hour and for 15 minutes were studied by cyclic voltammetry, in phosphate-buffered saline (PBS) solutions. A total of 11 cycles were performed (**Figure 2.49**) and the films appeared stable. The current differences could be attributed to minimal film detaching from the electrode.

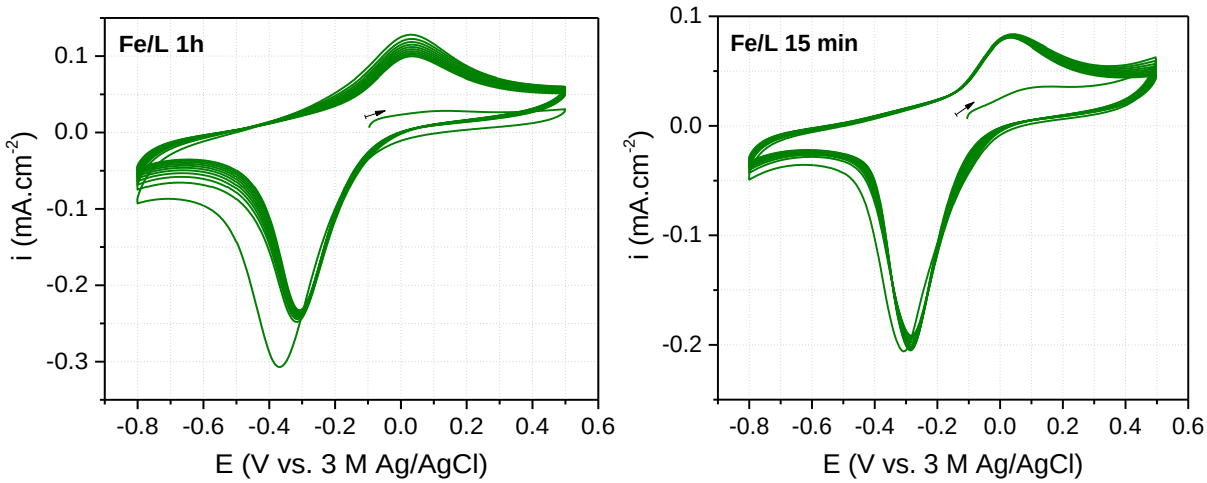

Figure 2.49 - Cyclic voltammograms of the 1-hour and 15-minute **Fe/L** films (2:1:1 ratio of **M:H$_4$L:PB**, respectively) deposited on the FTO working electrode (0.7 cm^2). CVs were performed in 10 mL of N_2 saturated PBS buffer and recorded at 100 mV.s^{-1}. The one-compartment electrochemical cell was also constituted by platinum wire as counter and 3 M Ag/AgCl as reference electrodes.

The UA detection was further tested with differential pulse voltammetry (DPV) (**Figure 2.50**). Concentrations of UA were added in a range of 300 to 550 µM and the current response was measured with a potential range between 0.4 and 1.1 V. The 15-minute **Fe/L** film showed a sensing tendency only between 300 and 350 µM of UA, by what seemed to have reached a limit. On the other hand, the 1-hour film did not show a tendency at all. The voltammograms started by showing an oxidation peak at 0.4 V by the addition of 300 µM of uric acid. When adding 350 µM, which was the second addition of uric acid, this peak unfolded into two peaks, at 0.4 and ~0.85 V and it was not possible to produce a calibration curve.

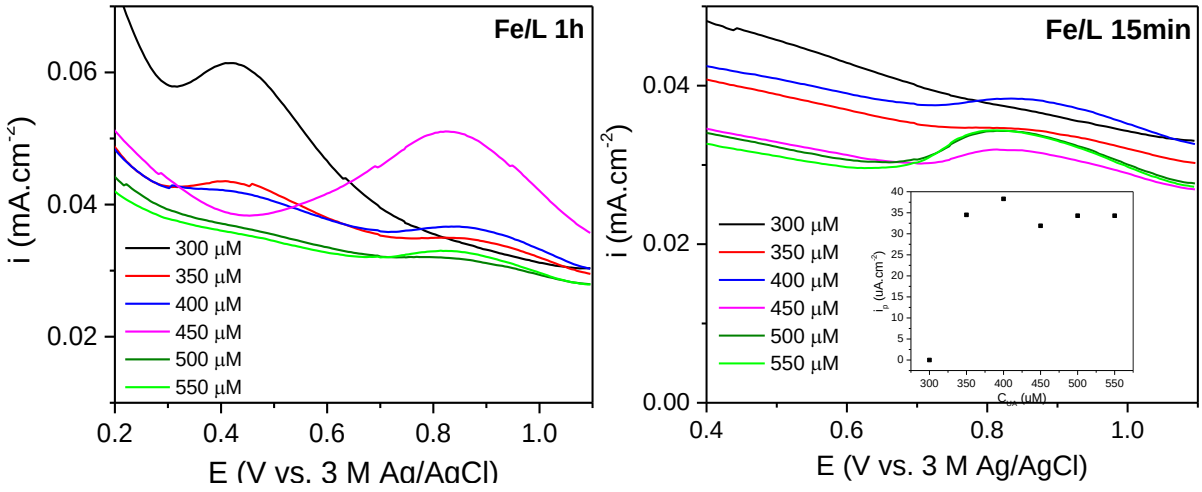

Figure 2.50 - DPV voltammograms of UA concentrations on a range of 300 to 550 µM on 1-hour and 15-minutes **Fe/L** films (2:1:1 ratio of **M:H4L:PB**, respectively) in PBS buffer.

Qualitatively, after the electrochemical sensing measurements, the dark-blue film turned white (**Figure A.96** in Annexes). This proved that the films sensing abilities were being perturbed by the simultaneous adsorption of a white component of the buffer, possibly the phosphate anions. To overcome this limitation, the buffer solution was replaced by tris-HCl buffer. The stability of the 1-hour and 15-minute **Fe/L** films in tris was analysed by performing CVs with 6 cycles (**Figure 2.51**). It was possible to observe a minor decrease of the current as the number of cycles increased, and that could also be associated with film detaching from the electrode.

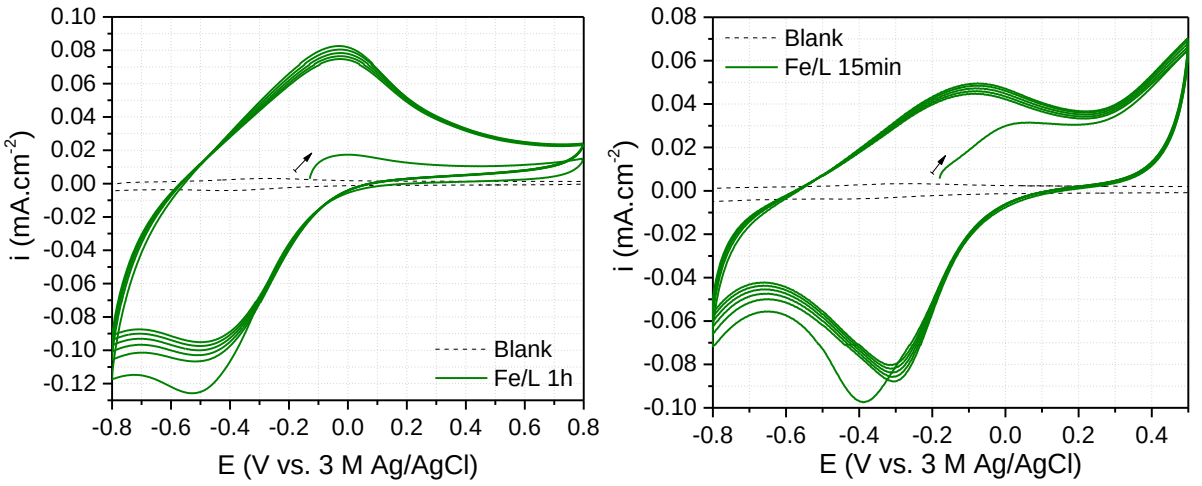

Figure 2.51 - Cyclic voltammograms of the 1-hour and 15-minute **Fe/L** films (2:1:1 ratio of **M:H4L:PB**, respectively) deposited on the FTO working electrode (0.7 cm^2). CVs were performed in 10 mL of N_2 saturated 0.1 M of tris-HCl buffer and recorded at 100 $mV.s^{-1}$. The one-compartment electrochemical cell was also constituted by platinum wire as counter and 3 M Ag/AgCl as reference electrodes.

The response of the films towards different concentrations of uric acid was once again measured by DPV. Uric acid was added at concentrations between 5 and 325 µM and from the maximum peak currents, calibration curves were obtained.

The response of the unmodified FTO electrode was recorded to be compared with the **Fe/L** films (**Figure 2.52**). It resulted in a linear regression of $i_p = 0.0322\ C_{UA} + 4.033$ (R^2=0.9867) with a linear range of 85-325 µM.

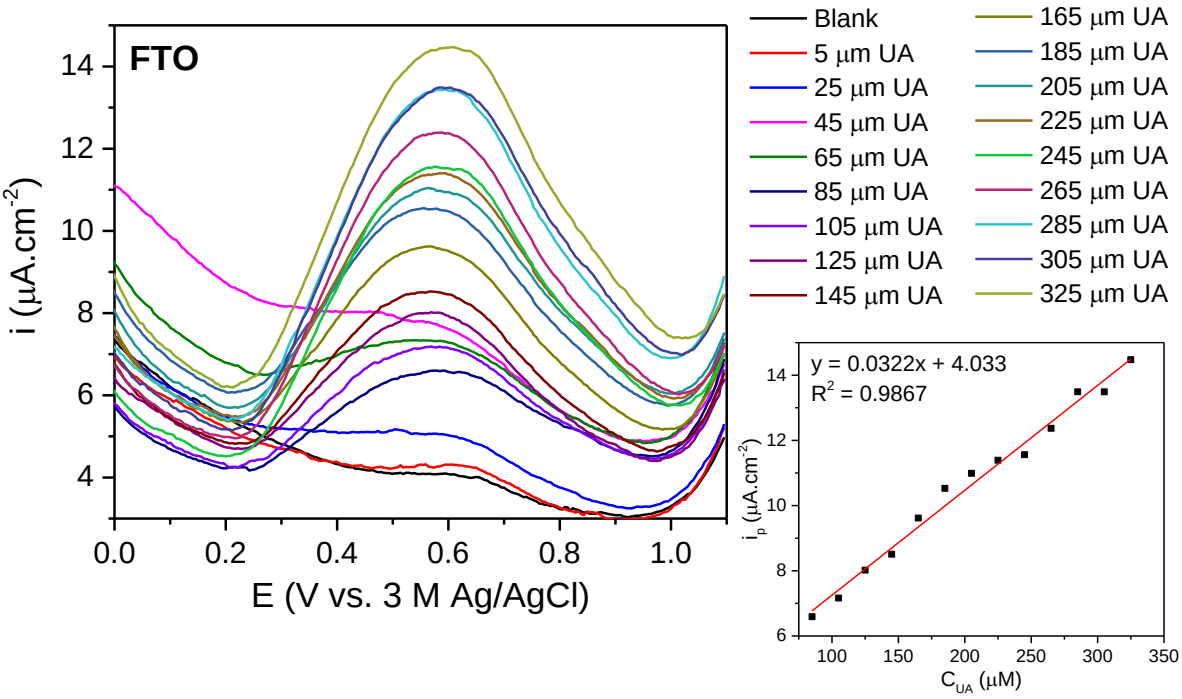

Figure 2.52 - DPV voltammograms of UA concentrations on a range of 50 to 325 mM on FTO electrode in tris buffer.

The response of the **Fe/L** film deposited for 1 hour on FTO was also measured (**Figure 2.53**). It resulted in a linear regression of of $i_p = 0.01158\ C_{UA} + 28.01$ (R^2=0.989) with a linear range of 25-305 µM.

The response of the **Fe/L** film deposited for 15 minutes was also obtained by DPV (**Figure A.97** in Annexes). This time, the peaks attributed to uric acid oxidation shifted to different potentials and did not show a current increasing tendency. The 15-minute film was far thinner than the 1-hour **Fe/L** film. Moreover, the 15-minute film had visible film holes, exposing the FTO electrode. The uric acid response irregularities could be influenced by the simultaneous response of the FTO electrode and so, the 15-minute film was not viable for the uric acid sensing studies.

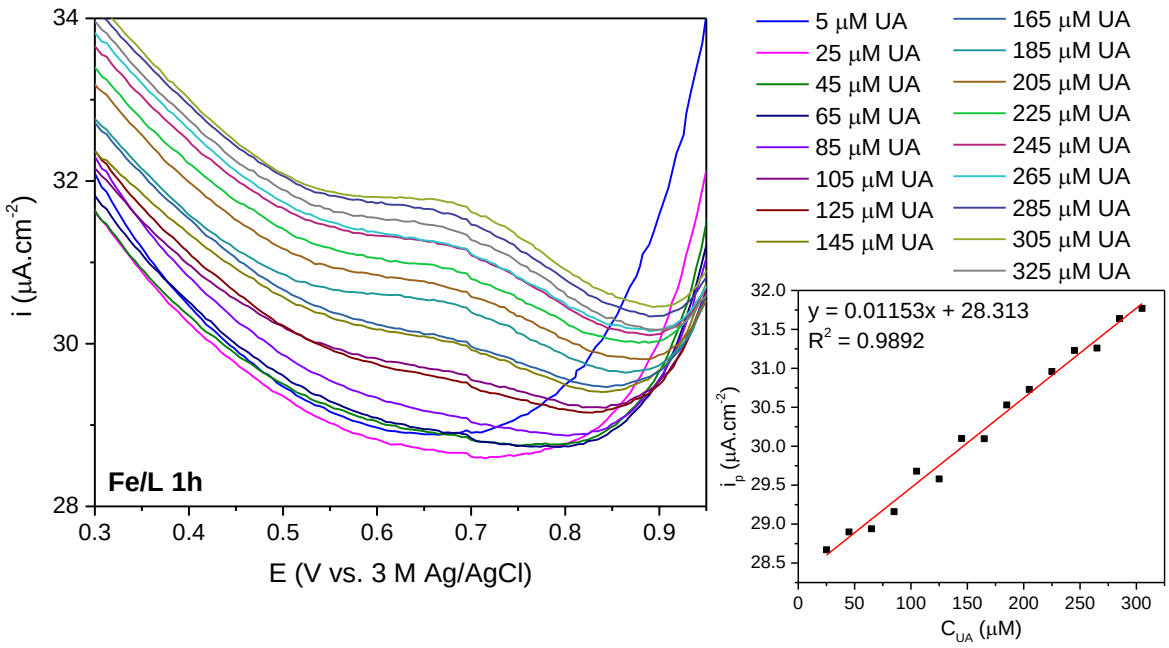

Figure 2.53 - DPV voltammograms of UA concentrations on a range of 50 to 325 mM on 1-hour **Fe/L** film in tris buffer.

To conclude about the applicability of the **Fe/L** film, sensing parameters such as the limit of detection (LOD, calculated by **Equation 7**), sensitivity and standard deviation (σ) were obtained and presented in **Table 2.5**.

$$LOD = \frac{3.3\sigma}{S} \qquad \textbf{(Equation 7)}$$

where σ (µA.cm^{-2}): standard deviation and S (µA.µM^{-1}.cm^{-2}): slope of the curve.

As noticed, FTO electrode revealed a smaller linear range than the **Fe/L** film. In terms of sensitivity, they both display an approximately linear response to the quantity of uric acid, which is a positive result. Nevertheless, the **Fe/L** film similar sensitivity to the FTO. The standard deviation is higher for FTO. This means that the **Fe/L** film displayed a more accurate result and so, remains advantageous against bare FTO.

Table 2.5 - Sensing parameters obtained for **Fe/L** film deposited on FTO and for bare FTO.

	Linear range (µM)	Sensitivity (µA.µM^{-1}.cm^{-2})	σ (µA.cm^{-2})	LOD (mM)
Fe/L	25-305	0.012	1.037	0.296
FTO	85-325	0.032	2.523	0.259

As stated above in **Chapter 1.1**, normal uric acid levels range from 0.13-0.46 mM in blood and 1.49-4.5 mM in urine. **Fe/L** showed a LOD of 0.296 mM, which was slightly higher than the FTO. Moreover, it will not allow to quantify lower concentrations of uric acid in urine samples. Comparing these results with the reported,[30] the sensor of this work presents an abnormally

high LOD, since the ones reported are produced with a LOD in a μM scale and so, further sensor optimisations are needed. Due to time limitations, **Fe/L1-L3** films were still not tested for uric acid sensing.

2.6 Conclusions and perspectives

In this thesis, three pro-ligands were synthesised, **H_4L1**, **H_4L2** and **H_4L3**. **H_4L1** has been previously reported and, to the best knowledge, **H_4L2** and **H_4L3** are new pro-ligands. All structures were characterised by NMR and FTIR. Additionally, **H_4L2** and **H_4L3** were also characterised by EA. Attempts to synthesise other pro-ligands, by the insertion of benzobistrialoze or benzobisthiadialoze moieties, proved to be unsuccessful. For future work, the synthesis of the remaining pro-ligands by alternative routes is planned.

The original M-MOF-74, based on the **H_4L** pro-ligand, is reported as crystalline when produced by conventional methods (solvothermal/hydrothermal).[84] Attempts to grow the M-MOF-74 by electrochemical methods proved unsuccessful as it was not possible to obtain a crystalline film. The optimised/original conditions were established by depositing the **Fe/L** film with a 2:1:1 ratio (**M:H_4L:PB**) with a growth potential of -1.3 V for 1 hour. Changes to the original conditions were attempted to induce film crystallinity, which were also not successful (**Figure 2.54**). Moreover, all attempts performed in **Chapter 2.2.5** show identical DRIFT spectra to the original **Fe/L** film, suggesting similar morphologies.

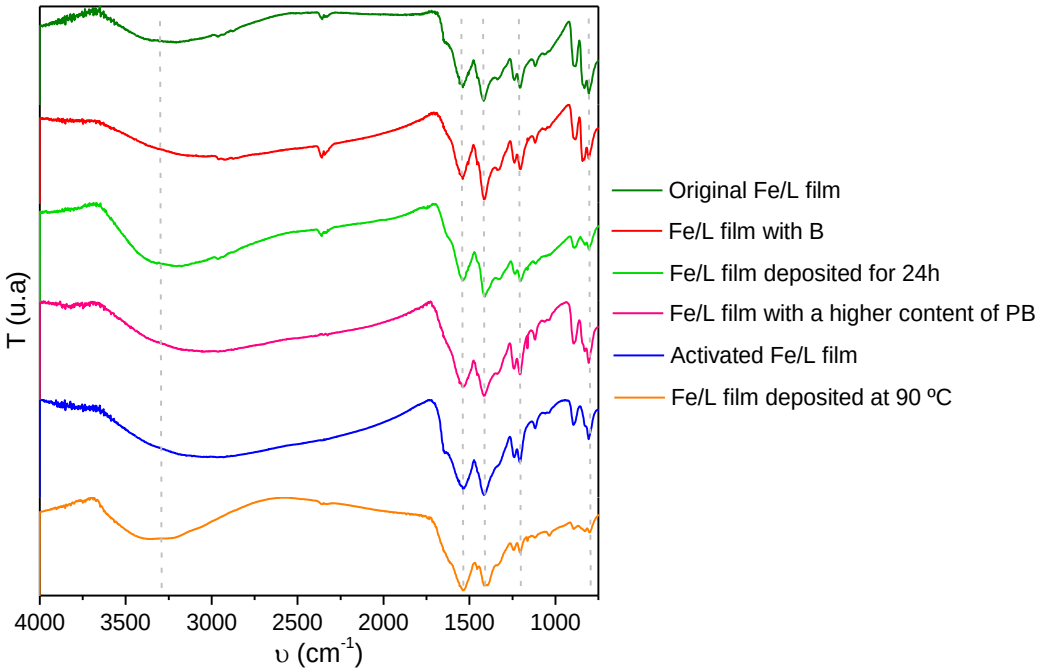

Figure 2.54 - DRIFT spectra of all the films produced in **Chapter 2.2.5**, compared with the original **Fe/L** film.

The absence of crystallinity could be explained by the presence of a mixed valence $Fe^{3+/2+}$ or by impurities (DMF, H_2O, Et_3N, Cl^- and OH^-) that could condition the formation of organised structures during film growth. To ensure the presence of amorphous films constituted by the iron metal ion and the **H_4L** pro-ligand, these were characterised by a range of techniques, such as FTIR, SEM BET, EA, XPS, PIXE and AFM. Altogether, these allowed to conclude about the morphology as well as the composition of the films and indicated the presence of an unorganised coordination polymer, constituted by the metal ion coordinated to the ligand. Moreover, the presence of an iron oxide/hydroxide pre-layer was also proved. However, these techniques did not allow to unequivocally conclude about the oxidation states of the $Fe^{3+/2+}$ mixed valence film. For that, Mössbauer would be a useful characterisation technique to inform about the oxidation state of the iron in the films.

Non-crystalline films could also have resulted because of the use of very negative potentials. AFM demonstrated the organised growth of the films from the first seconds of deposition. Nevertheless, after 15 minutes, it was clear that an unorganised morphology was already present. As a solution, the deposition could be tested in the presence of MOF modulators (monocarboxylic acids, e.g., formic or acetic acids).[162] These would compete with the organic ligands and prevent the formation of deposited impurities, simultaneously decreasing the MOF nucleation rate and enhancing the crystallinity.

Although MOF-74 is already comprehensively studied in the form of powder, it has never been reported by direct deposition methods. Herein, it was possible to produce new films comprised of **Fe/L**, **Fe/L1** and inspired by the respective MOF powders.[81] Moreover, **Fe/L2** and **Fe/L3** were also produced as new films attempting to obtain novel MOFs. As a follow up, the optimisation of the direct deposition of the films should be attempted.

The **Fe/L** film was tested for uric acid sensing with a linear range of 25 to 305 μM, a LOD of 0.296 mM, and a SD of 1.037 $\mu A.cm^{-2}$. It presented a much higher LOD than the ones reported in the literature.[30] To obtain a more extensive study, **Fe/L1**, **Fe/L2** and **Fe/L3** films should also be tested for the detection of uric acid. As an alternative, the films could applied to phosphate adsorption, which was observed in the case of the **Fe/L** film, that turned white when exposed to the PBS solution.

3

MATERIALS AND METHODS

3.1 Chemicals and solvents

If not stated otherwise, all chemicals were used without further purification and purchased from TCI, Sigma Aldrich, Fluorochem and Acros Organics. When indicated, solvents such as anhydrous tetrahydrofuran, ethyl acetate and *p*-dioxane were purified as described by Amarin and Perrin.[163]

3.2 General experimental conditions

Thin-layer chromatography (TLC) was carried out using, pre-coated silica gel 60 F_{254} metal plates, which were observed under UV light (254 or 365 nm). Column chromatography was carried out using flash technique using silica-gel Geduran® Si 60 (0.040-0.063 mm).

Solution NMR technique was employed to obtain unidimensional and bidimensional ^{1}H and ^{13}C NMR spectra, recorded on a Bruker Advance 400 MHz spectrometer. The chemical shifts ( ), given in ppm, are referenced to the residual proton or carbon signal of the deuterated solvent.

Powder FTIR spectra were obtained on a Nicolet Nexus 6700 FTIR spectrophotometer in the 4000-400 cm^{-1} range with 4 cm^{-1} resolution using KBr pellets with 64 scans. DRIFT spectra were obtained with the same spectrophotometer with the diffuse reflectance accessory in the 4000-750 cm^{-1} range with 4 cm^{-1} resolution and 256 scans.

Elemental analysis for C, H and N quantifications were performed on a Fisons Carlo Erba EA110 and HR-MS/ESI on a Bruker FTMS (APEXIII) at C.A.C.T.I., University of Vigo.

XPS was performed by Prof. Dr. Ana Maria Rego and Dr. Ana Ferraria from Instituto Superior Técnico. Analyses were performed with a dual anode (Al/Mg) non-monochromatic spectrometer XSAM800 from KRATOS. The X-radiation Mg Kα (hν = 1253.6 eV) used to irradiate the samples, was produced with a high voltage of 12 kV and filaments current equal to 10 mA.

Samples were fixed to the XPS holder with a metal spring and positioned in the analysis chamber at a take-off angle of 90º relative to the surface. The analysis, at room temperature, started once the chamber attained an ultra-high vacuum (UHV), typically a pressure ~10-9 mbar. Spectra were acquired in a Fixed Analyser Transmission (FAT) mode, with a pass energy of 20 eV, and collected and stored in 300 to 400 channels with a step of 0.1 eV using the software Vision 2 for Windows, Version 2.2.9 (Kratos). No flood gun was used to compensate the charge accumulation. Charge shift was corrected from the spectra using as reference the binding energy (BE) of aliphatic carbon bonded to carbon and/or hydrogen, set at 285 eV. Source satellites and Shirley backgrounds were subtracted at each region of interest. Component peaks with pseudo-Voigt profiles were fitted in each region with a nonlinear least-squares algorithm using the XPSPeak 4.1 software (freeware), which allows to optimize simultaneously peaks position, area, full width at half maximum and Gaussian-Lorentzian %. The sensitivity factors used in the quantification were the following: C 1s: 0.318; O 1s: 0.736; N 1s: 0.505; Fe 2p3/2: 1.965; Cl 2p: 0.964; P 2p: 0.530; P 2s: 0.344; F 1s: 1.000; Sn 3d5/2: 4.946; Na 1s: 1.378.

BET measurement was made in collaboration with Prof. Dr. João Silva with physical adsorption of nitrogen at -196 C, using a Quantachrome NOVA 2200e instrument. The film sample was previously degassed in vacuum at 150 C for 3 h The specific surface area was calculated by using the relative pressure data in the 0.05–0.3 range.

X-ray diffractograms were acquired by Prof. Dr. Estrela Jorge, using a Philips Analytical PW 3050/60 X'Pert PRO automatic diffractometer (q/2q), equipped with an X'Celerator detector, with automatic data acquisition using the X'Pert Data Collector software, version 2.0b. As incident radiation, the K line of a copper bulb was used, operating with a current of 30 mA and a voltage of 40 kV. To record the diffractograms, a continuous scan of the Bragg angles was performed, for values of 2θ, between 10 and 90 , with a step of 0.017 (2θ) and an acquisition time of 20 s/step.

PIXE and RBS were performed by Dr. Victoria Corregidor and Dr. Luis Alves from Campus Tecnológico e Nuclear of Instituto Superior Ténico. It was used a 2MeV proton beam generated by a 2.5 MV singe ended Van de Graaff accelerator and directed to the microprobe beam line through a 90º bending magnet. The nuclear microprobe has an Oxford Microbeams magnetic quadrupole triplet used to focus the beam. It is applied a maximum area of 2.6x2.6 mm^2 and the experiment is performed under vacuum. The X-rays were detected with a 30 mm^2 Bruker Si SDD detector with 8 μm Be window and 145 eV resolution at 5.9 keV, positioned at 135º with the beam direction at a distance of 20 mm from the sample. The backscattered protons were detected with a 200 mm^2 PIPS detector with 30 keV resolution, positioned at 140 scattering angle in Cornell geometry at a distance of 50 mm from the sample. Operation and basic data manipulation, this including elemental distribution mapping, was achieved through the OMDAQ software code and quantitative analysis done with GUPIX software. The results are

expressed in weight percent normalised to 100%. NDF v9.6a code simultaneously fits the PIXE and RBS spectra to obtain a self-consistent solution. Thickness values are given in areal density (i.e., atoms/cm2), the standard units in IBA analyses.

SEM was performed by Dr. Telmo Nunes. Specimens were mounted in stubs and coated with gold in a JEOL JFC-1200 sputtering chamber. Subsequently specimens were observed in a JEOL JSM-5200LV scanning electron microscope.

AFM was performed by Prof. Dr. Ana Viana. The images were collected in a Multimode atomic force microscope running on the NanoScope IIIa controller (digital instrument Veeco).

3.3 Electrochemical measurements

3.3.1 General conditions

Except for the depositions with an applied magnetic field (**Chapter 2.2.5**), all electrochemical experiments were performed with a potentiostat PGSTAT 12 AUT71019 controlled by NOVA 2.0 software. For the apparatus, it was used a three-electrode heart-shaped glass cell (**Figure 3.1**). The deposition with an applied magnetic field was performed in a Teflon cell (**Figure 3.2**) was used with a Potentiostat MP 81 without software. Both cells were assembled with FTO as the working (WE), platinum wire as the counter (CE) and 3 M Ag/AgCl (0.278 V vs NHE) as the reference (RE) electrodes. FTO glasses (A= 0.7 or 1 cm^2) were washed ultrasonically before experiments with a detergent/water solution, followed by methanol and acetone for 15 minutes. Before any electrochemical measurements, the cell solutions were purged with N_2 for a minimum of 30 minutes each essay. If not stated otherwise, the **Fe/L** films were produced by precursor solution containing 7 mM or 4 mM (indicated in text) of $FeCl_3.6H_2O$ (**M**), 2 mM of **H_4L** and 2 mM of Et_3NHCl (**PB**). The **Fe/L1**, **Fe/L2** and **Fe/L3** films were produced by precursor solution containing 4 mM of $FeCl_3.6H_2O$ (**M**), 2 mM of **H_4L1**, **H_4L2** or **H_4L3** and 2 mM of Et_3NHCl (**PB**).

When working with an organic medium (DMF), 0.1 M of $TBAPF_6$ was used as the supporting electrolyte, which was previously recrystalised from hot ethanol.

When working with an aqueous medium, 10 mL of a 0.1 M of phosphate buffer solution (PBS) or 0.1 M of tris-HCl buffer solution were used (pH ~7).

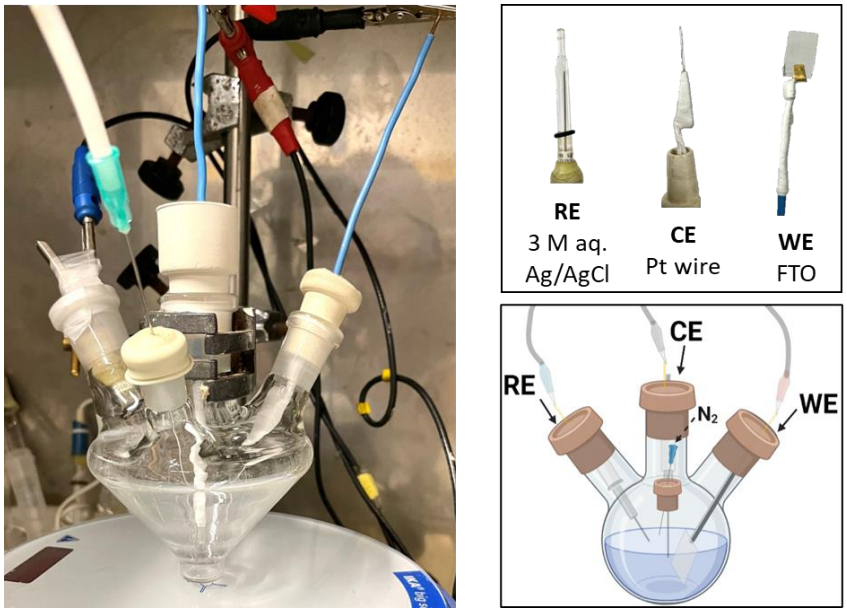

Figure 3.1 - Assembly of the electrochemical heart-shaped glass cell.

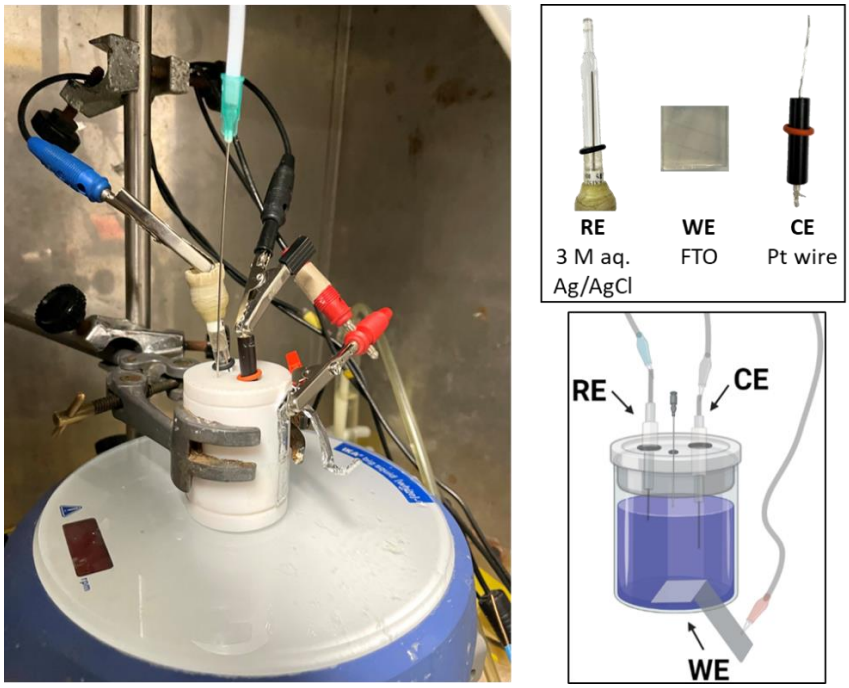

Figure 3.2 - Assembly of the electrochemical Teflon cell.

Cyclic voltammetry (CV) was only performed with the heart-shaped glass cell apparatus with scan rates ranging from 0.01 to 0.5 Vs^{-1}. If not stated otherwise, CVs were performed with a potential window between -1.4 to 1.4 V with a total of three cycles. For simplicity, only the first cycle was displayed throughout the thesis. Exceptionally, the CVs of the stability studies in the buffer solutions (**Chapter 2.5**) are performed with a total of 10 or 5 cycles with a potential window ranging from -0.8 to 0.5 V or -0.8 to 0.8 V, respectively.

Chronoamperometry was performed with potentials ranging from -1.4 V to -1.0 V and with deposition times ranging from 8 seconds to 24 hours. Optimised conditions show chronoamperograms with a potential of -1.3 V for 1 hour.
Different Pulse Voltammetry (DPV) was performed for uric acid detection in an aqueous medium with 10 mL of 0.1 M of PBS or tris buffer solutions (pH ~7), discussed in **Chapter 2.5**. DPV measurements were carried out with a potential window ranging from -0.05 to 1.1 V, a pulse amplitude of 50 mV, a quiet time of 1 s, a step of 5 mV and a modulation time of 5 ms, with an overall scan rate of 5 mVs^{-1}.

3.4 Synthesis and characterisations

3.4.1 General conditions

The following conditions were adapted with slight modifications from the literature.[137]
Sukuzi-Miyaura coupling: A *p*-dioxane/H_2O mixture (2:1 V/V, 0.12 M based on the limiting reagent) was purged with N_2. The Schlenk flask was then charged with the limiting reagent, **IB** and CsF (3 eqv.). It was once again purged with N_2 and, finally, $Pd(dppf)Cl_2$ (10 mol%) was added. The mixture was heated under reflux overnight. The resulting mixture was extracted with CH_2Cl_2 (3×50 mL) and concentrated to yield a crude brown powder that was purified by flash chromatography (1:9 acetone/petroleum ether).
Catalytic hydrogenation: The starting material was dissolved in anhydrous THF. The Pd/C catalyst was added (20 w%) under an atmosphere of N_2. The reaction mixture was stirred for 48h under an atmosphere of H_2, filtered over a Celite plug, washed with solvent, and concentrated to yield a white powder.
Basic hydrolysis: The starting material was stirred in a THF/0.5 M NaOH aq. (1:1 V/V) mixture at 50 ºC overnight. The THF was then removed in vacuo and the aqueous layer was acidified with concentrated HCl until a pH<2 was obtained. The resulting precipitate was collected by vacuum, washed with distilled H_2O and dried.

3.4.2 Characterisation of H_4L

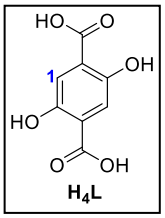

^1H NMR (400 MHz, $(CD_3)_2SO$, 25ºC): δ= 10.62 (s, COOH), 7.27 (s, H1). FTIR (KBr, cm^{-1}): 3520 (w, ν_{O-H}), 3082 (w/br, ν_{O-H}), 2880 (w, ν_{C-H}), 1646 (s, $\nu_{C=O}$), 1357-1182 (s, ν_{C-O}), 905-696 (var, δ_{C-H}) . UV-vis (DMF, nm): 369.

3.4.3 Synthesis and characterisation of I_A

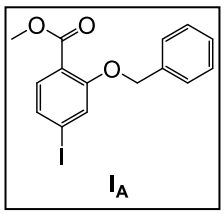

This synthetic procedure was adapted from ref.[137] Solid K_2CO_3 (1.47 g, 10.4 mmol) was added to a solution of methyl 4-iodosalicylate (1.47 g, 5.3 mmol) in 15 mL of CH_3CN at room temperature. Benzyl bromide (0.95 mL, 7.95 mmol) was added with a syringe, and the reaction mixture was warmed to 80 ºC and stirred overnight. The next morning, the reaction was monitored by TLC (petroleum ether as eluent). When completed, the reaction mixture was then cooled to room temperature and filtered to remove insoluble salts, which were washed further with CH_3CN. The mixture was concentrated in vacuo and a yellowish oil was obtained. To remove benzyl bromide residues, the compound was recrystallized in hot hexanes and **I_A** was yielded as white needles (1,53 g, 77%). ^{1}H NMR (400 MHz, $CDCl_3$, 25 ºC): δ = 7.54 (d, *J*= 8.0 Hz, 1H), 7.49 (d, *J*= 8.0 Hz, 2H), 7.42–7.31 (m, 5H), 5.14 (s, 2H), 3.89 ppm (s, 3H). ^{13}C NMR (100 MHz, $CDCl_3$, 25 ºC): δ = 166.24, 158.36, 136.15, 133.02, 130.02, 128.71, 128.09, 126.96, 123.27, 120.23, 99.98, 70.93, 52.27.

3.4.4 Synthesis and characterisation of I_B

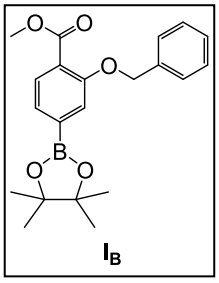

This synthetic procedure was adapted from ref.[137] Anhydrous *p*-dioxane (14 mL) was added to a Schlenk flask, followed by **I_A** (1 g, 2.72 mmol), KOAc (80.1 g, 8.26 mmol) and $Pd(PPh_3)_2Cl_2$ (0.0573 g, 0.0816 mmol). The mixture was purged with N_2 for 30 minutes, and bis(pinacolato)diboron (0.813 g, 3.02 mmol) was then added. The flask was heated under reflux overnight. When complete by TLC (1:9 acetone/petroleum ether) the reaction mixture was cooled to room temperature and filtered to remove insoluble salts, which were washed further with EtOAc. The filtrate was concentrated in vacuo and dissolved in EtOAc. Activated charcoal was added and the resulting solution was warmed to reflux for 30 min. The insoluble material was removed by hot filtration through a pad of Celite to obtain a yellow solution. It was concentrated in vacuo resulting in a red oil and placed in the freezer overnight. The crude was purified by flash-chromatography in a silica gel column (1:9 acetone/petroleum ether) and recrystallized in petroleum ether, yielding **I_B** as white needles. (0,6494 g, 65%). ^{1}H NMR (400 MHz, $CDCl_3$, 25 ºC): δ = 7.81 (d, *J*= 7.5 Hz, 1H), 7.54 (d, *J*=7.5 Hz, 2H), 7.48 (s, 1H), 7.45 (d, *J*=7.5 Hz, 1H), 7.40 (t, *J*=8.0 Hz, 2H), 7.31 (t, *J*=7.5 Hz, 1H), 5.22 (s, 2H), 3.90 (s, 3H), 1.36 ppm (s, 12H). ^{13}C NMR (100 MHz, $CDCl_3$, 25 ºC): δ = 166.99, 157.50, 136.99, 131.01, 128.58, 127.81, 127.08, 127.02, 123.21, 119.42, 84.36, 70.71, 52.18, 25.00.

3.4.5 Synthesis and characterisation of I_C

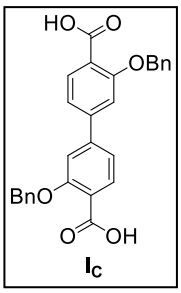

I_C

General Suzuki coupling conditions were employed between I_A (0.2289 g, 0.62 mmol) as the limiting reagent and I_B (0.2518 g, 0.68 mmol), yielding the product as white needles (0.199 g, 66%). ^{1}H NMR (400 MHz, $CDCl_3$, 25 ºC): δ = 7.91 (d, *J*=8.0 Hz, 2H), 7.52 (d, *J*=7.5 Hz, 4H), 7.41 (t, *J*=7.5 Hz, 4H), 7.33 (t, *J*=7.5 Hz, 2H), 7.16 (dd, *J*=8.0, 1.5 Hz, 2H), 7.08 (d, *J*=1.5 Hz, 2H), 5.23 (s, 4H), 3.93 ppm (s, 6H). ^{13}C NMR (100 MHz, $(CD_3)_2SO$, 25 ºC): δ = 166.53, 158.60, 145.42, 136.75, 132.60, 128.79, 128.06, 127.03, 120.29, 119.60, 113.12, 70.94, 52.27.

3.4.6 Synthesis and characterisation of H_4L1

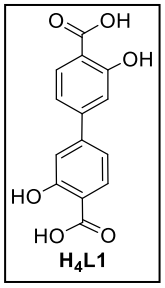

H_4L1

I_C (0.199 g, 0.41 mmol) was deprotected by one-pot catalytic hydrogenation and saponification general procedures, yielding **H_4L1** as a white powder (0.0662 g, 59%). ^{1}H NMR (400 MHz, $(CD_3)_2SO$, 25 ºC): δ = 11.40 (s, 2H), 7.87 (d, *J* = 8.6 Hz, 2H), 7.31 – 7.19 (m, 4H). ^{13}C NMR (100 MHz, $(CD_3)_2SO$, 25 ºC): δ = 171.69, 161.42, 145.61, 131.01, 118.01, 115.30, 112.90. FTIR (KBr, cm^{-1}): 3417 (w, ν_{O-H}), 3011 (w/br, ν_{O-H}), 2959 (w, ν_{C-H}), 1667-1619 (s, $\nu_{C=O}$), 1453-1462 (s, δ_{C-O-H}), 1291-1222 (s, ν_{C-O}), 1095-770 (w, δ_{C-H}).

3.4.7 Synthesis and characterisation of I_D

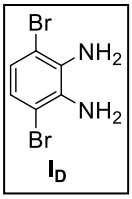

I_D

This synthetic procedure was adapted from ref.[135] 4,7-dibromobenzo[*c*][1,2,5]thiadiazole (0.5527 g, 1.88 mmol) was dissolved in EtOH (20 mL) in a round bottom flask. $NaBH_4$ (1.3269 g, 35,1 mmol) was added at 0 ºC portion-wise for 45 minutes. The flask was equipped with a bubbler because it released H_2S gas. It was left reacting at room temperature overnight. The next day, the temperature was reduced again to 0 ºC and water (~10 mL) was added. The organic solvent was removed by reduced pressure. The mixture was extracted with CH_2Cl_2 and brine, dried with Na_2SO_4 and concentrated, yielding I_D as a beige solid (0,46 g, η= 92%). ^{1}H NMR (400 MHz, $(CD_3)_2SO$, 25 ºC): δ= 6.63 (s, 2H), 5.02 (s, 4H).

3.4.8 Synthesis and characterisation of I_E

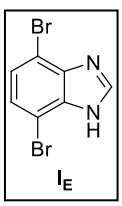

I_E

This synthetic procedure was adapted from ref.[136] I_D (0.16 g, 0.6 mmol) was added into a round bottom flask, followed by 1,5 mL of HCOOH. The flask was sealed with a septum and warmed up to 85 ºC. After 45 minutes, the reaction mixture was cooled to room temperature and an aqueous solution of sodium hydroxide (10% w/V) was added dropwise to attain a pH~8. The suspension was filtered, washed

with ice-cold water, and dried. The product was purified by recrystallization with hot methanol, yielding a beige solid (0,11 g, η= 70%). ^{1}H NMR (400 MHz, $(CD_3)_2SO$, 25 °C): δ = 13.24 (s, 1H), 8.40 (s, 1H), 7.38 (s, 2H).

3.4.9 Synthesis and characterisation of I_F

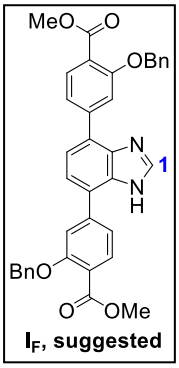

I_F, suggested

General Suzuki coupling conditions were employed between **I_E** (0.074 g, 0.27 mmol) as the limiting reagent and **I_B** (0.2173 g, 0.59 mmol), yielding **I_F** as white needles (0.11 g, 68%). ^{1}H NMR (400 MHz, $(CD_3)_2SO$, 25 °C): δ= 12.86 (s, 1H, NH), 8.40 (s, 1H, H_1), 7.86 (d, *J*=7.8 Hz, 3H), 7.55 (d, *J*=7.3 Hz, 6H), 7.42 (t, *J*=7.5 Hz, 5H), 7.33 (t, *J*=7.4 Hz, 3H).

3.4.10Synthesis and characterisation of H_4L2

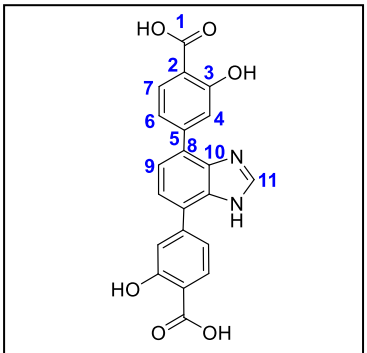

H_4L2

EA: 3**H_4L2**.4CH_2Cl_2.3Et_2O.9H_2O

I_B (0.12 g, 0.20 mmol) was deprotected by one-pot catalytic hydrogenation and saponification general procedures, yielding **H_4L2** as a beige solid (0.0723 g, 92%). ^{1}H NMR (400 MHz, $(CD_3)_2SO$, 25 °C): δ = 11.42 (s, 2H, COOH), 8.46 (s, 1H, 11), 7.93 (d, *J*=8.2 Hz, 2H, 7), 7.55 (m, 4H, 4, 9), 7.47 (d, *J*=7.6 Hz, 2H, 6). ^{13}C NMR (100 MHz, $(CD_3)_2SO$, 25 °C): δ= 171.87 (1), 161.25 (3), 144.67 (2), 143.50 (11), 130.61 (7), 127.03 (10), 122.32 (9), 119.52 (6), 116.90 (4), 112.03 (5, 8). FTIR (KBr, cm^{-1}): 3407 (w, ν_{O-H}), 3126 (w/br, ν_{O-H}), 2959-2842 (w, ν_{C-H}), 1670-1576 (s, $\nu_{C=O}$/$\nu_{C=N}$), 1438 (s, δ_{C-O-H}), 1337-1153 (s, ν_{C-O}), 879-695 (var, δ_{C-H}). EA for **3L2**.4CH_2Cl_2.3Et_2O.9H_2O - calculated (%): 52.55 (C), 34.94 (H), 4.90 (N); EA - found (%): 51.84 (C), 4.92 (H), 4.66 (N).

3.4.11Synthesis and characterisation of I_G

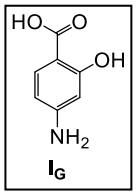

I_G

I_G was synthesised following the general hydrolysis procedure. Methyl 4-amino-2-hydroxybenzoate (3.27 g, 19.6 mmol) was stirred in a THF/0.5M NaOH mixture at 75 °C overnight. THF was removed in reduced pressure and the aqueous phase was acidified with 5M HCl until reaching a pH<2. The precipitate was filtered, washed with H_2O and dried, yielding **I_G** as a beige powder (2.55 g, 85%). ^{1}H NMR (400 MHz, $(CD_3)_2SO$, 25 °C): δ = 11.41 (s, 1H) 7.46 (d, *J*=8.6 Hz, 1H), 6.17 (dd, *J*=8.6, 1.9 Hz, 1H), 6.07 (d, *J*=1.8 Hz, 1H).

3.4.12Synthesis and characterisation of H_4L3

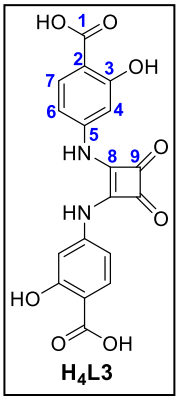

This synthetic procedure was adapted from refs.[75,140] To a stirred solution of 3,4-dihydroxycyclobut-3-ene-1,2-dione (0.288 g, 2.5 mmol) in anhydrous ethanol (15 mL) triethyl orthoformate (1.3 mL, 7.6 mmol) was added at room temperature. The mixture was heated to reflux at 80 ºC and left for 48 h before being concentrated under reduced pressure. The green-fluorescent solution was concentrated and resulted in a brown oil, which was directly used for the next step. IG (0.75 g, 5 mmol) was added to a previously degassed Shlenk flask containing crude 4-diethoxy-3-cyclobutene-1,2-dione, 9 mL of dry toluene and 0,45 mL of NMP. Finally $Zn(Otf)_2$ (0.36, 1 mmol) was added to the reaction mixture and was heated to reflux and stirred for 24 h under a N_2 atmosphere. The mixture was hot filtered, washed multiple times with hot methanol and concentrated in vacuo. The crude recrystallized in methanol and yielded **H_4L3** as a yellow solid (0.0695 g, mmol, 9%). ^1H NMR (400 MHz, $(CD_3)_2SO$, 25 ºC): δ= 11.51 (s, 2H, COOH), 10.15 (s, 2H, NH), 7.78 (d, *J*= 8.6 Hz, 2H, 7), 7.22 (d, *J*= 1.3 Hz, 2H, 4), 6.93 (dd, *J*= 4, 10 Hz, 2H, 6). ^{13}C NMR (100 MHz, $(CD_3)_2SO$, 25 C): d= 182.18 (9), 171.70 (1), 166.11 (8), 162.59 (3), 144.65 (2), 131.86 (7), 109.74 (6), 107.70 (5), 105.50 (4). FTIR (KBr, cm^{-1}): 3473-3417 (w, ν_{O-H}/ ν_{N-H}), 3296 (w/br, ν_{O-H}), 3084-2860 (w, ν_{C-H}), 1789 (s, $\nu_{C=O}$), 1684-1606 (s, $\nu_{C=O}$/ $\nu_{C=O}$) 1404 (s, δ_{C-O-H}), 1295 - 1173 (s, ν_{C-O}), 957-620 (w, δ_{C-H}). EA for $C_{18}H_{12}N_2O_8$ - calculated (%): 56.26 (C), 3.15 (H), 7.29 (N); EA - found (%): 55.47 (C), 3.54 (H), 7.10 (N).

REFERENCES

[1] W. Li, S. Lv, Y. Wang, L. Zhang, X. Cui, *Sens. Actuators, B* **2019**, *281*, 652.

[2] S. A. Hira, S. Nagappan, D. Annas, Y. A. Kumar, K. H. Park, *Electrochem. Commun.* **2021**, *125*, 107012.

[3] X.-Q. Wu, P.-Q. Feng, Z. Guo, X. Wei, *Langmuir* **2020**, *36*, 14123.

[4] X. Zhao, Y. Zhang, J. Han, H. Jing, Z. Gao, H. Huang, Y. Wang, C. Zhong, *Microporous Mesoporous Mater.* **2018**, *268*, 88.

[5] P. Shi, Y. Zhang, Z. Yu, S. Zhang, *Sci. Rep.* **2017**, *7*, 6500.

[6] Y.-S. Chang, J.-H. Li, Y.-C. Chen, W. H. Ho, Y.-D. Song, C.-W. Kung, *Electrochim. Acta* **2020**, *347*, 136276.

[7] W. Liu, X. Qu, C. Zhu, Y. Gao, C. Mao, J. Song, H. Niu, *Microchim. Acta* **2020**, *187*, 136.

[8] X. Wang, B. Liu, J. Li, Y. Zhai, H. Liu, L. Li, H. Wen, *Electroanalysis* **2021**, *33*, 1484.

[9] C. Feng, S. Dai, L. Wang, *Biosens. Bioelectron.* **2014**, *59*, 64.

[10] S. Carrasco, *Biosensors* **2018**, *8*, 92.

[11] M. Santos-Cancel, L. W. Simpson, J. B. Leach, R. J. White, *ACS Chem. Neurosci.* **2019**, *10*, 2070.

[12] L. Lu, *Biosens. Bioelectron.* **2018**, *110*, 180.

[13] L.-J. Han, Y.-J. Kong, G.-Z. Hou, H.-C. Chen, X.-M. Zhang, H.-G. Zheng, *Inorg. Chem.* **2020**, *59*, 7181.

[14] Y. Li, K. Hu, Y. Yu, S. A. Rotenberg, C. Amatore, M. V. Mirkin, *J. Am. Chem. Soc.* **2017**, *139*, 13055.

[15] X. Fang, B. Zong, S. Mao, *Nano-Micro Lett.* **2018**, *10*, 64.

[16] K. Chen, W. Chou, L. Liu, Y. Cui, P. Xue, M. Jia, *Sensors* **2019**, *19*, 3676.

[17] M. Fumagalli, D. Lecca, M. P. Abbracchio, S. Ceruti, *Front. Pharmacol.* **2017**, 8, 941.

[18] W. L. Nyhan, *Mol. Genet. Metab.* **2005**, *86*, 25.

[19] R. Thangaraj, A. S. Kumar, *Anal. Methods* **2012**, *4*, 2162.

[20] F. Zhang, P. Ma, X. Deng, Y. Sun, X. Wang, D. Song, *Microchim. Acta* **2018**, *185*, 499.

[21] X. L. Jin Jun Luo, *Brain Disord. Ther.* **2013**, *2*, 109.

[22] F. Mazzara, B. Patella, G. Aiello, A. O'Riordan, C. Torino, A. Vilasi, R. Inguanta, *Electrochim. Acta* **2021**, *388*, 138652.
[23] N. Lavanya, C. Sekar, R. Murugan, G. Ravi, *Mater. Sci. Eng., C* **2016**, *65*, 278.
[24] S. Qu, Z. Li, Q. Jia, *ACS Appl. Mater. Interfaces* **2019**, *11*, 34196.
[25] S. Zhou, R. Zuo, Z. Zhu, D. Wu, K. Vasa, Y. Deng, Y. Zuo, *Anal. Methods* **2013**, 5, 1307.
[26] P. Monostori, G. Klinke, J. Hauke, S. Richter, J. Bierau, S. F. Garbade, G. F. Hoffmann, C.-D. Langhans, D. Haas, J. G. Okun, *PLoS One* **2019**, *14*, e0212458.
[27] Y.-p. Sun, J. Chen, H.-y. Qi, Y.-p. Shi, *J. Chromatogr. B* **2015**, *1004*, 53.
[28] X. Lian, B. Yan, *Inorg. Chem.* **2017**, *56*, 6802.
[29] J. M. Amigo, J. Coello, S. Maspoch, *Anal. Bioanal. Chem.* **2005**, *382*, 1380.
[30] L. Liu, L. Liu, Y. Wang, B.-C. Ye, *Talanta* **2019**, *199*, 478.
[31] Y. Wang, L.-l. Tong, *Sens. Actuators, B* **2010**, *150*, 43.
[32] R. Ojani, A. Alinezhad, Z. Abedi, *Sens. Actuators, B* **2013**, *188*, 621.
[33] B. Xu, Q. Song, H. Wang, *Anal. Methods* **2013**, *5*, 2335.
[34] Y. Yang, M. Li, Z. Zhu, *Talanta* **2019**, *201*, 295.
[35] S. Zhu, H. Li, W. Niu, G. Xu, *Biosens. Bioelectron.* **2009**, *25*, 940.
[36] P. Wang, Y. Li, X. Huang, L. Wang, *Talanta* **2007**, *73*, 431.
[37] W. He, Y. Ding, W. Zhang, L. Ji, X. Zhang, F. Yang, *J. Electroanal. Chem.* **2016**, *775*, 205.
[38] N. Lavanya, E. Fazio, F. Neri, A. Bonavita, S. G. Leonardi, G. Neri, C. Sekar, *J. Electroanal. Chem.* **2016**, *770*, 23.
[39] C. Ma, P. Li, L. Xia, F. Qu, R.-M. Kong, Z.-L. Song, *Microchim. Acta* **2021**, *188*, 259.
[40] J. Tang, S. Jiang, Y. Liu, S. Zheng, L. Bai, J. Guo, J. Wang, *Microchim. Acta* **2018**, *185*, 486.
[41] T. S. Thanh, P. T. Qui, N. T. T. Tu, T. T. T. Toan, T. T. B. Hoa, L. V. T. Son, D. M. Nguyen, T. N. Tuyen, D. Q. Khieu, *J. Nanomater.* **2021**, *2021*, 9914062.
[42] N. Setoudeh, S. Jahani, M. Kazemipour, M. M. Foroughi, H. H. Nadiki, *J. Electroanal. Chem.* **2020**, *863*, 114045.
[43] H. T. Ngo, L. T. Hoa, N. T. Khanh, T. T. B. Hoa, T. T. T. Toan, T. X. Mau, N. H. Phong, H. S. Thang, D. Q. Khieu, *J. Nanomater.* **2020**, *2020*, 7915878.
[44] X.-Y. Zhao, Q.-S. Yang, J. Wang, D.-L. Fu, D.-K. Jiang, *Spectrochim. Acta, Part A* **2021**, *262*, 120065.
[45] S. A. Abrori, N. L. W. Septiani, F. N. Hakim, A. Maulana, Suyatman, Nugraha, I. Anshori, B. Yuliarto, *IEEE Sens. J.* **2021**, *21*, 170.
[46] J. Zhang, L. Gao, Y. Zhang, R. Guo, T. Hu, *Microporous Mesoporous Mater.* **2021**, *322*, 111126.
[47] V. K. Sharma, F. Jelen, L. Trnkova, *Sensors* **2015**, *15*, 1564.
[48] O. M. Yaghi, G. Li, Li Hailian, *Nature* **1995**, *378*, 703.

[49] O. M. Yaghi, H. Li, *J. Am. Chem. Soc*. **1995**, *117*, 10401.

[50] B. F. Hoskins, R. Robson, *J. Am. Chem. Soc*. **1990**, *112*, 1546.

[51] X.-L. Tong, H.-L. Lin, J.-H. Xin, F. Liu, M. Li, X.-P. Zhu, *J. Nanomater*. **2013**, *2013*, 616501.

[52] Ü. Kökçam-Demir, A. Goldman, L. Esrafili, M. Gharib, A. Morsali, O. Weingart, C. Janiak, *Chem. Soc. Rev*. **2020**, *49*, 2751.

[53] J. A. Mason, M. Veenstra, J. R. Long, *Chem. Sci*. **2014**, *5*, 32.

[54] H. Wang, Q.-L. Zhu, R. Zou, Q. Xu, *Chem* **2017**, *2*, 52.

[55] Y. Sun, H.-C. Zhou, *Sci. Technol. Adv. Mater*. **2015**, *16*, 054202.

[56] S. Yuan *et al.*, *Adv. Mater*. **2018**, *30*, 1704303.

[57] S.-H. Lo, D. S. Raja, C.-W. Chen, Y.-H. Kang, J.-J. Chen, C.-H. Lin, *Dalt. Trans*. **2016**, *45*, 9565.

[58] W. Lu *et al.*, *Chem. Soc. Rev*. **2014**, *43*, 5561.

[59] D. Sud, G. Kaur, *Polyhedron* **2021**, *193*, 114897.

[60] M. Bláha, V. Valeš, Z. Bastl, M. Kalbá , H. Shiozawa, *J. Phys. Chem. C* **2020**, *124*, 24245.

[61] Y. Cui, Y. Yue, G. Qian, B. Chen, *Chem. Rev*. **2012**, *112*, 1126.

[62] H. Li, L. Li, R.-B. Lin, W. Zhou, Z. Zhang, S. Xiang, B. Chen, *J. Energy Chem* **2019**, *1*, 100006.

[63] J. Lei, R. Qian, P. Ling, L. Cui, H. Ju, *TrAC, Trends Anal. Chem*. **2014**, *58*, 71.

[64] D.-W. Lim, H. Kitagawa, *Chem. Soc. Rev*. **2021**, *50*, 6349.

[65] J. Pei, K. Shao, L. Zhang, H. M. Wen, B. Li, G. Qian, *Top. Curr. Chem*. **2019**, *377*, 33.

[66] D. Yang, B. C. Gates, *ACS Catal*. **2019**, *9*, 1779.

[67] Y. Sun, L. Zheng, Y. Yang, X. Qian, T. Fu, X. Li, Z. Yang, H. Yan, C. Cui, W. Tan, *Nano-Micro Lett*. **2020**, *12*, 103.

[68] F. Ren, P. Ji, *Catalysts* **2020**, *10*, 1441.

[69] R. Ricco, L. Malfatti, M. Takahashi, A. J. Hill, P. Falcaro, *J. Mater. Chem. A* **2013**, *1*, 13033.

[70] Y. Deng, Y. Wu, G. Chen, X. Zheng, M. Dai, C. Peng, *Chem. Eng. J*. **2021**, *405*, 127004.

[71] N. S. Bobbitt, M. L. Mendonca, A. J. Howarth, T. Islamoglu, J. T. Hupp, O. K. Farha, R. Q. Snurr, *Chem. Soc. Rev*. **2017**, *46*, 3357.

[72] H. Furukawa, K. E. Cordova, M. O'Keeffe, O. M. Yaghi, *Science* **2013**, *341*, 1230444.

[73] S. A. A. Razavi, A. Morsali, *Coord. Chem. Rev*. **2019**, *399*, 213023.

[74] L. J. Wang, H. Deng, H. Furukawa, F. Gándara, K. E. Cordova, D. Peri, O. M. Yaghi, *Inorg. Chem.* **2014**, *53*, 5881.

[75] X. Zhang, Z. Zhang, J. Boissonnault, S. M. Cohen, *Chem. Commun*. **2016**, *52*, 8585.

[76] C. Song, J. Hu, Y. Ling, YL. Feng, R. Krishna, D.-l. Chen, Y. He, *J. Mater. Chem. A* **2015**, *3*, 19417.

[77] M. Zhang, B. Li, Y. Li, Q. Wang, W. Zhang, B. Chen, S. Li, Y. Pan, X. You, J. Bai, *Chem. Commun*. **2016**, *52*, 7241.

[78] B. Li, H.-M. Wen, H. Wang, H. Wu, T. Yildirim, W. Zhou, B. Chen, *Energy Environ. Sci*. **2015**, *8*, 2504.

[79] N. H. Alsmail et al., *Chem. Eur. J*. **2014**, *20*, 7317–7324.

[80] B. Zheng, H. Liu, Z. Wang, X. Yu, P. Yi, J. Bai, *CrystEngComm* **2013**, *15*, 3517.

[81] H. Deng *et al*., *Science* **2012**, *336*, 1018.

[82] T. Xiao, D. Liu, *Microporous Mesoporous Mater*. **2019**, *283*, 88.

[83] N. L. Rosi, J. Kim, M. Eddaoudi, B. Chen, M. O'Keeffe, O. M. Yaghi, *J. Am. Chem. Soc*. **2005**, *127*, 1504.

[84] W. L. Queen *et al*., *Chem. Sci*. **2014**, *5*, 4569.

[85] L. Sun, T. Miyakai, S. Seki, M. Dincă, *J. Am. Chem. Soc*. **2013**, *135*, 8185.

[86] D. Britt, H. Furukawa, B. Wang, T. G. Glover, O. M. Yaghi, *PNAS* **2009**, *106*, 20637.

[87] J. H. Choe, H. Kim, C. S. Hong, *Mater. Chem. Front.* **2021**, *5*, 5172.

[88] H. Kim, H. Y. Lee, D. W. Kang, M. Kang, J. H. Choe, W. R. Lee, C. S. Hong, *Inorg. Chem*. **2019**, *58*, 14107.

[89] A. M. Fracaroli, H. Furukawa, M. Suzuki, M. Dodd, S. Okajima, F. Gándara, J. A. Reimer, O. M. Yaghi, *J. Am. Chem. Soc*. **2014**, 136, 8863.

[90] S. R. Caskey, A. G. Wong-Foy, A. J. Matzger, *J. Am. Chem. Soc*. **2008**, *130*, 10870.

[91] V. Stavila, R. K. Bhakta, T. M. Alam, E. H. Majzoub, M. D. Allendorf, *ACS Nano* **2012**, *6*, 9807.

[92] B. T. Nguyen, H. L. Nguyen, T. C. Nguyen, K. E. Cordova, H. Furukawa, *Chem. Mater*. **2016**, *28*, 6243.

[93] Y. B. N. Tran, P. T. K. Nguyen, Q. T. Luong, K. D. Nguyen, *Inorg. Chem*. **2020**, *59*, 16747.

[94] X.-l. Zhang, S.-m. Li, S. Chen, F. Feng, J.-q. Bai, J.-r. Li, *Ecotoxicol. Environ. Saf.* **2020**, *187*, 109821.

[95] Y. Zhang, Y. Hu, G. Li, R. Zhang, *Microchim. Acta* **2019**, *186*, 477.

[96] B. Zhang, P. Huang, J. Chen, X. Dang, Y. Hu, Y. Ai, D. Zheng, H. Chen, *Appl. Surf. Sci*. **2020**, 504, 144504.

[97] L. S. Xie, G. Skorupskii, M. Dincă, *Chem. Rev*. **2020**, *120*, 8536.

[98] E. D. Bloch *et al*., *J. Am. Chem. Soc*. **2011**, *133*, 14814.

[99] M. Märcz, R. E. Johnsen, P. D. C. Dietzel, H. Fjellvåg, *Microporous Mesoporous Mater*. **2012**, *157*, 62.

[100] Q. Wang, F. Wei, D. Manoj, Z. Zhang, J. Xiao, X. Zhao, F. Xiao, H. Wang, S. Wang, *Chem. Commun*. **2019**, *55*, 11307.

[101] D. Zacher, O. Shekhah, C. Wöll, R. A. Fischer, *Chem. Soc. Rev*. **2009**, *38*, 1418.

[102] I. Strauss *et al.*, *ACS Appl. Mater. Interfaces* **2019**, *11*, 14175.
[103] A. A. Talin *et al.*, *Science* **2014**, *343*, 66.
[104] M. G. Campbell, M. Dincă, *Sensors* **2017**, *17*, 1108.
[105] Z. Jia, S. Hao, J. Wen, S. Li, W. Peng, R. Huang, X. Xu, *Microporous Mesoporous Mater.* **2020**, *305*, 110322.
[106] A. Chidambaram, K. C. Stylianou, *Inorg. Chem. Front.* **2018**, *5*, 979.
[107] P. Pashazadeh-Panahi, S. Belali, H. Sohrabi, F. Oroojalian, M. Hashemzaei, A. Mokhtarzadeh, M. de la Guardia, *TrAC, Trends Anal. Chem.* **2021**, *141*, 116285.
[108] D. Yin, J. Liu, X. Bo, M. Li, L. Guo, *Electrochim. Acta* **2017**, *247*, 41.
[109] Z. Zhai, X. Zhang, X. Hao, B. Niu, C. Li, *Adv. Mater. Technol.* **2021**, *6*, 2100127.
[110] Y. Li, A.-S. Xiao, B. Zou, H.-X. Zhang, K.-Le Yan, Y. Lin, *Polyhedron* **2018**, *154*, 83.
[111] X. Wang, L. Zhang, J. Yang, F. Liu, F. Dai, R. Wang, D. Sun, *J. Mater. Chem. A* **2015**, **3**, 12777.
[112] L. Wang, G. Fan, X. Xu, D. Chen, L. Wang, W. Shi, P. Cheng, *J. Mater. Chem. A* **2017**, *5*, 5541.
[113] L. Li, Q. Chen, Z. Niu, X. Zhou, T. Yang, W. Huang, *J. Mater. Chem. C* **2016**, *4*, 1900.
[114] P. Xing, D. Wu, J. Chen, J. Song, C. Mao, Y. Gao, H. Niu, *Analyst* **2019**, *144*, 2656.
[115] C. Wang, L. Tian, W. Zhu, S. Wang, P. Wang, Y. Liang, W. Zhang, H. Zhao, G. Li, *ACS Appl. Mater. Interfaces* **2017**, *9*, 20076.
[116] M. D. Allendorf, A. Schwartzberg, V. Stavila, A. A. Talin, *Chem. Eur. J.* **2011**, *17*, 11372.
[117] A. Bétard, R. A. Fischer, *Chem. Rev.* **2012**, *112*, 1055.
[118] X. Ma, Y. Chai, P. Li, B. Wang, *Acc. Chem. Res.* **2019**, *52*, 1461.
[119] H. Al-Kutubi, J. Gascon, E. J. R. Sudhölter, L. Rassaei, *ChemElectroChem* **2015**, *2*, 462.
[120] Y. Zhang, C.-H. Chang, *Processes* **2020**, *8*, 377.
[121] M. V. Varsha, G. Nageswaran, *J. Electrochem. Soc.* **2020**, *167*, 155527.
[122] W.-J. Li, M. Tu, R. Cao, R. A. Fischer, *J. Mater. Chem. A* **2016**, *4*, 12356.
[123] L.-T. Zhang, Y. Zhou, S.-T. Han, *Angew. Chem. Int. Ed.* **2021**, *133*, 15320.
[124] S. Xie, W. Monnens, K. Wan, W. Zhang, W. Guo, MW. Xu, I. F. J. Vankelecom, X. Zhang, J. Fransaer, *Angew. Chem. Int. Ed.* **2021**, *60*, 24950.
[125] U. Mueller, M. Schubert, F. Teich, H. Puetter, K. Schierle-Arndt, J. Pastré, *J. Mater. Chem.* **2006**, *16*, 626.
[126] M. Li, M. Dincă, *J. Am. Chem. Soc.* **2011**, *133*, 12926.
[137] M. Li, M. Dincă, *Chem. Sci.* **2014**, *5*, 107.
[128] Y. Xiao, Z. Wu, Q. Zhang, P. Li, H. Yu, G. Lu, *Cryst. Growth Des.* **2020**, *20*, 3997.
[129] L. Ji, J. Wang, K. Wu, N. Yang, *Adv. Funct. Mater.* **2018**, *28*, 1706961.
[130] D. Li, X. Cao, Q. Zhang, X. Ren, L. Jiang, D. Li, W. Deng, H. Liu, *J. Mater. Chem. A* **2019**, *7*, 14108.

[131] L. Ji, J. Hao, K. Wu, N. Yang, *J. Phys. Chem. C* **2019**, *123*, 2248.

[132] H. Liu, H. Wang, T. Chu, M. Yu, Y. Yang, *J. Mater. Chem. C* **2014**, *2*, 8683.

[133] M. Naseri, L. Fotouhi, A. Ehsani, S. Dehghanpour, *J. Colloid Interface Sci*. **2016**, *484*, 314.

[134] S. Grunder, C. Valente, A. C. Whalley, S. Sampath, J. Portmann, Y. Y. Botros, J. F. Stoddart, *Chem. Eur. J.* **2012**, *18*, 15632.

[135] L.-K. Wang, J.-J. Zhou, Y.-B. Lan, S.-Y. Ding, W. Yu, W. Wang, *Angew. Chem. Int. Ed*. **2019**, *58*, 9443.

[136] Q.-Y. Li, Y-.A. Li, Q. Guan, W.-Y. Li, X.-J. Dong, Y.-B. Dong, *Inorg. Chem*. **2019**, *58*, 9890.

[137] K. Oisaki, Q. Li, H. Furukawa, A. U. Czaja, O. M. Yaghi, *J. Am. Chem. Soc*. **2010**, *132*, 9262.

[138] T. L. Tam, H. H. R. Tan, W. Ye, S. G. Mhaisalkar, A. C. Grimsdale, *Org. Lett*. **2012**, *14*, 532.

[139] T. L. Tam, H. Li, F. Wei, K. J. Tan, C. Kloc, Y. M. Lam, S. G. Mhaisalkar, A. C. Grimsdale, *Org. Lett*. **2010**, *12*, 3340.

[140] S. M. Cohen, Z. Zhang, J. A. Boissonnault, *Inorg. Chem*. **2016**, *55*, 7281.

[141] L. Zhao, C. Hu, X. Cong, G. Deng, L. L. Liu, M. Luo, X. Zeng, *J. Am. Chem. Soc*. **2021**, *143*, 1618.

[142] P. Ryan, Y. Shi, M. von Itzstein, S. Rudrawar, *Bioorg. Chem*. **2021**, *110*, 104738.

[143] A. Connell, P. J. Holliman, E. W. Jones, L. Furnell, C. Kershaw, M. L. Davies, C. D. Gwenin, M. B. Pitak, S. J. Coles, G. Cooke, *J. Mater. Chem. A* **2015**, *3*, 2883.

[144] T. Baba, T. Matsui, K. Kamiya, M. Nakano, Y. Shigeta, *Int. J. Quantum Chem*. **2014**, *114*, 1128.

[145] S. Maheshwari, A. Chowdhury, N. Sathyamurthy, H. Mishra, H. B. Tripathi, M. Panda, J. Chandrasekhar, *J. Phys. Chem. A* **1999**, *103*, 6257.

[146] X.-Y. Zhao, H. Yang, W.-Y. Zhao, J. Wang, Q.-S. Yang, *Dalt. Trans*. **2021**, *50*, 1300.

[147] G. Accardo, R. Cioffi, F. Colangelo, R. d'Angelo, L. De Stefano, F. Paglietti, *Materials* **2014**, *7*, 457.

[148] A. P. G. Carvalho, E. C. B. A. Alegria, A. Fantoni, A. M. Ferraria, A. M. B. do Rego, A. P. C. Ribeiro, *Biosensors* **2022**, *12*, 163.

[149] G. Beamson, D. Briggs, *High Resolution XPS of Organic Polymers: The Scienta Esca300 Database*, Wiley, Chichester, England, **1992**.

[150] NIST, "NIST X-ray Photoelectron Spectroscopy (XPS) Database", can be found under https://srdata.nist.gov/xps/main_search_menu.aspx, **2000**.

[151] Z. Jia, S. Hao, J. Wen, S. Li, W. Peng, R. Huang, X. Xu, *Microporous Mesoporous Mater*. **2020**, *305*, 110322.

[152] W. Wu, G. E. Decker, A. E. Weaver, A. I. Arnoff, E. D. Bloch, J. Rosenthal, *ACS Cent. Sci*. **2021**, *7*, 1427.

[153] J. Zhong, Y. Zeng, Z. Yin, M. Zhang, D. Yan, Z. Su, P. Chen, M. Fu, D. Ye, *J. Mater. Chem. A* **2021**, *9*, 6890.

[154] C. E. Housecroft, A. G. Sharpe, *Inorganic Chemistry*, Pearson, Harlow, England, **2012**.

[155] C. Guo, Y. Zhang, Y. Guo, L. Zhang, Y. Zhang, J. Wang, *Chem. Commun*. **2018**, *54*, 252.

[156] L. Garzón-Tovar, A. Carné-Sánchez, C. Carbonell, I. Imaz, D. Maspoch, *J. Mater. Chem. A* **2015**, *3*, 20819.

[157] A. Tayal *et al.*, *Inorg. Chem*. **2018**, *57*, 10072.

[158] J. Cai, Y. Li, M. Zhang, Z. Li, *Inorg. Chem*. **2019**, *58*, 7997.

[159] M. Li, M. Dincă, *Chem. Mater*. **2015**, *27*, 3203.

[160] D. Li, A. Levesque, A. Franczak, Q. Wang, J. He, J.-P. Chopart, *Talanta* **2013**, *110*, 66.

[161] K. Kołodziejczyk, E. Mi ko , M. Zieli ski, M. Jaksender, D. Szczukocki, K. Czarny, B. Krawczyl, *J. Solid State Electrochem.* **2018**, *22*, 1629.

[162] R. S. Forgan*, Chem. Sci.* **2020**, *11*, 4546.

[163] W. L. F. Armarego, D. D. Perin, *Purification of Laboratory Chemicals*, Butterworth-Heinemann, Oxford, England, **1996**.

A

ANNEXES

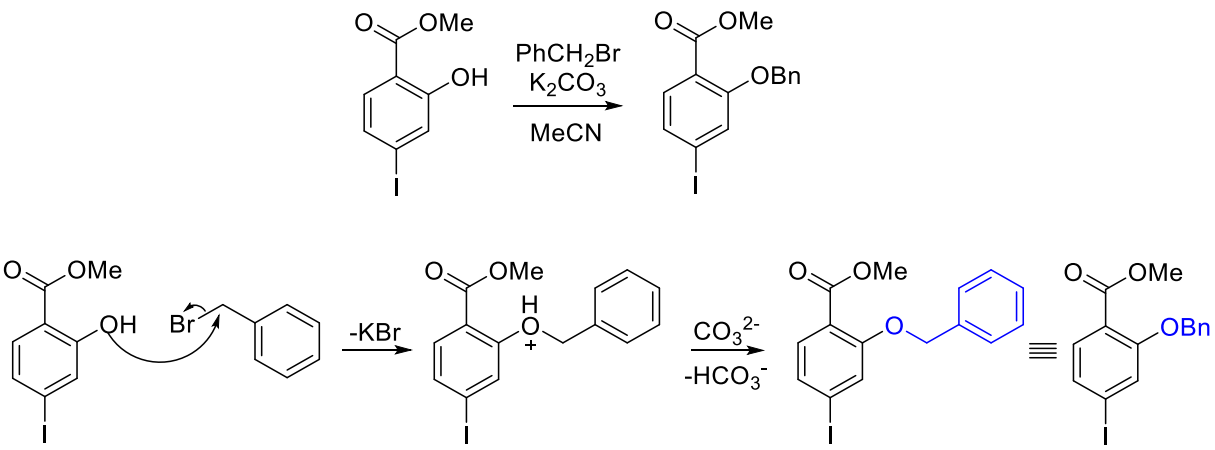

Scheme A.1 - Suggested reaction mechanism to obtain **IA**.

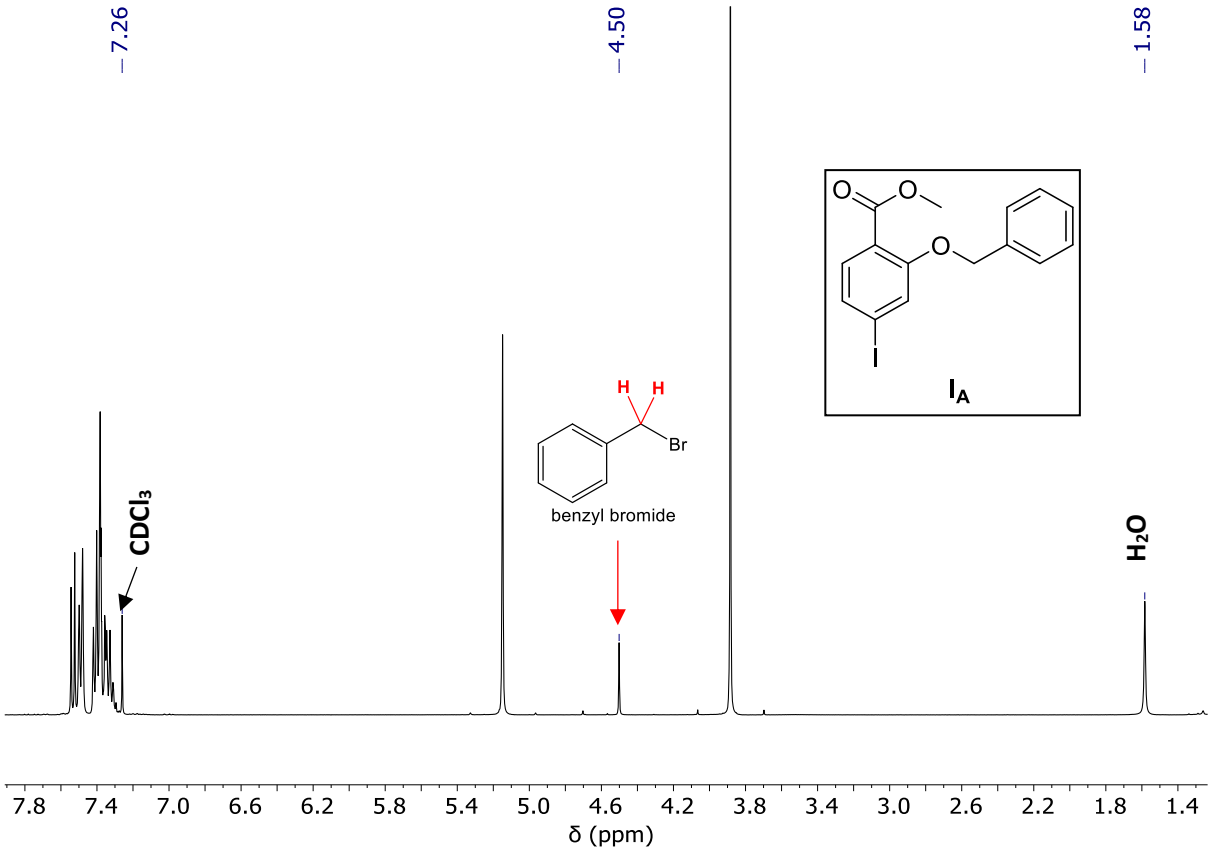

Figure A.1 - ^{1}H NMR spectrum of **I_A** reaction crude in $CDCl_3$.

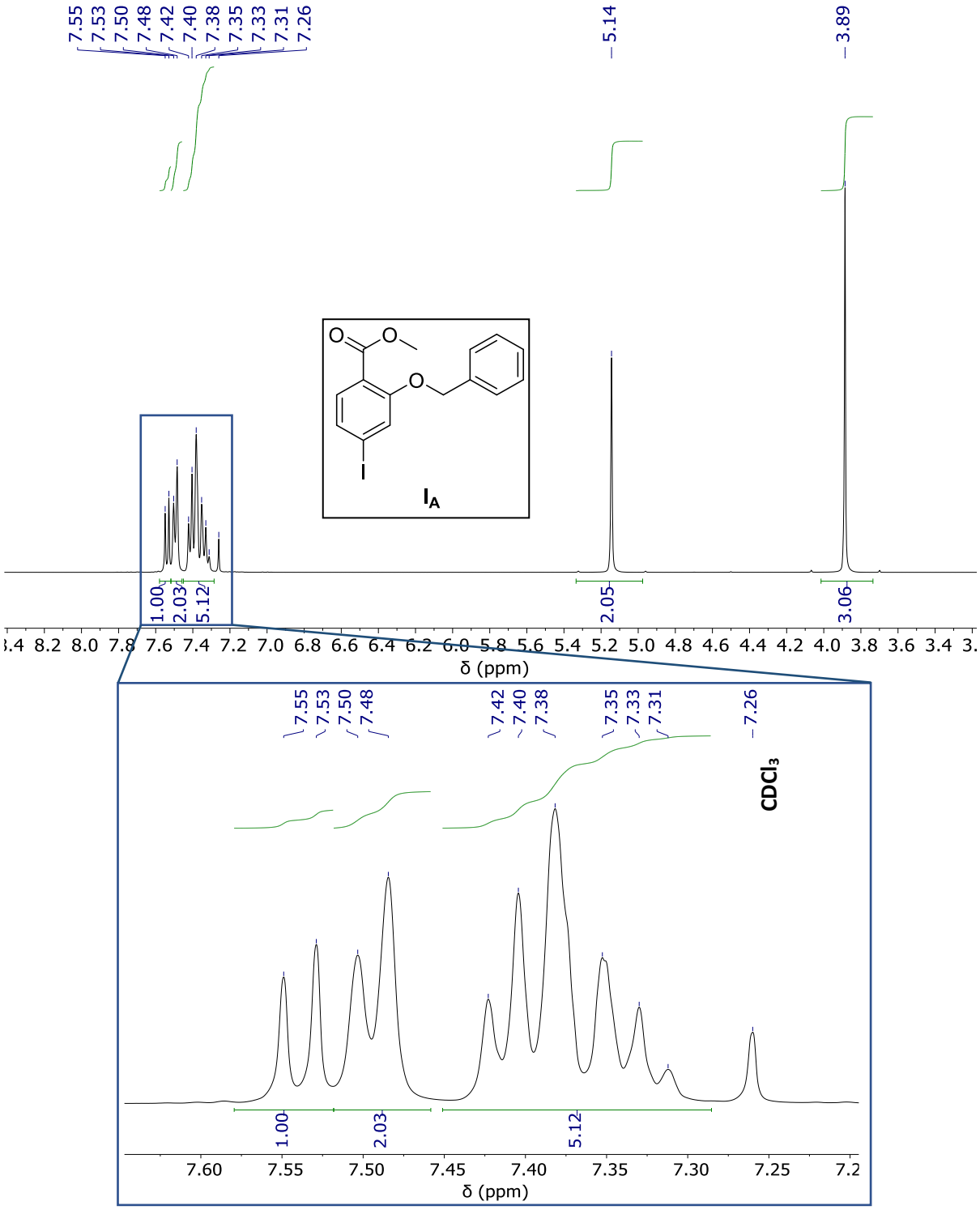

Figure A.2 - ^{1}H NMR spectrum of **I_A** Intermediate in $CDCl_3$.

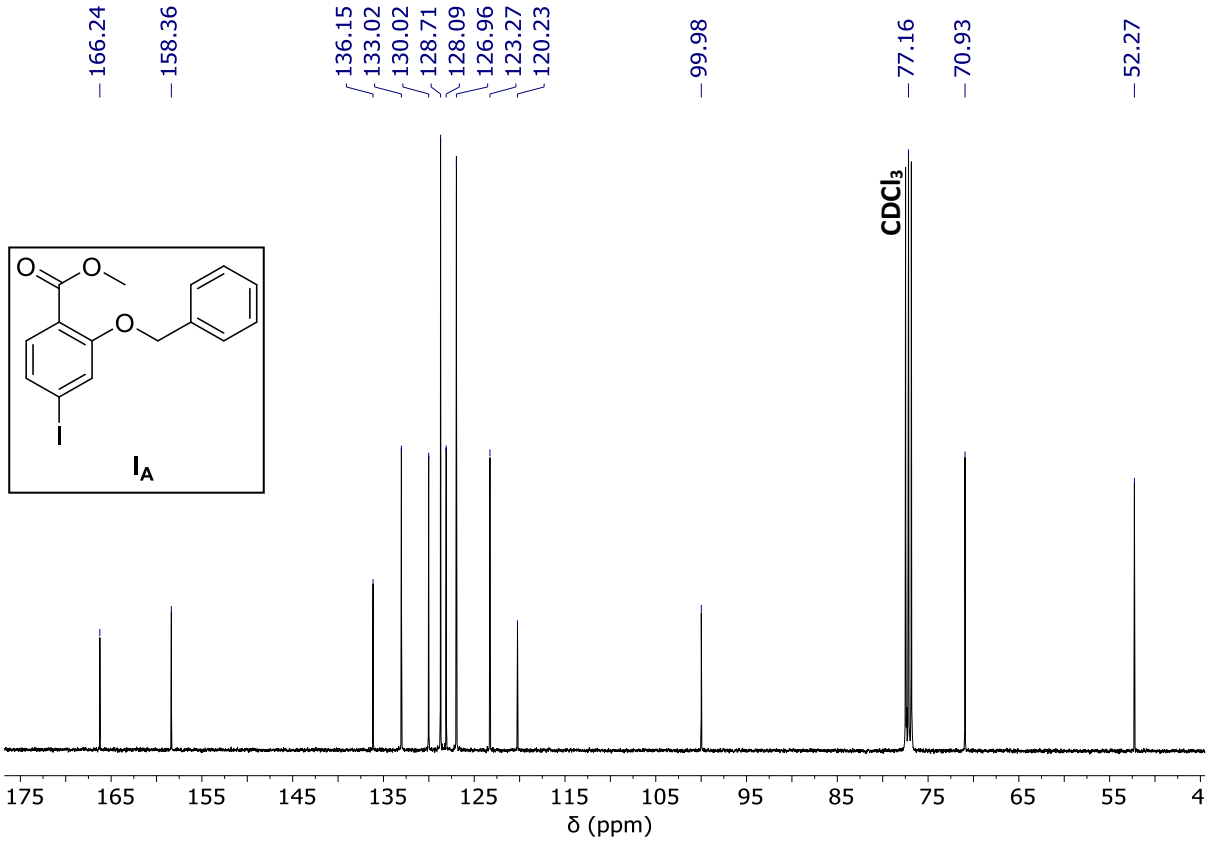

Figure A.3 - ^{13}C NMR spectrum of **I_A** intermediate in $CDCl_3$.

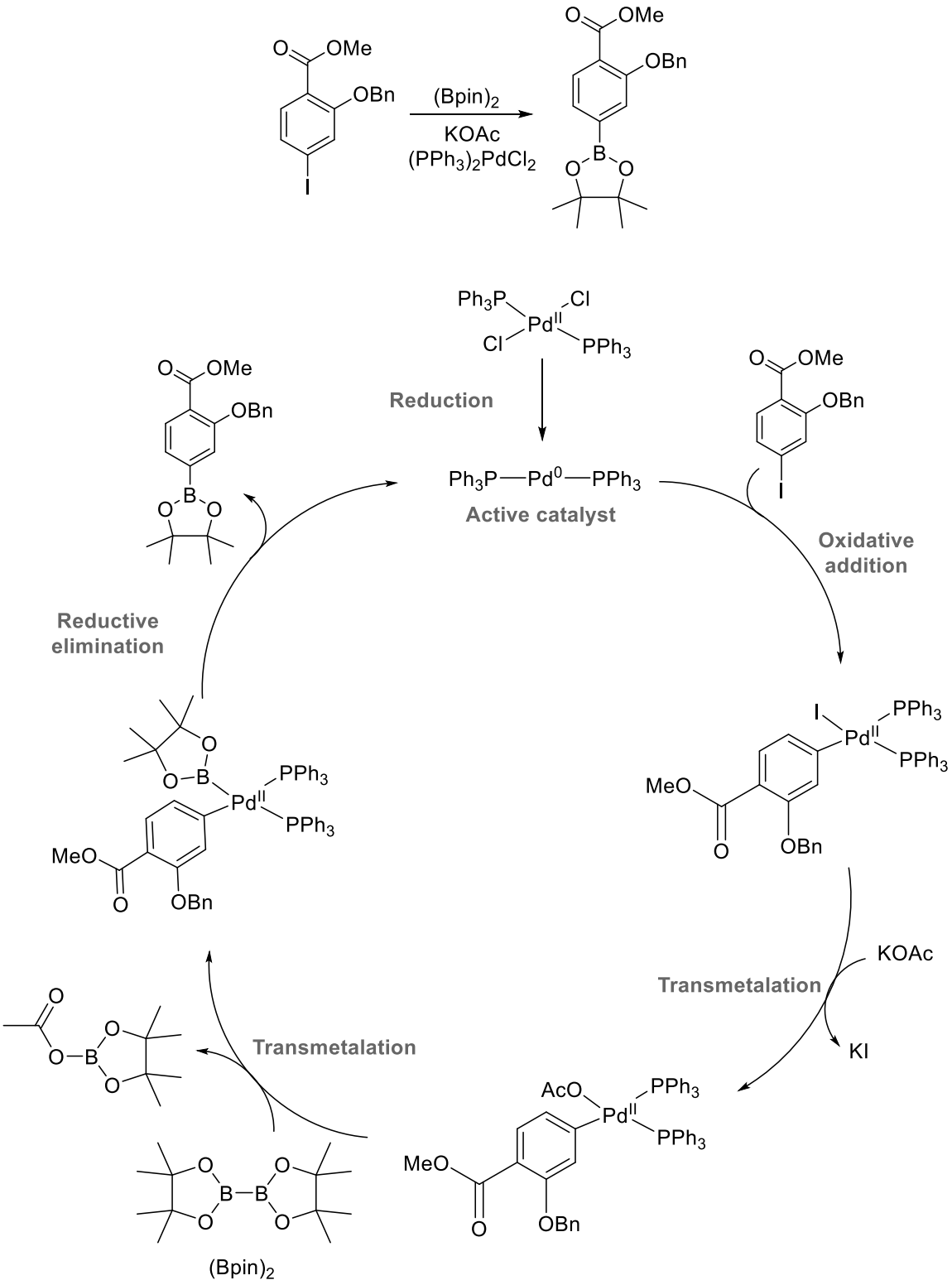

Scheme A.2 - Suggested mechanism to obtain **IB**.

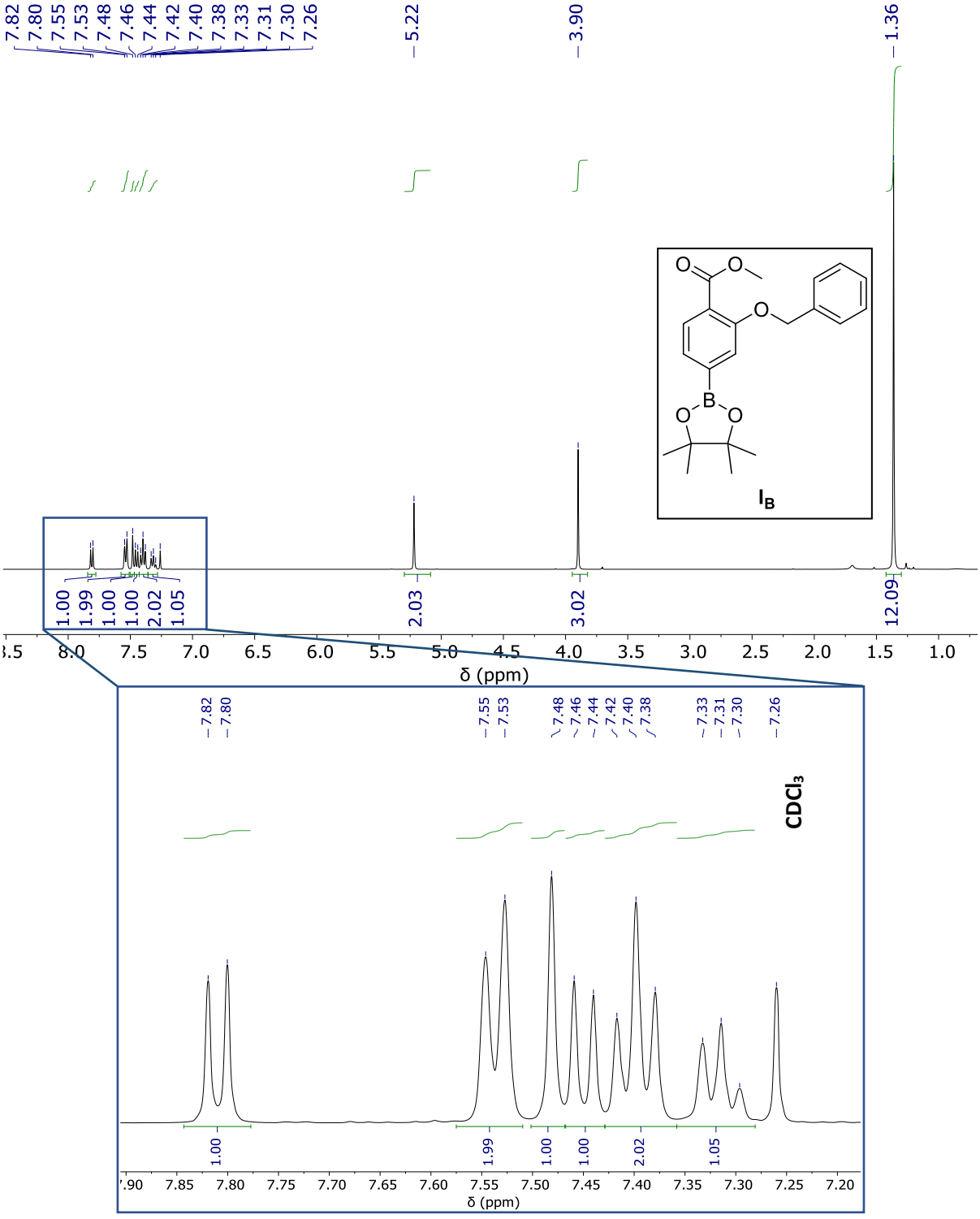

Figure A.4 - ^{13}C NMR spectrum of I_B intermediate in $CDCl_3$.

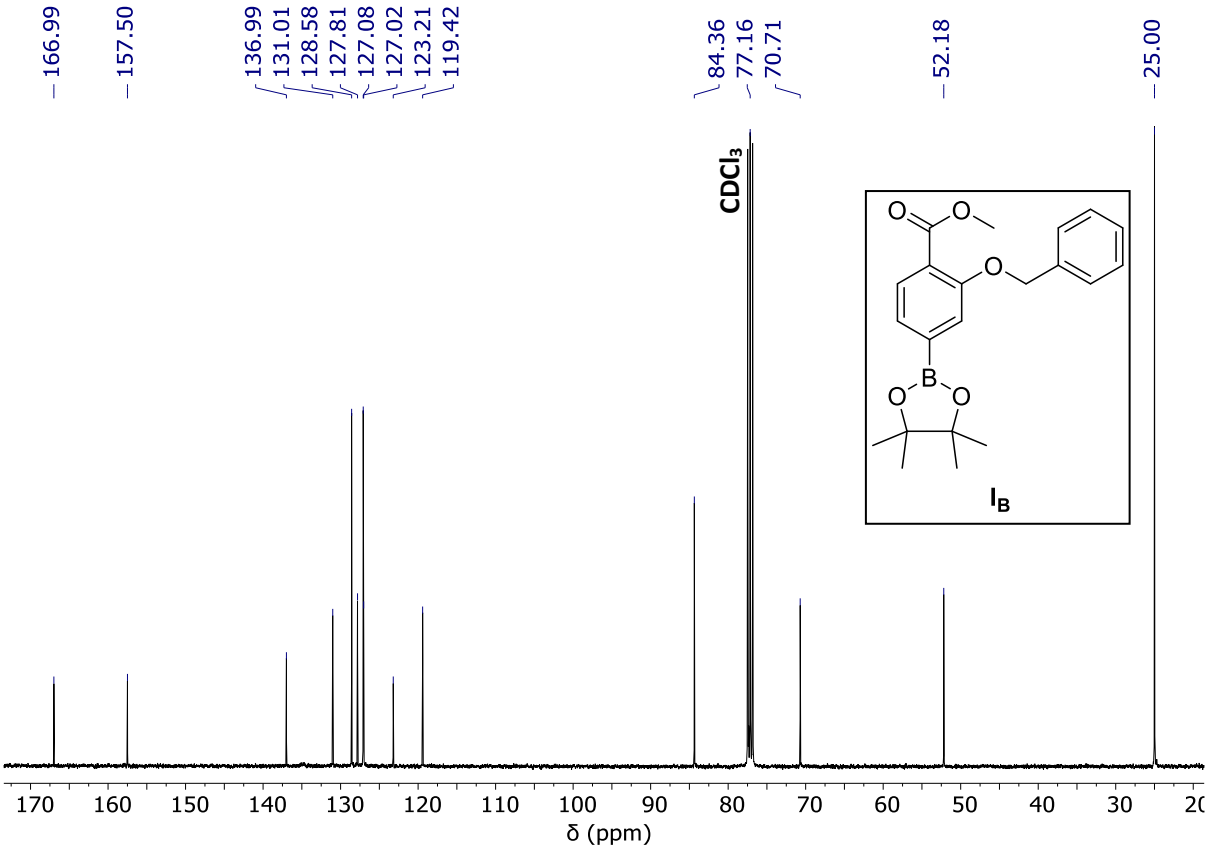

Figure A.5 - ^{13}C NMR spectrum of **I_B** intermediate in $CDCl_3$.

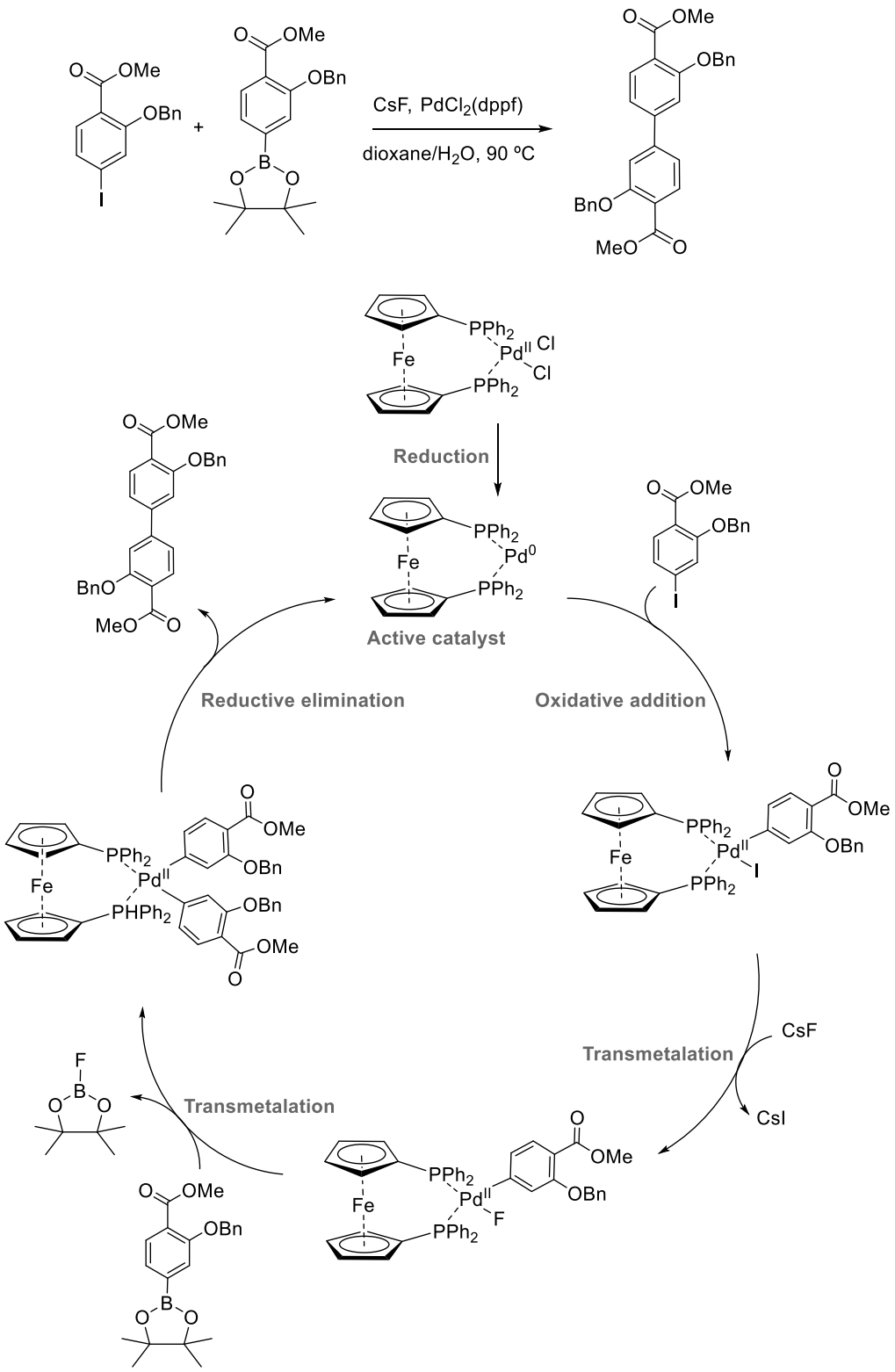

Scheme A.3 - Suggested mechanism to obtain **Ic**.

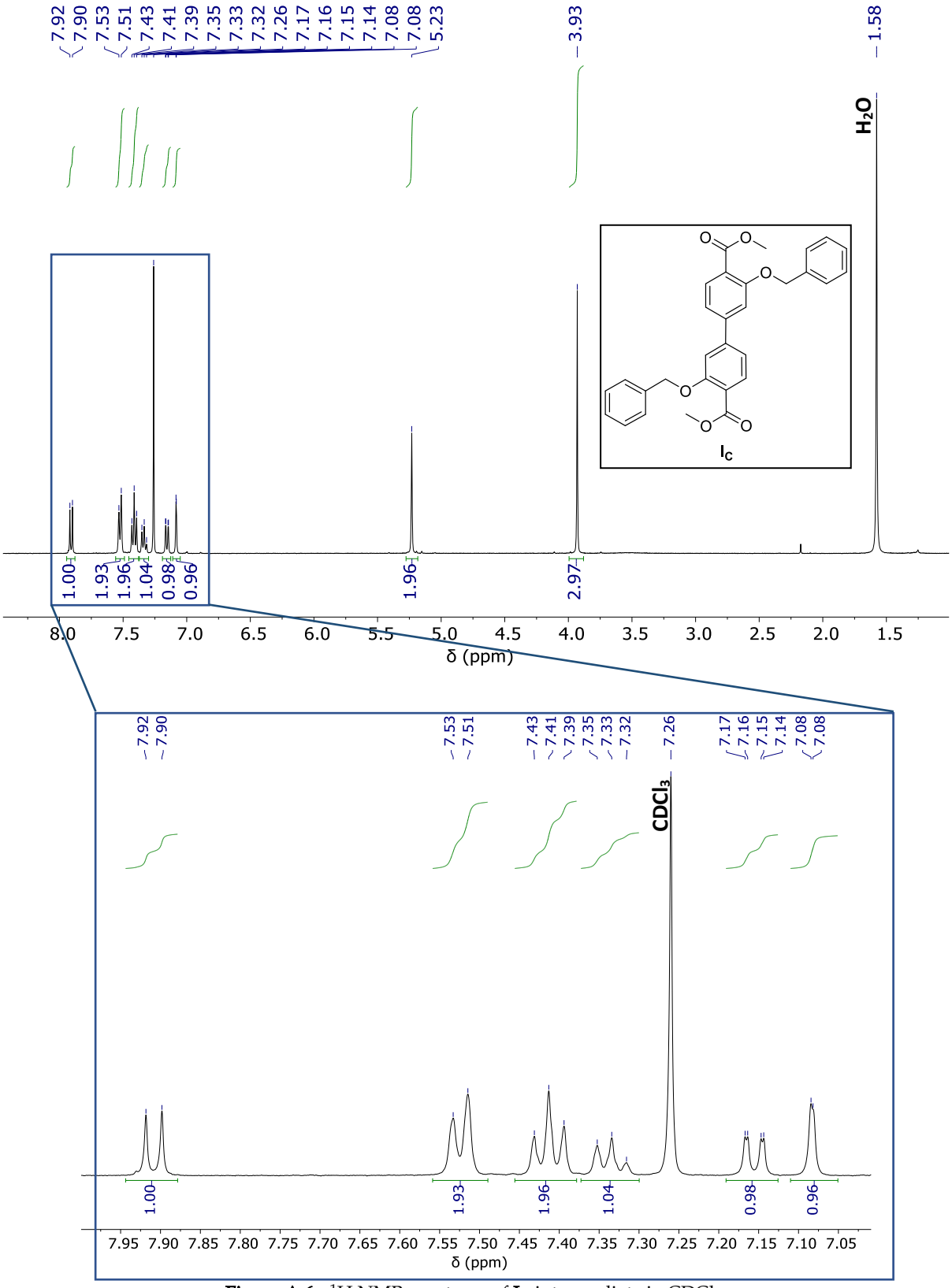

Figure A.6 - ^{1}H NMR spectrum of **Ic** intermediate in $CDCl_3$.

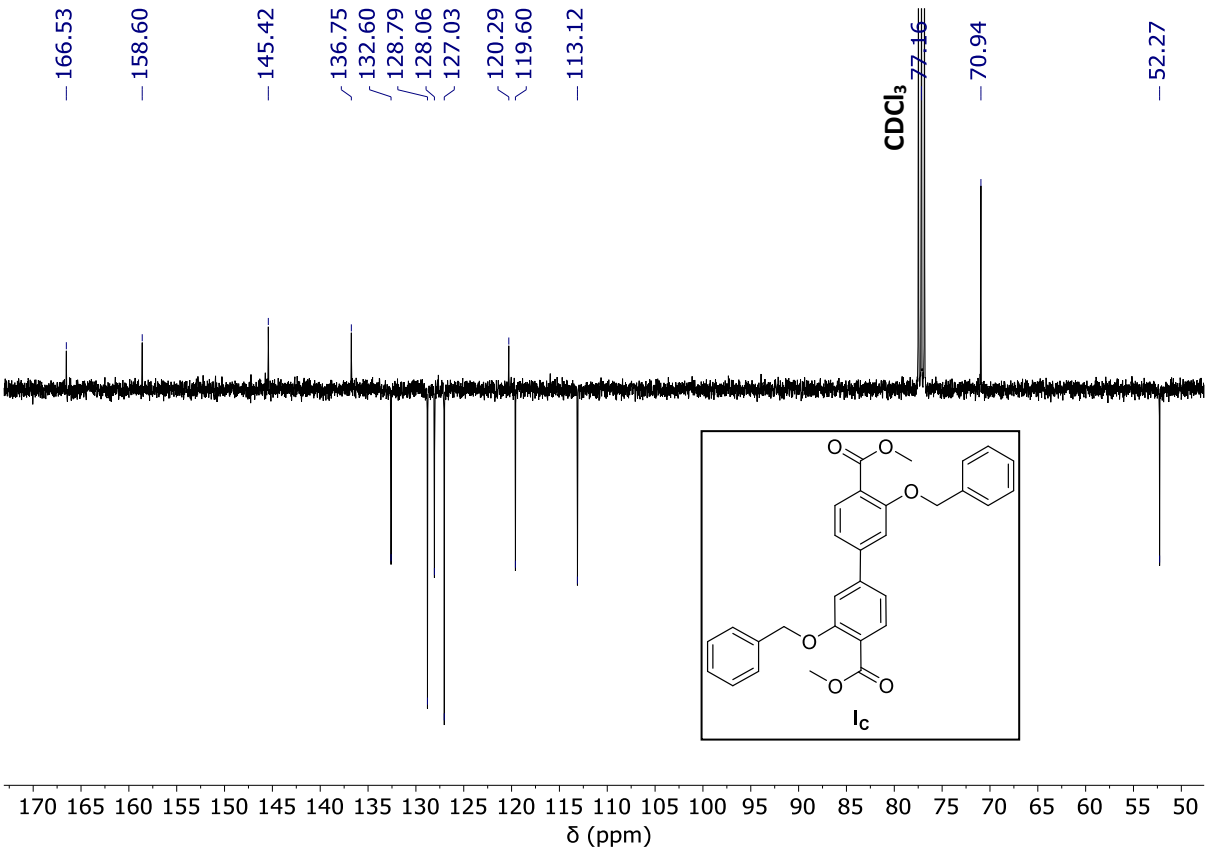

Figure A.7 - ^{13}C APT NMR spectrum of **Ic** intermediate in $CDCl_3$.

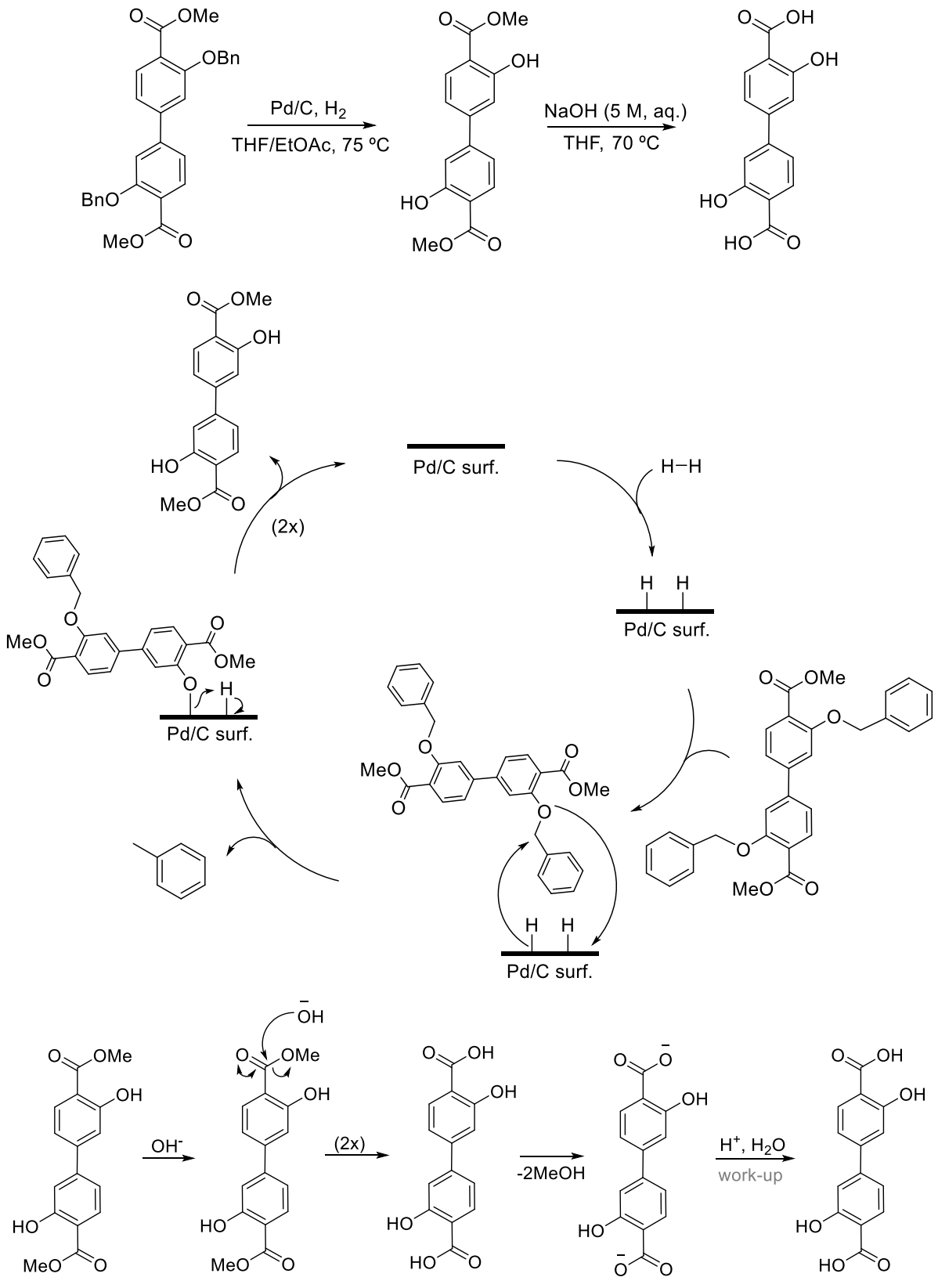

Scheme A.4 - Suggested mechanisms to obtain **H_4L1**.

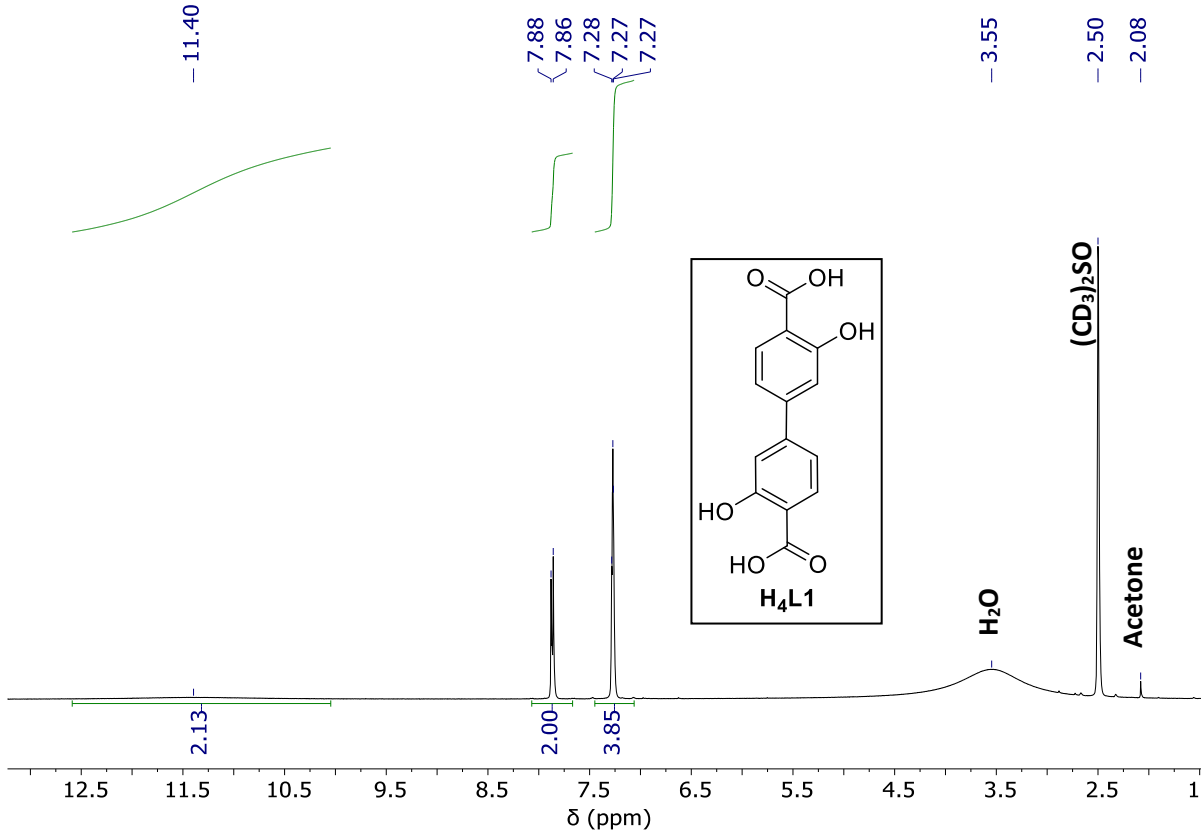

Figure A.8 - ^{1}H NMR spectrum of **H_4L1** intermediate in $(CD_3)_2SO$.

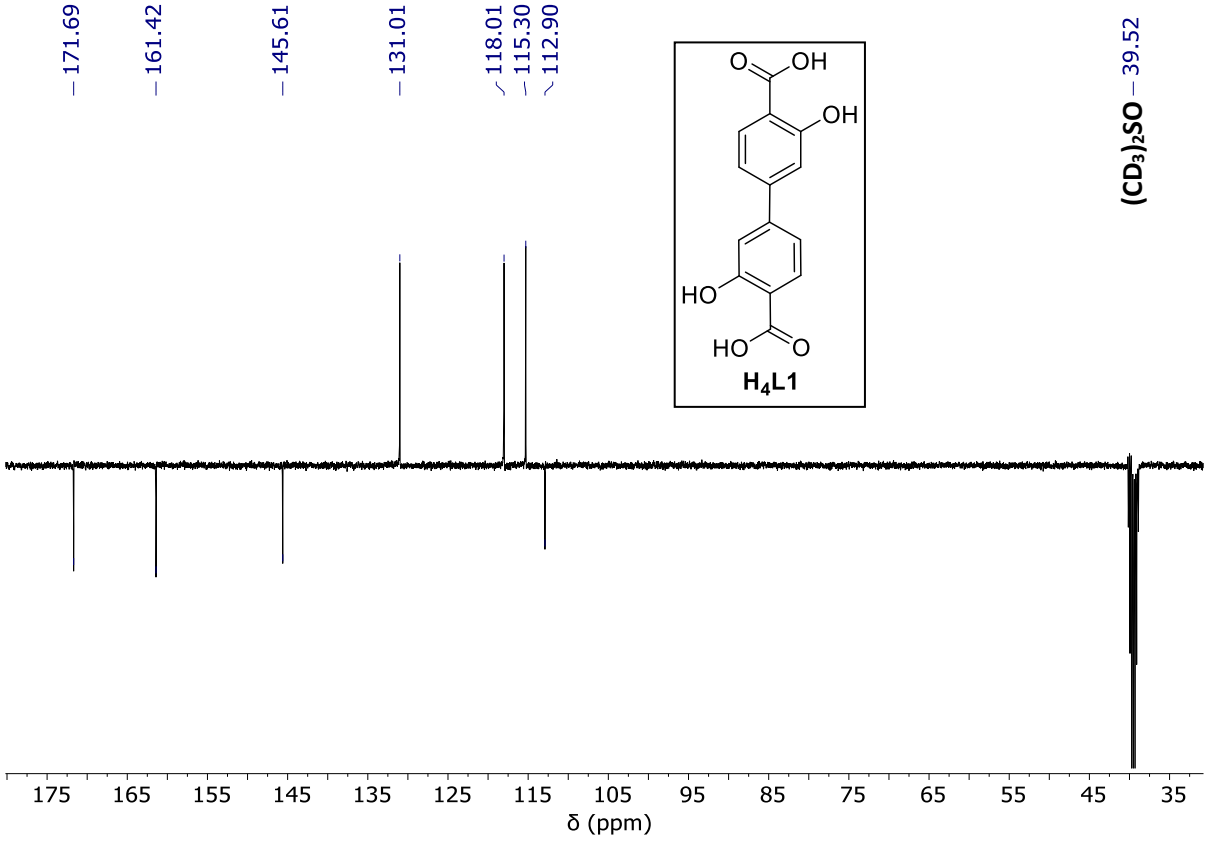

Figure A.9 - ^{13}C APT NMR spectrum of **H_4L1** intermediate in $(CD_3)_2SO$.

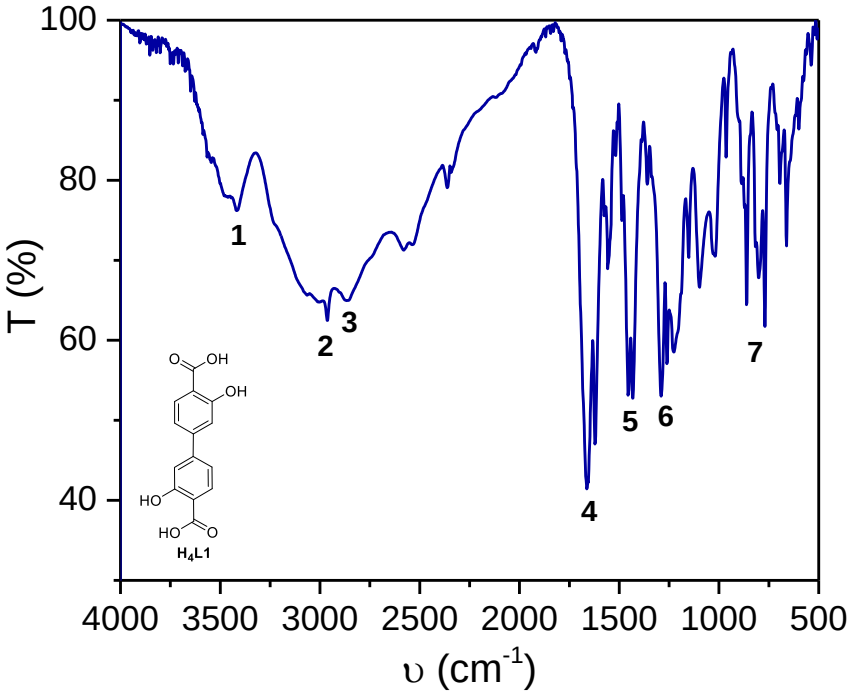

Figure A.10 - FTIR spectrum of **H_4L1** in KBr pellets. Spectrum was recorded in a range of 4000-500 cm^{-1}.

Table A.1 - H_4L1 FTIR spectrum bands attribution.

		FTIR (KBr pellets)	
Band/group	**(cm^{-1})**	**Intensity**	**Bond/functional group**
1	3417	w	ν_{O-H} (phenol)
2	3011	w, br	ν_{O-H} (acid)
3	2959	w	ν_{C-H} (aromatic)
4	1667-1619	s	$\nu_{C=O}$
5	1453-1462	s	δ_{C-O-H} (acid)
6	1291-1222	s	ν_{C-O} (phenol/acid)
7	1095-770	m	δ_{C-H} (aromatic)

Legend: s-strong, m-medium, w-weak, br- broad

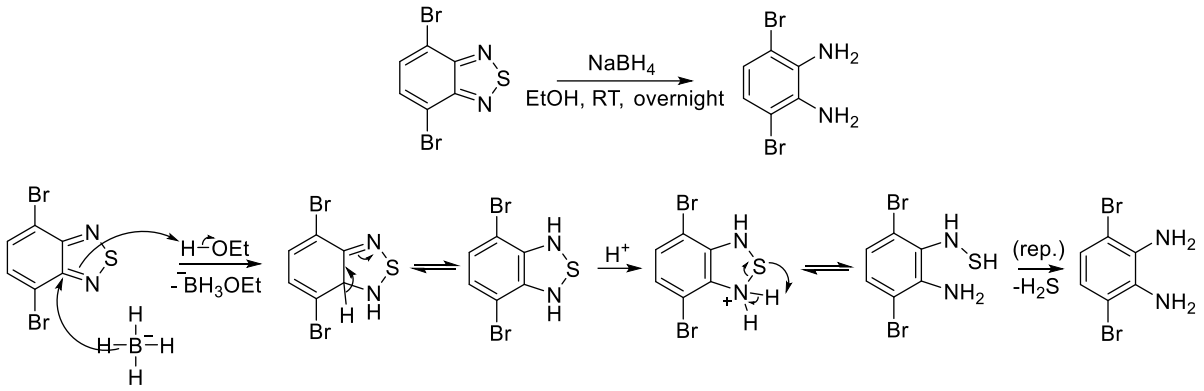

Scheme A.5 - Suggested mechanisms to obtain I_D.

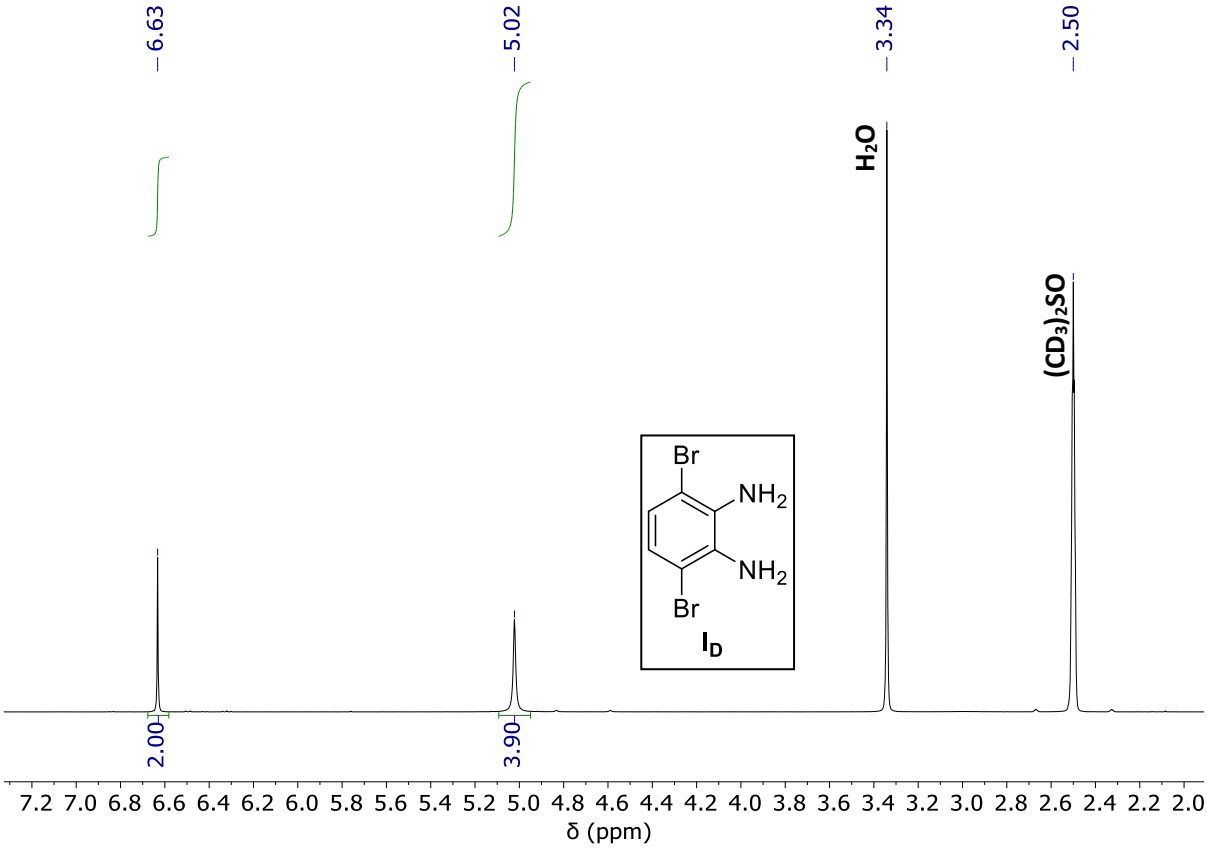

Figure A.11 - ^{1}H NMR spectrum of I_D intermediate in $(CD_3)_2SO$.

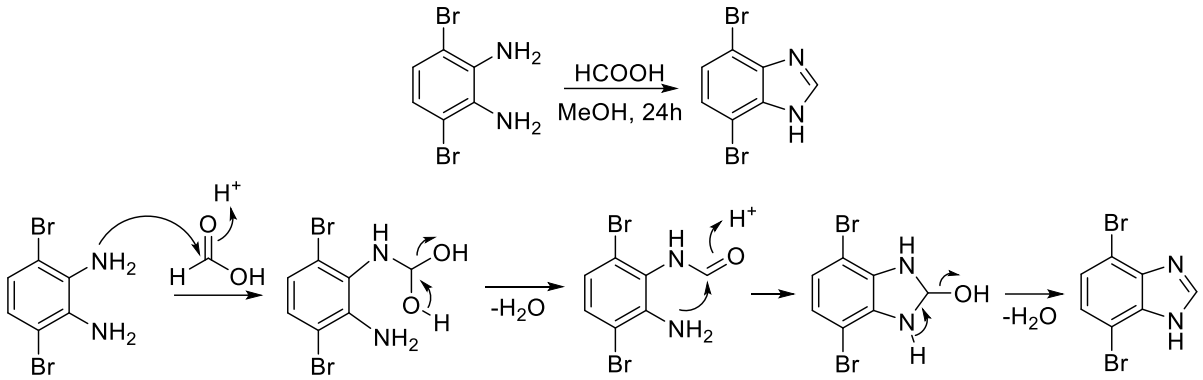

Scheme A.6 - Suggested mechanisms to obtain I_E.

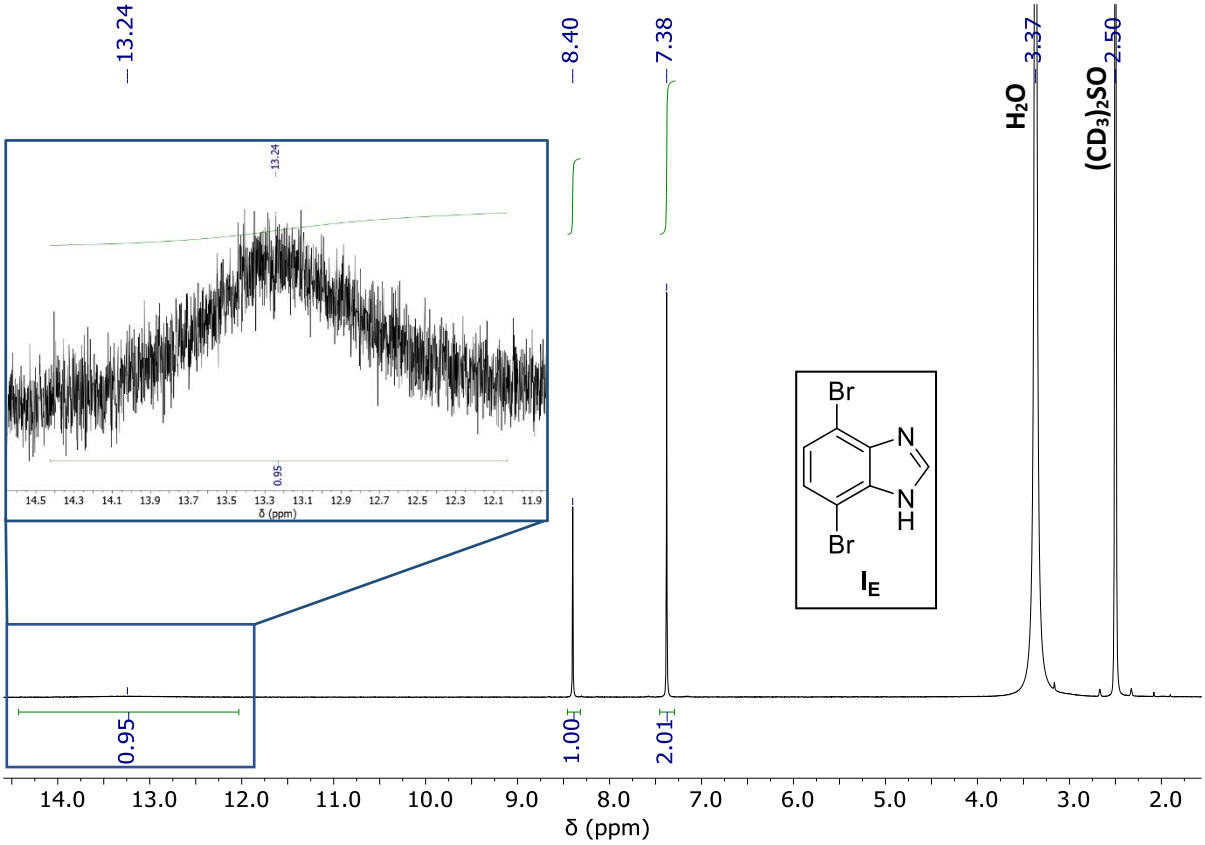

Figure A.12 - ^{1}H NMR spectrum of I_E in $(CD_3)_2SO$.

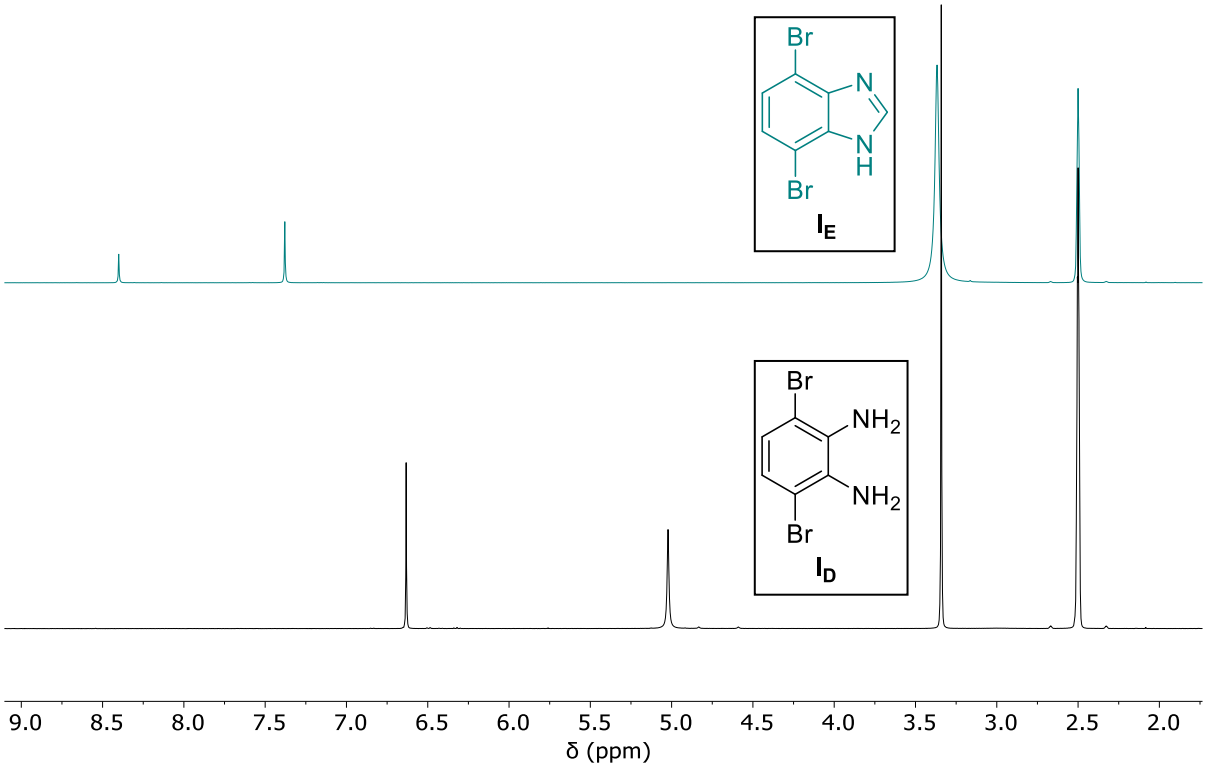

Figure A.13 - ^{1}H NMR spectra of I_E (**turquoise**) and I_D (**black**) in $(CD_3)_2SO$.

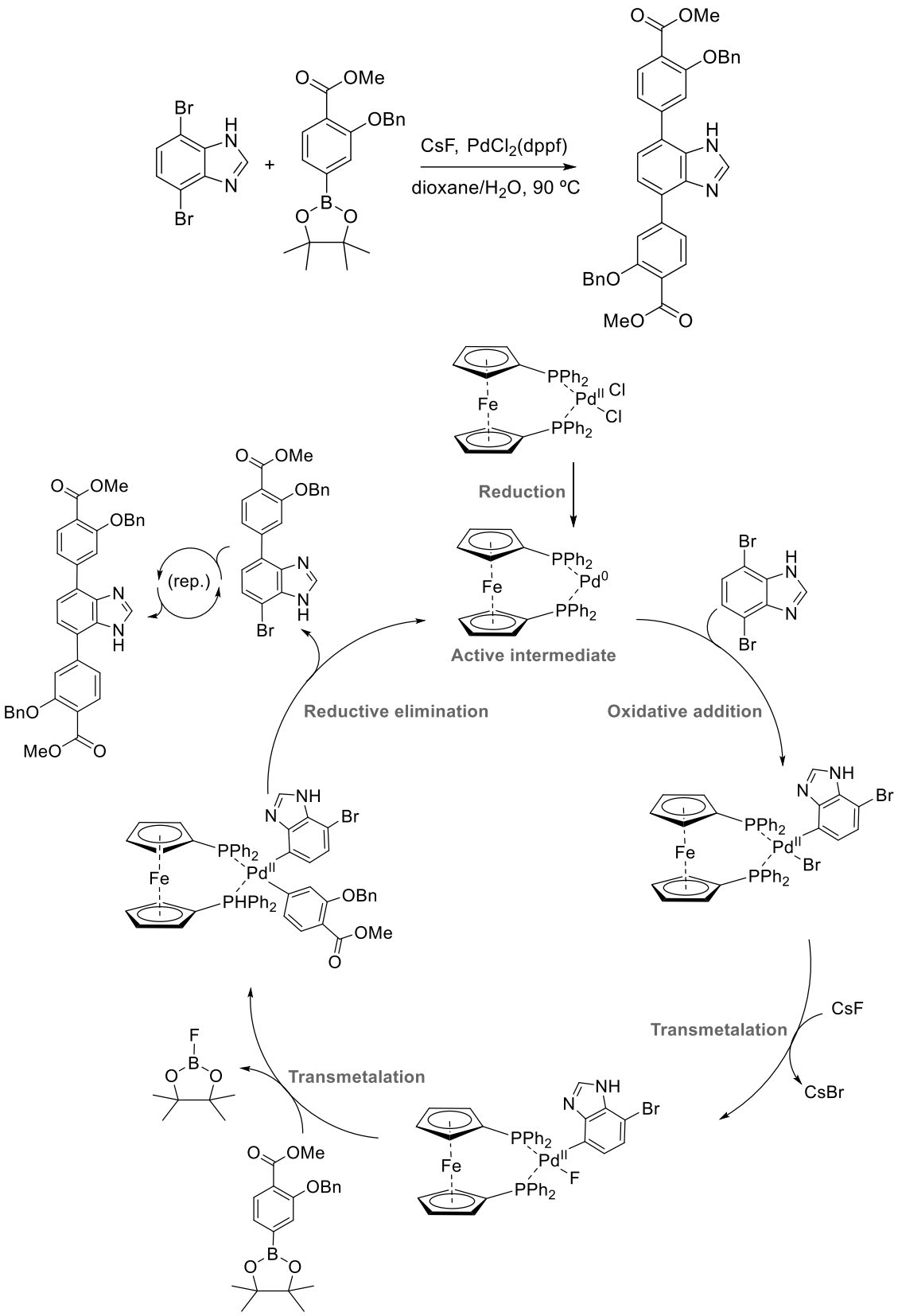

Scheme A.7 - Suggested mechanisms to obtain **IF**.

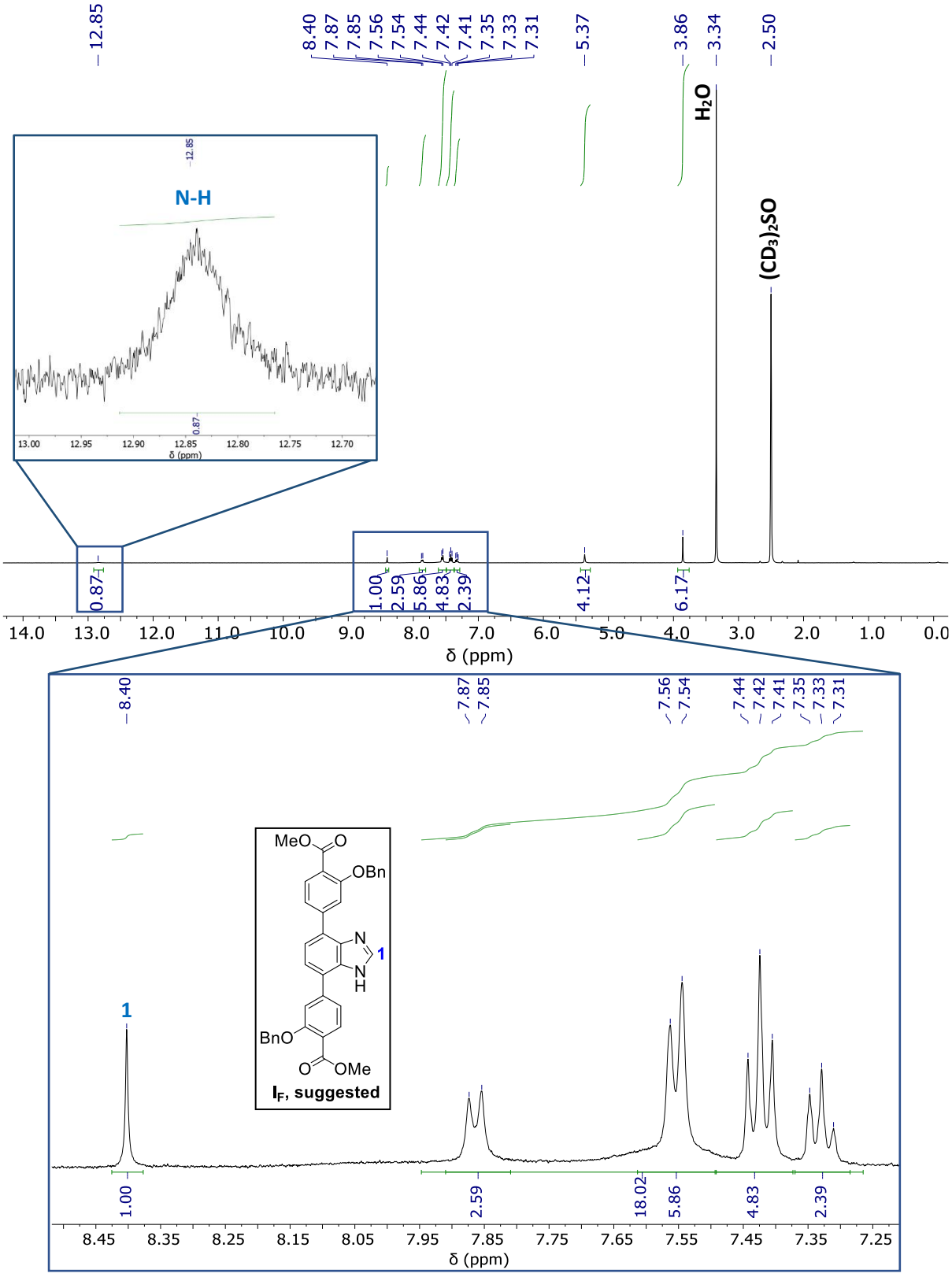

Figure A.14 - ^{1}H NMR spectrum of $\mathbf{I_E}$ intermediate in $(CD_3)_2SO$.

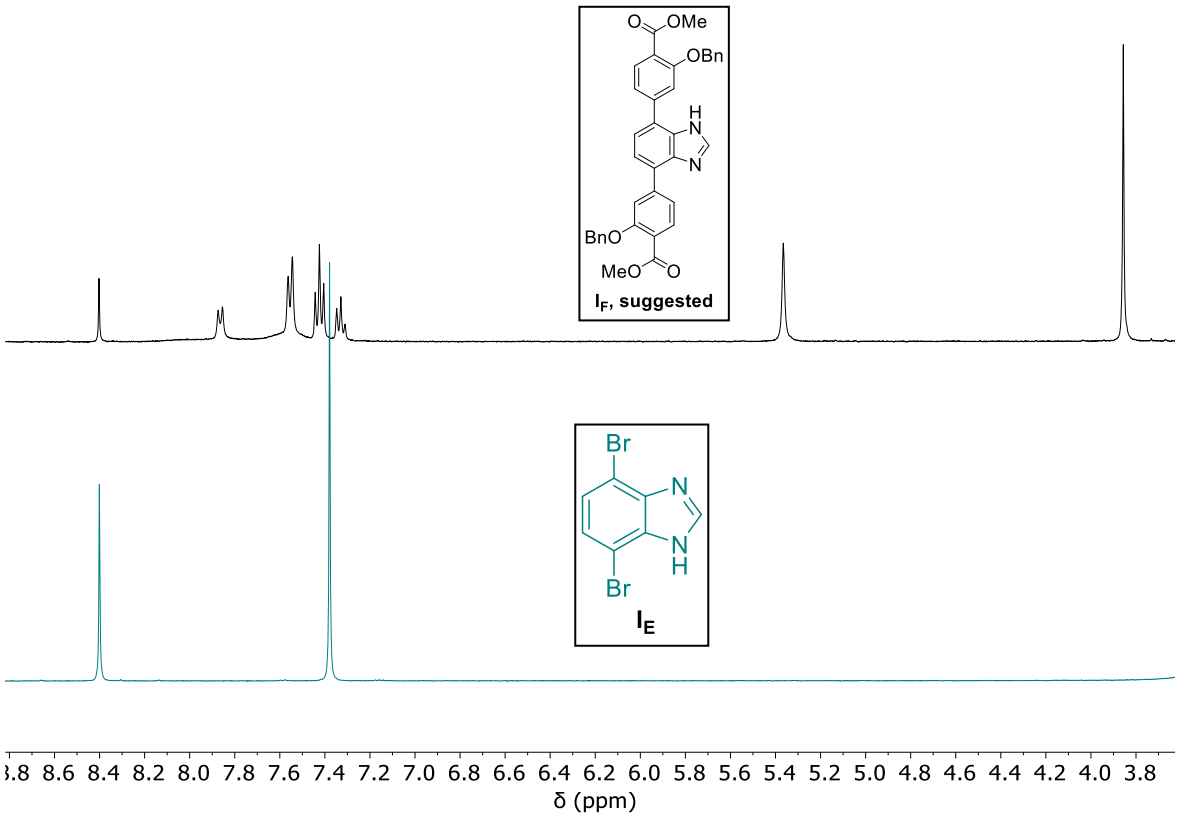

Figure A.15 - ^{1}H NMR superposed spectra of I_F (**black**) and I_E (**turquoise**) intermediate in $(CD_3)_2SO$.

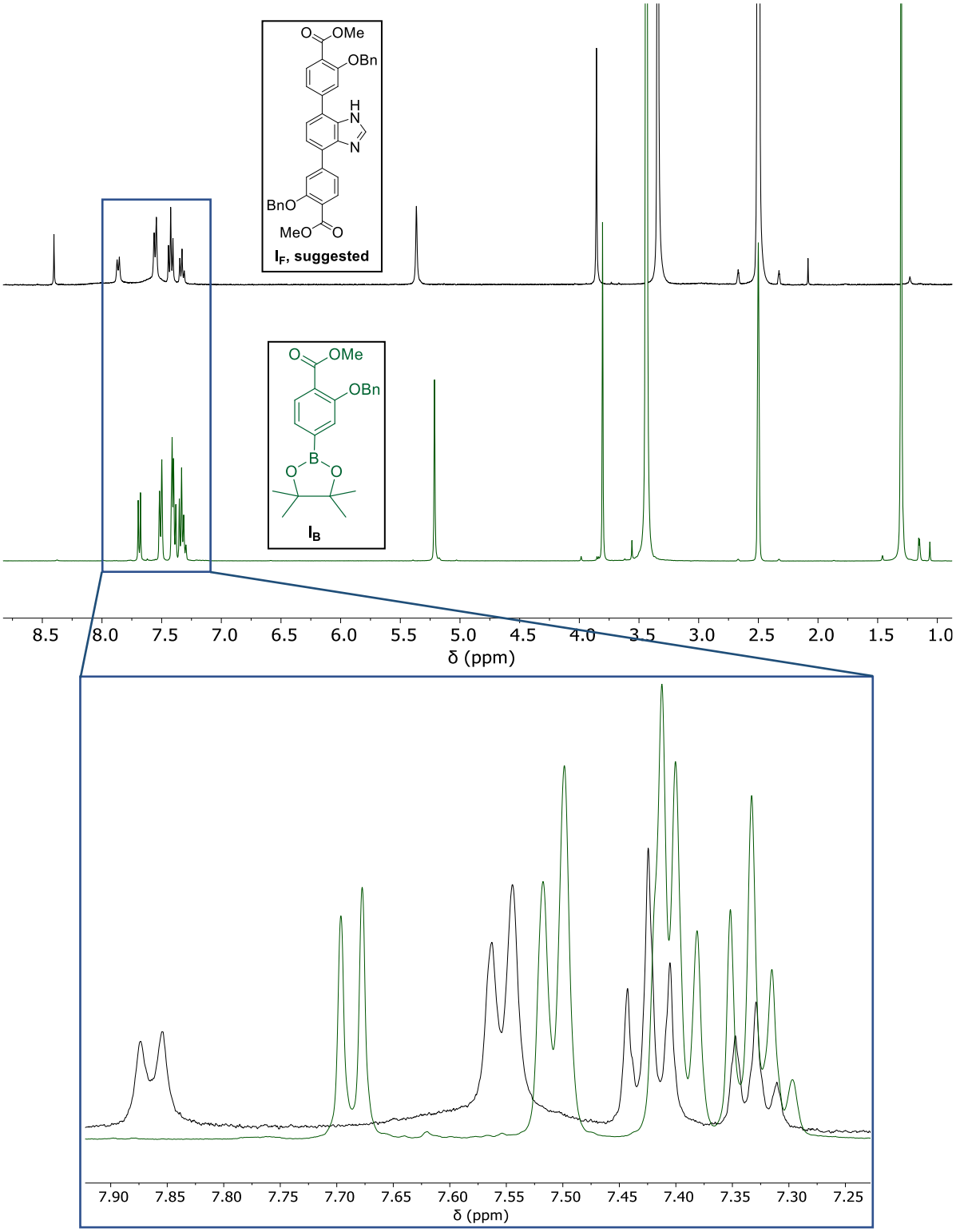

Figure A.16 - ^{1}H NMR stacked and superimposed spectra of $\mathbf{I_F}$ (**black**) and $\mathbf{I_B}$ (**green**) intermediate in $(CD_3)_2SO$.

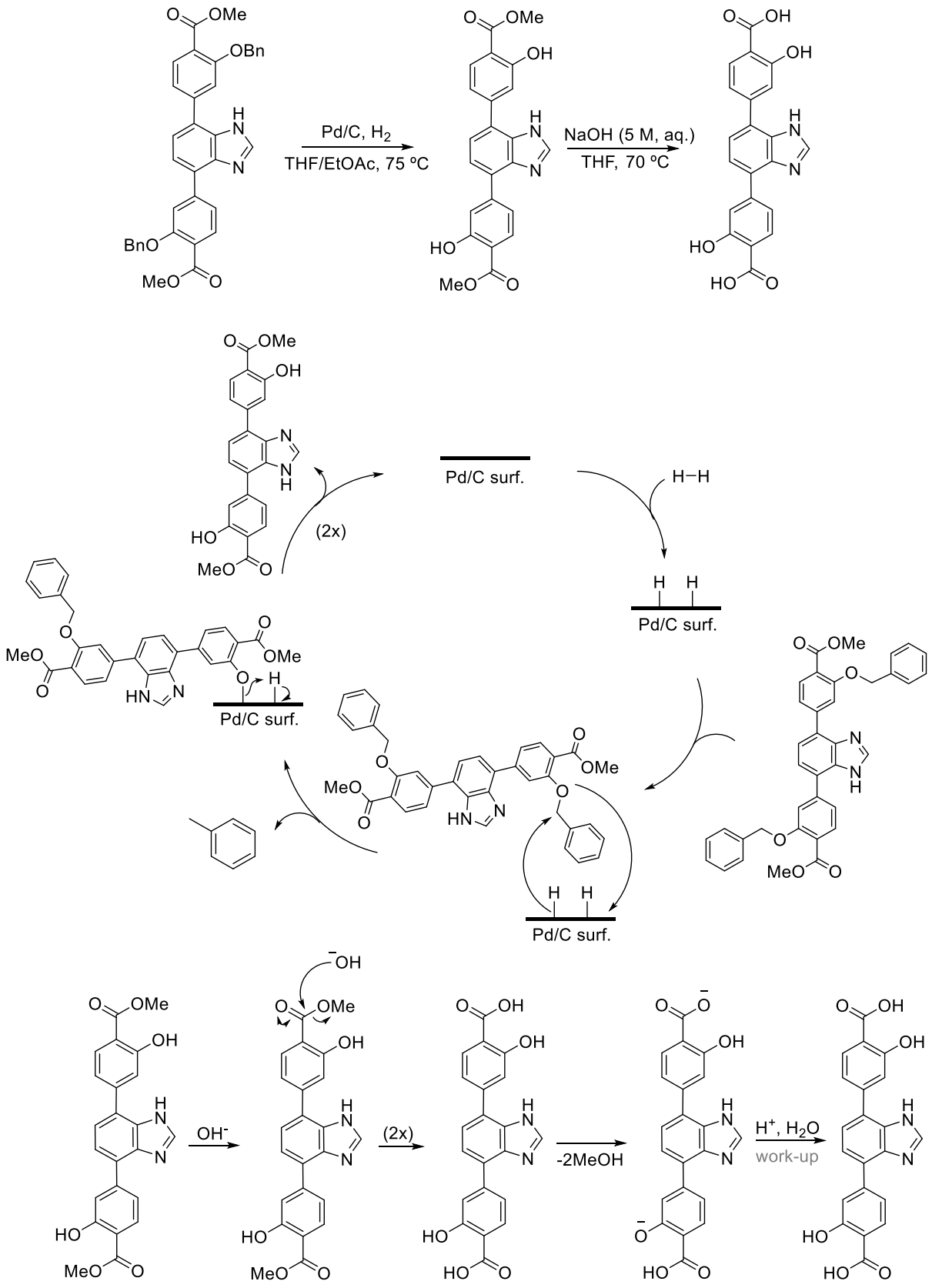

Scheme A.8 - Suggested mechanisms to obtain **H_4L2**.

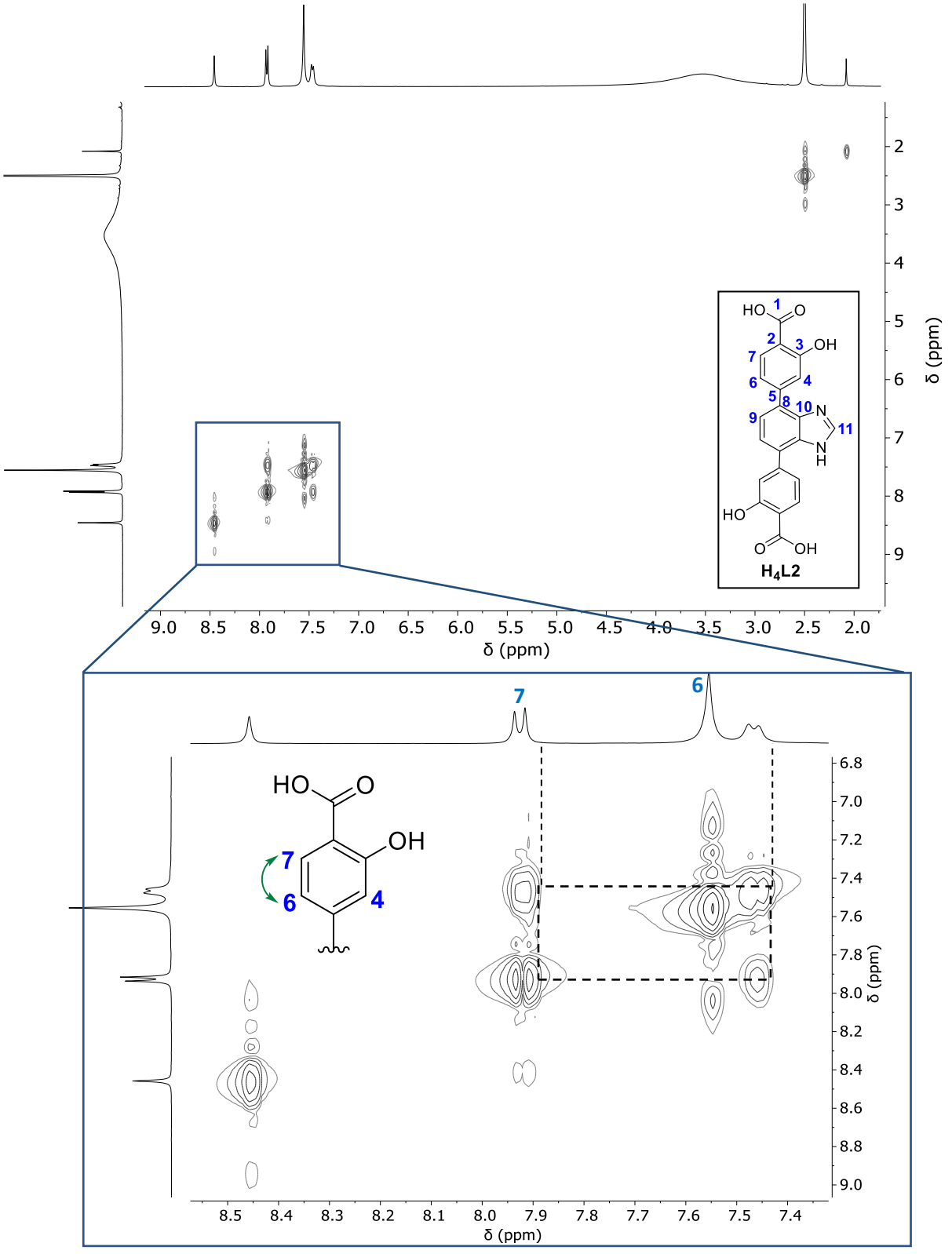

Figure A.17 - COSY spectrum of **H_4L2**. in $(CD_3)_2SO$.

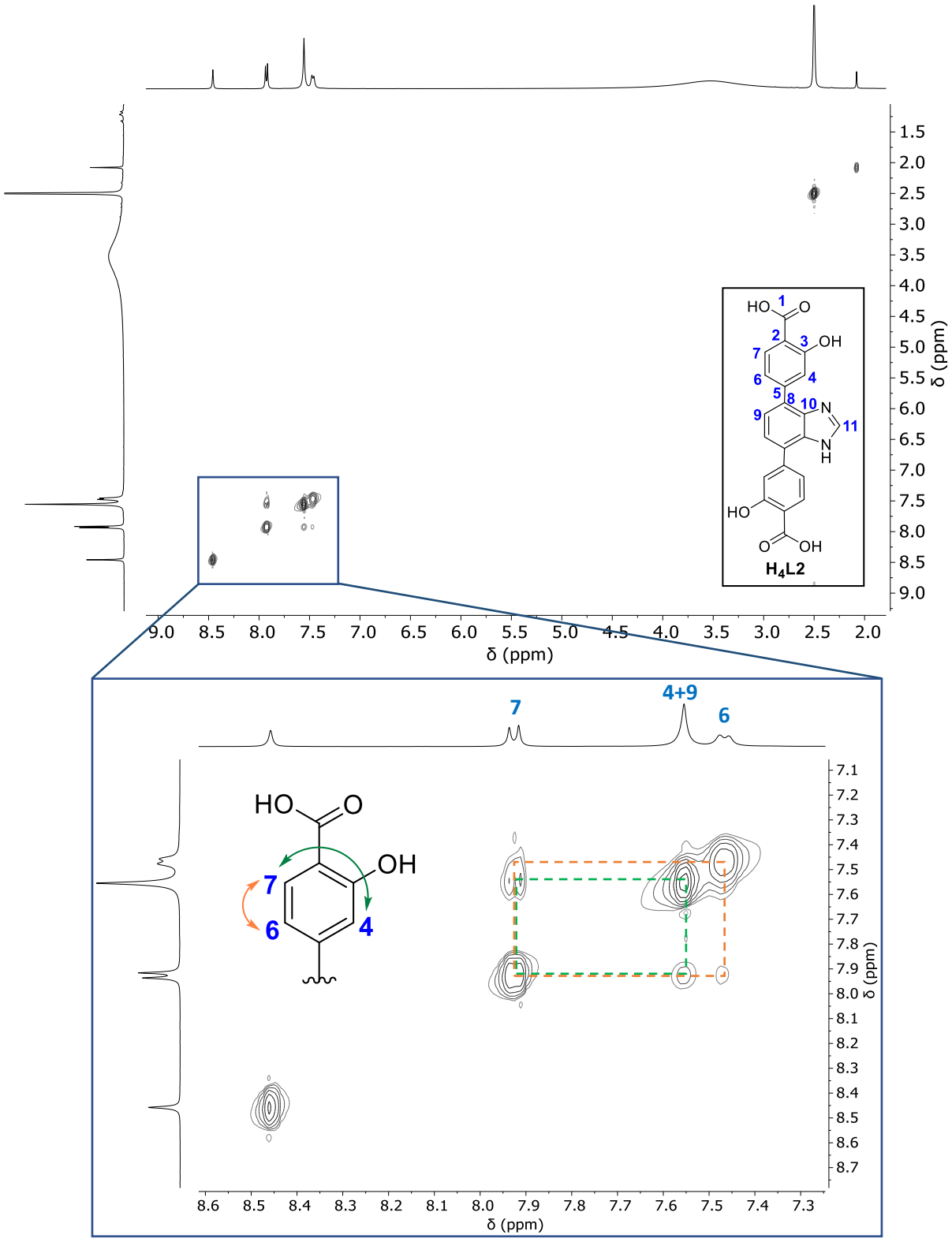

Figure A.18 - TOCSY spectrum of **H_4L2**. in $(CD_3)_2SO$.

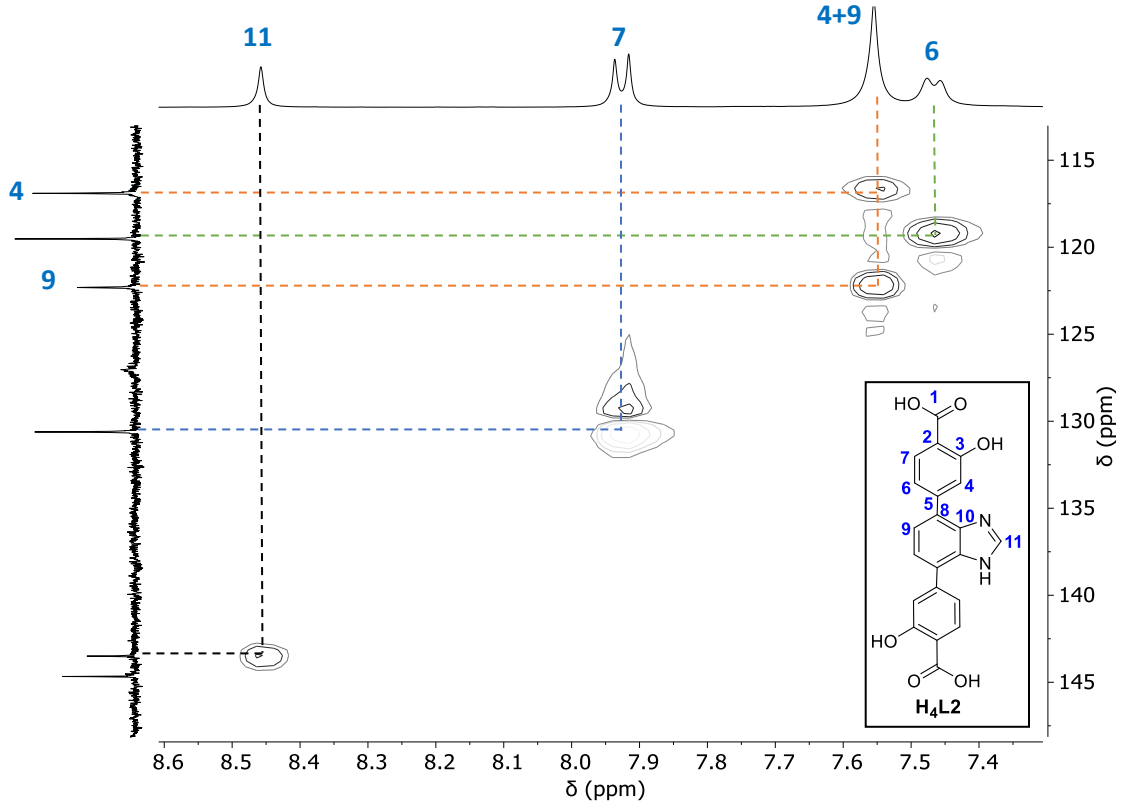

Figure A.19 - HSQC spectrum of **H_4L2**. in $(CD_3)_2SO$.

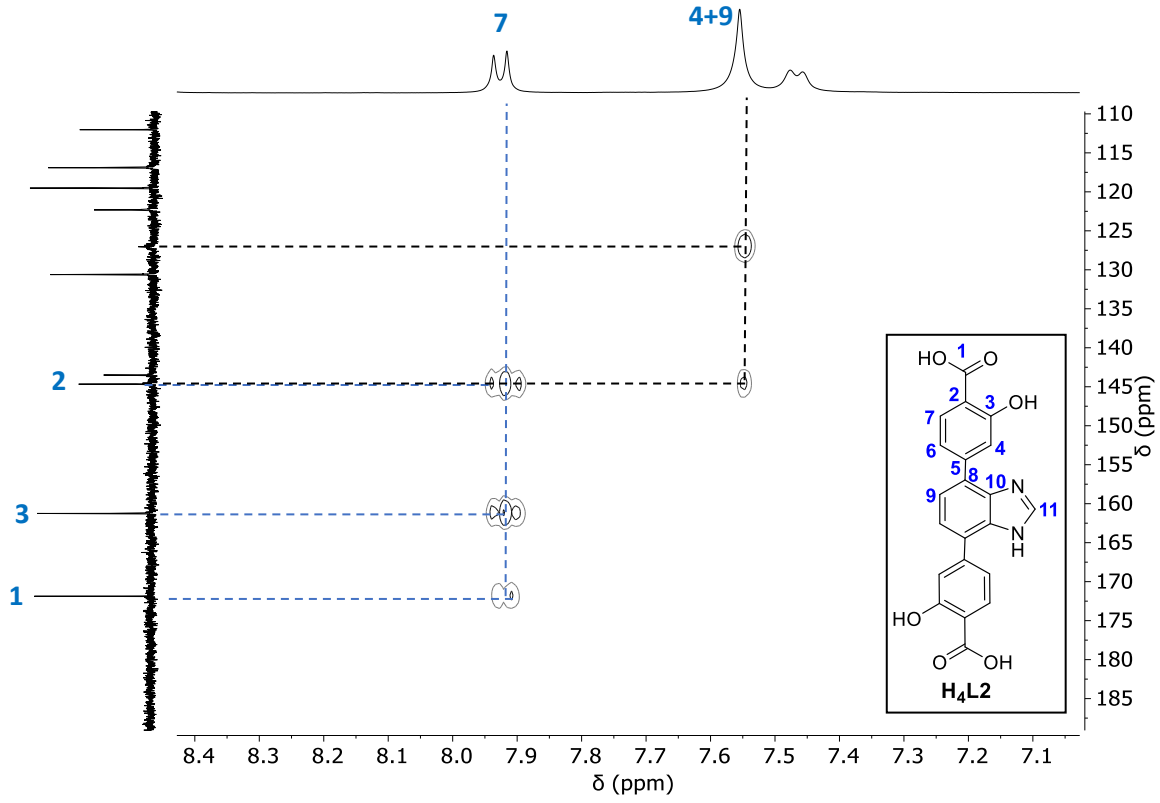

Figure A.20 - HMBC spectrum of **H_4L2**. in $(CD_3)_2SO$.

Table A.2 - Peaks attribution from **H_4L2**. NMR spectra.

	^{1}H NMR				^{13}C NMR
	δ (ppm)	Multiplicity	*J* (Hz)	Integration	δ (ppm)
1	-	-	-	-	171.87
2	-	-	-	-	144.67
3	-	-	-	-	161.25
4[a]	7.55	Multiplet	-	4	116.90
5	-	-	-	-	112.03
6	7.47	Doublet	7.6	2	119.52
7	7.93	Doublet	8.2	2	130.61
8	-	-	-	-	112.03
9[a]	7.55	Multiplet	-	4	122.32
10	-	-	-	-	127.03
11	8.46	Singlet	-	1	143.50
COOH	11.42	singlet	-	2	-

[a] These protons are part of a peak mixture.

Structure:

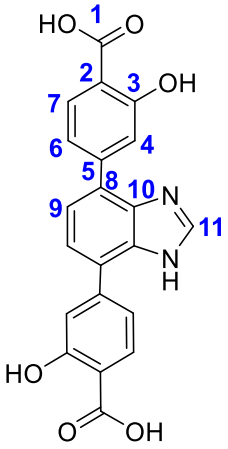

H_4L2

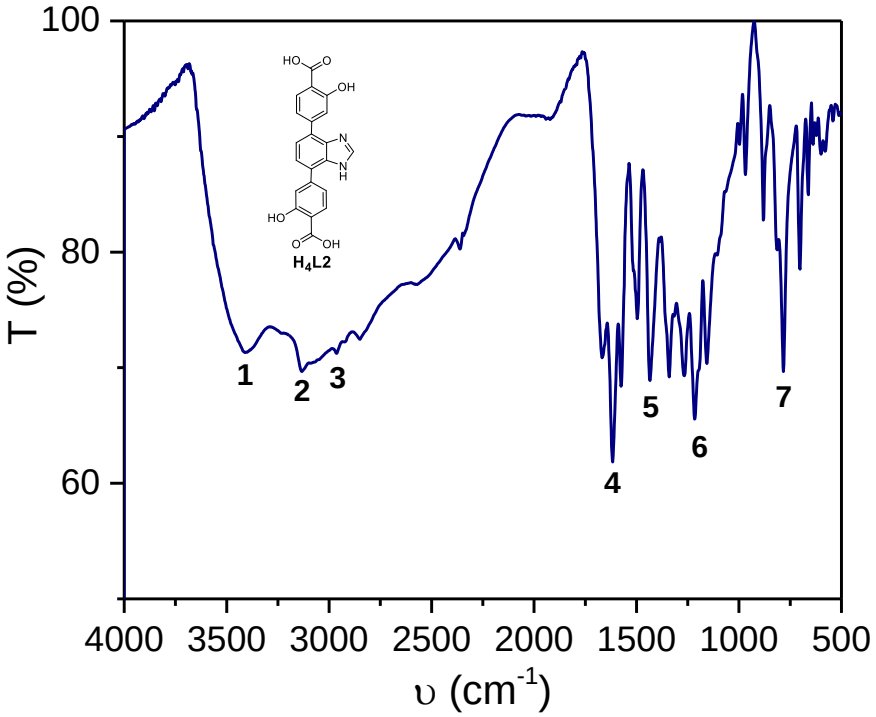

Figure A.21 - FTIR spectrum of **H_4L2** in KBr pellets. Spectrum was recorded in a range of 4000-500 cm^{-1}.

Table A.3 - H_4L2 FTIR spectrum bands attribution.

	FTIR (KBr pellets)		
Band/group	**(cm^{-1})**	**Intensity**	**Bond/functional group**
1	3407	w	ν_{O-H} (phenol)
2	3126	w, br	ν_{O-H} (acid)
3	2959-2842	w	ν_{C-H} (aromatic)
4	1670-1576	s	$\nu_{C=O}$, $\nu_{C=N}$
5	1438	s	δ_{C-O-H} (acid)
6	1337- 1153	s	ν_{C-O} (phenol/acid)
7	879-695	var	δ_{C-H} (aromatic)

Legend: s-strong, m-medium, w-weak, br- broad, var - variable

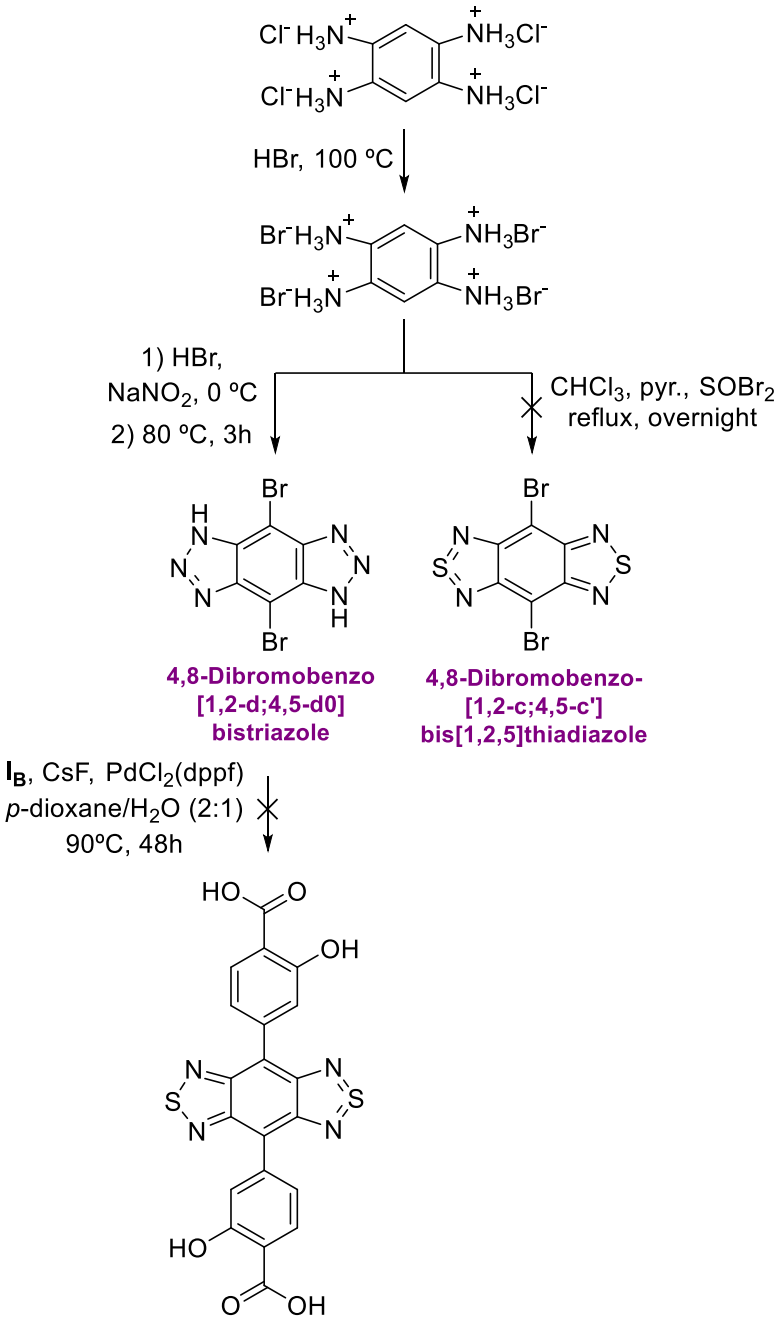

Scheme A.9 - Attempted synthetic steps to obtain benzobistriazole- and bisthiadiazole-based moieties.

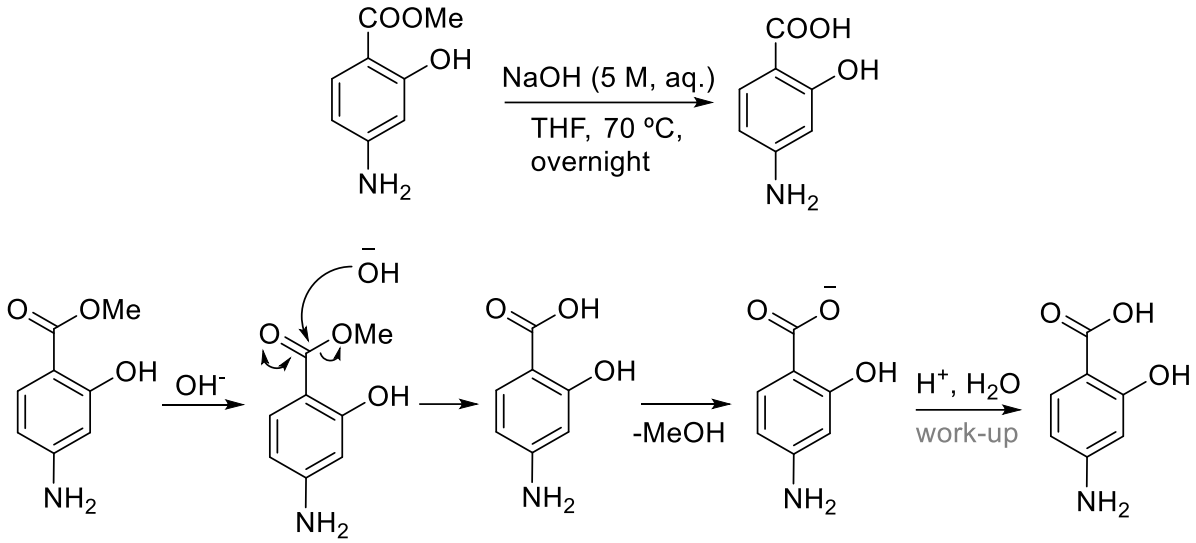

Scheme A.10 - Suggested mechanisms to obtain **IG**.

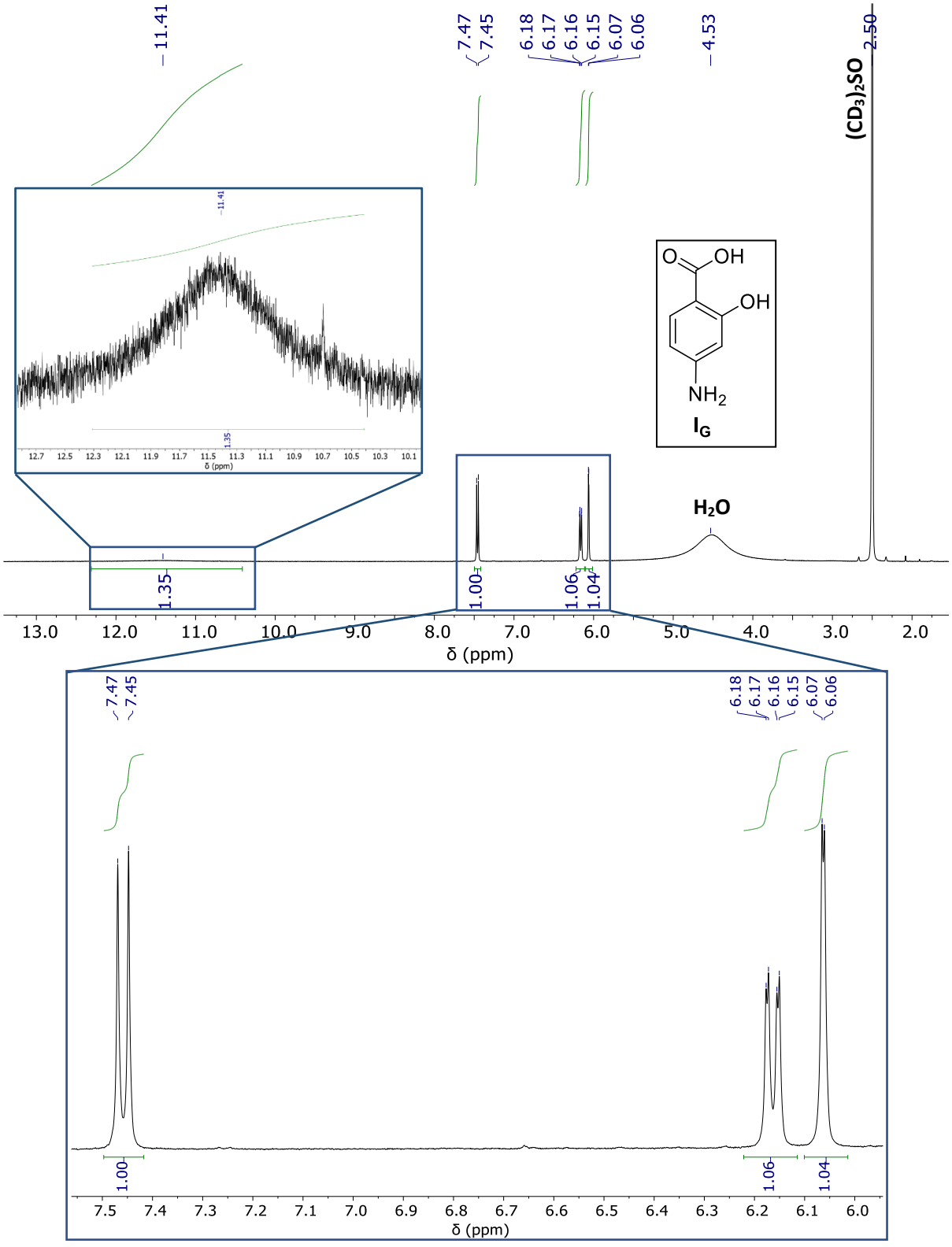

Figure A.22 - ^{1}H NMR spectrum of **IG** in $(CD_3)_2SO$.

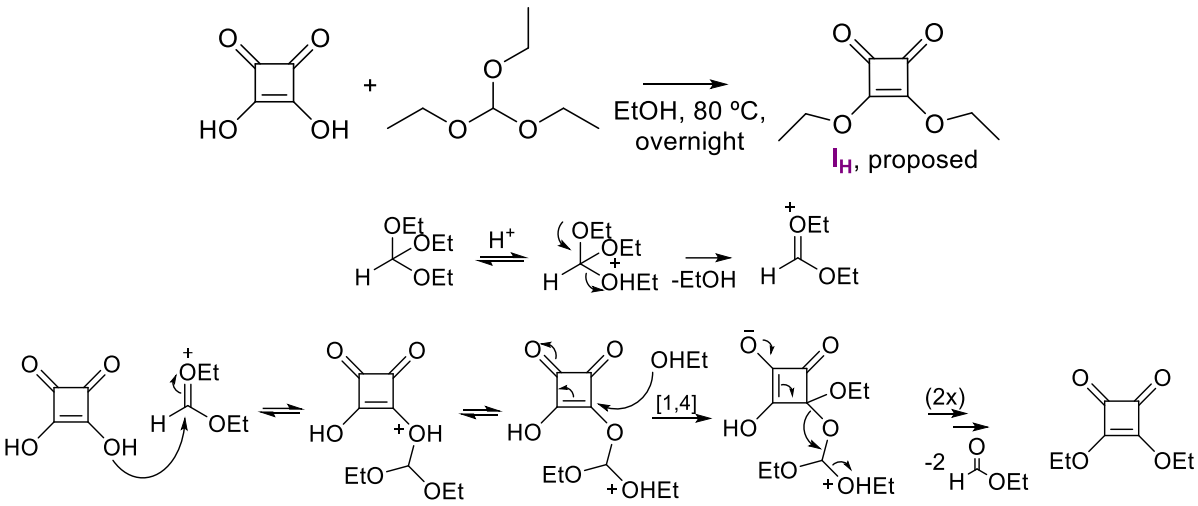

Scheme A.11 - Suggested mechanism to obtain I_H.

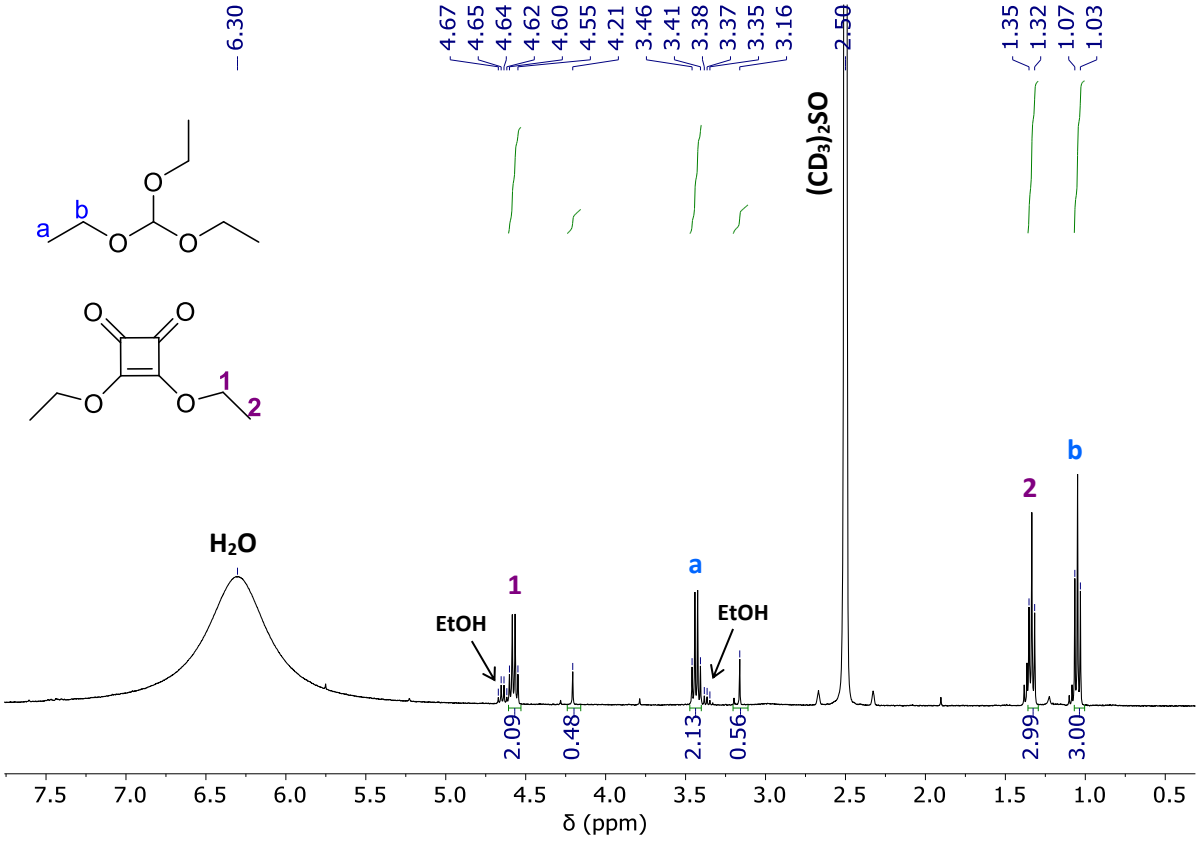

Figure A.23 - ^{1}H NMR spectrum of I_H in $(CD_3)_2SO$.

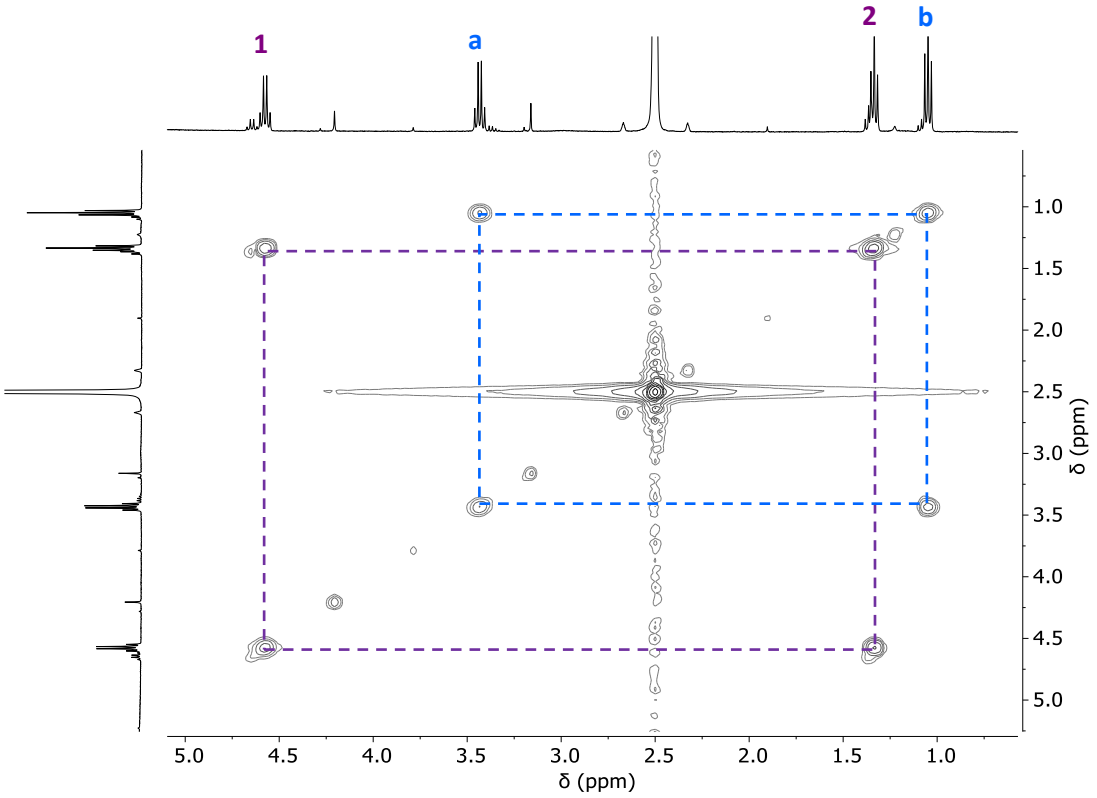

Figure A.24 - COSY spectrum of I_H in $(CD_3)_2SO$.

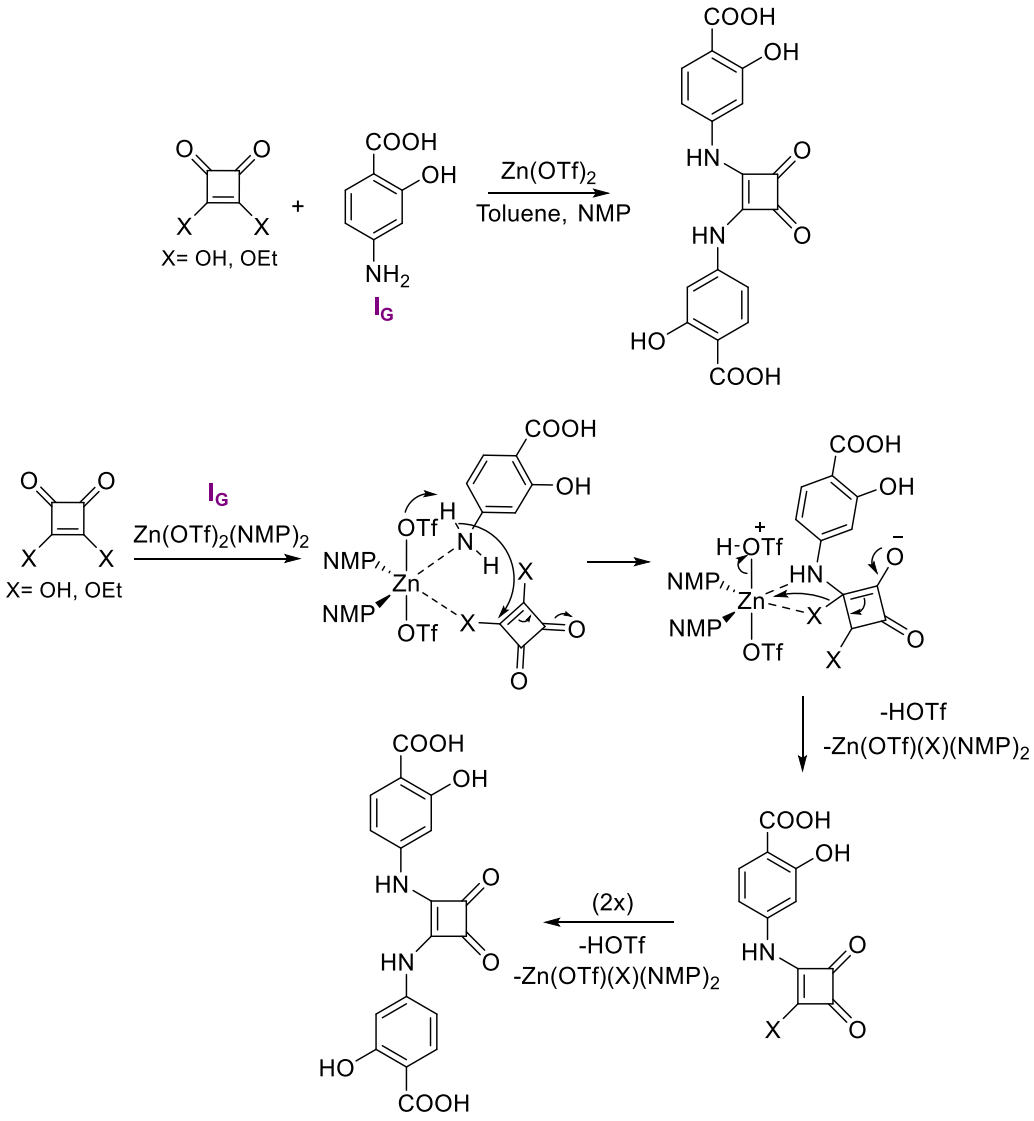

Scheme A.12 - Suggested mechanism to obtain **H_4L3**.

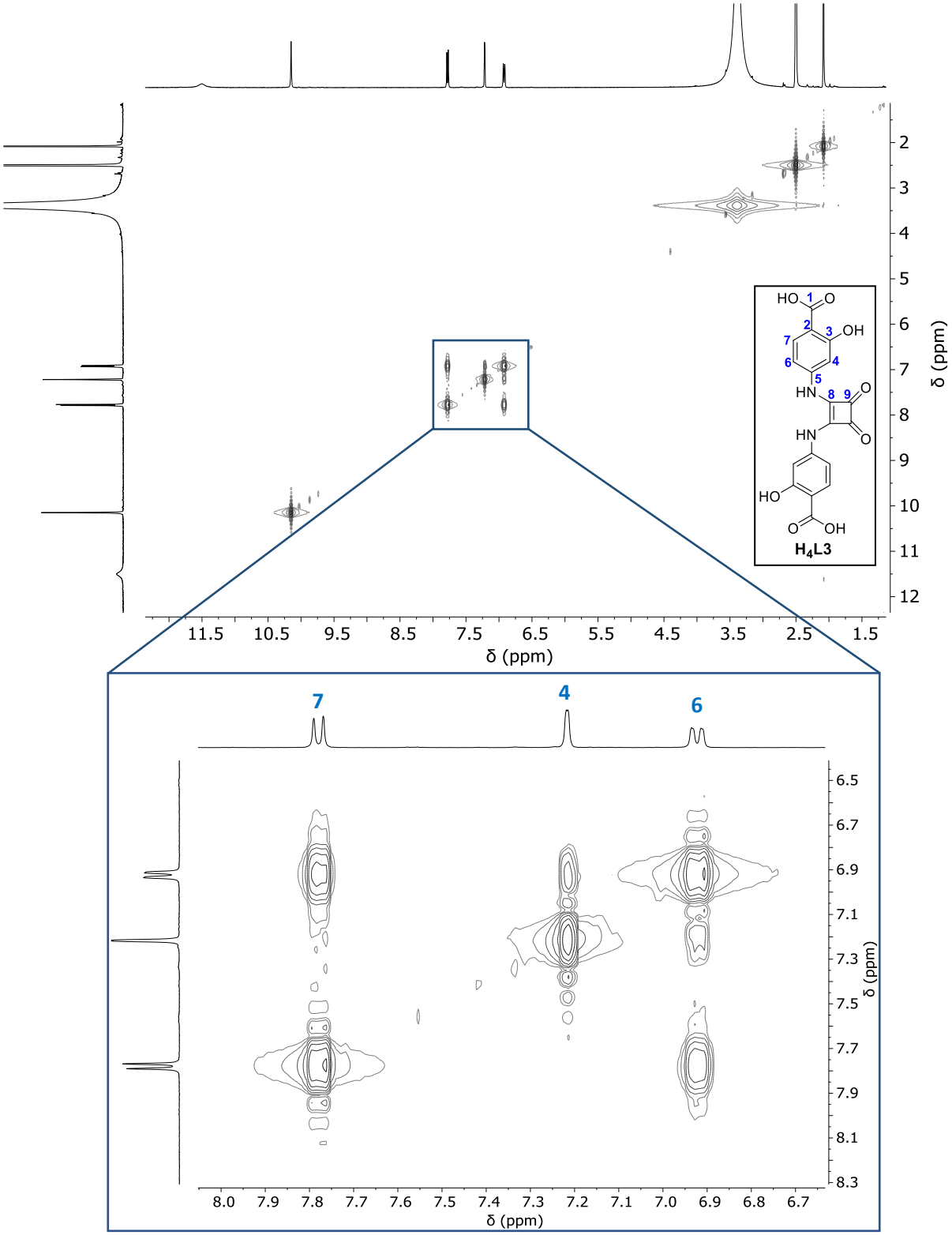

Figure A.25 - COSY spectrum of **H_4L3** in $(CD_3)_2SO$.

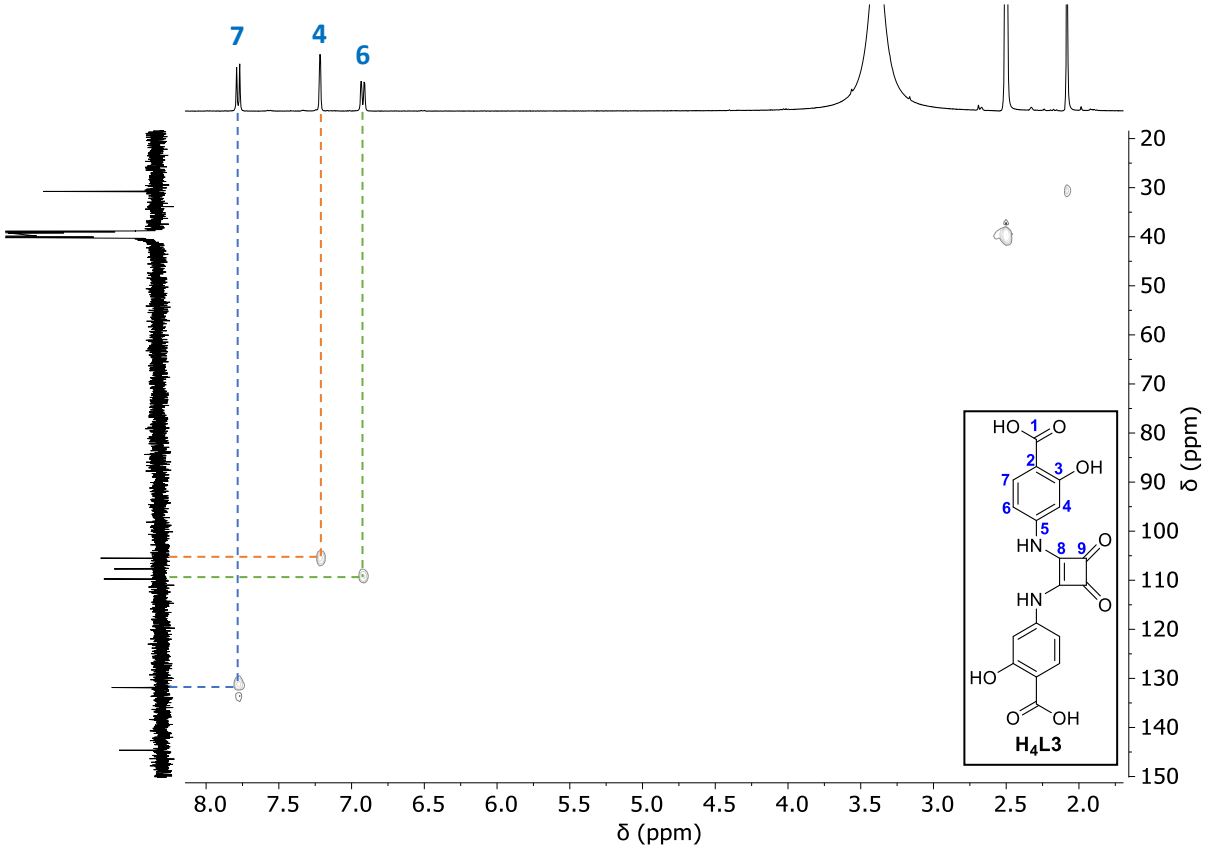

Figure A.26 - HSQC spectrum of **H_4L3** in $(CD_3)_2SO$.

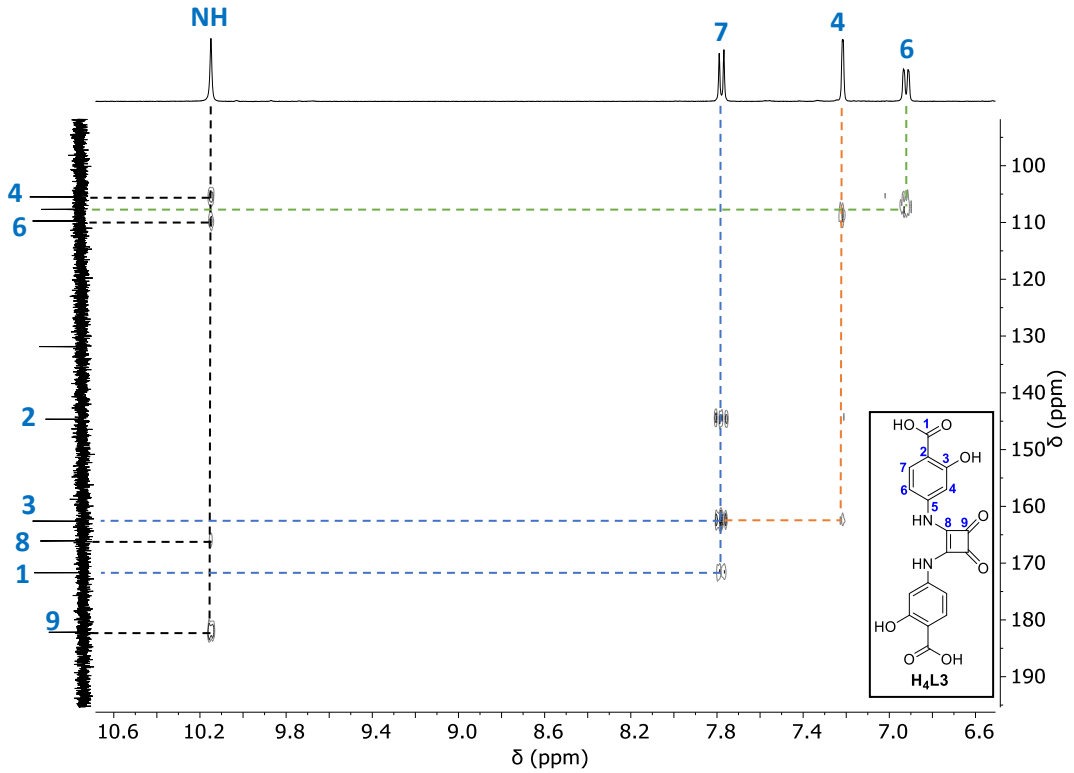

Figure A.27 - HMBC spectrum of **H_4L3** in $(CD_3)_2SO$.

Table A.4 - Peaks attribution from **H_4L3** NMR spectra.

	^{1}H NMR				^{13}C NMR
	δ (ppm)	Multiplicity	J (Hz)	Integration	δ (ppm)
1	-	-	-	-	171.70
2	-	-	-	-	144.65
3	-	-	-	-	162.59
4	7.22	Doublet	1.3	2	105.50
5	-	-	-	-	107.70
6	6.93	Doublet of doublets	4, 10	2	109.74
7	7.78	Doublet	8	2	131.86
8	-	-	-	-	166.11
9	-	-	-	-	182.18
COOH	11.51	-	-	2	-
NH	10.15	-	-	2	-

Structure:

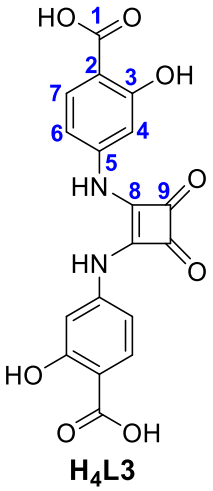

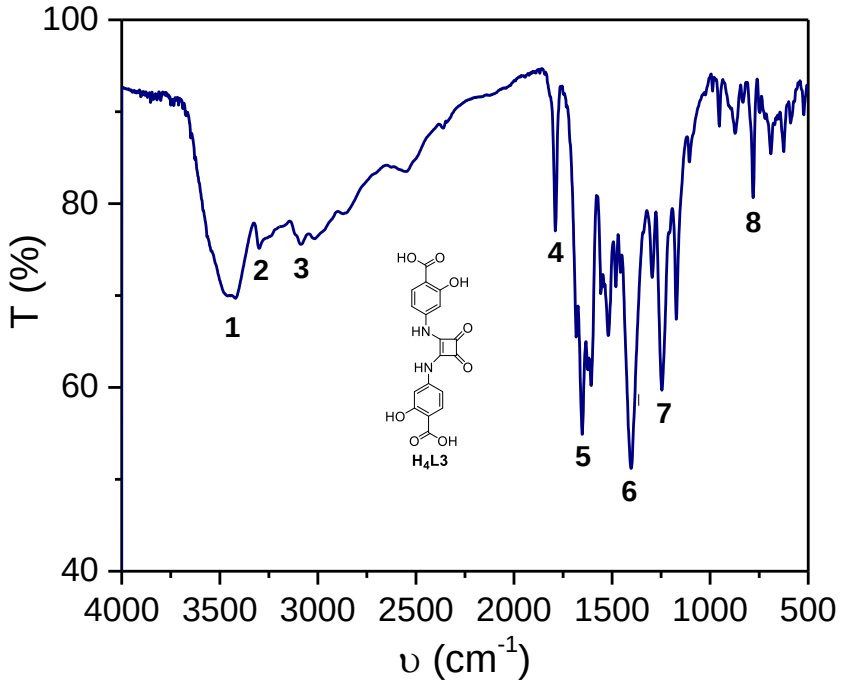

Figure A.28 - FTIR spectrum of **H_4L3** in KBr pellets. Spectrum was recorded in a range of 4000-500 cm^{-1}.

Table A.5 - H_4L3 FTIR spectrum bands attribution.

	FTIR (KBr pellets)		
Band/group	**(cm^{-1})**	**Intensity**	**Bond/functional group**
1	3473-3417	w, br	ν_{O-H} (phenol) and ν_{N-H}
2	3296	w, br	ν_{O-H} (acid)
3	3084-2860	w	ν_{C-H} (aromatic)
4	1789	m	$\nu_{C=O}$ (ketone)
5	1684-1606	s	$\nu_{C=O}$ (acid) and $\nu_{C=C}$ (α,β-ketone)
6	1404	s	δ_{C-O-H} (acid)
7	1295 - 1173	s	ν_{C-O} (phenol/acid)
8	957-620	w	δ_{C-H} (aromatic)

Legend: s-strong, m-medium, w-weak, br- broad

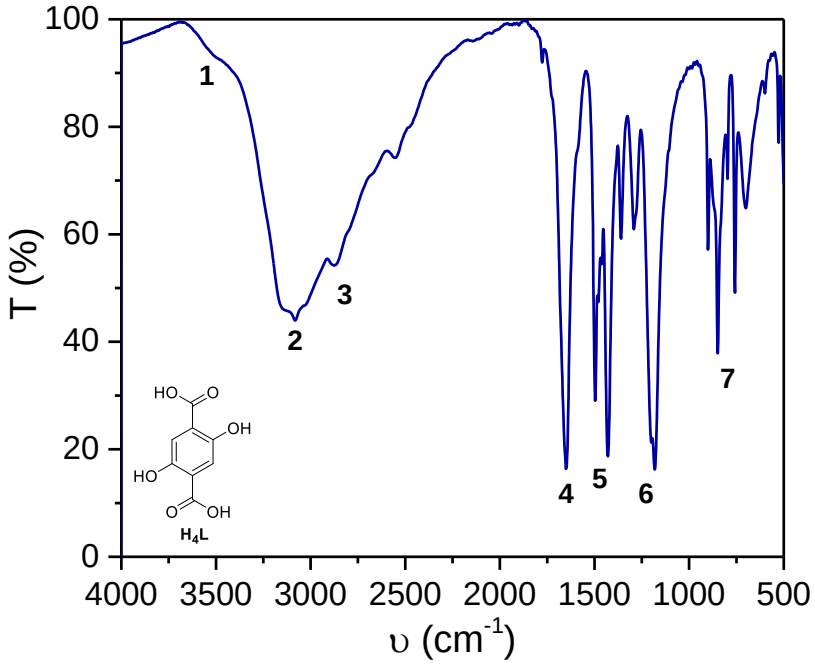

Figure A.29 - FTIR spectrum of **H_4L** in KBr pellets. Spectrum was recorded in a range of 4000-500 cm^{-1}.

Table A.6 - FTIR bands attribution of **H_4L**.

	FTIR (KBr pellets)		
Band/group	**(cm^{-1})**	**Intensity**	**Bond/functional group**
1	3520	w	ν_{O-H} (phenol)
2	3082	w, br	ν_{O-H} (acid)
3	2880	w	ν_{C-H} (aromatic)
4	1646	s	$\nu_{C=O}$
5	1427	s	δ_{C-O-H} (acid)
6	1357-1182	s	ν_{C-O} (acid/phenol)
7	905-696	var	δ_{C-H} (arom)

Legend: s-strong, m-medium, w-weak, br- broad, var-variable

Table A.7 - DRIFT bands attribution of the **Fe/L** film deposited at -1.4 V.

DRIFT (gold coated plate)		
(cm^{-1})	Intensity	Bond/functional group
3226	w, br	νO-H (water)
2963-2861	w	νC-H
1537	s	νO-C-O (symmetric)
1422	s	νO-C-O (assymmetric)
1236-1204	s	νC-O (phenoxide)
890-802	m	δC-H
560	w	νFe-O

Legend: s-strong, m-medium, w-weak, br- broad

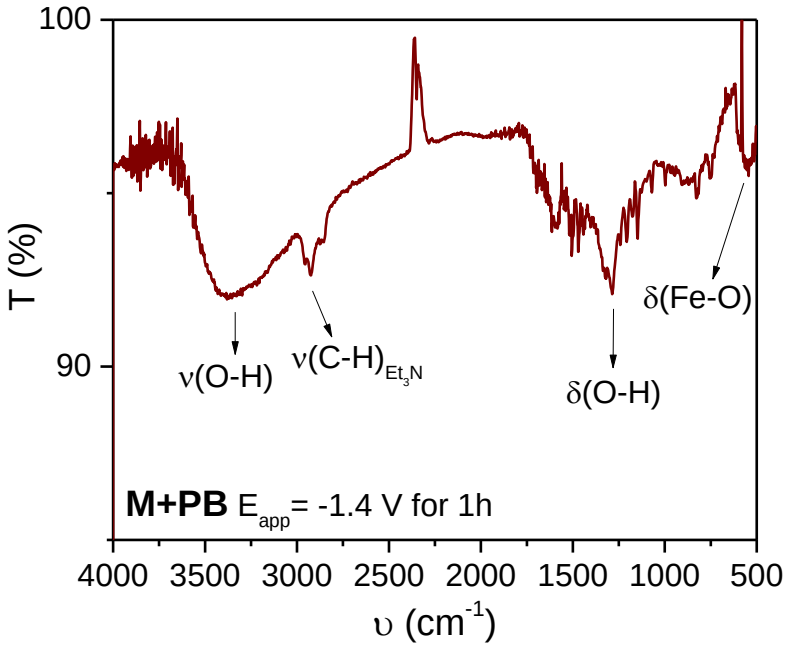

Figure A.30 - FTIR spectra of the **M+PB** films deposited at -1.4 V for 1 hour. Spectra were obtained in a range of 4000-500 cm^{-1} and blank was measured with a gold coated plate.

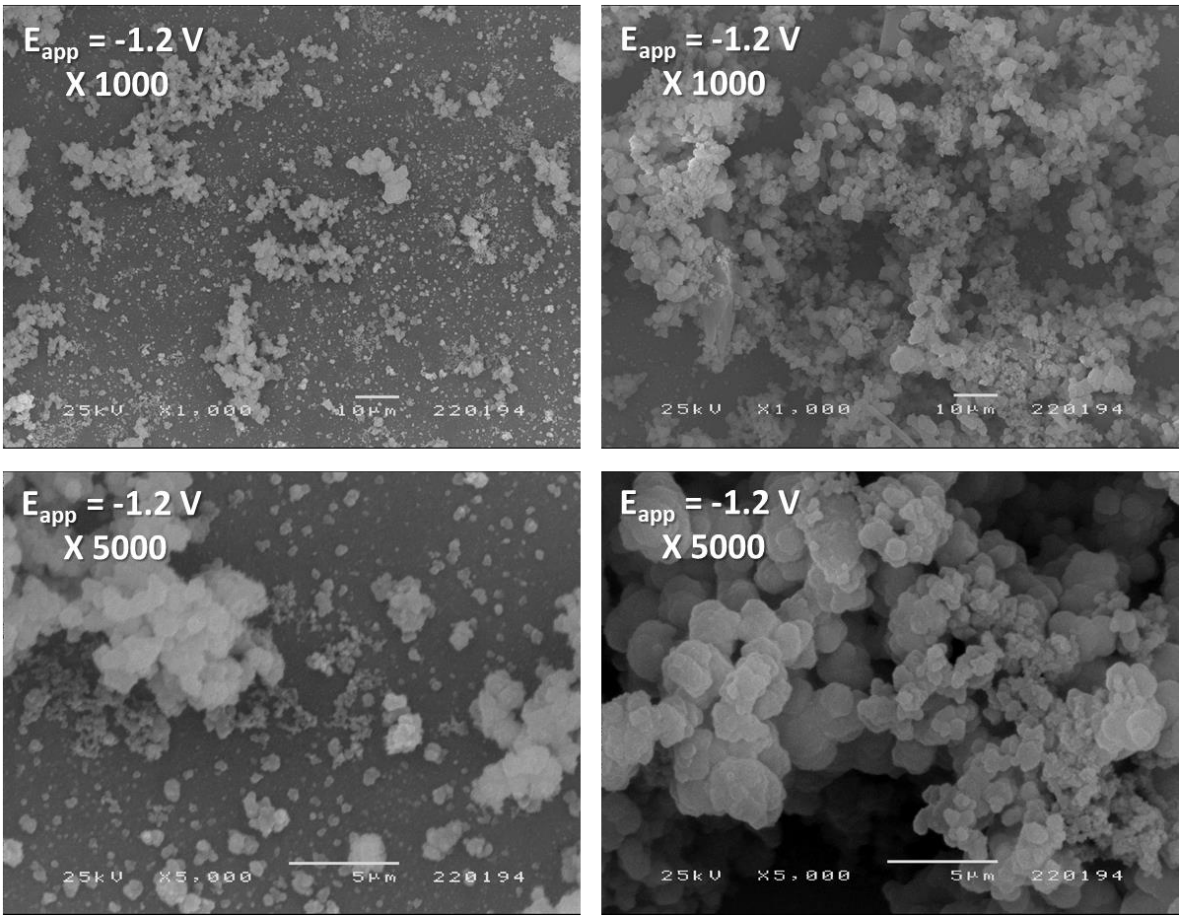

Figure A.31 - SEM images of the **Fe/L film** (7:2:2 ratio of **M**: **H_4L**:**PB**, respectively) deposited at -1.2 V. Images were magnified at x1000 (above) and x5000 (below).

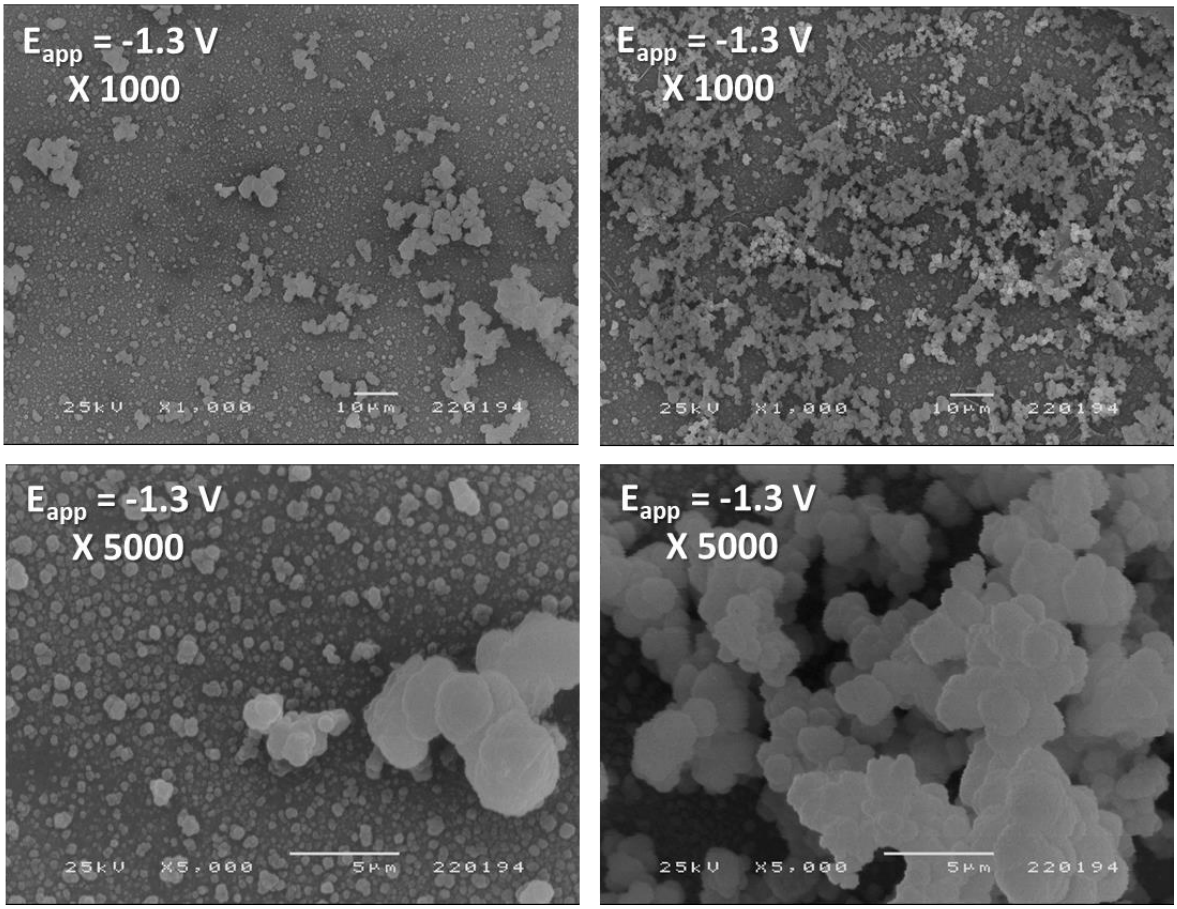

Figure A.32 - SEM images of the **Fe/L film** (7:2:2 ratio of **M**:**H_4L**:**PB**, respectively) deposited at -1.3 V. Images were magnified at x1000 (above) and x5000 (below).

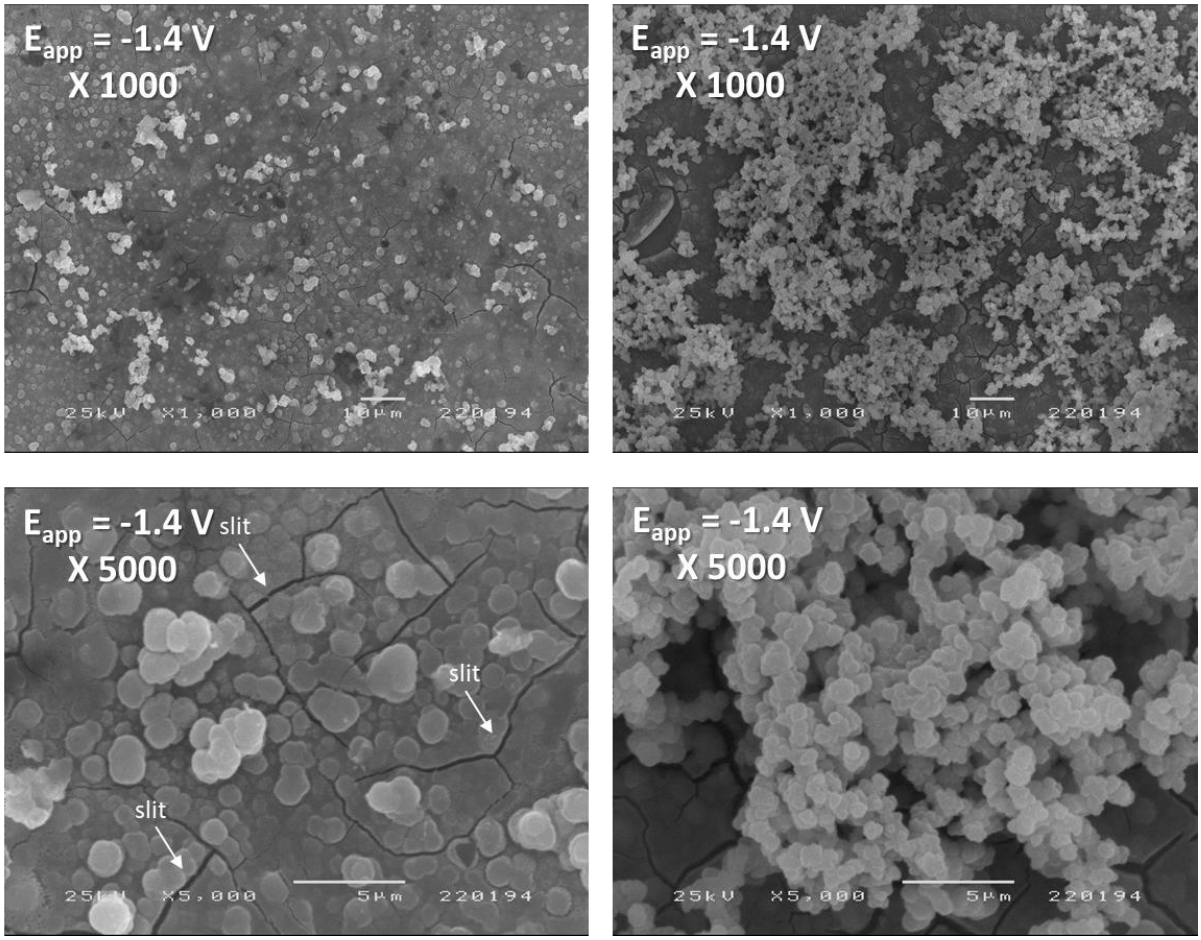

Figure A.33 - SEM images of the **Fe/L film** (7:2:2 ratio of **M**:**H4L**:**PB**, respectively) deposited at -1.4 V. Images were magnified at x1000 (above) and x5000 (below).

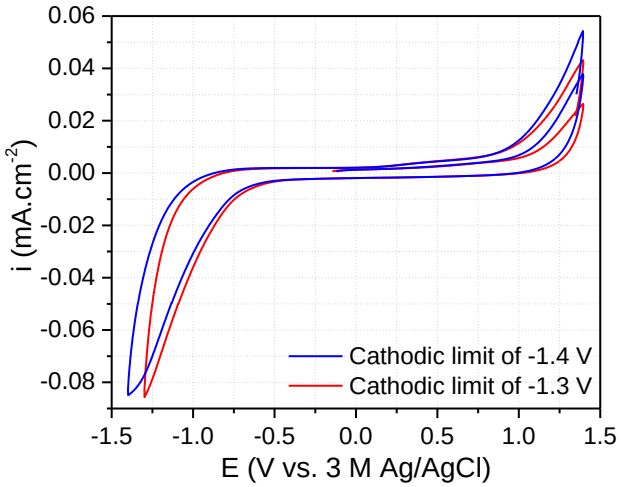

Figure A.34 - Cyclic voltammograms of FTO electrode with different a cathodic limit of -1.4 (**blue**) and -1.3 V (**red**). Studies were performed in 10 mL of N_2 saturated DMF with $TBAPF_6$ as the supporting electrolyte and recorded at 100 $mV.s^{-1}$. The one-compartment electrochemical cell was also constituted by FTO as working, platinum wire as counter and 3 M Ag/AgCl as reference electrodes.

Table A.8 - Peak deconvolution of C 1s, Fe 2p and O 1s from the XPS survey spectra of the **Fe/L** (7:2:2 ratio of **M**:**H4L**:**PB**, respectively) and M+PB (7:2 ratio of **M**:**PB**, respectively) films, deposited at -1.4 V.

	Fe/L film (-1.4 V)	M+PB film (-1.4 V)	Attribution
C 1s	285.0	285.0	C-C and C-H
	-	286.8	C-N
	286.7	-	$C\text{-}O^-$
	288.9	-	$O{=}C\text{-}O^-$
	-	288.6	O=C-N
	291.5	-	π–π* excitations
Fe 2p	710.0	710.2	$Fe(OH)_2$
	711.2	711.3	Fe_3O_4
	712.5	712.6	Fe_2O_3
	715.0	714.2	$Fe(OH)_3$
	717.3	717.2	Satellite
	720.0	719.2	Satellite
O 1s	-	530.0	O-Fe
	-	531.3	HO-Fe
	-	532.1	HO-Fe

Table A.9 - Atomic concentration (%) of Fe, C and O from the **Fe/L** (7:2:2 ratio of **M**:**H4L**:**PB**, respectively) and **M**+**PB** (7:2 ratio of **M**:**PB**, respectively) films, deposited at -1.4 V.

	Fe/L film (-1.4 V)	M+PB film (-1.4 V)	Theorical for Fe_2L
Fe	4.9	12.9	12.5
C	53.0	35.8	50
O	37.4	45.7	37.5

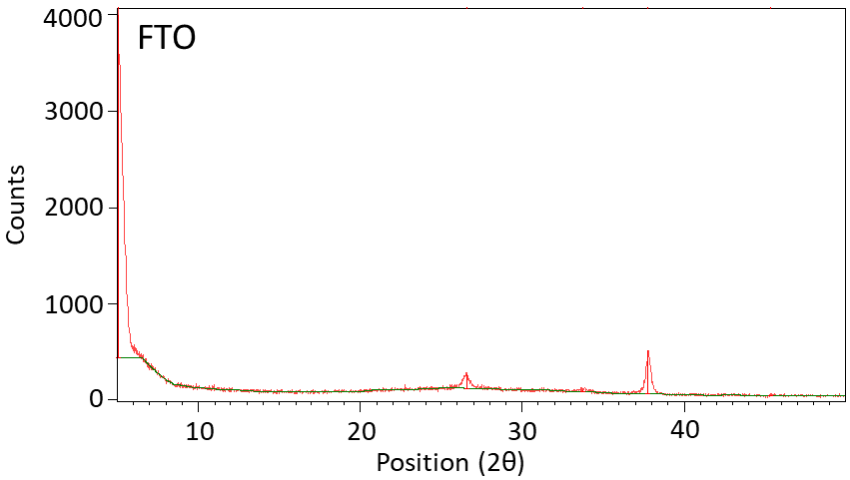

Figure A.35 - Diffractogram of the FTO working electrode.

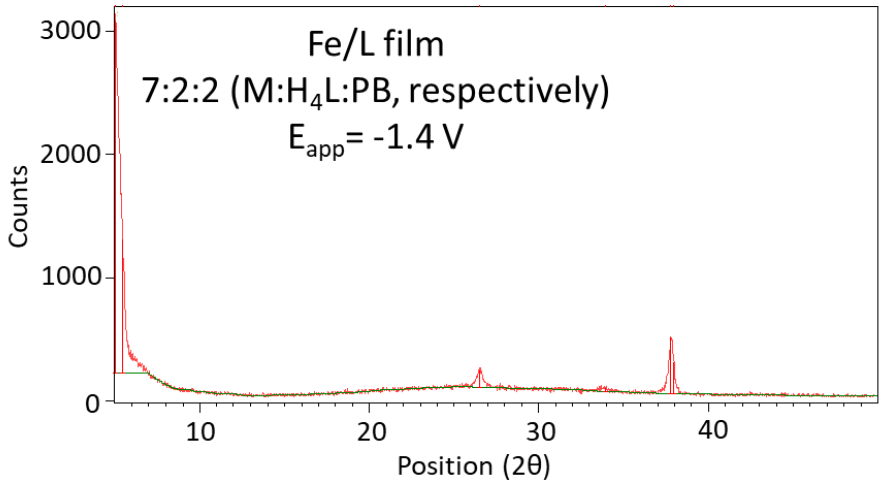

Figure A.36 - Diffractogram of the **Fe/L** film (7:2:2 ratio of **M**:**H$_4$L**:**PB**, respectively) deposited at -1.4 V.

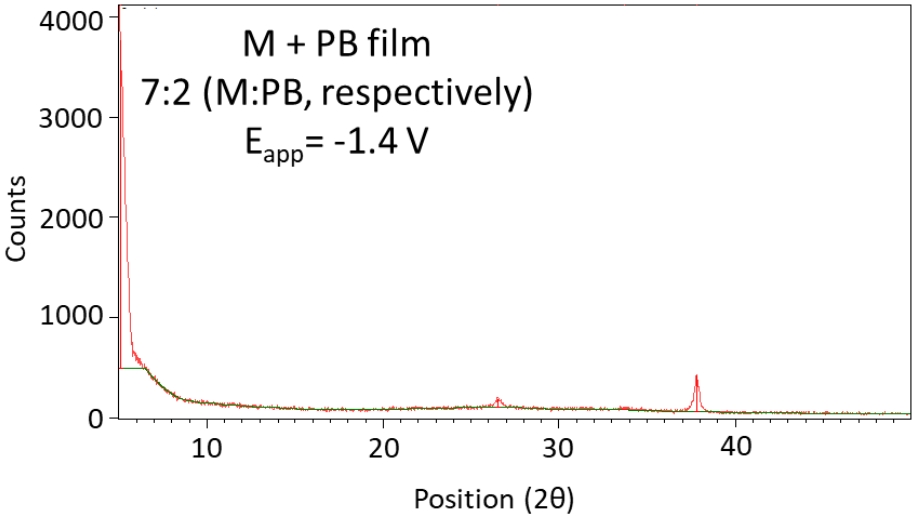

Figure A.37 - Diffractogram of **M**+**PB** film (7:2 ratio of **M**:**PB**, respectively) deposited at -1.4 V.

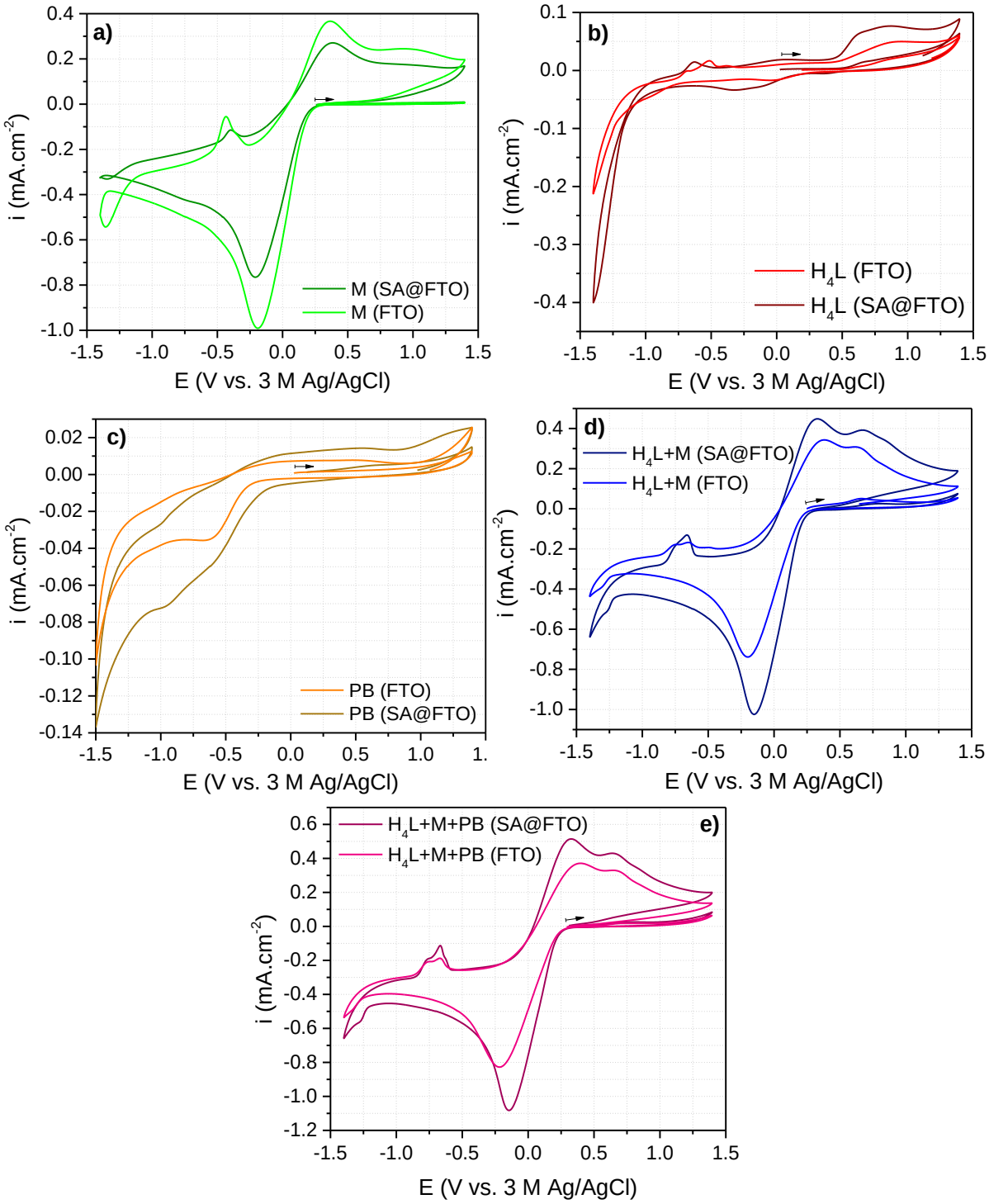

Figure A.38 - Cyclic voltammograms of a) **M** on **FTO** and **SA@FTO**, b) **H_4L** on **FTO** and **SA@FTO**, c) **PB** on **FTO** and **SA@FTO**, d) **H_4L**+**M** mixture on **FTO** and **SA@FTO** and e) **H_4L**+**M**+**PB** mixture on **FTO** and **SA@FTO**. Studies were performed in 10 mL of N_2 saturated DMF with $TBAPF_6$ as the supporting electrolyte and recorded at 100 $mV.s^{-1}$. The one-compartment electrochemical cell was also constituted by FTO as working, platinum wire as counter and 3 M Ag/AgCl as reference electrodes. Species quantities: 7 mM of **M**, 2 mM of **H_4L** and 2 mM of **PB**.

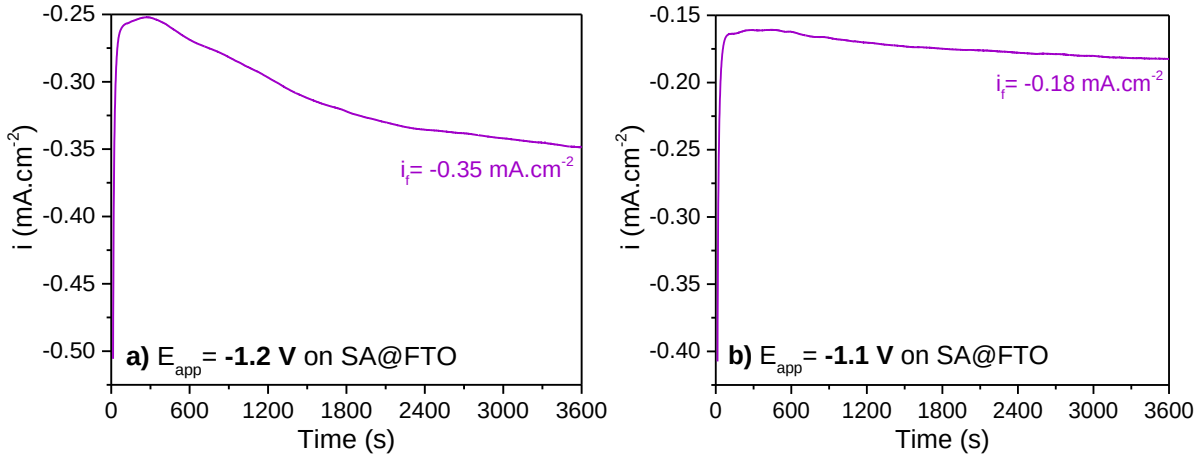

Figure A.39 - Chronoamperograms following the electrodeposition of the **Fe/L** film on SA@FTO with growth potentials of a) -1.2 V and b) -1.1 V. Electrodepositions were performed in 10 mL of N_2 saturated DMF with $TBAPF_6$ as the supporting electrolyte and recorded at 100 $mV.s^{-1}$. The one-compartment electrochemical cell was also constituted by FTO as working, platinum wire as counter and 3 M Ag/AgCl as reference electrodes. Species quantities: 7 mM of **M**, 2 mM of **H_4L** and 2 mM of **PB**.

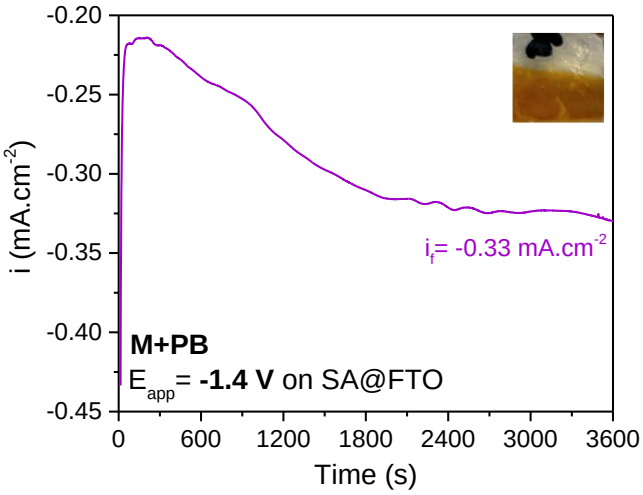

Figure A.40 - Chronoamperogram following the electrodeposition of **M**+**PB** film on SA@FTO at -1.4 V. Electrodepositions were performed in 10 mL of N_2 saturated DMF with $TBAPF_6$ as the supporting electrolyte and recorded at 100 $mV.s^{-1}$. The one-compartment electrochemical cell was also constituted by FTO as working, platinum wire as counter and 3 M Ag/AgCl as reference electrodes. Species quantities: 7 mM of **M** and 2 mM of **PB**.

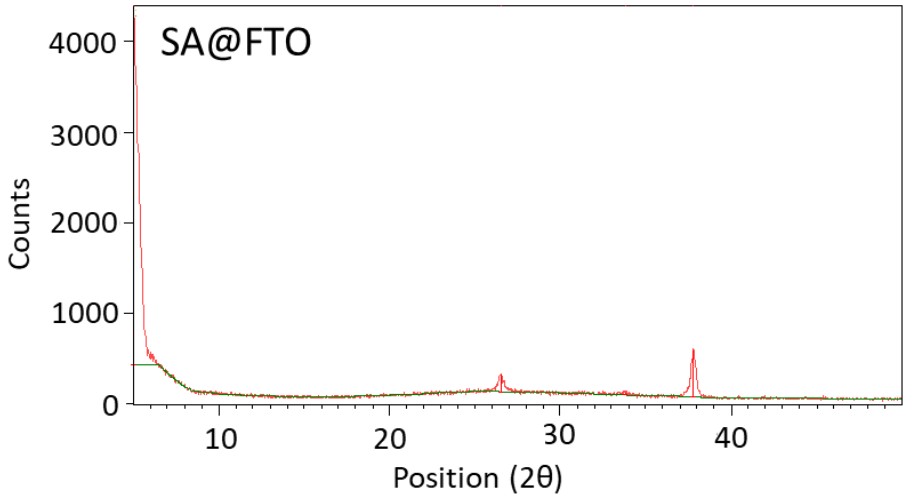

Figure A.41 - Diffractogram of SA@FTO.

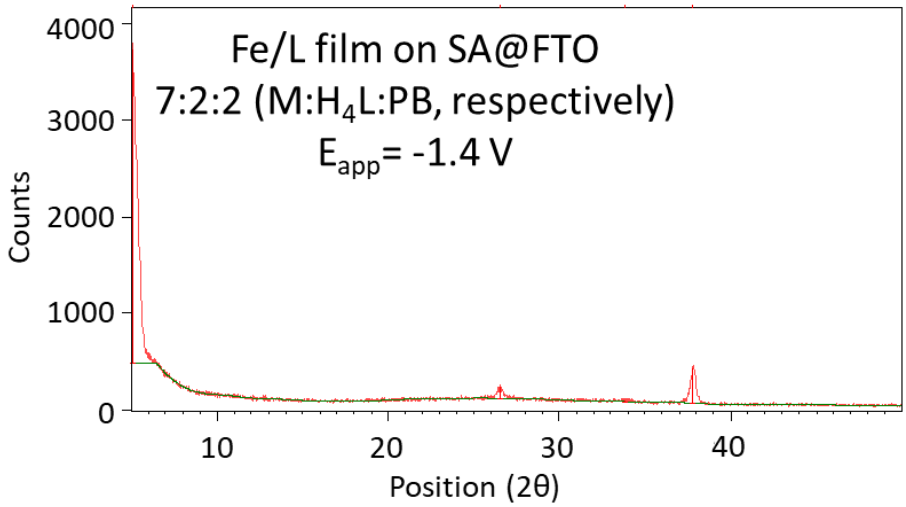

Figure A.42 - Diffractogram of the **Fe/L** film (7:2:2 ratio of **M**:**H4L**:**PB**, respectively) deposited at -1.4 V on SA@FTO.

at

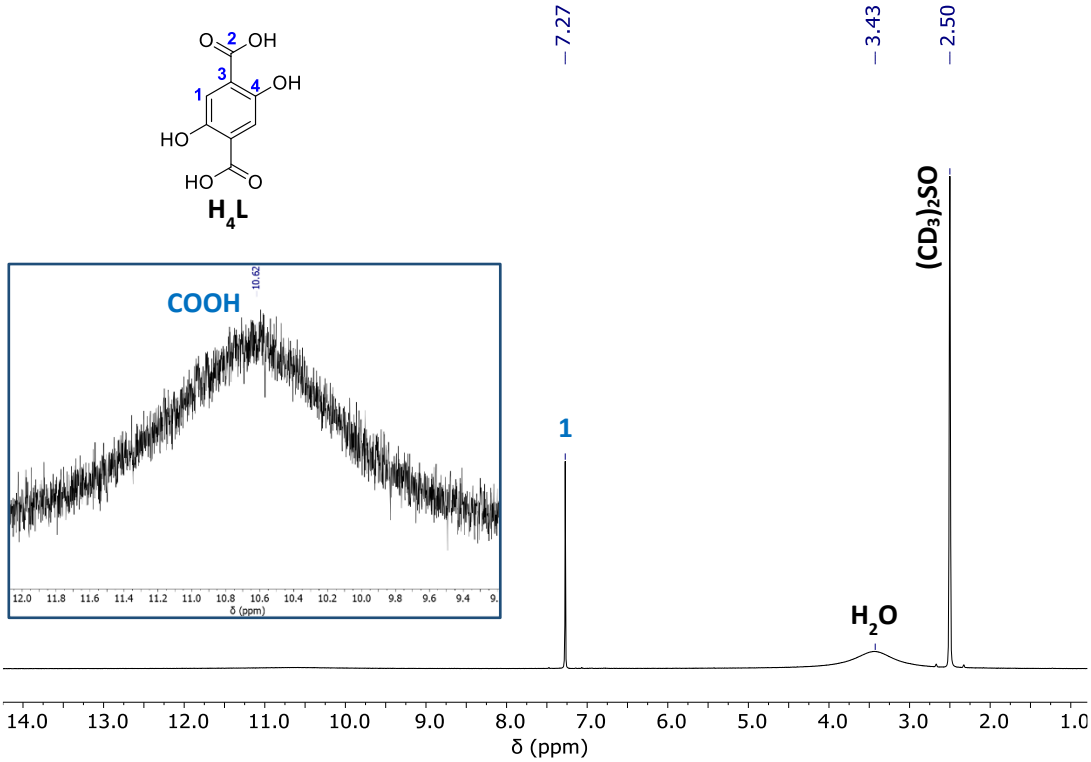

Figure A.43 - ^{1}H NMR spectrum of **H_4L** in $(CD_3)_2SO$.

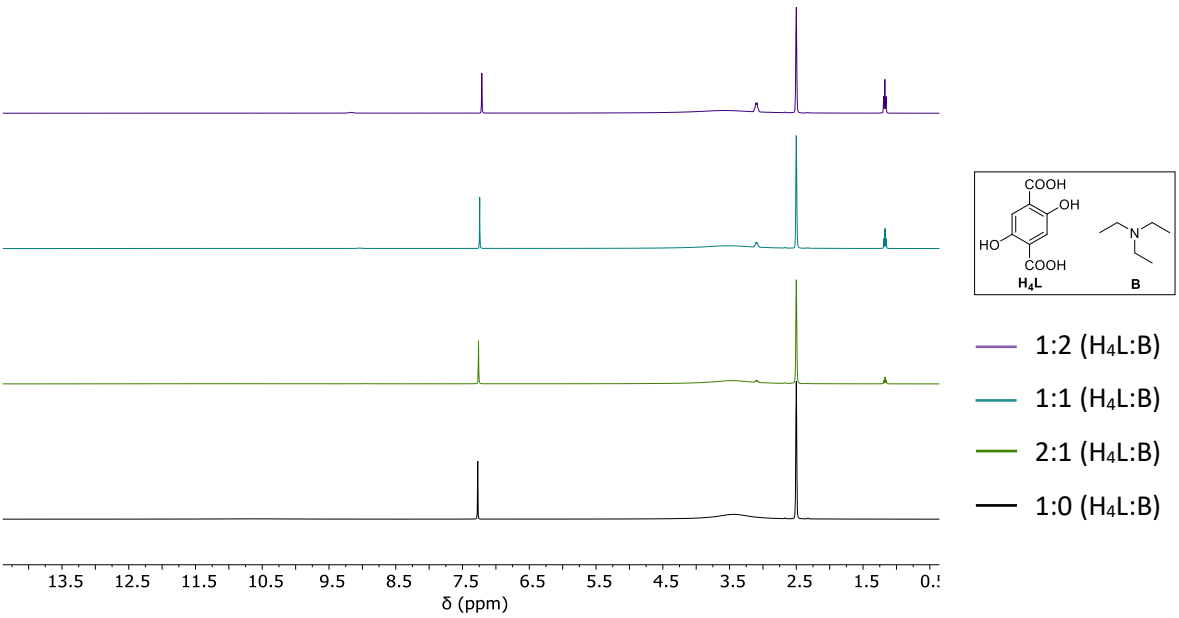

Figure A.44 - ^{1}H NMR spectra of **H_4L**:**B** mixtures in ratios of 1:2 (purple), 1:1 (turquoise), 2:1 (green) and 1:0 (**black**) of **H_4L**:**B**, respectively, in $(CD_3)_2SO$.

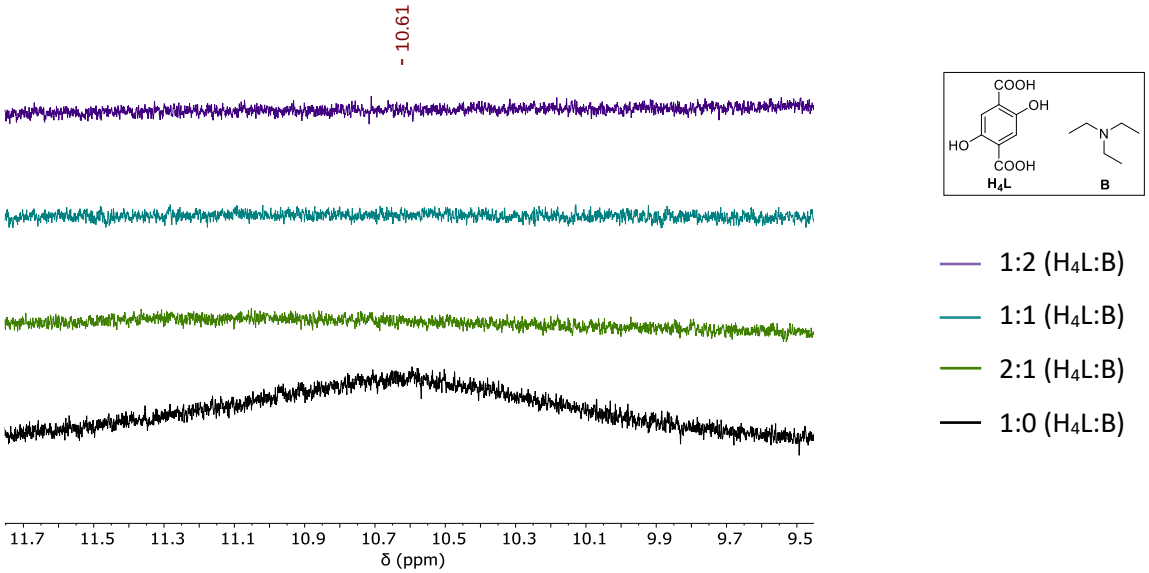

Figure A.45 - ^{1}H NMR spectra overlapping of **H_4L** and **B** mixtures in ratios of 1:2 (**purple**), 1:1 (**turquoise**), 2:1 (**green**) and 1:0 (**black**) of **H_4L:B**, respectively, in $(CD_3)_2SO$. Spectra were approximated in the range of 11.7-9.5 ppm.

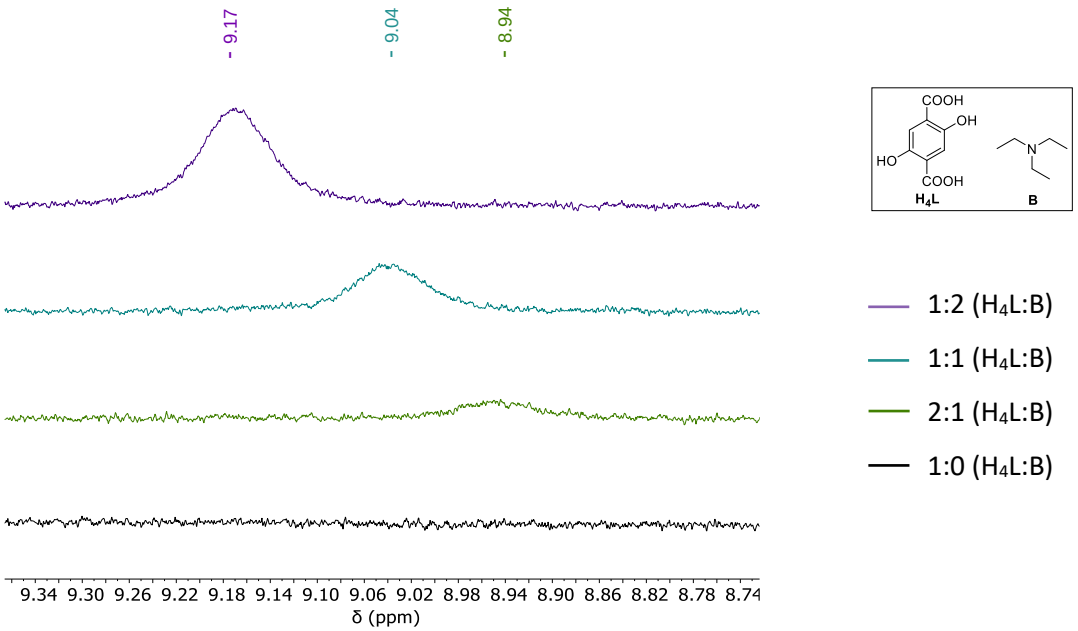

Figure A.46 - ^{1}H NMR spectra of **H_4L:B** mixtures in ratios of 1:2 (**purple**), 1:1 (**turquoise**), 2:1 (**green**) and 1:0 (**black**), respectively, in $(CD_3)_2SO$. Spectra were approximated in the range of 9.34-8.74 ppm.

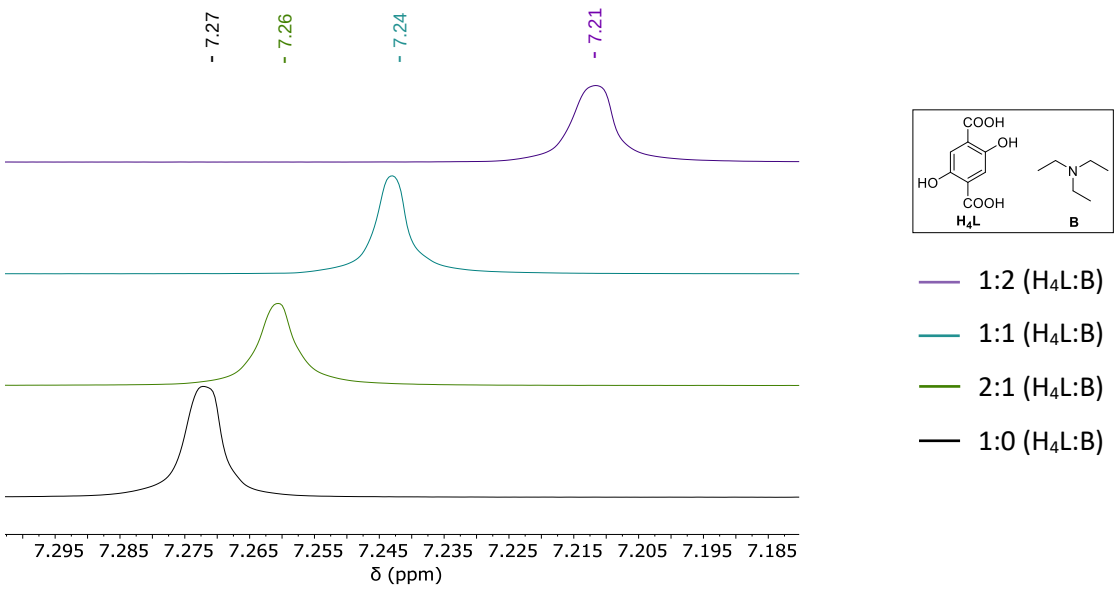

Figure A.47 - ^{1}H NMR spectra of **H$_4$L**:**B** mixtures in ratios of 1:2 (**purple**), 1:1 (**turquoise**), 2:1 (**green**) and 1:0 (**black**), respectively, in $(CD_3)_2SO$. Spectra were approximated in the range of 7.295-7.185 ppm.

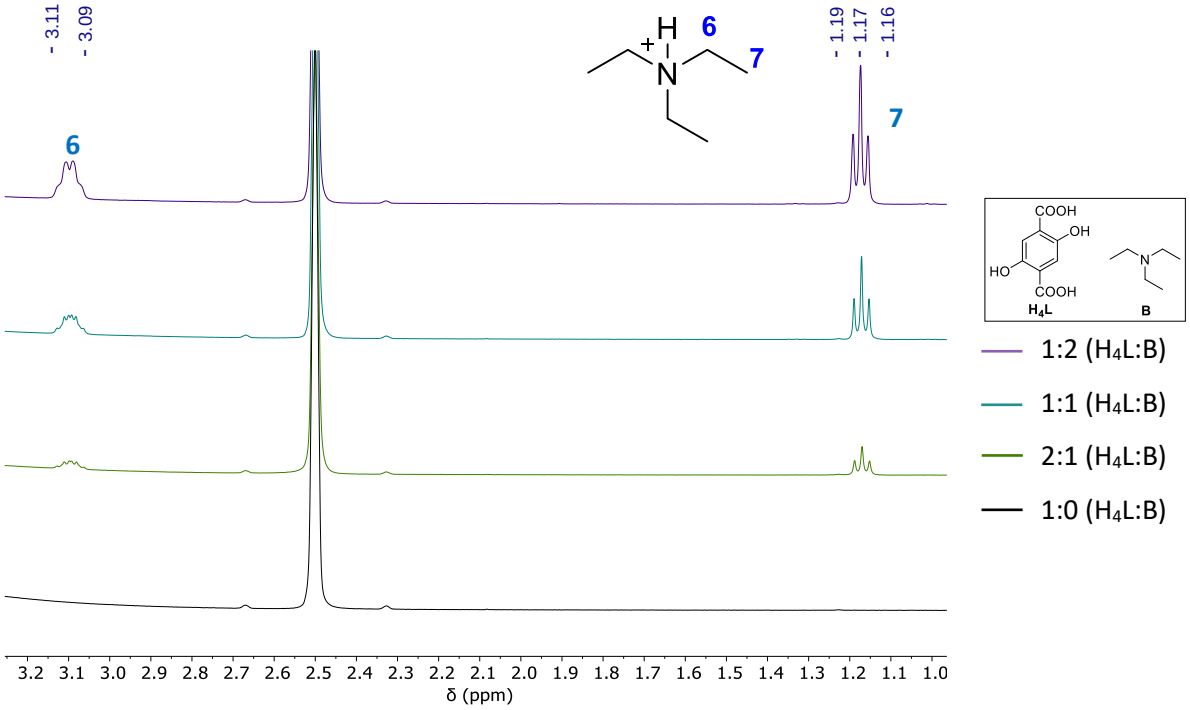

Figure A.48 - ^{1}H NMR spectra of **H$_4$L**:**B** mixtures in ratios of 1:2 (**purple**), 1:1 (**turquoise**), 2:1 (**green**) and 1:0 (**black**), respectively, in $(CD_3)_2SO$. Spectra were approximated in the range of 3.1-1.0 ppm.

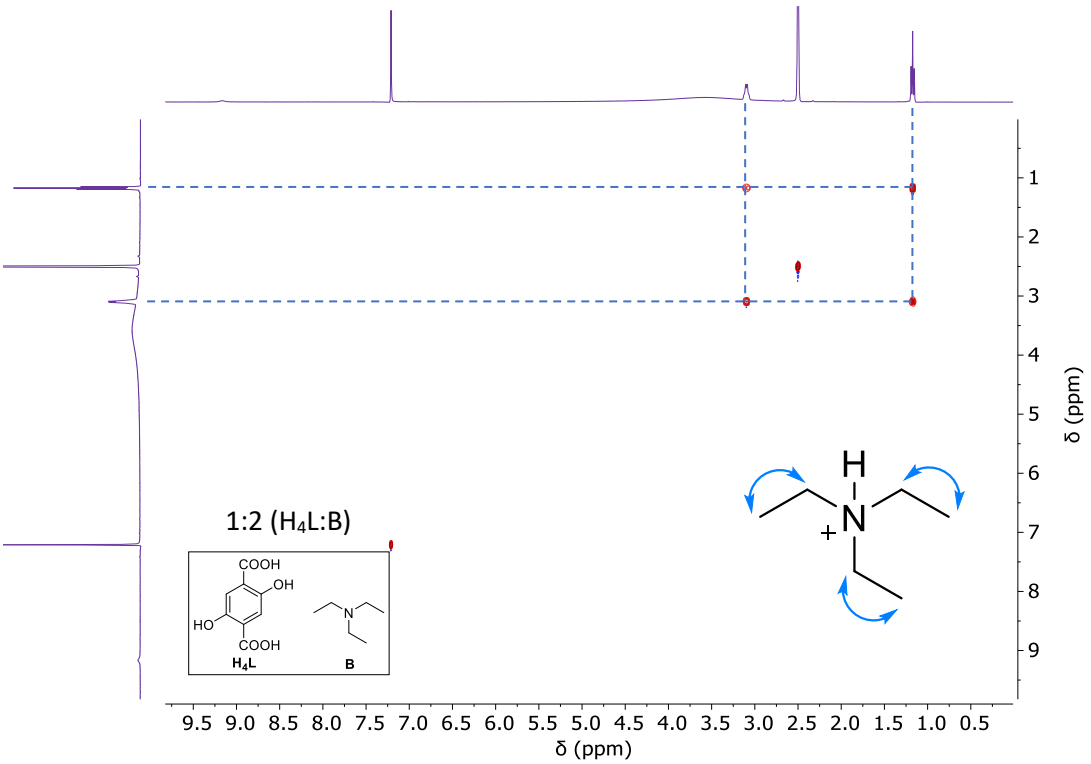

Figure A.49 - COSY spectrum of the **H_4L:B** mixture in a ratio of 1:2, respectively, in $(CD_3)_2SO$.

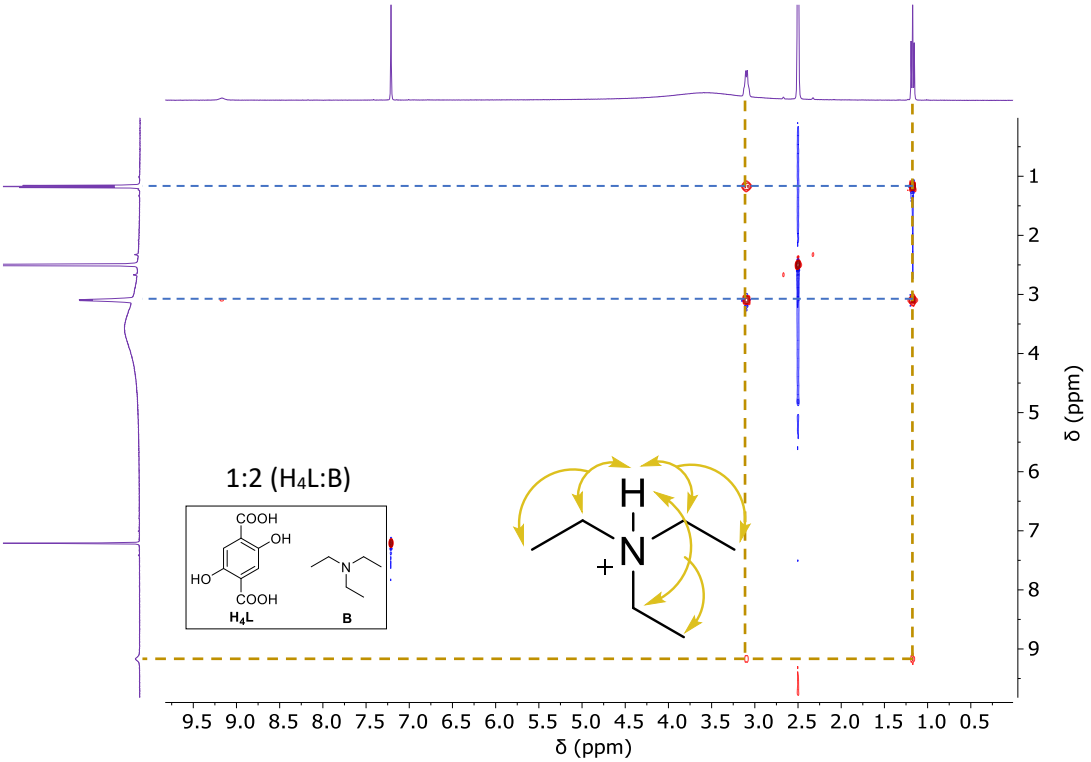

Figure A.50 - TOCSY spectrum of the **H_4L:B** mixture in a ratio of 1:2 , respectively, in $(CD_3)_2SO$.

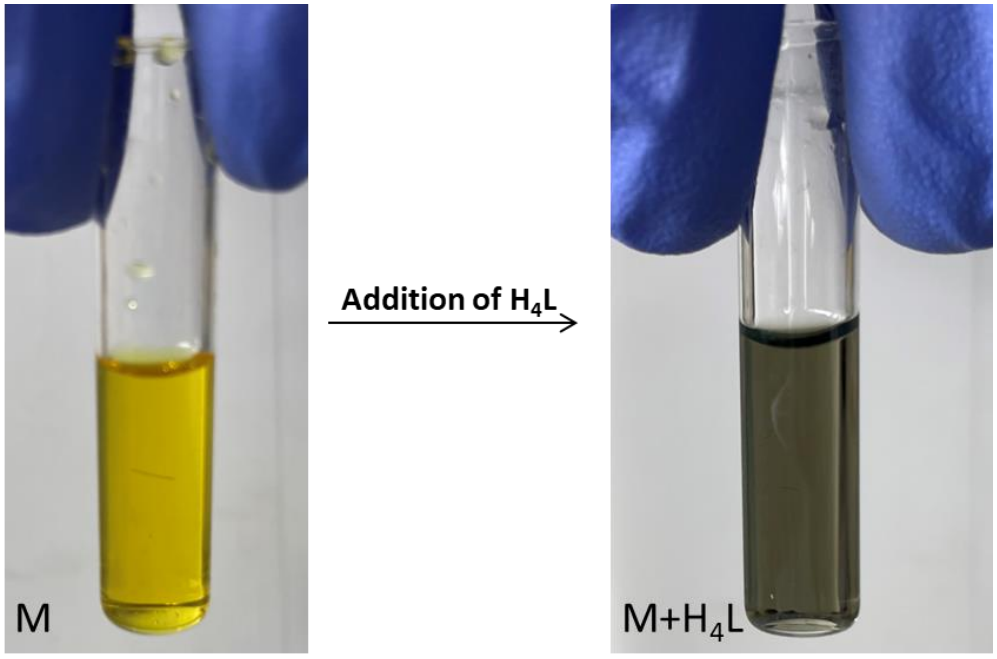

Figure A.51 - Colour differences of a **M** solution and a mixture of **M**+**H_4L**, in DMF Precursor quantities: 7 mM of **M** and 2 mM of **H_4L**.

Table A.10 - UV-vis peaks of **M**, **H_4L** and **L+M** spectra in DMF.

Sample	λ (nm)	C (mol.dm^{-3})	Abs	ε_{max} (dm^3.mol^{-1}.cm^{-1})
M	275	0.1 mM	0.898	8976
	325		0.622	6220
	360		0.361	3608
	522		0.054	538
L	369	0.1 mM	0.517	5170
L+M mixture (1:1)	298	0.1 mM L + 0.1 mM M	0.771	3855
	316		0.738	3690
	364		0.883	4415
	580		0.107	535

Table A.11 - UV-vis peaks from the overlayed spectra of the **H_4L+M** mixture with different **M** concentrations in DMF.

λ (nm)	C (mol.dm^{-3})	Abs	ε_{max} (dm^3.mol^{-1}.cm^{-1})
~580	0.1 mM L + 0.025 mM M	0.064	511
	0.1 mM L + 0.050 mM M	0.086	574
	0.1 mM L + 0.075 mM M	0.099	566
	0.1 mM L + 0.100 mM M	0.107	534
	0.1 mM L + 0.125 mM M	0.133	591
	0.1 mM L + 0.150 mM M	0.157	628
	0.1 mM L + 0.175 mM M	0.164	596
	0.1 mM L + 0.200 mM M	0.148	494
	0.1 mM L + 0.225 mM M	0.161	495
	0.1 mM L + 0.250 mM M	0.170	486
	0.1 mM L + 0.275 mM M	0.164	438

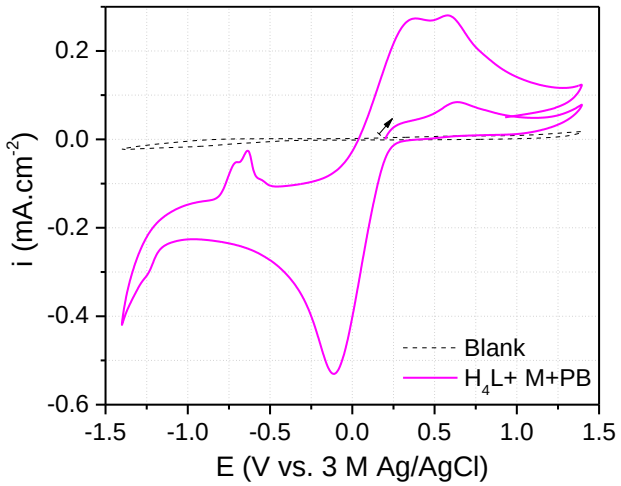

Figure A.52 - Cyclic voltammogram of the **H_4L**+**M**+**PB** mixture. Species were added in 10 mL of N_2 saturated DMF with $TBAPF_6$ as the supporting electrolyte and recorded at 100 $mV.s^{-1}$. The one-compartment electrochemical cell was also constituted by FTO as working, platinum wire as counter and 3 M Ag/AgCl as reference electrodes. Species quantities: 4 mM of **M**, 2 mM **H_4L** and 2 mM of **PB**.

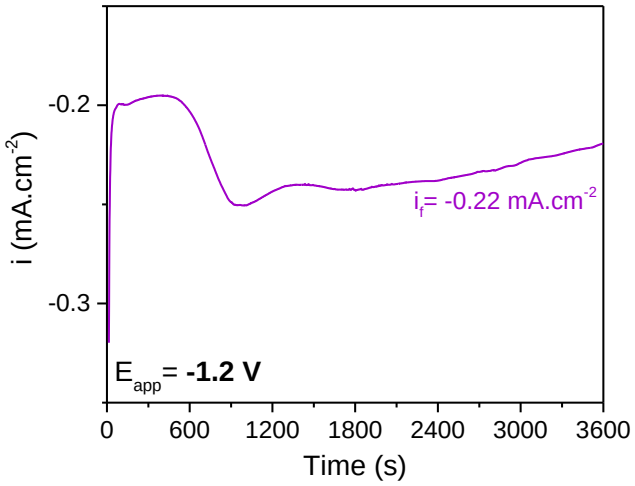

Figure A.53 - Chronoamperogram following the electrodeposition of the **Fe/L** film with a growth potential of -1.2 V. Electrodepositions were performed in 10 mL of N_2 saturated DMF with $TBAPF_6$ as the supporting electrolyte and recorded at 100 $mV.s^{-1}$. The one-compartment electrochemical cell was also constituted by FTO as working, platinum wire as counter and 3 M Ag/AgCl as reference electrodes. Species quantities: 4 mM of **M**, 2 mM of **H_4L** and 2 mM of **PB**.

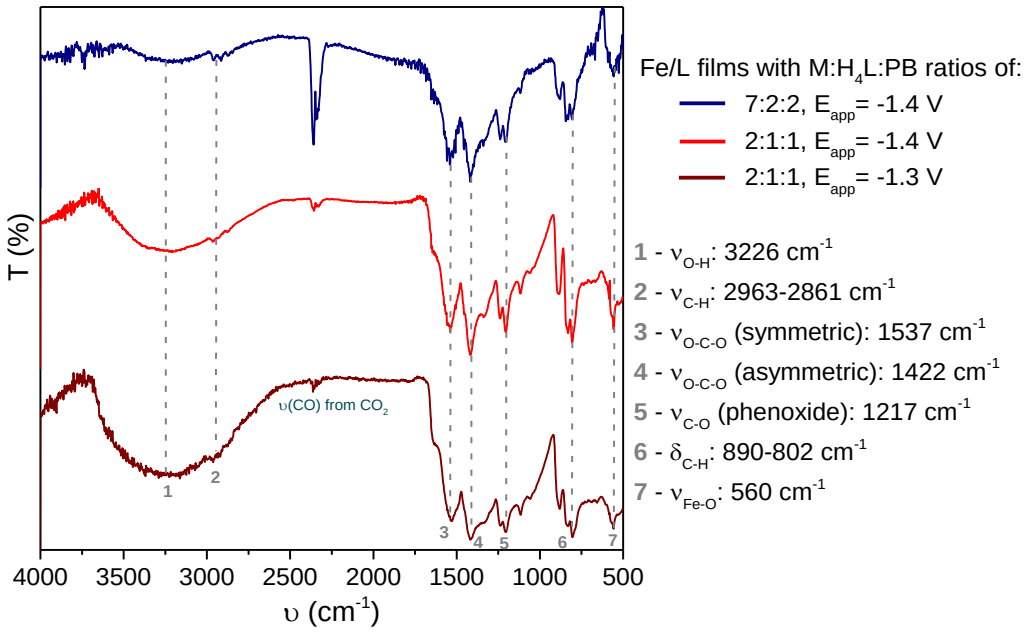

Figure A.54 - DRIFT spectra of the **Fe/L** film (7:2:2 ratio of **M**:**H4L**:**PB**, respectively) deposited at -1.4 V (**blue**) and the **Fe/L** films (2:1:1 ratio of **M**:**H4L**:**PB**, respectively) deposited at -1.4 (**red**) and -1.3 V (**burgundy**) for 1 hour. Spectra were obtained in a range of 4000-500 cm^{-1} and blank was measured with a gold coated plate.

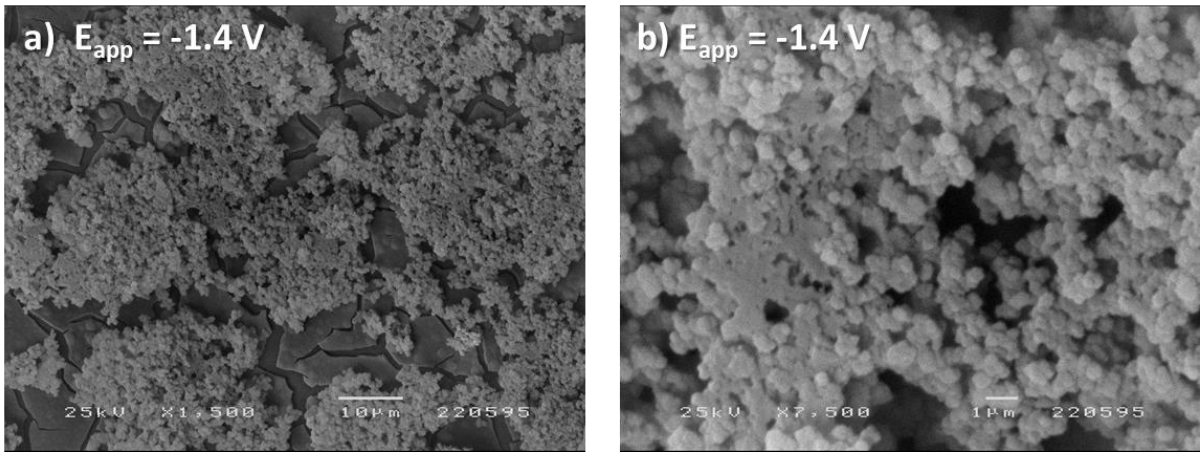

Figure A.55 - SEM images of the **Fe/L** film (2:1:1 ratio of **M**:**H4L**:**PB**, respectively) deposited at -1.4 V and magnified at a) x1500 and b) x7500.

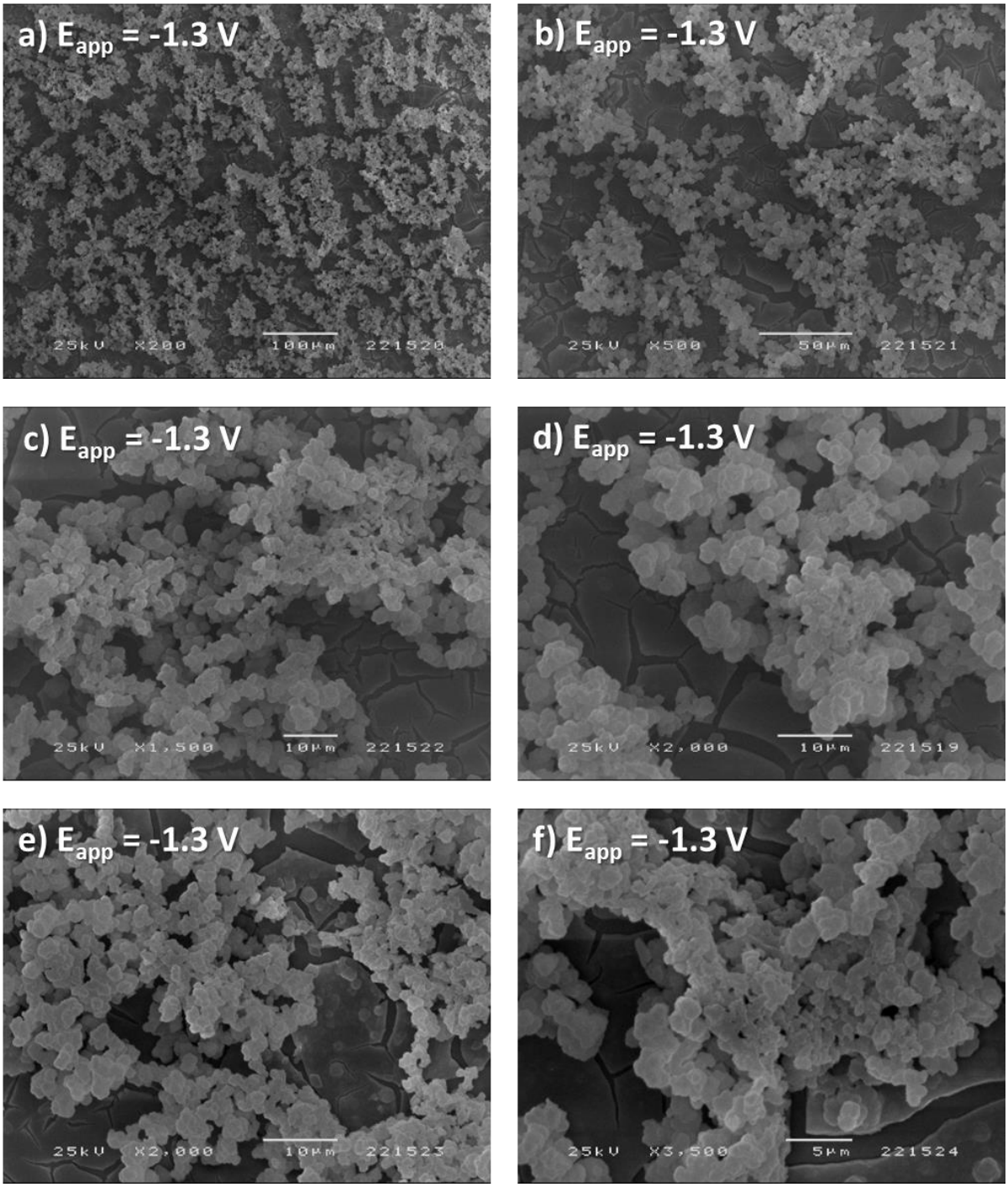

Figure A.56 - SEM images of the **Fe/L** film (2:1:1 ratio of **M:H_4L:PB**, respectively) deposited at -1.3 V and magnified at a) x200, b) x500, c) x1500, d) x2000, e) x2000 and f) x3500.

Table A.12 - Peak deconvolution of C 1s, Fe 2p and O 1s from the XPS survey spectra of the **Fe/L** films (2:1:1 ratio of **M**:**H_4L**:**PB**, respectively) deposited at -1.4 and -1.3 V.

	Fe/L film (-1.4 V)	Fe/L film (-1.3 V)	Attribution
C 1s	285.0	285.0	C-C and C-H
	286.5	286.9	C-O^-
	288.7	288.8	O=C-O^-
Fe 2p	707.4	709.6	FeO
	710.2	-	$Fe(OH)_2$
	711.7	711.2	Fe_3O_4
	-	712.4	Fe_2O_3
	713.6	713.6	$Fe(OH)_3$
	-	715.0	Satellite
	-	717.9	Satellite
O 1s	530.3	-	O-Fe
	531.8	531.6	$^-$O-C=O
	532.4	532.5	O-C

Table A.13 - Atomic concentration (%) of Fe, C and O of the **Fe/L** films (2:1:1 ratio of **M:H_4L:PB,** respectively) deposited at -1.4 and -1.3 V.

	Fe/L film (-1.4 V)	Fe/L film (-1.3 V)	Theorical for Fe_2L
Fe	4.9	3.5	12.5
C	46.4	54.5	50
O	42.7	35.0	37.5

Table A.14 - Structural suggestions based on the elemental composition of the **Fe/L** film (2:1:1 ratio of **M:H_4L:PB,** respectively) deposited at -1.3 V.

	Found (wt%)	Theory for $Fe_2(L)(DMF)_2$ or $C_{14}H_{16}Fe_2N_2O_8$	Theory for $Fe_2(L)(Et_3N)_2$ or $C_{20}H_{32}Fe_2N_2O_6$	Theory for $Fe_2(L)(H_2O)_2$ or $C_8H_6Fe_2O_8$
C	**14.98**	37.20	47.27	28.11
N	**0.84**	6.20	5.51	0
H	**1.79**	3.57	6.35	1.77

Table A.15 - Additional structural suggestions based on the elemental composition of the **Fe/L** film (2:1:1 ratio of **M:H_4L:PB**, respectively) deposited at -1.3 V.

	Found (wt%)	Theory for $Fe_{14}(L)_7Cl_7(DMF)_3(OH)_4(Fe_2O_3)_8[Fe(OH)_3]_{12}$ or $C_{65}H_{75}Cl_7Fe_{42}N_3O_{109}$	Theory for $Fe_{14}(L)_7Cl_7(DMF)_3(OH)_4(Fe_2O_3)_{13}(H_2O)_{26}$ or $C_{65}H_{91}Cl_7Fe_{40}N_3O_{114}$	Theory for $Fe_{14}(L)_7Cl_{10}(DMF)_3(OH)(H_2O)[Fe(OH)_3]_{23}$ or $C_{65}H_{107}Cl_{10}Fe_{37}N_3O_{116}$
C	**14.98**	14.91	14.96	14.99
N	**0.84**	0.80	0.80	0.81
H	**1.79**	1.44	1.76	2.07

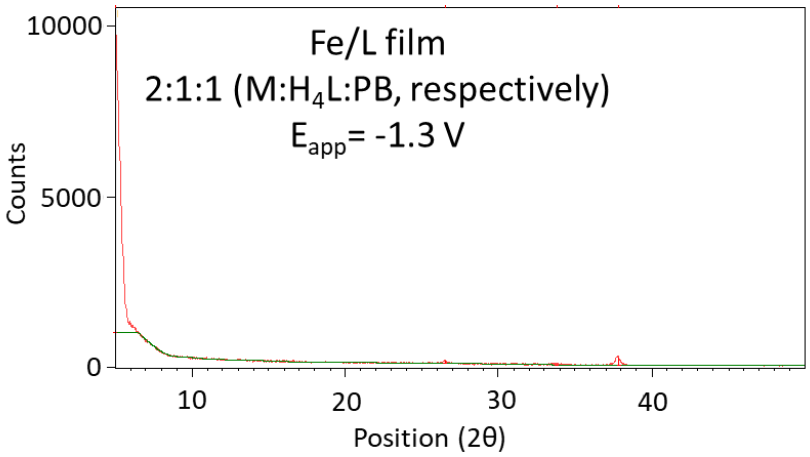

Figure A.57 - Diffractogram of the **Fe/L** film (2:1:1 ratio of **M:H_4L:PB**, respectively) deposited at -1.3 V.

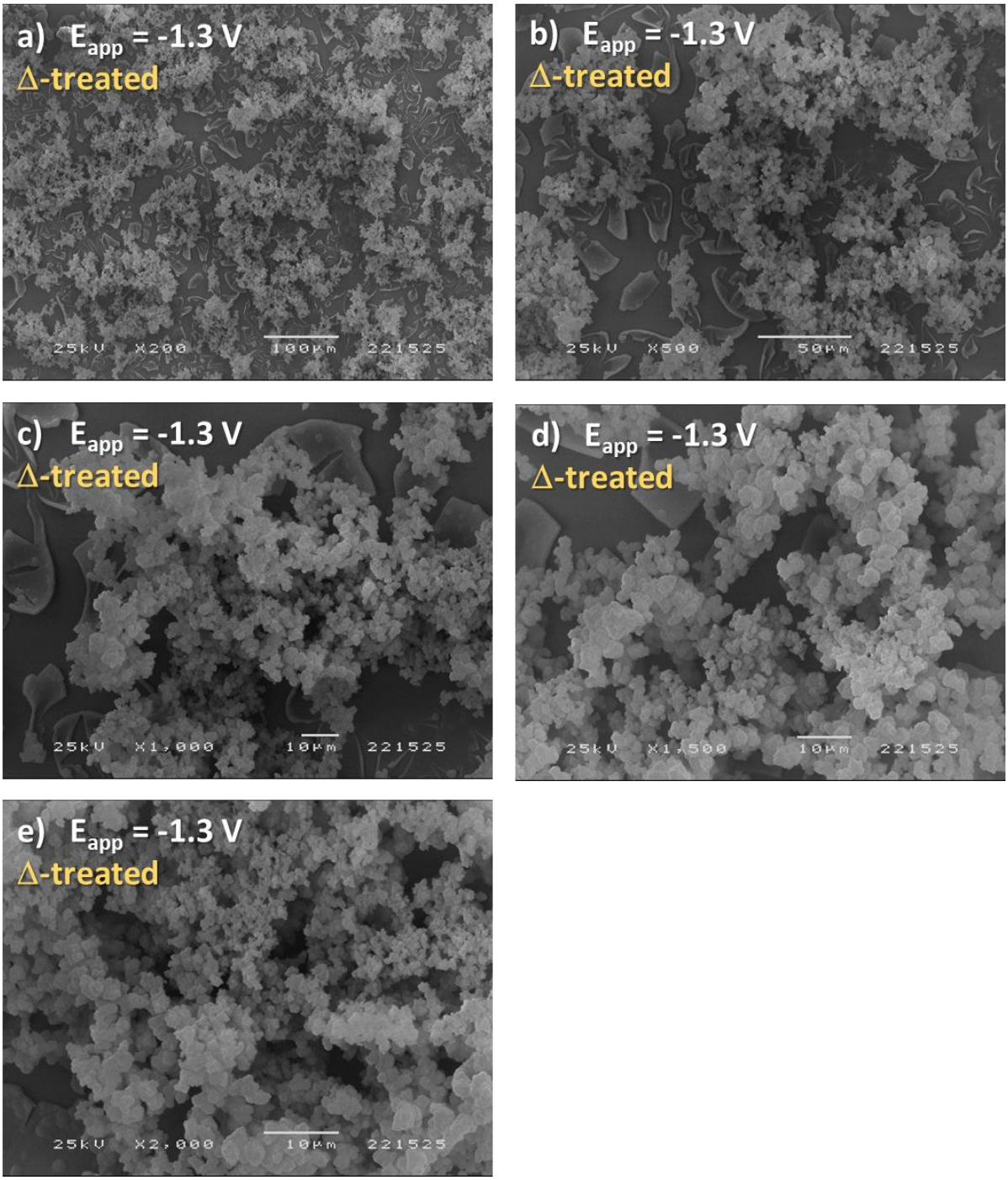

Figure A.58 - SEM images of the temperature-treated **Fe/L** film (2:1:1 ratio of **M:H_4L:PB**, respectively) deposited at -1.3 V, magnified at a) x200, b) x500, c) x1000, d) x1500 and e) x2000.

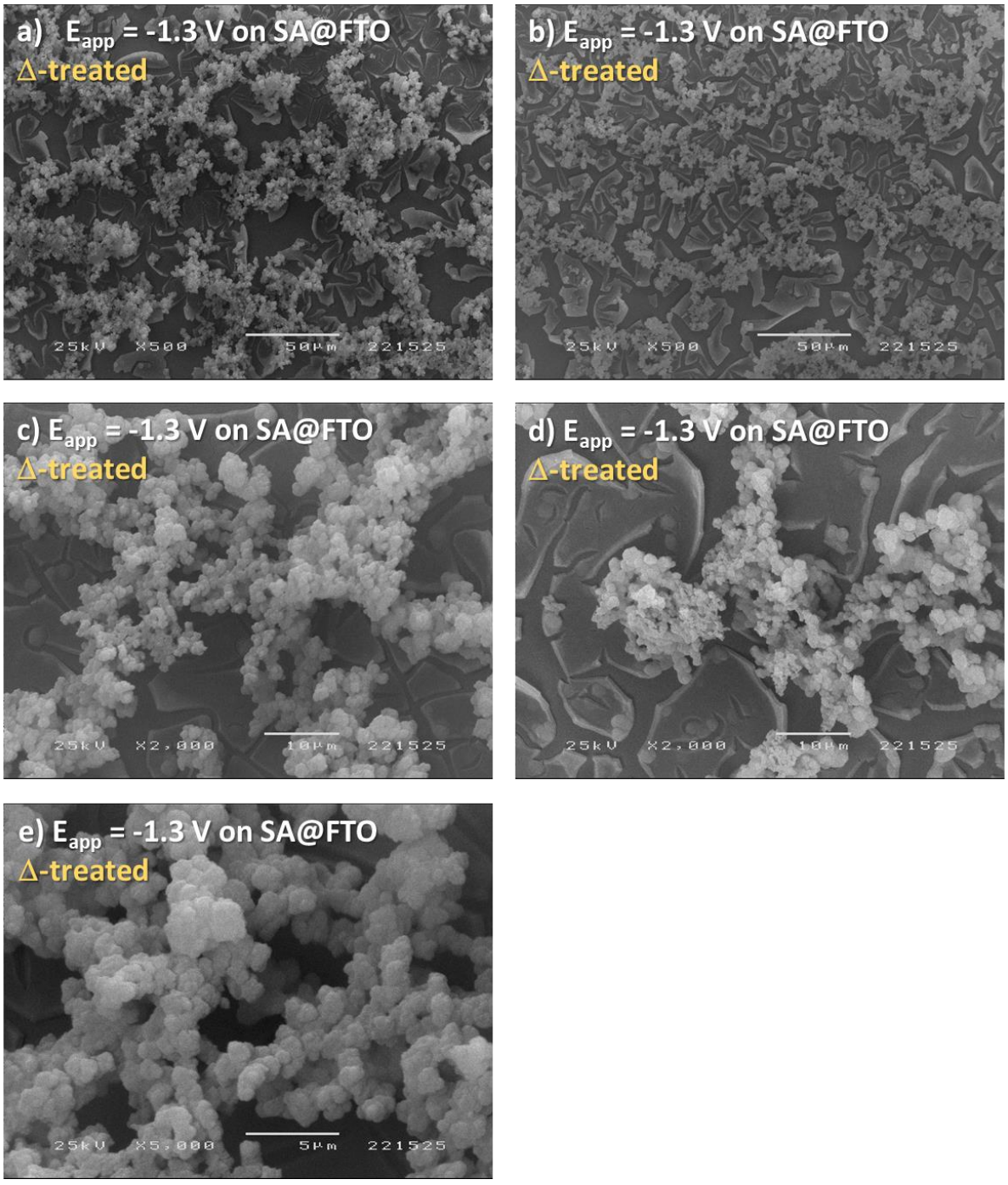

Figure A.59 - SEM images of the temperature-treated **Fe/L** film (2:1:1 ratio of **M:H_4L:PB**, respectively) deposited at -1.3 V on SA@FTO after, magnified at a) x500, b) x500, c) x2000, d) x2000 and e) x5000.

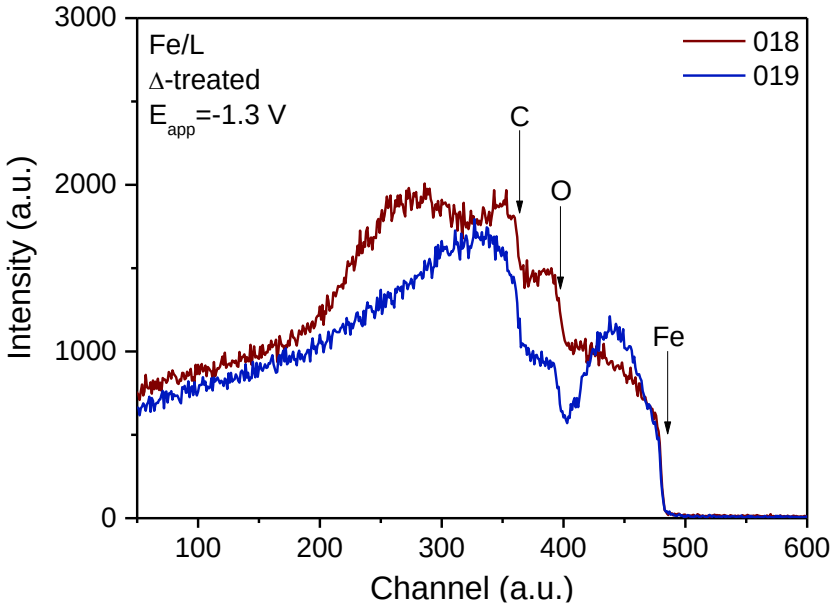

Figure A.60 - RBS spectra (beam dimension: 3x4 μm^2) obtained by different zones of the temperature-treated **Fe/L** film (2:1:1 ratio of **M:H4L:PB**, respectively) deposited at -1.3 V, identified as 018 and 019.

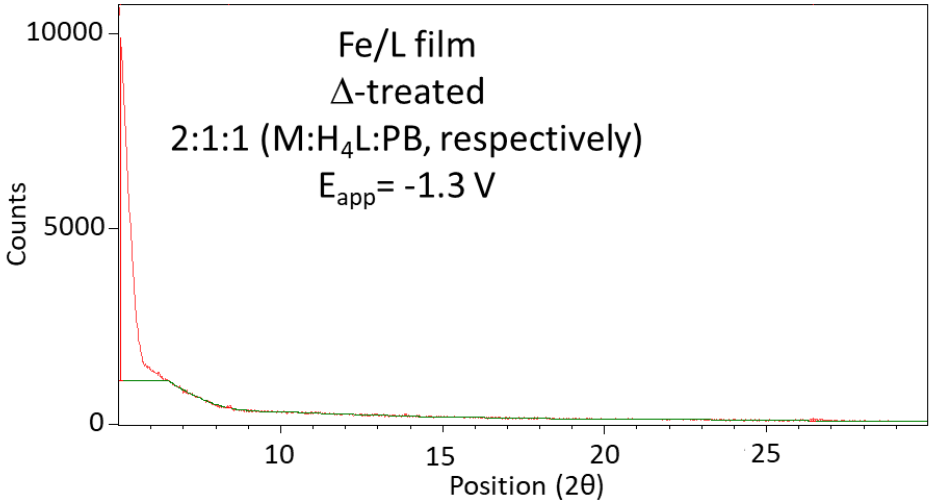

Figure A.61 - Diffractogram of the temperature-treated **Fe/L** film (2:1:1 ratio of **M:H4L:PB**, respectively) deposited at -1.3 V.

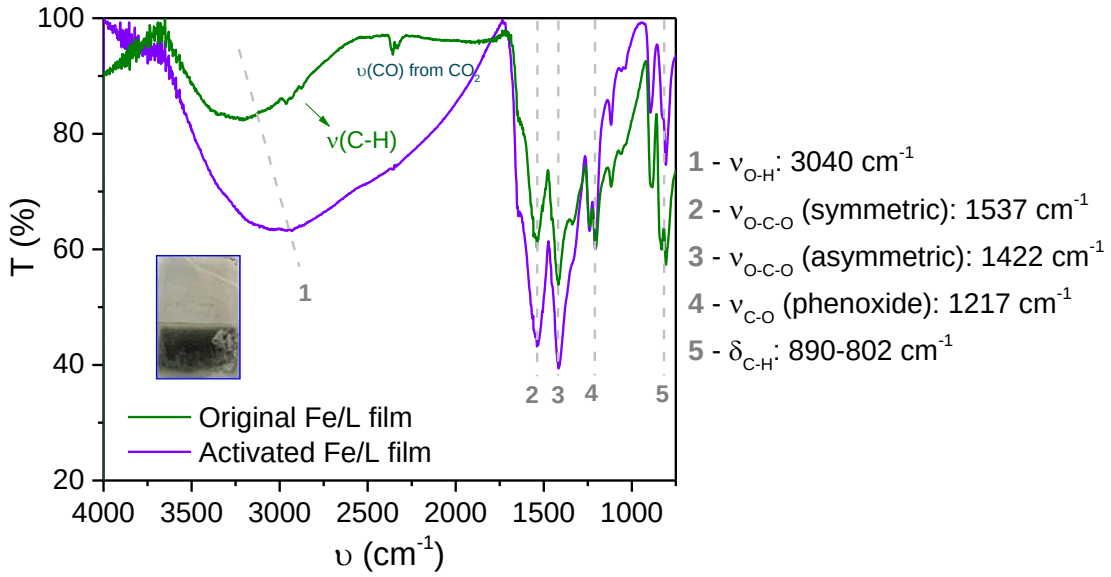

Figure A.62 - DRIFT spectra of the original (green) and activated (blue) **Fe/L** films (2:1:1 ratio of **M:H4L:PB**, respectively) deposited at -1.3 V. Spectra were recorded in a range of 4000-750 cm^{-1} and the blank was measured with a gold coated plate.

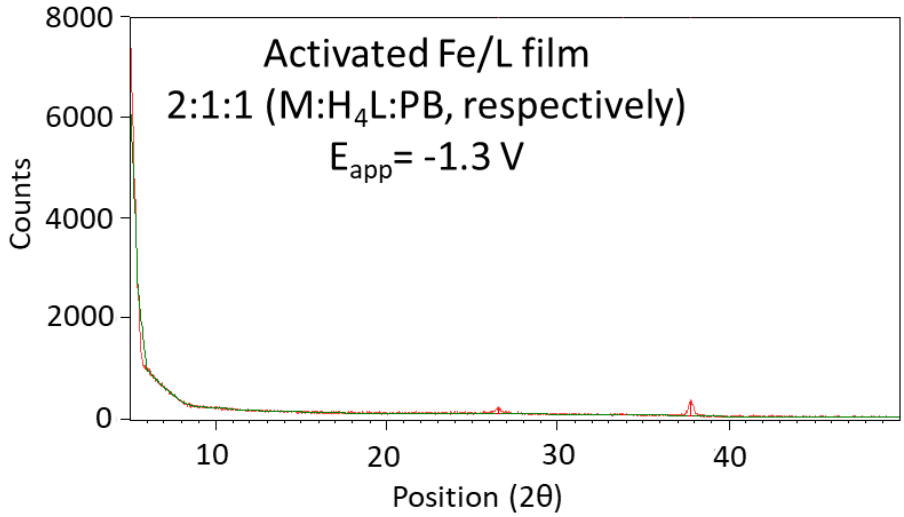

Figure A.63 - Diffractogram of the activated **Fe/L** film (2:1:1 ratio of **M:H4L:PB**, respectively) deposited at -1.3 V.

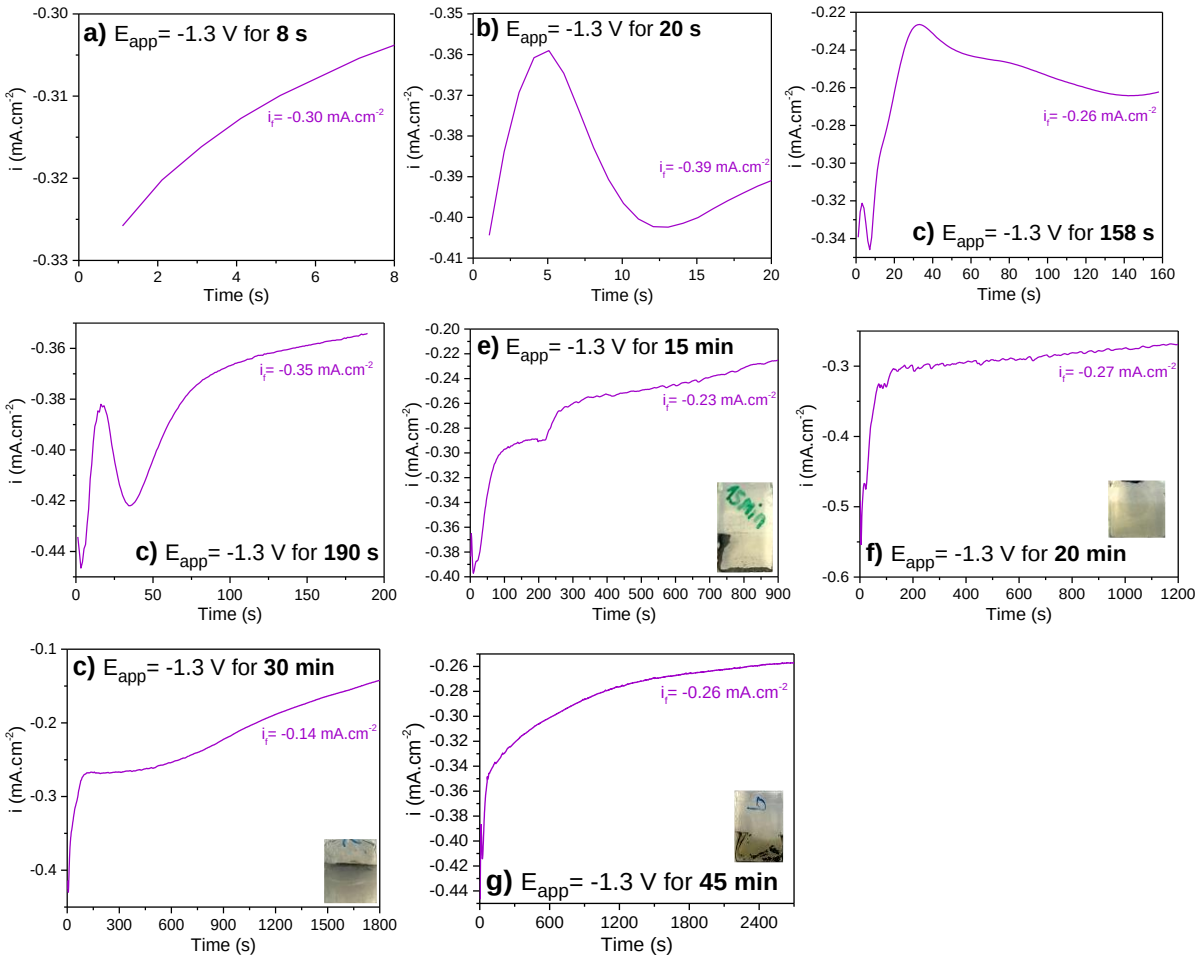

Figure A.64 - Chronoamperogram following the deposition of the **Fe/L** films at -1.3 V for a) 8 seconds; b) 20 seconds; c) 158 seconds; d) 190 seconds; e) 15 minutes; f) 20 minutes; g) 30 minutes; g) 45 minutes. Electrodepositions were performed in 10 mL of N_2 saturated DMF with $TBAPF_6$ as the supporting electrolyte and recorded at 100 $mV.s^{-1}$. The one-compartment electrochemical cell was also constituted by FTO as working, platinum wire as counter and 3 M Ag/AgCl as reference electrodes. Species quantities: 4 mM of **M**, 2 mM of **H_4L** and 2 mM of **PB**.

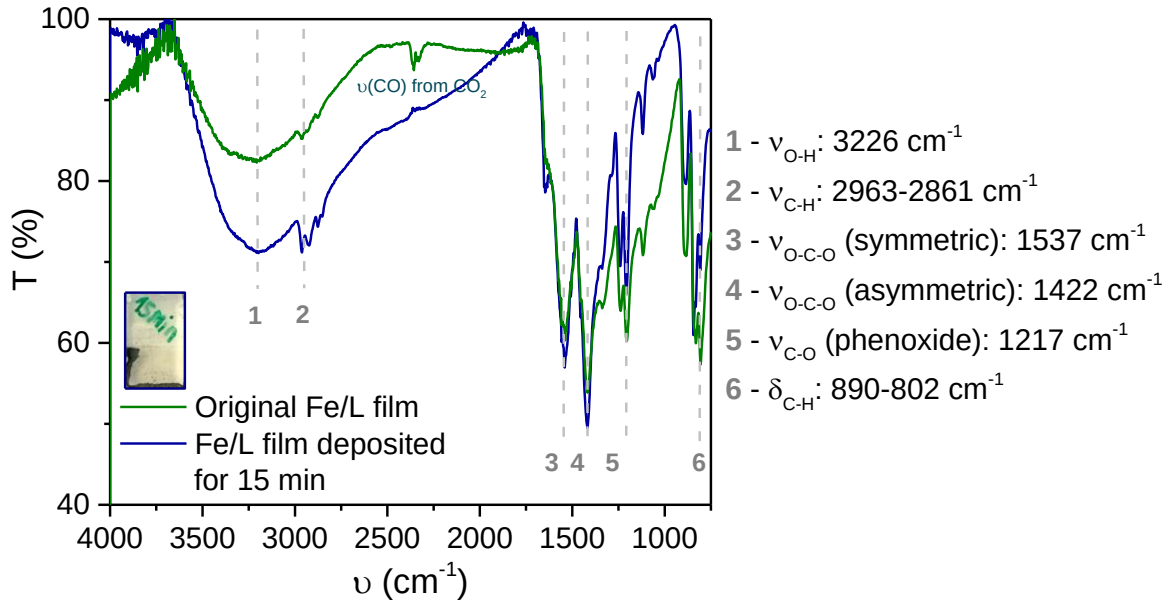

Figure A.65 - DRIFT spectra of original (green) and 15-minute (blue) **Fe/L** films (2:1:1 ratio of **M:H4L:PB**, respectively) deposited at -1.3 V. Spectra were recorded in a range of 4000-750 cm^{-1} and the blank was measured with a gold coated plate.

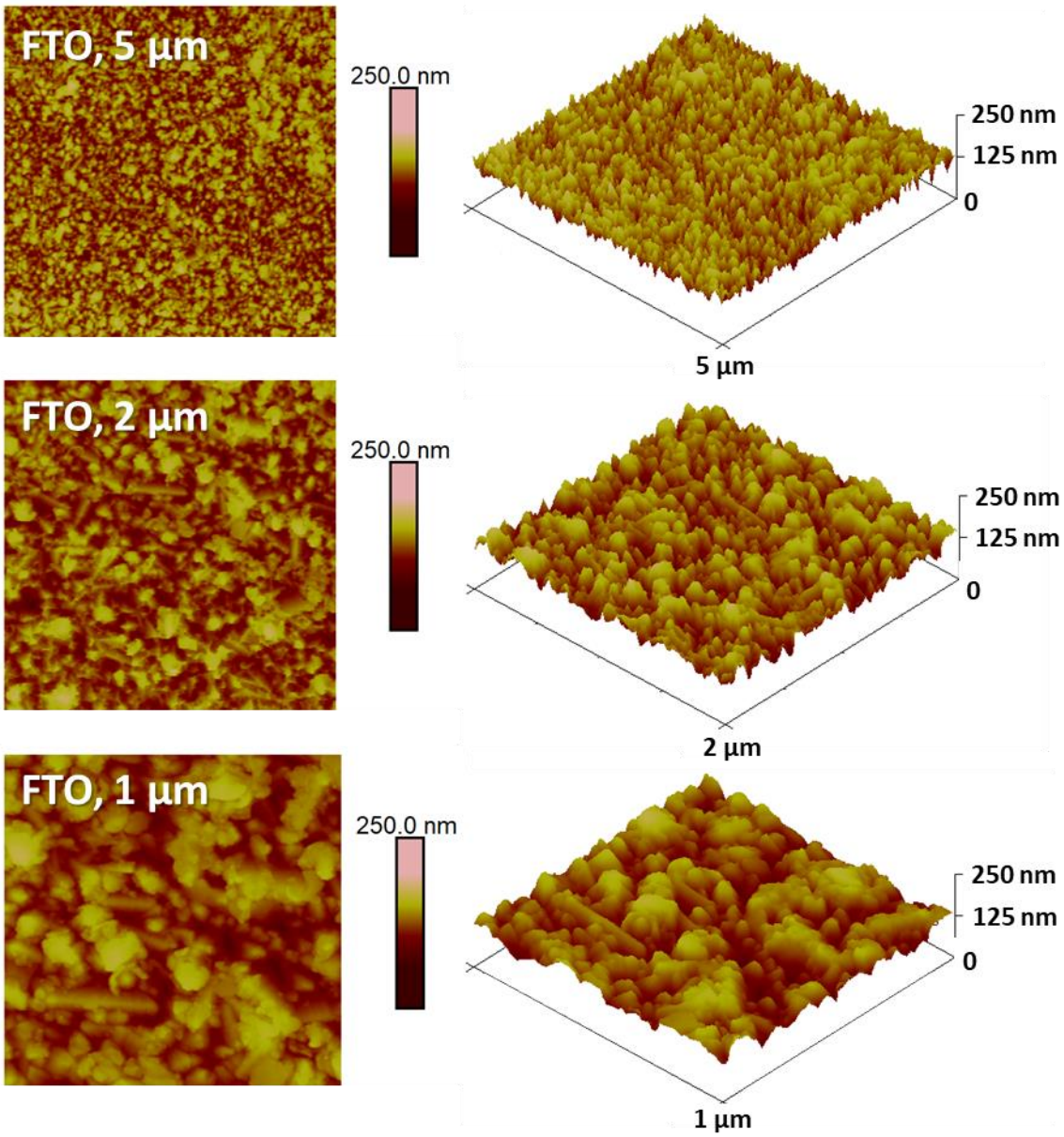

Figure A.66 - 2D and 3D AFM images of the FTO electrode with dimensions of 1x1 µm, 2x2 µm and 5x5 µm.

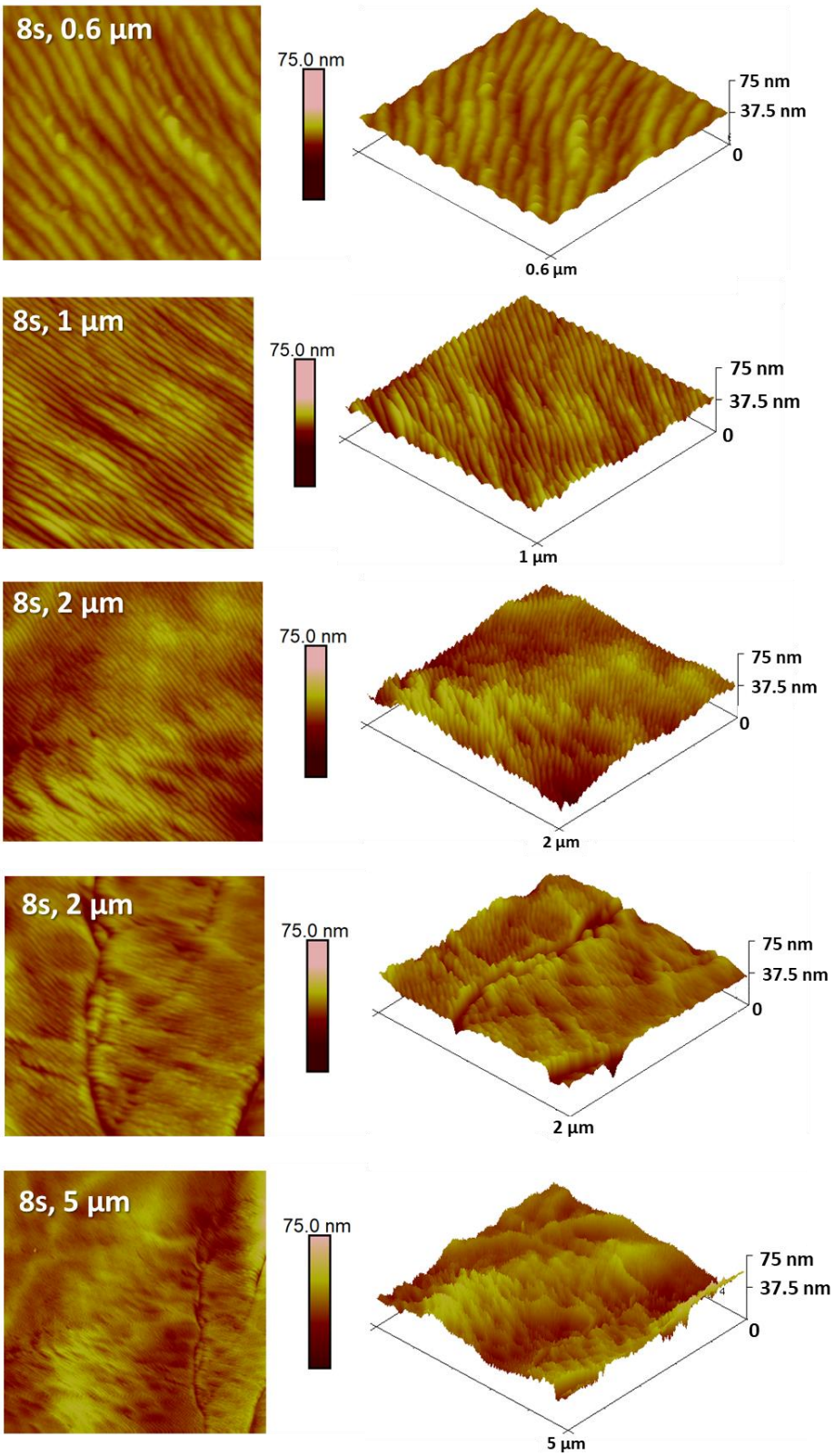

Figure A.67 - 2D and 3D AFM images of the **Fe/L** film (2:1:1 ratio of **M:H4L:PB**, respectively) deposited at -1.3 V for 8 seconds, with dimensions of 0.6x0.6 µm, 1x1 µm, 2x2 µm and 5x5 µm.

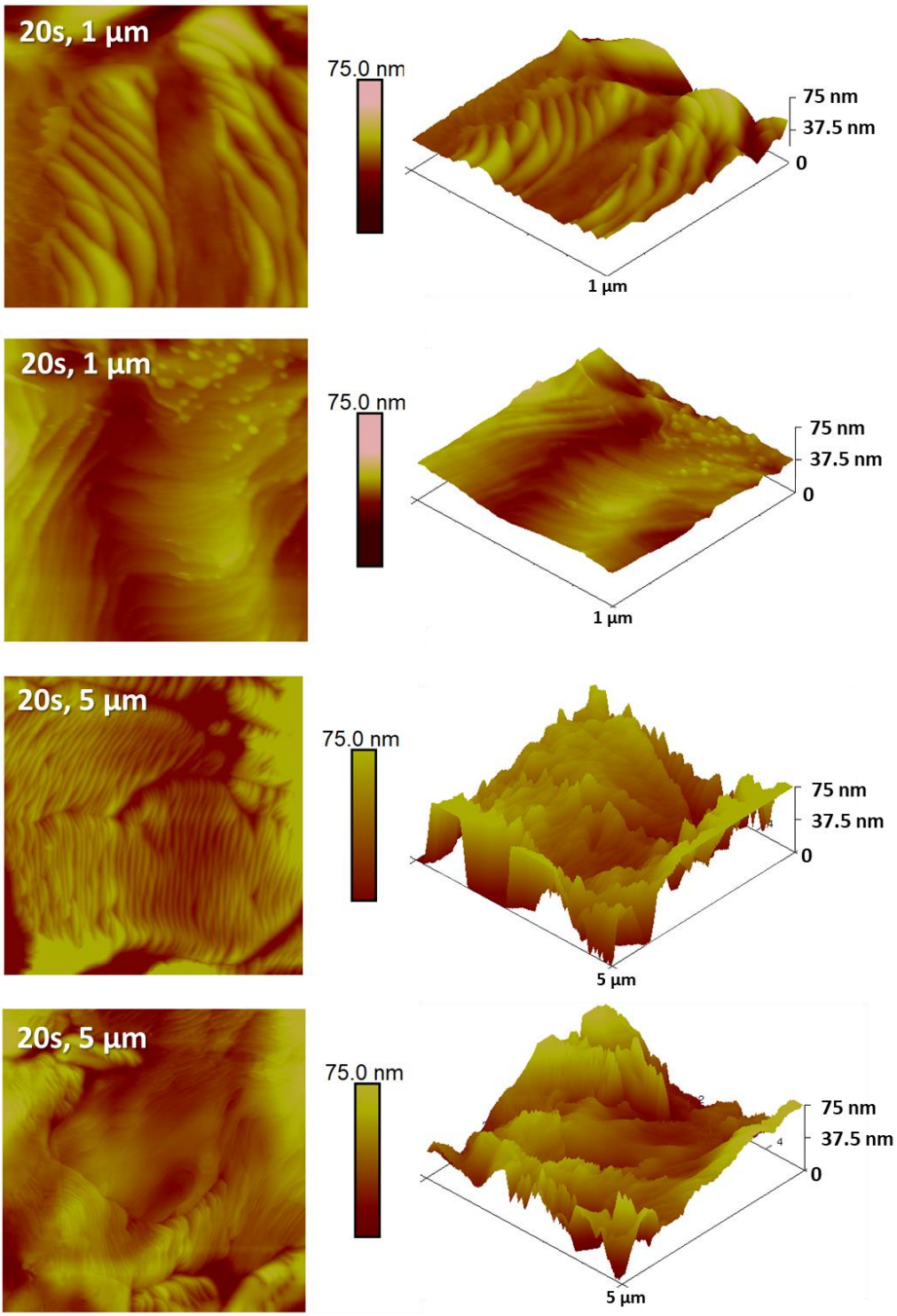

Figure A.68 - 2D and 3D AFM images of the **Fe/L** film (2:1:1 ratio of **M:LH4:PB**, respectively) deposited at -1.3 V for 20 seconds, with dimensions of 1x1 µm, and 5x5 µm.

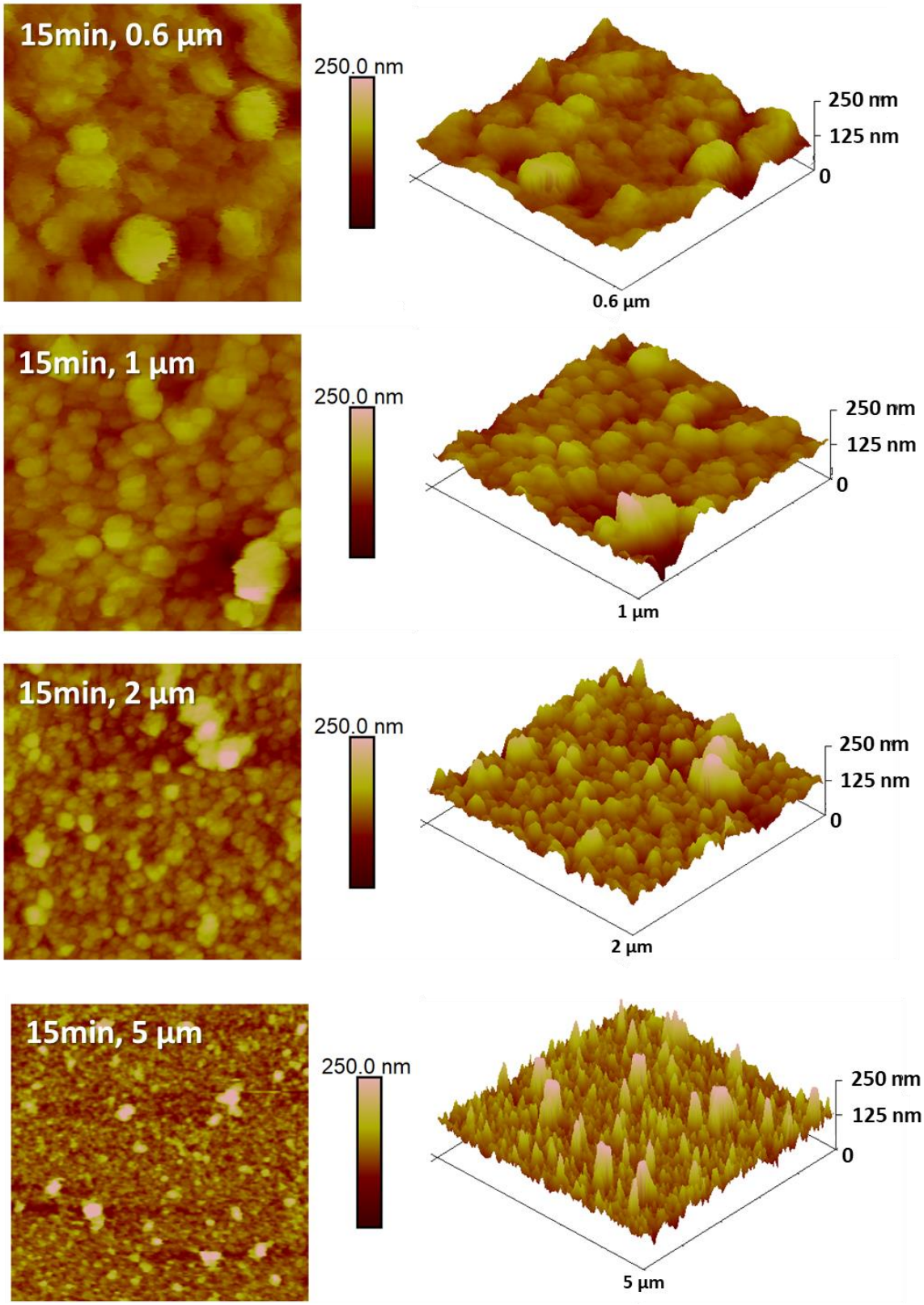

Figure A.69 - 2D and 3D AFM images of the **Fe/L** film (2:1:1 ratio of **M:H_4L:PB**, respectively) deposited at -1.3 V for 15 minutes, with dimensions of 0.6x0.6 µm, 1x1 µm, 2x2 µm and 5x5 µm.

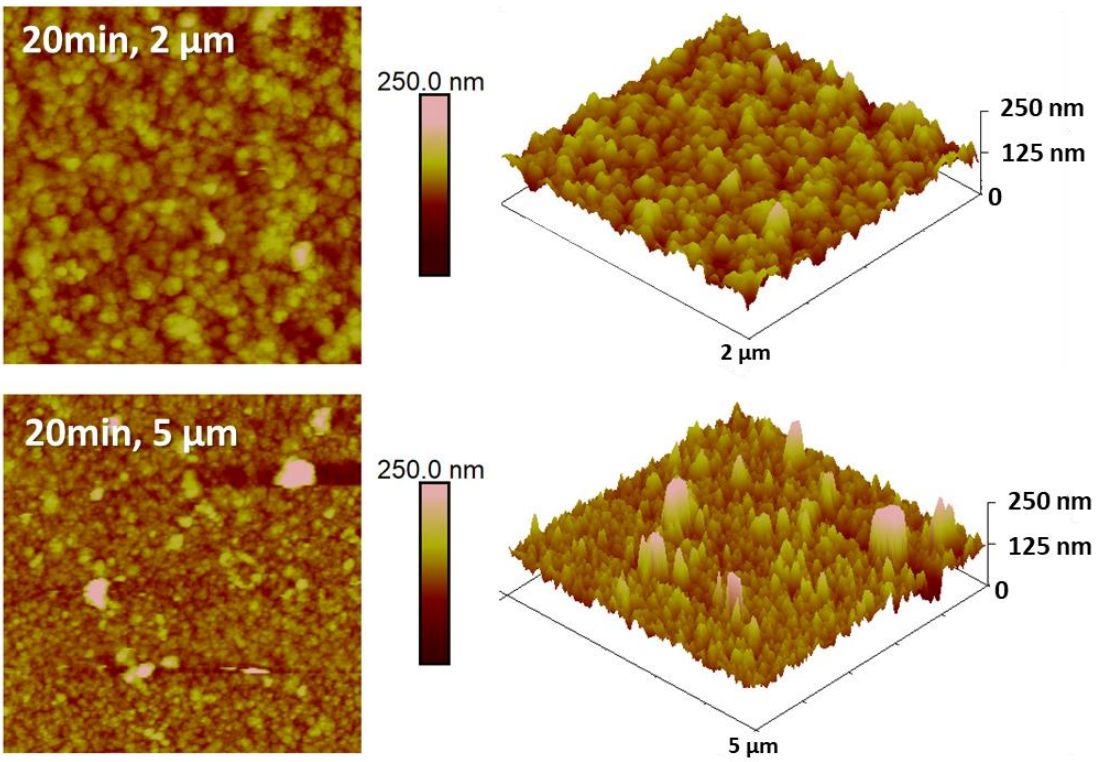

Figure A.70 - 2D and 3D AFM images of the **Fe/L** film (2:1:1 ratio of **M:H4L:PB**, respectively) deposited at -1.3 V for 20 minutes, with dimensions of 2x2 µm and 5x5 µm.

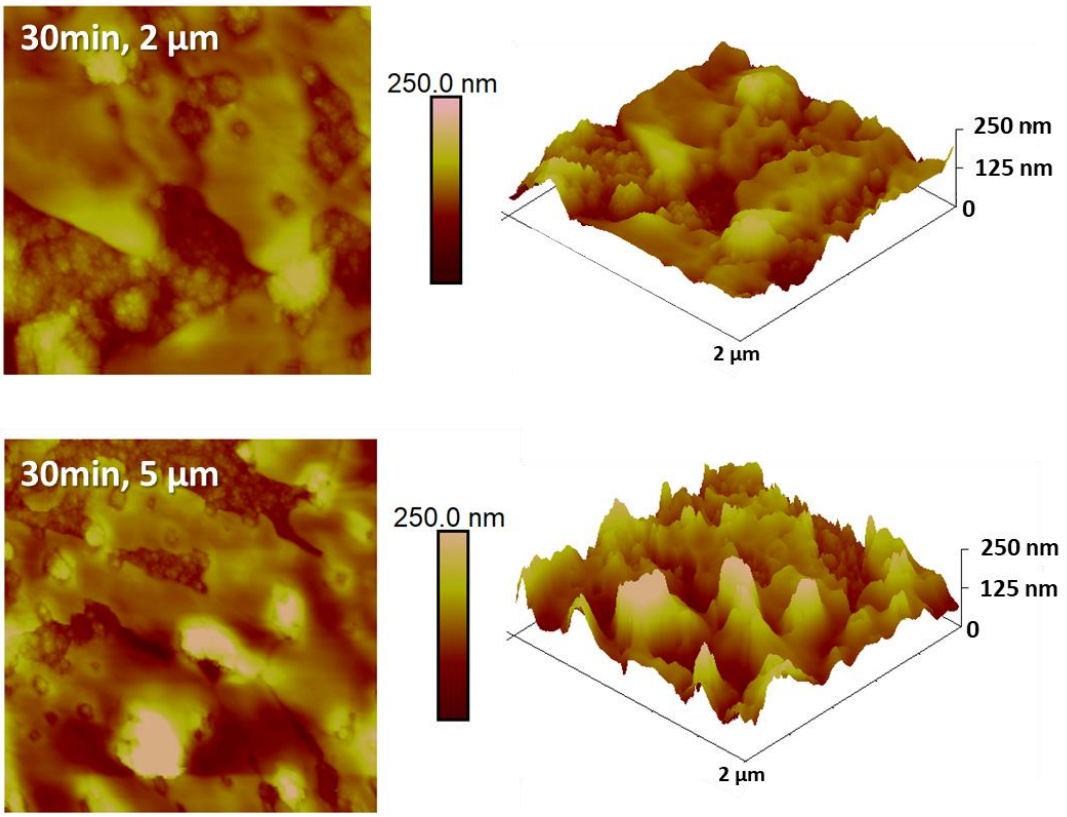

Figure A.71 - 2D and 3D AFM images of the **Fe/L** film (2:1:1 ratio of **M:H4L:PB**, respectively) deposited at -1.3 V for 30 minutes, with dimensions of 2x2 µm and 5x5 µm.

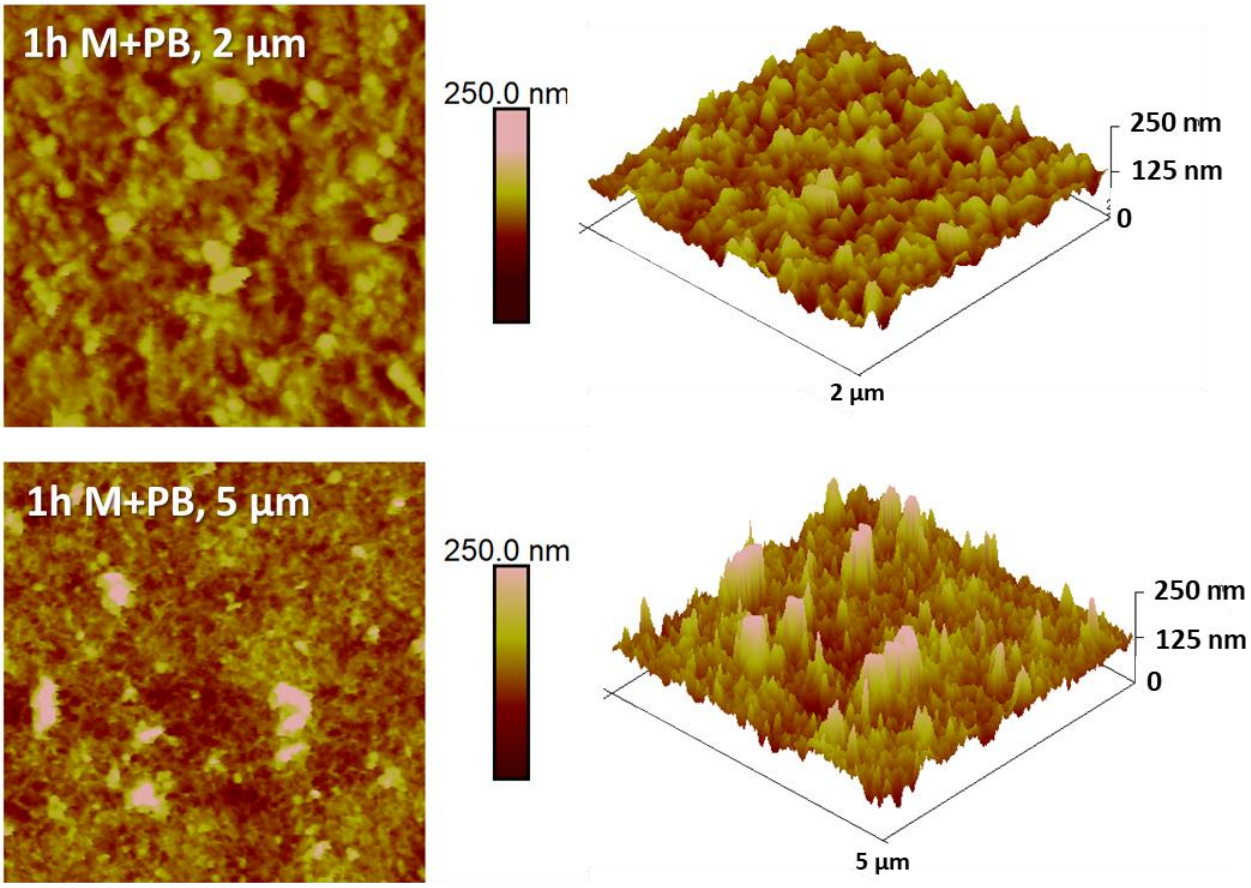

Figure A.72 - 2D and 3D AFM images of the **M+PB** film (2:1 ratio of **M:PB**, respectively) deposited at -1.3 V for 1 hour, with dimensions of 2x2 µm and 5x5 µm.

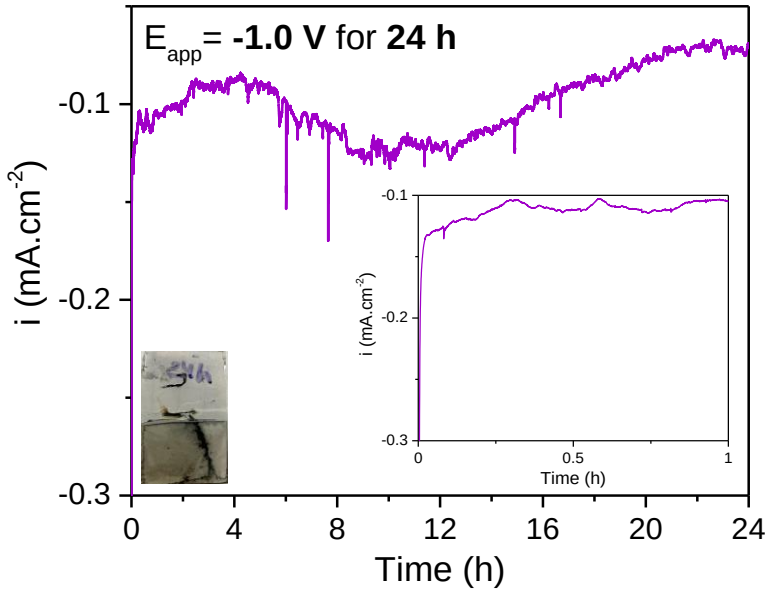

Figure A.73 - Chronoamperograms following the deposition of the **Fe/L** film with a growth potential of -1.0 V. Electrodepositions were performed in 10 mL of N_2 saturated DMF with $TBAPF_6$ as the supporting electrolyte and recorded at 100 $mV.s^{-1}$. The one-compartment electrochemical cell was also constituted by FTO as working, platinum wire as counter and 3 M Ag/AgCl as reference electrodes. Species quantities: 4 mM of **M**, 2 mM of **H_4L** and 2 mM of **PB**.

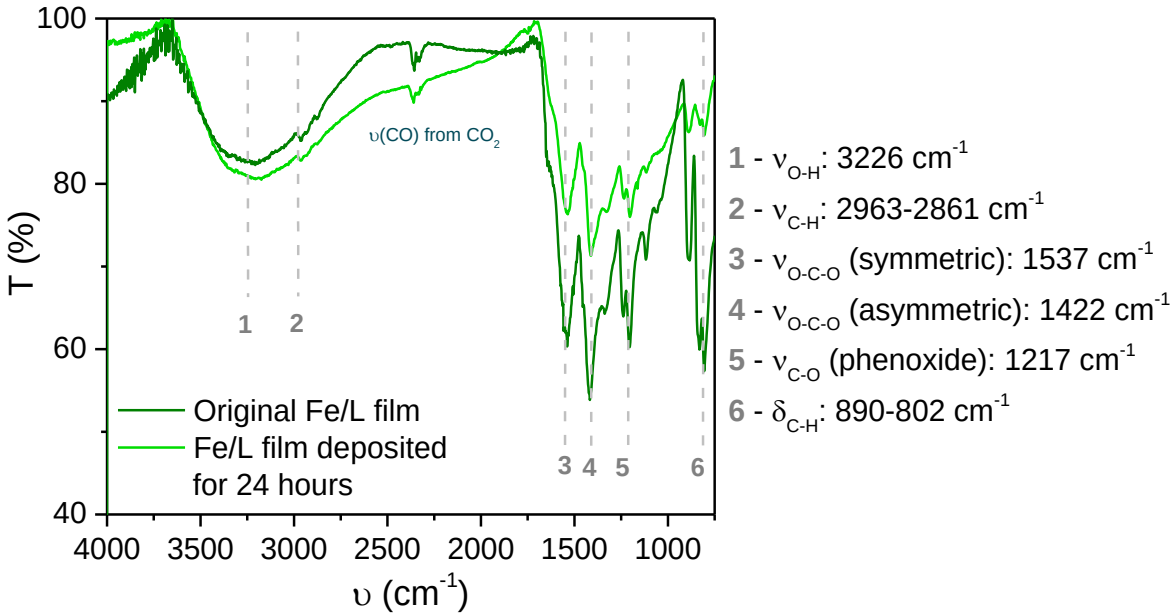

Figure A.74 - DRIFT spectra of the original (green) and the -1.0 V for 24 hours (dark green) **Fe/L** films (2:1:1 ratio of **M:H_4L:PB**, respectively). Spectra were recorded in a range of 4000-750 cm^{-1} and the blank was measured with a gold coated plate.

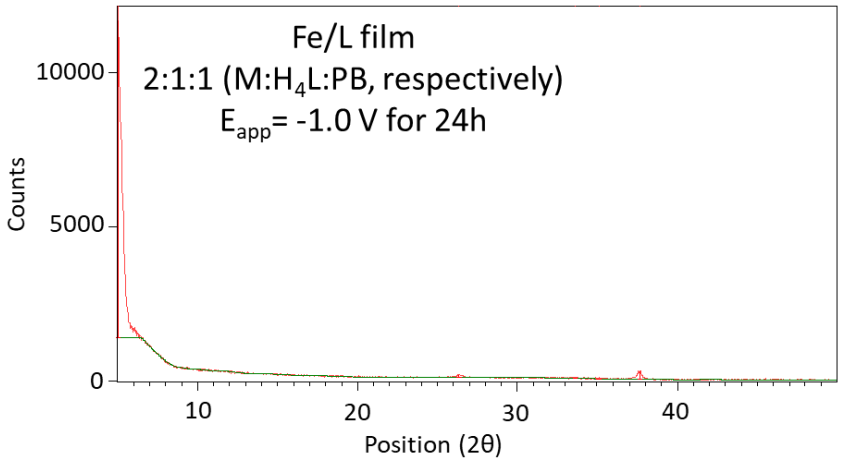

Figure A.75 - Diffractogram of the **Fe/L** film (2:1:1 ratio of **M:H4L:PB**, respectively) deposited at -1.0 V for 24 hours.

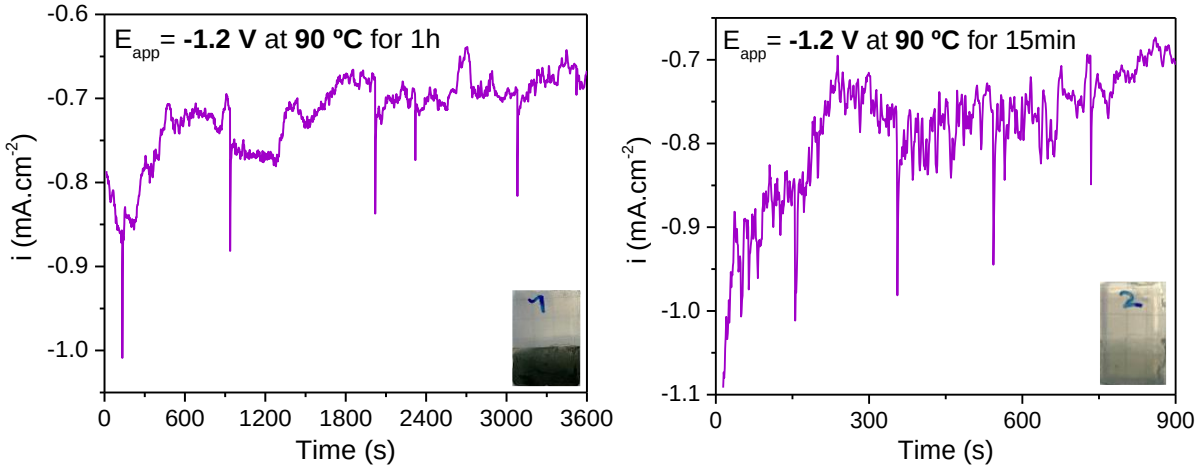

Figure A.76 - Chronoamperograms following the depositions of the **Fe/L** films with growth potentials of -1.2 V for a) 1 hour and b) 15 minutes. Electrodepositions were performed in 10 mL of N_2 saturated DMF, constituted by $TBAPF_6$ as supporting electrolyte, FTO as working, platinum wire as counter and 3 M Ag/AgCl as reference electrodes. Precursor quantities: 4 mM of **M**, 2 mM of **H4L** and 2 mM of **PB**.

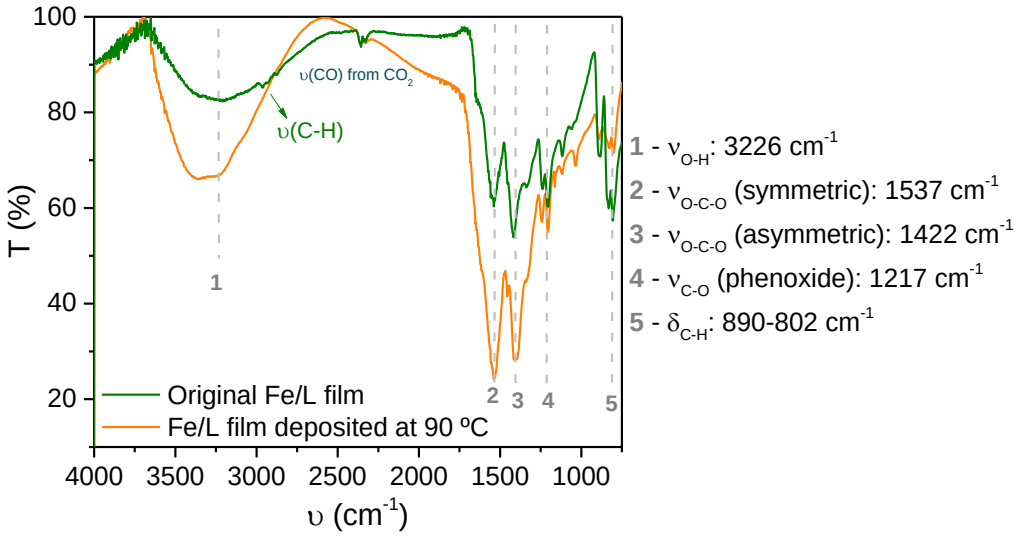

Figure A.77 - DRIFT spectra of the original (green) and the Fe/L film deposited at 90º C (orange) **Fe/L** films (2:1:1 ratio of **M:H4L:PB**, respectively). Spectra were recorded in a range of 4000-750 cm^{-1} and the blank was measured with a gold coated plate.

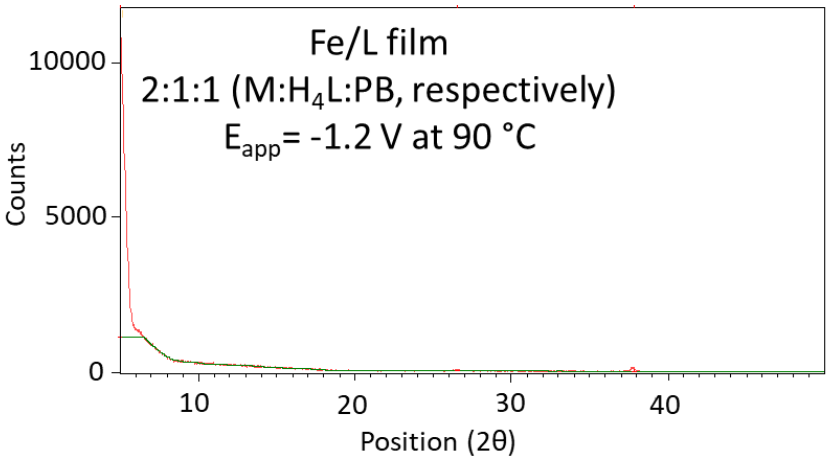

Figure A.78 - Diffractogram of the **Fe/L** film (2:1:1 ratio of **M:H_4L:PB**, respectively) deposited at -1.2 and 90 ºC for 1 hour.

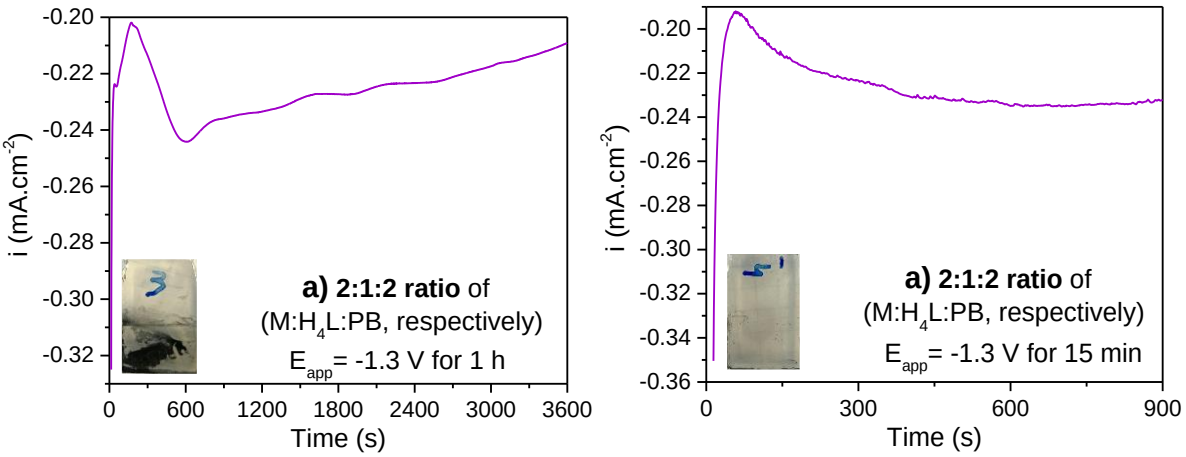

Figure A.79 - Chronoamperograms following the depositions of the **Fe/L** films at -1.3 V for a) 1 hour and b) 15 minutes. Electrodepositions were performed in 10 mL of N_2 saturated DMF with $TBAPF_6$ as the supporting electrolyte and recorded at 100 $mV.s^{-1}$. The one-compartment electrochemical cell was also constituted by FTO as working, platinum wire as counter and 3 M Ag/AgCl as reference electrodes. Species quantities: 4 mM of **M**, 2 mM of **H_4L** and 2 mM of **PB**.

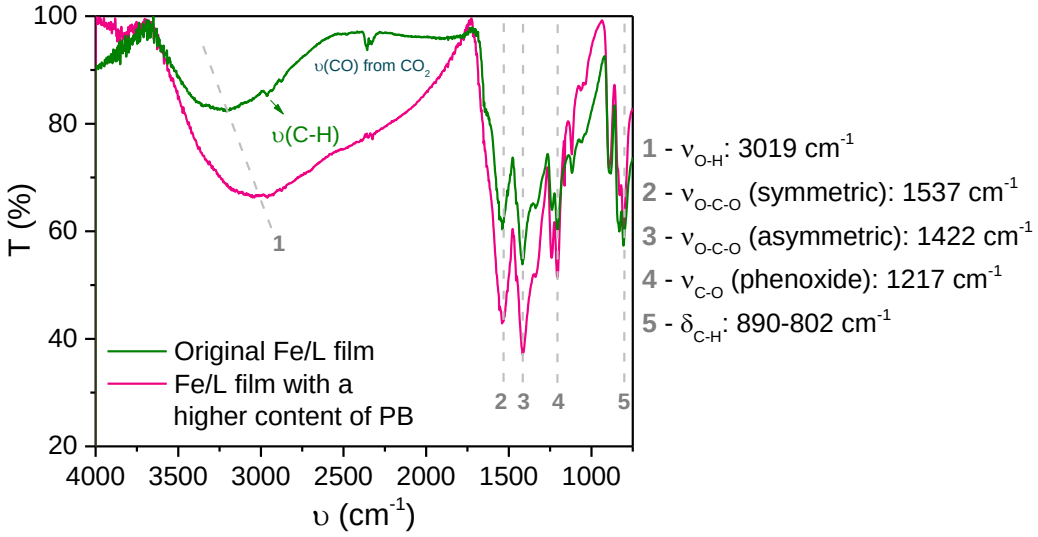

Figure A.80 - DRIFT spectra of the original (green) and with 4 mM of PB (pink) **Fe/L** films. Spectra were recorded in a range of 4000-750 cm^{-1} and the blank was measured with a gold coated plate.

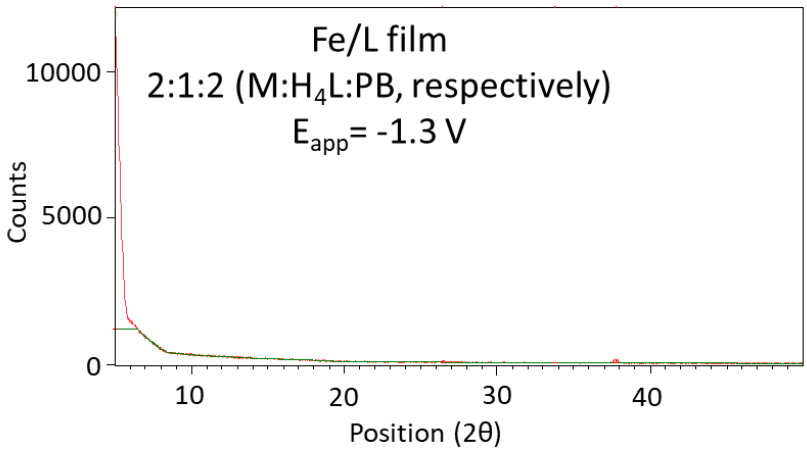

Figure A.81 - Diffractogram of the **Fe/L** film (2:1:2 ratio of **M:H_4L:PB**, respectively) deposited at -1.3 V for 1 hour.

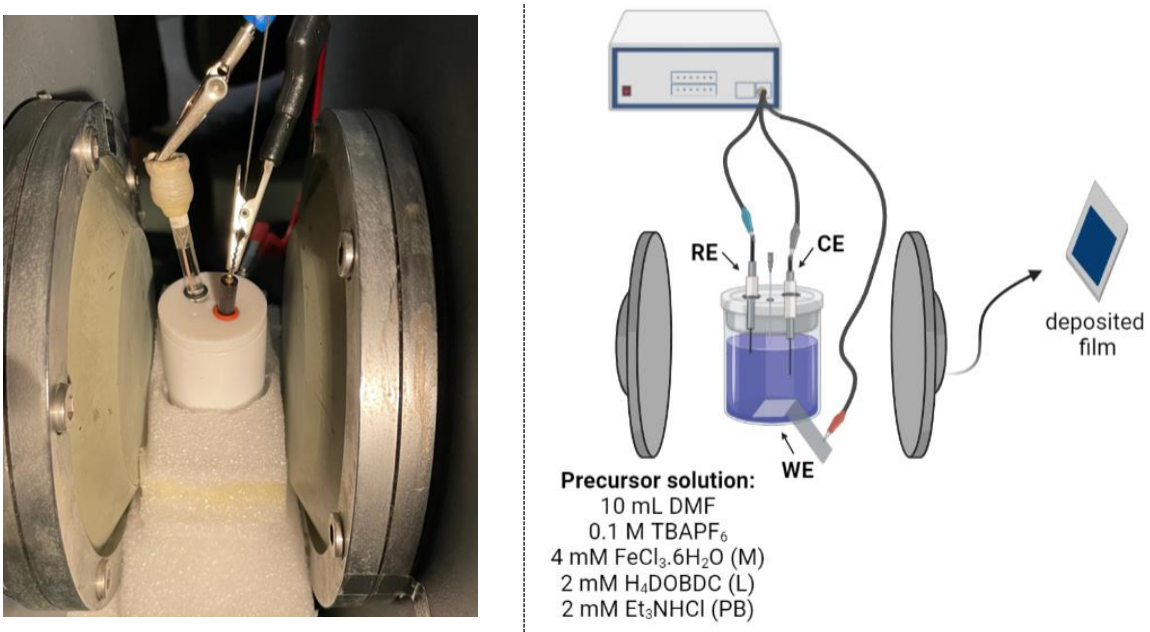

Figure A.82 - Assembly of the electrodeposition with an external magnetic field.

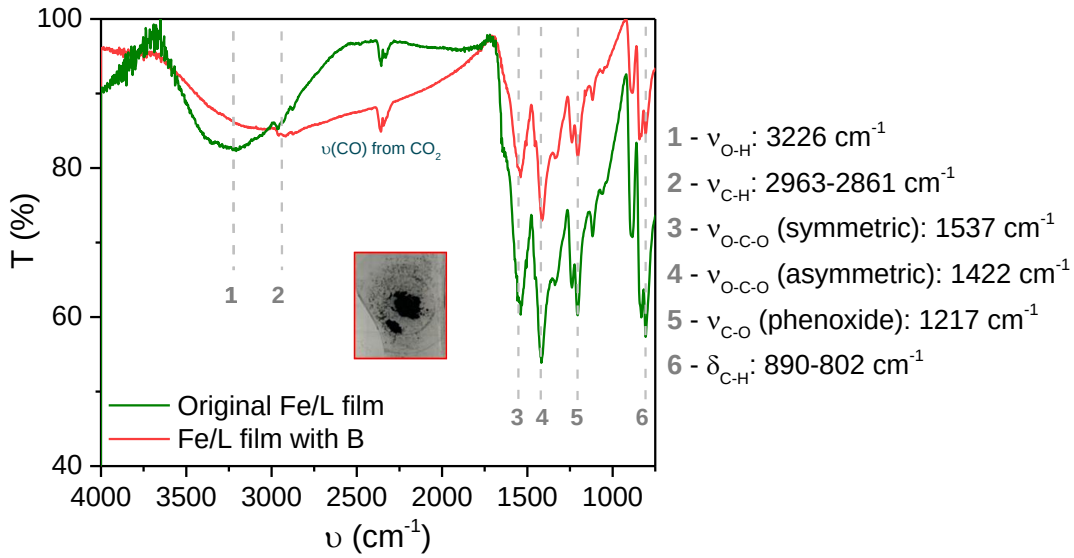

Figure A.83 - DRIFT spectra of the original (green) and the magnetic field (red) **Fe/L** films (2:1:1 ratio of **M:H4L:PB**, respectively), deposited at -1.3 V. Spectra were recorded in a range of 4000-750 cm^{-1} and the blank was measured with a gold coated plate.

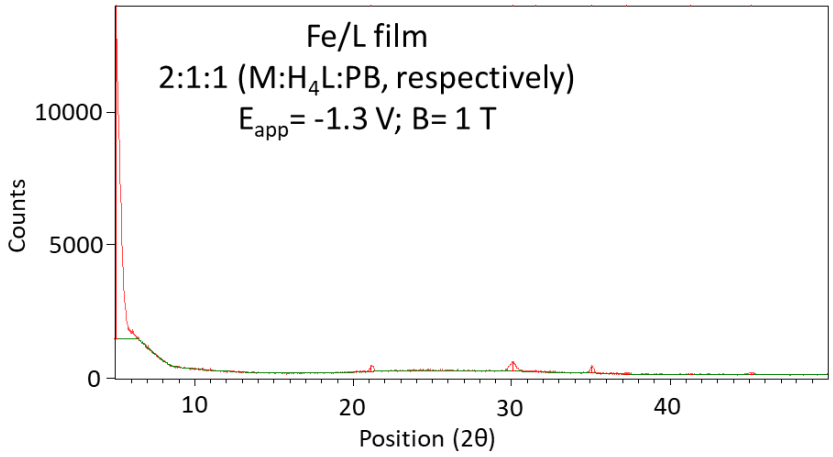

Figure A.84 - Diffractogram of the **Fe/L** film (2:1:1 ratio of **M:H4L:PB**, respectively) deposited at -1.3 V and 1 T.

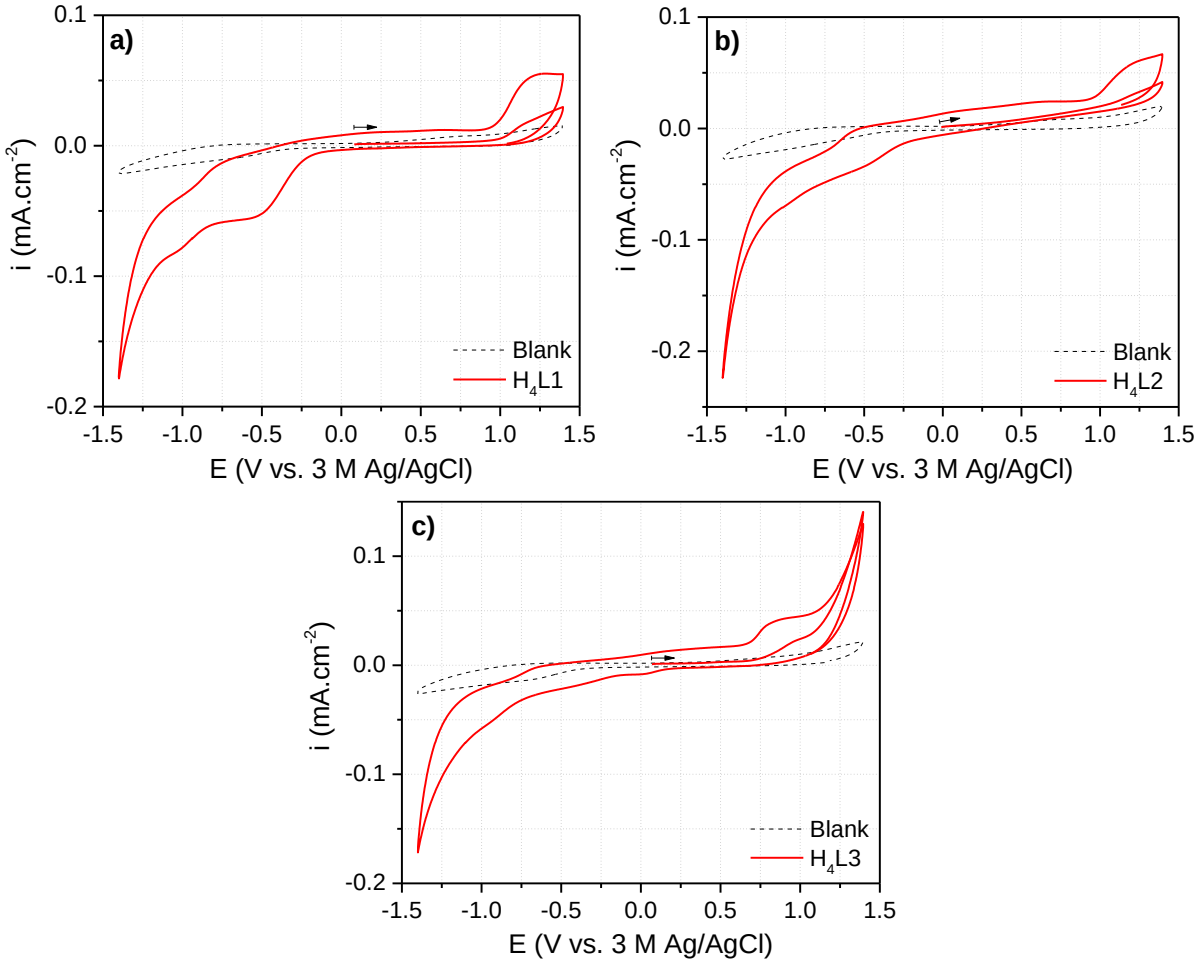

Figure A.85 - Cyclic voltammograms of a) **H_4L1** b) **H_4L2** and c) **H_4L3**. CVs were performed in 10 mL of N_2 saturated DMF with $TBAPF_6$ as the supporting electrolyte and recorded at 100 $mV.s^{-1}$. The one-compartment electrochemical cell was also constituted by FTO as working, platinum wire as counter and 3 M Ag/AgCl as reference electrodes. Species quantities: 2 mM of **H_4L1**, **H_4L2** or **H_4L3**.

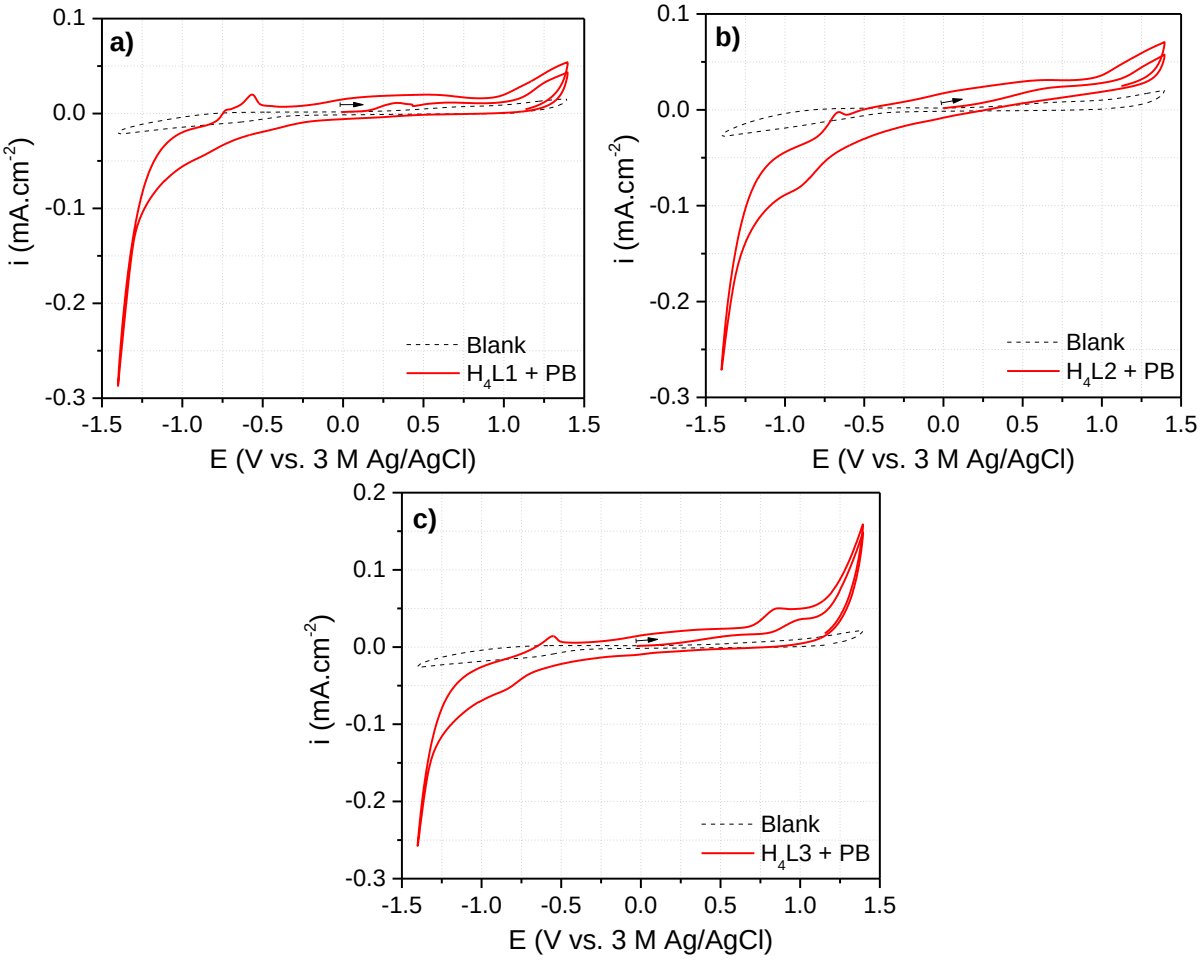

Figure A.86 - Cyclic voltammograms of a) **H_4L1+PB** b) **H_4L2+PB** and c) **H_4L3+PB**. CVs were performed in 10 mL of N_2 saturated DMF with $TBAPF_6$ as the supporting electrolyte and recorded at 100 $mV.s^{-1}$. The one-compartment electrochemical cell was also constituted by FTO as working, platinum wire as counter and 3 M Ag/AgCl as reference electrodes. Species quantities: 2 mM of **H_4L1**, **H_4L2** or **H_4L3** and 2 mM of **PB**.

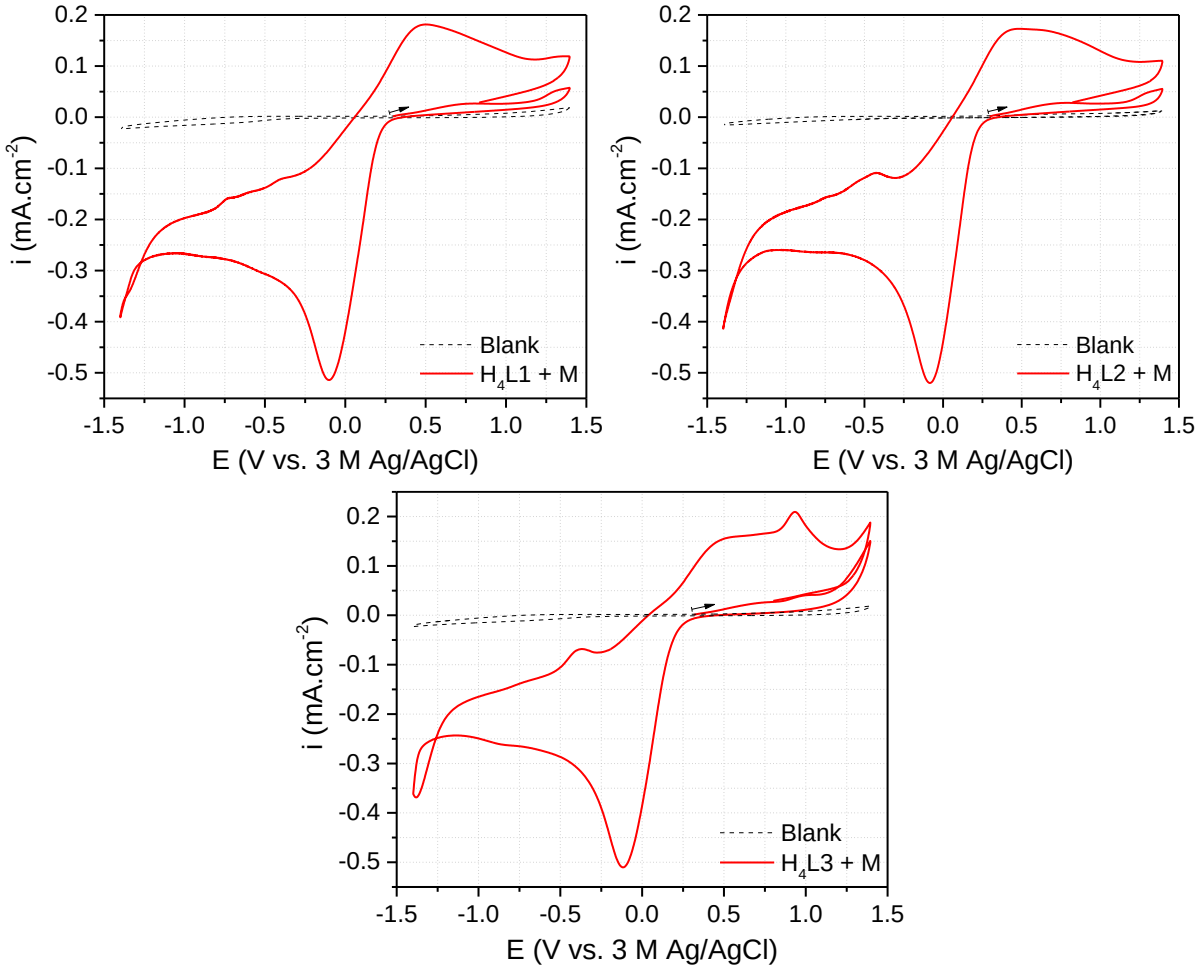

Figure A.87 - Cyclic voltammograms of a) **H_4L1+M** b) **H_4L2+M** and c) **H_4L3+M**. CVs were performed in 10 mL of N_2 saturated DMF with $TBAPF_6$ as the supporting electrolyte and recorded at 100 $mV.s^{-1}$. The one-compartment electrochemical cell was also constituted by FTO as working, platinum wire as counter and 3 M Ag/AgCl as reference electrodes. Species quantities: 4 mM of **M**, 2 mM of **H_4L1**, **H_4L2** or **H_4L3**.

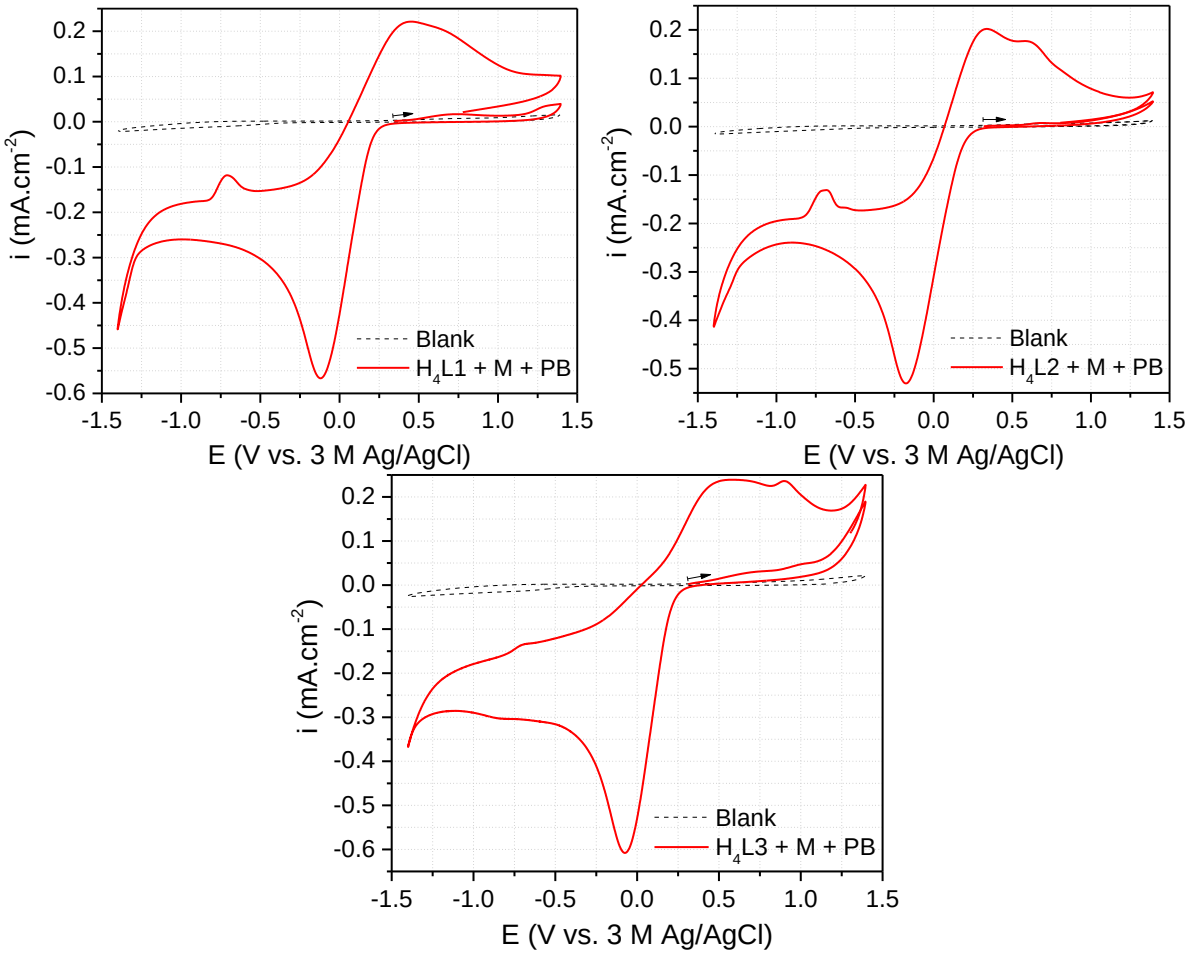

Figure A.88 - Cyclic voltammograms of a) **H_4L1+M+PB** b) **H_4L2+M+PB** and c) **H_4L3+M+PB**. CVs were performed in 10 mL of N_2 saturated DMF with $TBAPF_6$ as the supporting electrolyte and recorded at 100 $mV.s^{-1}$. The one-compartment electrochemical cell was also constituted by FTO as working, platinum wire as counter and 3 M Ag/AgCl as reference electrodes. Species quantities: 4 mM of **M**, 2 mM of **H_4L1**, **H_4L2** or **H_4L3** and 2 mM of **PB**.

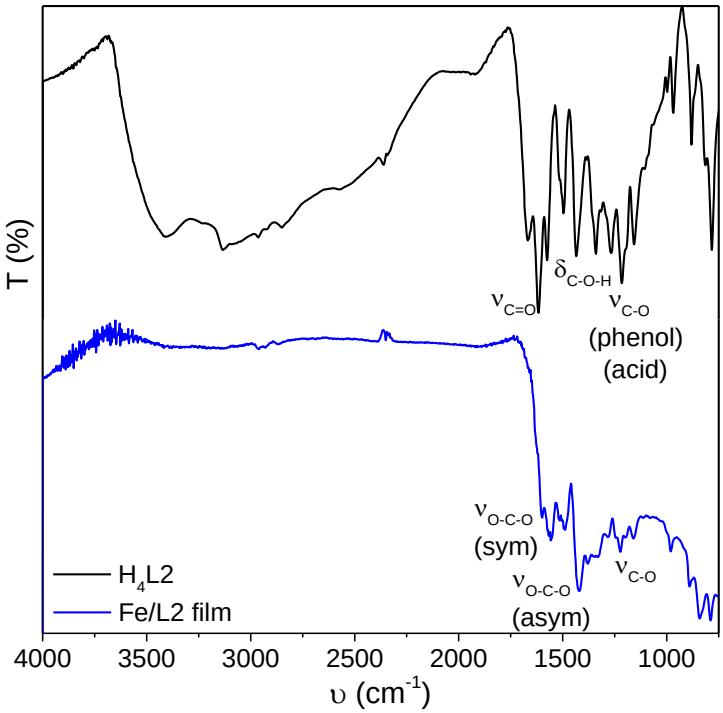

Figure A.89 - FTIR spectrum of **H_4L2** (**black**) and DRIFT spectrum of the **Fe/L2** film (**blue**) deposited at -1.3 V. Spectra were recorded in a range of 4000-500 cm^{-1}.

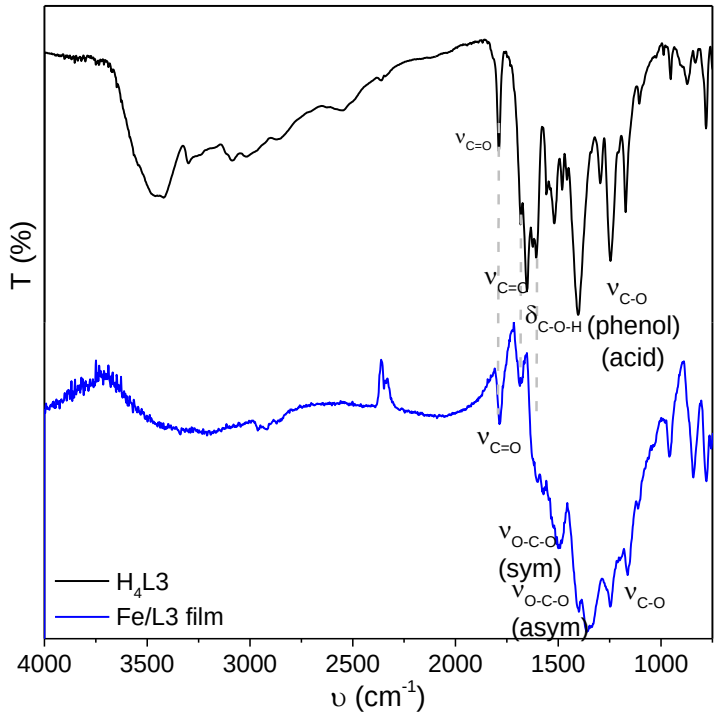

Figure A.90 - FTIR spectrum of **H_4L3** (**black**) and DRIFT spectrum of the **Fe/L3** film (**blue**) deposited at -1.3 V. Spectra were recorded in a range of 4000-500 cm^{-1}.

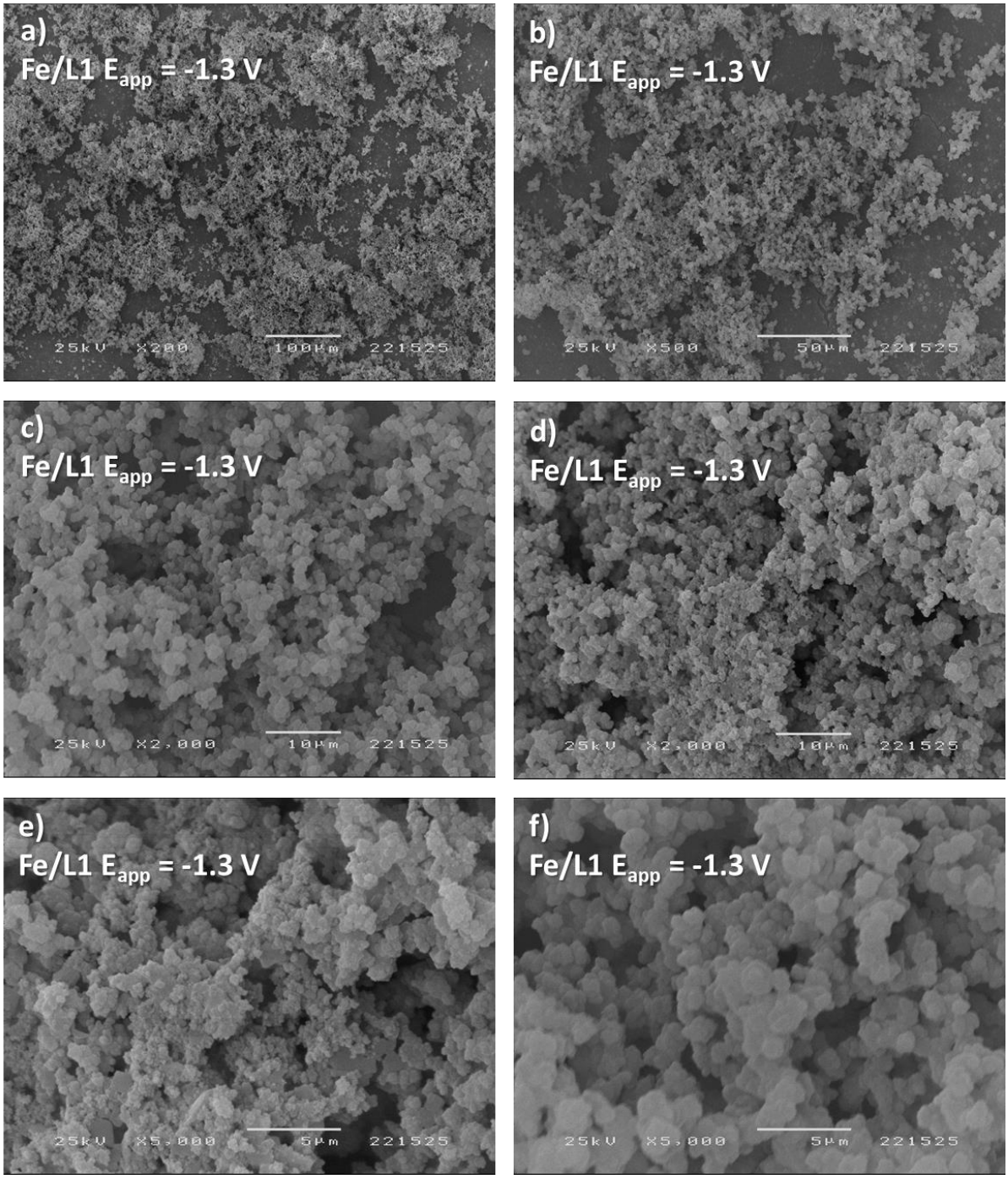

Figure A.91 - SEM images of the **Fe/L1** film deposited at -1.3 V, magnified at a) x200, b) x500, c) x2000, d) x2000, e) x5000 and f) x5000.

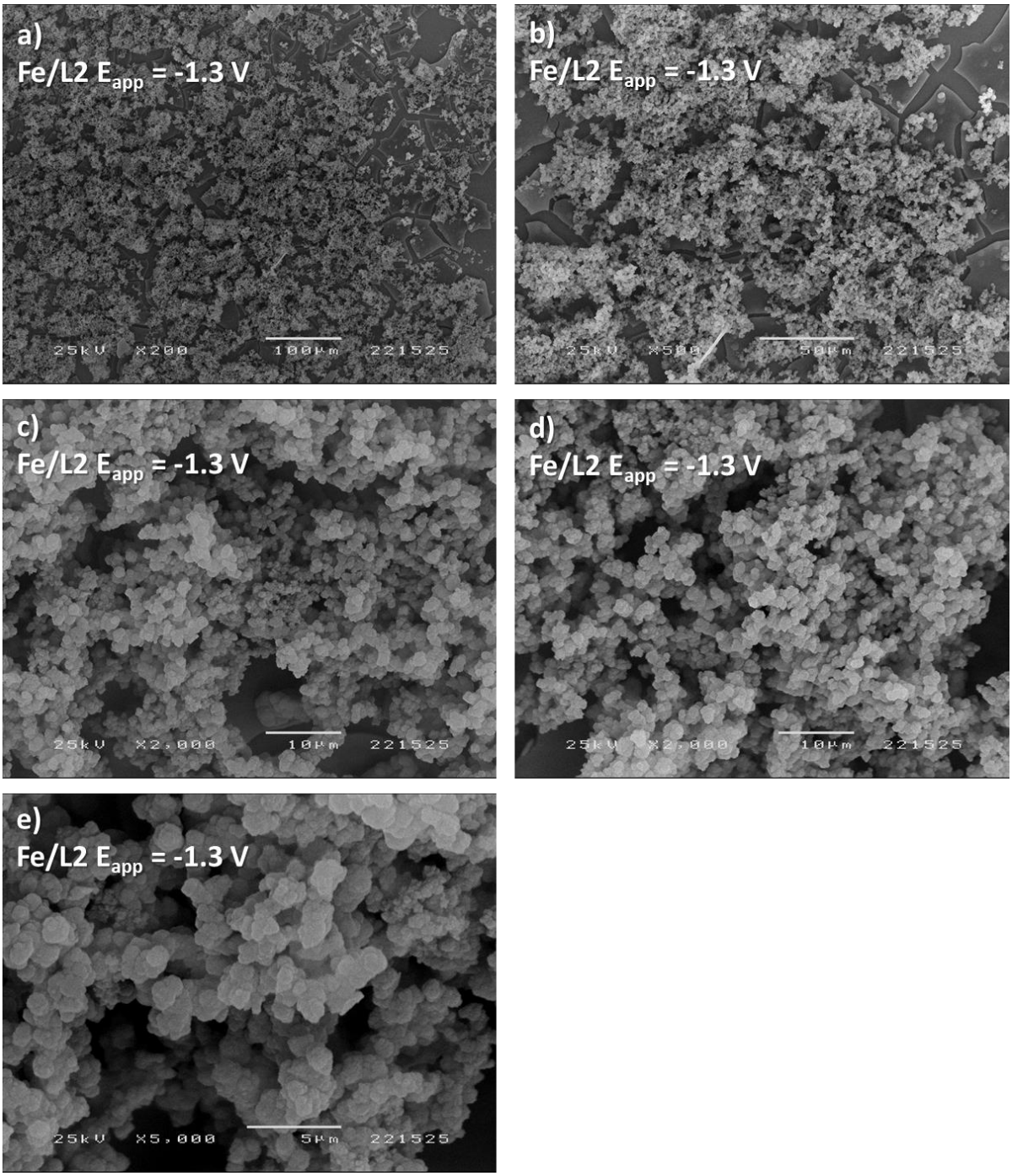

Figure A.92 - SEM images of the **Fe/L2** film deposited at -1.3 V, magnified at a) x200, b) x500, c) x2000, d) x2000 and e) x5000.

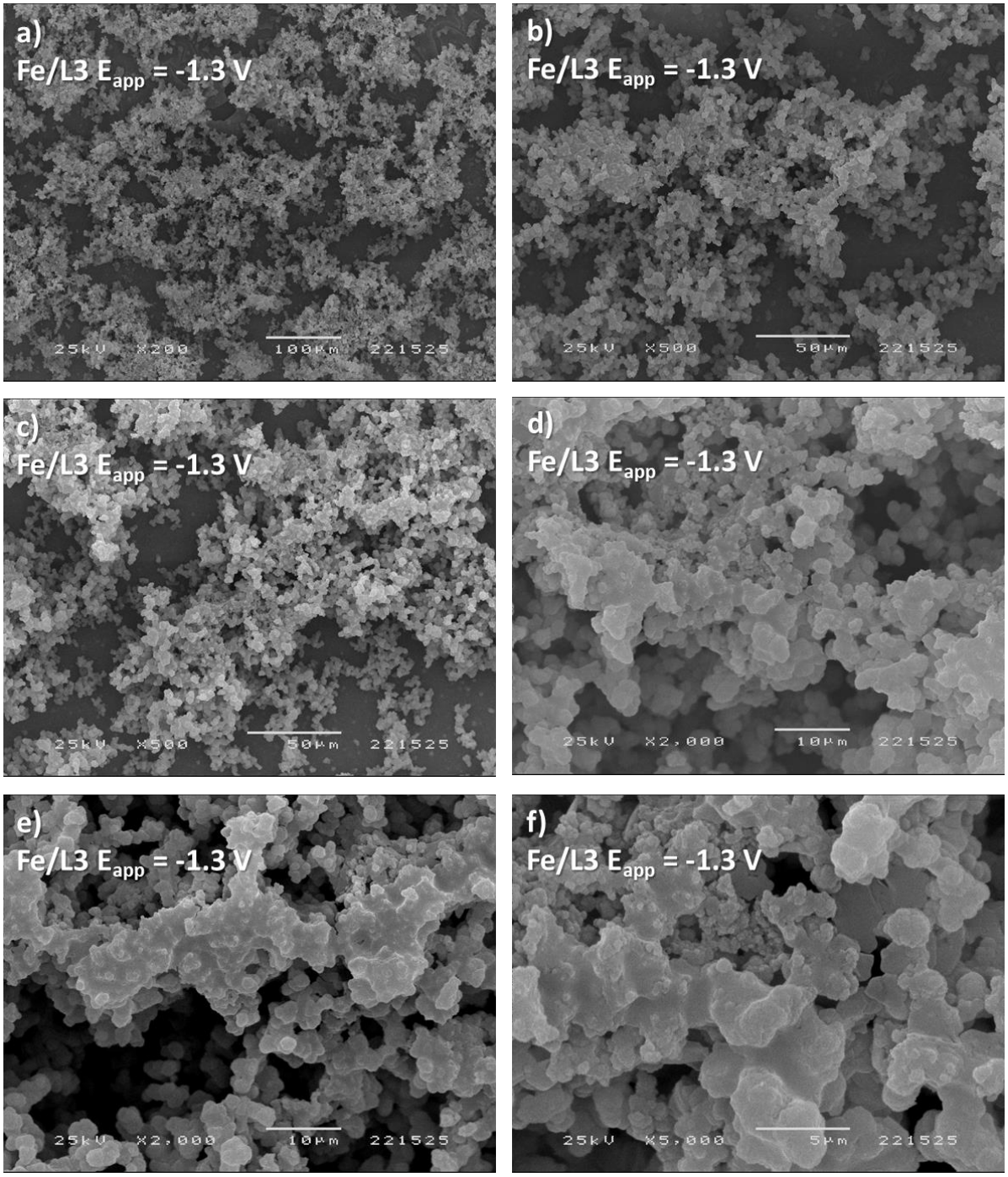

Figure A.93 - SEM images of the **Fe/L3** film deposited at -1.3 V, magnified at a) x200, b) x500, c) x500, d) x2000, e) x2000 and f) x5000.

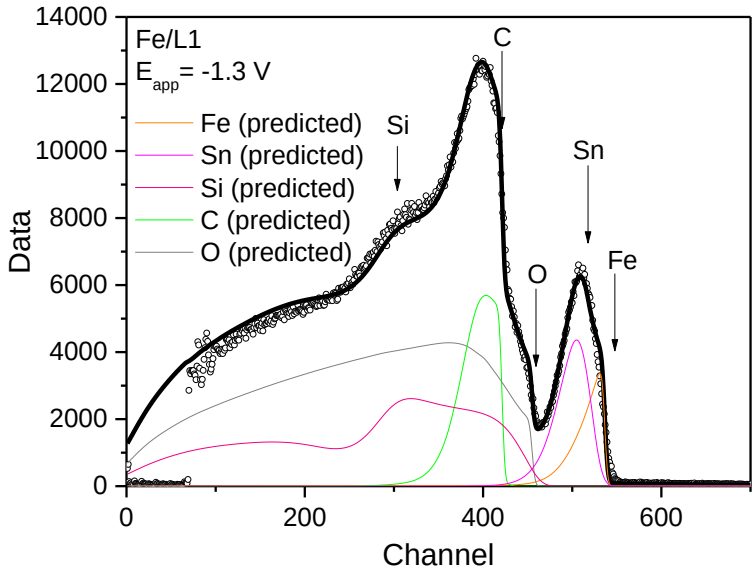

Figure A.94 - Adjusted RBS spectrum of the **Fe/L1** film deposited at -1.3 V in the zone Identified as 007 (beam dimension: 3x4 μm^2).

Table A.16 - Fe/O and Fe/C atomic ratios of the **Fe/L1** film, obtained from the RBS spectra.

Atomic ratio	Expected for Fe_2L1	006	007	008
Fe/O	0.33	0.49	0.24	0.38
Fe/C	0.14	0.23	0.11	0.14
Thickness (nm)	-	>2124	>2373	>1490

Table A.17 - Fe/O and Fe/C atomic ratios of the **Fe/L2** film, obtained from the RBS spectrum.

Atomic ratio	Expected for Fe_2L2	106
Fe/O	0.33	0.25
Fe/C	0.10	0.12
N/O	0.33	0.84
Thickness (nm)	-	>1897

Table A.18 - Fe/O and Fe/C atomic ratios of the **Fe/L3** film, obtained from the RBS spectra.

Atomic ratio	Expected for Fe_2L3	97	98
Fe/O	0.25	0.24	0.23
Fe/C	0.11	0.65	0.64
N/O	0.25	0.17	0.18
Thickness (nm)	-	>18045	>18884

Table A.19 - Peak deconvolution of C 1s, Fe 2p and O 1s from the XPS survey spectra of the **Fe/L1**, **Fe/L2** and **Fe/L3** films.

	Fe/L1 film (E_{app}= -1.3 V)	Fe/L2 film (E_{app}= -1.3 V)	Fe/L3 film (E_{app}= -1.3 V)	Attribution
C 1s	285.0	285.0	285.0	C-C and C-H
	286.3	286.4	286.4	$C\text{-}O^-$
	288.8	288.7	288.8	$O{=}C\text{-}O^-$
Fe 2p	-	709.2	-	FeO
	710.4	710.5	710.2	$Fe(OH)_2$
	-	-	711.4	Fe_3O_4
	711.7	711.8	712.5	Fe_2O_3
	713.4	713.0	-	$Fe(OH)_3$
	715.5	714.6	715.3	Satellite
	718.4	718.5	-	Satellite
	-	-	719.9	Satellite
O 1s	531.7	-	-	$^-O\text{-}C{=}O$
	532.7	-	-	$^-O\text{-}C$

Table A.20 - Atomic concentration (%) of Fe, C and O of the **Fe/L1** film.

	%atm		
	Fe/L1 film (E_{app}= -1.3 V)	Expected for Fe_2L1	Expected for $Fe_2L1(DMF)(H_2O)$
Fe	2.2	9.1	4.4
C	58.6	63.6	37.8
O	24.2	27.3	17.8
N	3.3	0	2.2

Table A.21 - Atomic concentration (%) of Fe, C and O of the **Fe/L2** film.

	%atm	
	Fe/L2 film (E_{app}= -1.3 V)	**Expected for Fe_2L2**
Fe	1.3	6.25
C	69.9	65.6
O	19.4	18.75
N	5.3	6.25

Table A.22 - Atomic concentration (%) of Fe, C and O of the **Fe/L2** film.

	%atm	
	Fe/L3 film (E_{app}= -1.3 V)	**Expected for Fe_2L3**
Fe	2.4	6.25
C	63.4	56.25
O	19.7	25
N	5.2	6.25

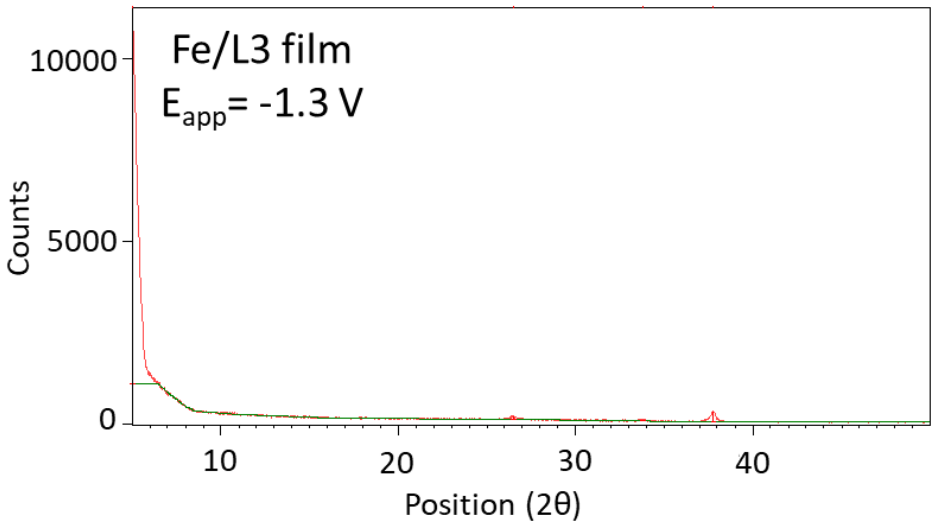

Figure A.95 - Diffractogram of the **Fe/L3** film deposited at -1.3 V for 1 hour.

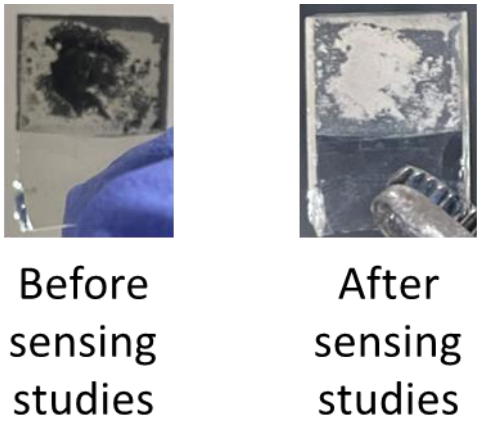

Figure A.96 - 15-minute **Fe/L** film (2:1:1 ratio of **M:H$_4$L:PB**, respectively) before UA sensing studies (black film) and after (white film) in PBS buffer.

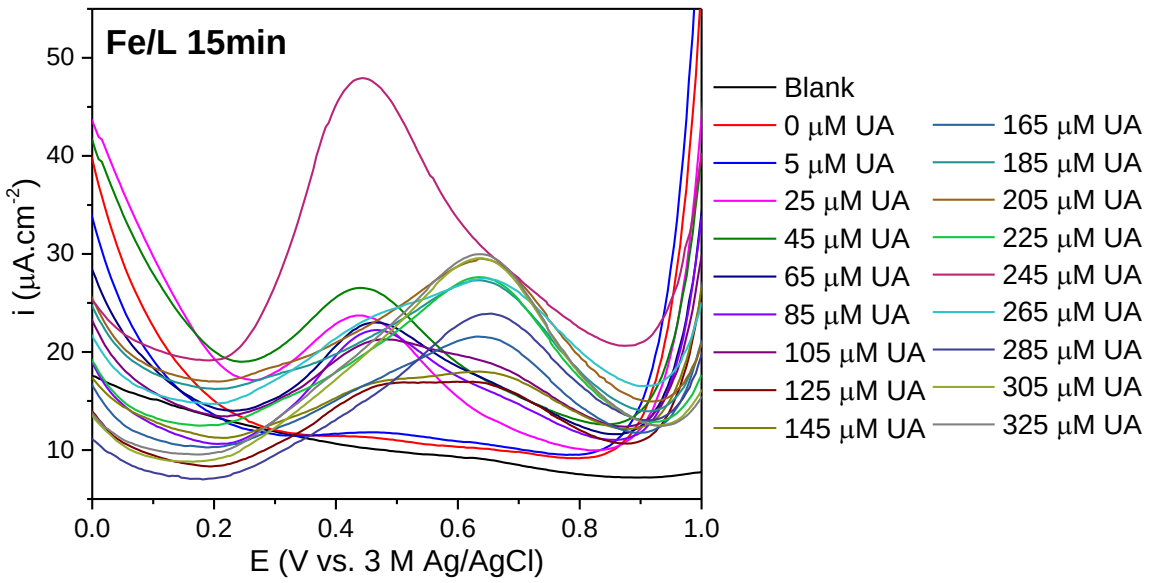

Figure A.97 -- DPV voltammograms of UA concentrations on a range of 50 to 325 mM on 15-minute **Fe/L film** in tris buffer.